DISPERSION IN A TWO-PHASE FLOW SULZER COLUMN

Eugenia T. Iacob Tudose

"Gheorghe Asachi" Technical University of Iasi, Faculty of Chemical Engineering and Environmental Protection, 73 Prof. Dr. Docent D.Mangeron Blvd, 700050, Iasi, Romania, e-mail:et_tudose@yahoo.com

Introduction

Axial mixing in a Sulzer packed-bed column in the case of a single liquid phase and two-phase (gas-liquid) flows, has been studied. Tap water and respectively, air have been counter-currently circulated. The pulse response technique was used to obtain the experimental residence time distribution, $E(\theta)_{exp}$, and the normalized dispersion, σ_θ^2, at different liquid and gas flow rates, to be compared to other models, namely the axial dispersion and the cellular model. Furthermore, the dispersion coefficient and its dependence on the superficial gas velocity has been established for the investigated flow rate range. Additionally, the liquid hold-up in the column was determined at different gas flow rates.

Experimental setup and method

The pulse response method consists of injecting an inert salt solution at the column entrance, followed by its concentration measurement at the column exit. All the experiments have been conducted at room temperature (~20°C), for different water flow rates of 200, 400, 600 and 800 L/h and gas flow rates of 0, 5, 10, 15, 20 m^3/h, using the experimental setup in Fig.1.

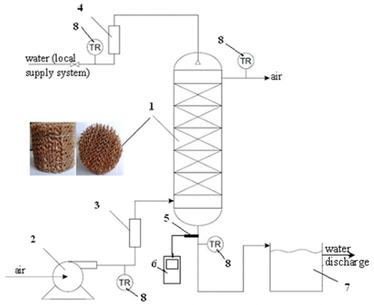

Fig.1 Experimental setup with a Sulzer column: 1 - centrifugal ventilator; 2-air rotameter; 3-Sulzer column (detail: one Sulzer package); 4- liquid rotameter, 5 – conductometer probe; 6-conductometer, 7-vessel; 8-digital thermometers

Results and discussions

The experimental concentration data have been used to calculate respectively, the residence time distribution function, *E(t)*, the normalized residence time distribution function, *E(θ)*, the mean residence time, τ, the normalized mean residence time, θ, the dispersion, σ^2 and the normalized dispersion, σ_θ^2, based on the equations (1-6) [1]. The obtained profiles are plotted in Fig.2, indicating an almost symmetrical distribution, especially at low gas and liquid flow rates. As the gas flow rate increases, the dispersion of experimental data increases, suggesting a more uneven distribution of the two phases over the cross-sectional column area.

$$E(t) = \frac{C(t)}{\int_0^\infty C(t)dt} \quad (1) \qquad E(\theta) = \tau E(t) \quad (2)$$

$$\tau = \frac{\sum t_i C_i \Delta t_i}{\sum C_i \Delta t_i} \quad (3) \qquad \theta = \frac{t_i}{\tau} \quad (4)$$

$$\sigma^2 = \frac{\int_0^\infty t^2 C dt}{\int_0^\infty C dt} - \tau^2 \quad (5) \qquad \sigma_\theta^2 = \frac{\sigma^2}{\tau^2} \quad (6)$$

$$\sigma_\theta^2 = \frac{2}{Pe_L} \quad (7) \qquad N = 1/\sigma_\theta^2 \quad (8)$$

$$E(\theta)\_disp = \sqrt{\frac{Pe_L}{4\pi\theta}} \exp\left[-\frac{Pe_L(1-\theta)^2}{4\theta}\right] \quad (9)$$

$$E(\theta)\_cel = \tau E(t) = \frac{N(N\theta)^{N-1}}{(N-1)!} e^{-N\theta} \quad (10)$$

$$\frac{D}{u_L H} = \frac{\sigma_\theta^2}{2} \quad (11)$$

D-axial dispersion coefficient, u_L-liquid superficial velocity, H –packed bed height.

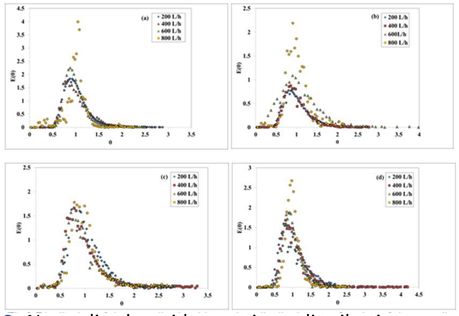

Fig.2 Normalized residence time distribution as a function of the normalized mean residence time, for different liquid flow rates, at constant gas flow rate (a) 5m^3/h, (b) 10m^3/h, (c) 15m^3/h, (d) 20 m^3/h

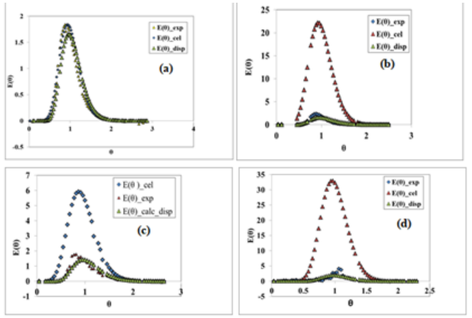

Fig.3 Residence time distribution, at a 5 m^3/h gas flow rate and different liquid flow rates: **a)** 200 L/h; **b)** 400 L/h; **c)** 600 L/h; **d)** 800 L/h

Comparisons of the experimental data to the axial dispersion and the cellular models were performed and rendered good similarities depending on the liquid flow rate. For the dispersion model, starting from the experimental value of the normalized dispersion, σ_θ^2, the liquid Péclet number, Pe_L, was calculated with equation (7), followed by the normalized distribution of the residence times E(θ)_disp for the axial dispersion model, given by equation (9) to be compared to the obstained experimental data. For the cellular model, starting from the experimental value of the normalized dispersion, σ_θ^2, the number of cells N was calculated using equation (8) and also, the model characteristic residence time distribution function, E(θ)_cel, using equation (10) to be compared to the E(θ)_exp. Some other comparisons are presented in Fig.3 and all the data are synthesized in Table 1.

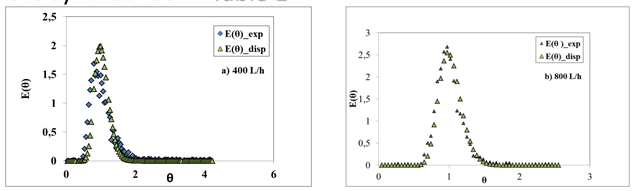

Fig.4 Residence time distribution, at a 20 m3/h gas flow rate and two liquid flow rates: **a)** 400 L/h; b) 800 L/h

Table1 Experimental residence time distribution comparison to axial dispersion (AD) and N-Tanks-in-series (TS) (cellular) models

M_{vL} (L/h) / M_{vG} (m^3/h)	200	400	600	800
0	~ TS	AD	AD	~`AD
5	TS / AD	AD	AD	AD
10	≈ AD	≈ AD	`AD	AD /flooding
15	AD	(flooding)	(flooding)	(flooding)
20	AD/flooding	(flooding)	(flooding)	AD

The experimental dispersion coefficient (eq.11) increased with the liquid superficial velocity, in accordance to other literature data [2], as seen in Fig.5.

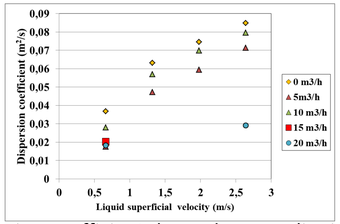

Fig.5 Dispersion coefficient dependence on liquid superficial velocity

The liquid holdup increases with the liquid specific flow rate, at different constant gas flow rates, as presented in Fig.6.

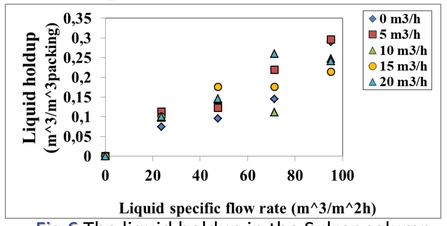

Fig.6 The liquid holdup in the Sulzer column

Conclusions

Residence time distributions were experimentally obtained in a 9-pack Sulzer column. Based on the obtained normalized dispersion, the distributions for the axial dispersion and N tanks-in-series models were obtained and compared to the experimental E(θ)_exp. It was established that at larger gas flow rates (>5 m^3/h) and liquid flow rates (>200 L/h), the axial dispersion model gives the best results, provided no column flooding occurs. Dispersion coefficient and liquid holdup were also determined.

References

1. Levenspiel, Chemical Reaction Engineering, 3rd Edition, John Wiley & Sons, New York, 1999.
2. Abdulrazzaq B.S., Investigation measurement of dispersion coefficient and mxing times in bubble column, Diyala Journalof Engineering Sciences, Vol. 03 , No. 02 , pp. 97-112, 2010.

CHEMICAL RECYCLING OF WASTEPAPER TO VALUABLE PRODUCTS

Aleksandra M. Mikhailidi[1], Nina E. Kotelnikova[2]

[1] *St. Petersburg State University of Industrial Technologies and Design, St. Petersburg, Russia; E-mail: amikhailidi@yahoo.com;*
[2] *Institute of Macromolecular Compounds, Russian Academy of Sciences, St. Petersburg, Russia*

Introduction

Waste utilisation is an environmental problem and an economic one as well because almost all wastes are considered to be a useful resource. Wastepaper recycling is of practical interest since this is a cellulose-containing raw material.

The **aim** of this study was to develop an environmentally friendly, effective and low-cost method for manufacturing cellulose-based hydrogels (HGs) from the wastepaper. Characterization of the properties of the HGs was the second goal of this study.

Materials and methods

Initial samples were of low quality grade newsprint (P) and various types of cardboard (C) without printing. They were dissolved in solutions of DMAc/LiCl (Flow chart).

Concentration of the waste paper in DMAc/LiCl was from 0.3 to 1.0 mass. %. The dissolving ability in DMAc/LiCl, equilibrium water content (EWC) and porosity of the samples were determined as described in [1].

Formation of the gels from the solutions occurred at the ambient atmosphere, when slow aggregation was accompanied by a spontaneous gelation. By the replacement of the solvent to water the super-swollen HGs were formed (Fig. 1). They were freeze-dried.

FTIR spectroscopy was used to characterize the functional content of the initial samples and HGs. WAXS was used to study the structure and SEM was applied to study the surface morphology.

Laboratory flow chart

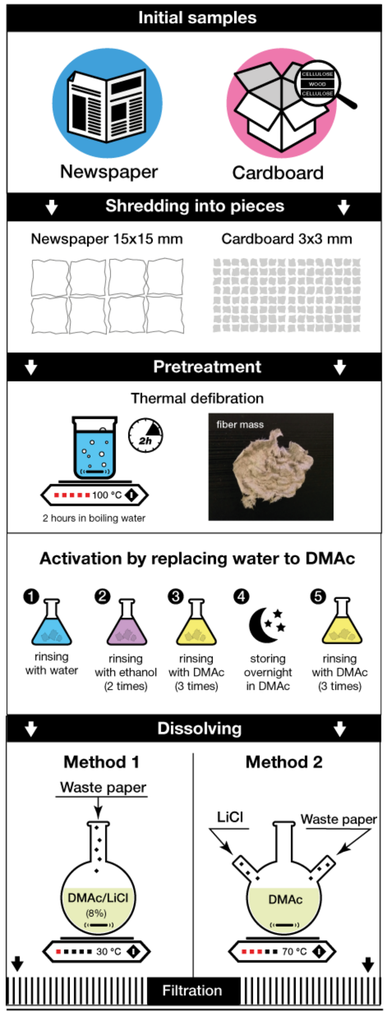

Results and discussions

The dissolving ability of waste samples in DMAc/LiCl mainly depended on the type of sample and additional grinding.

Table 1. The properties of the solutions and the hydrogels

N	t, °C	Dissolving ability, %	Hydrogel characterization	
			EWC, mass.%	Porosity, %
C-3	70	50	2913	98,26
C-5	25	100	1646	-
P-4	25	21	3717	98,87
P-5	70	25	1435	97,08
Flax	25	100	920	95,62

EWC values of the HGs of both species ranged from 1435 to 3717 mass.%, which is significantly higher than the EWC values for the HGs from pulps. These values show that the HGs are the super swollen systems.

According to FTIR analysis, the initial waste samples revealed a high content of cellulose, however, some amounts of hemicellulose and lignin were detected. The HGs regenerated from the solutions were of high chemical purity.

The X-ray pattern of the initial C had peaks characteristic of the cellulose I crystal structure (Fig 2, a). The pattern of the HG did not reveal any reflections of cellulose lattice (Fig. 2, b) and resembled the diffraction pattern of water. The freeze-dried HG formed the structure of partially ordered cellulose II (Fig. 2, c).

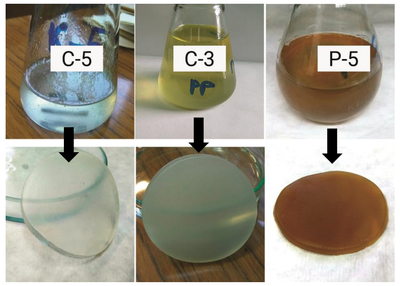

Fig. 1. *The solutions and HGs*

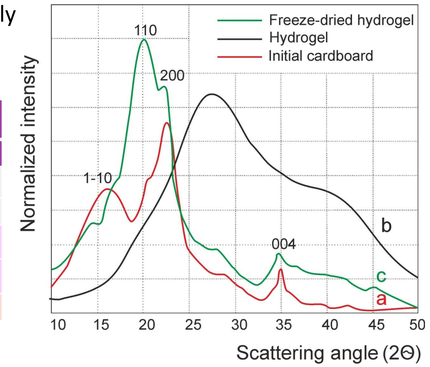

Fig. 2. *WAXS patterns of C and the HGs*

The sorption capacity (SC) of the swollen and freeze-dried HGs was studied in relation to the dye methylene blue. The swollen HGs had low apparent SC, while the freeze-dried samples exhibited much higher SC.

The SEM image of the freeze-dried HG showed uniformly distributed pores of different sizes. Obviously, this affected the high sorption capacity of the HG.

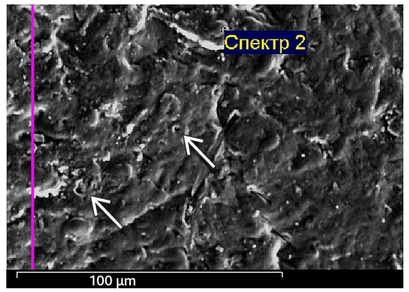

Fig. 3. *SEM image of the freeze-dried HG from C*

Conclusions

1. A cost-effective, efficient and environmentally friendly method of obtaining hydrogels from recycled paper and cardboard was performed.
2. The dissolution of wastepaper in the DMAc/LiCl dissolving system was studied and methods for regenerating samples from the solutions to prepare of the HGs were developed.
3. For the first time, stable HGs were obtained from wastepaper solutions. The HGs had the high EWC values (up to 3700 %) and the porous structure (porosity 98.9 %).
4. It was shown by wide-angle X-ray scattering that the crystallographic structure of the initial wastepaper samples corresponded to cellulose polymorph I.
5. The structure of the freeze-dried HGs corresponded to a partially ordered crystallographic cell of cellulose II.
6. According to FTIR spectroscopy, the functional composition of the regenerated HGs corresponded to cellulose of high chemical purity.
7. According to SEM, the freeze dried HGs had a system of uniformly distributed pores of different sizes, which determined their high sorption capacity. The sorption capacity of HGs is promising for their practical use.

Reference

[1] Kotelnikova, N.E., Mikhailidi, A.M., Martakova, Yu.V., Andersson S., *Cell Chem Tech* **50**(3-4), 545 (2016).

New equations for gas phase pressure drop in expanded metal sheet packings for transfer processes in packed columns

Krum A. Semkov, Tatyana. St. Petrova

Institute of Chemical Engineering, Bulgarian Academy of Sciences, Akad. G. Bonchev Str., bl.103, 1113 Sofia, Bulgaria

Introduction

The horizontal expanded metal sheet packing (called also Holpack) is designed and investigated for carrying out mass and heat transfer processes in column apparatuses (Kolev, 2006). The packing is made of expanded metal sheets, placed horizontally on certain distance from one another along the column height, and arranged consequently by rotating of 90^0 in the same direction – the so called "crosswise" arrangement. This construction leads to low specific weight and creates condition for highly effective heat and mass transfer at comparatively low gas pressure drop, as well as large specific effective surface area. The earlier models and equations for determination of the pressure drop of dry and irrigated Holpack packing as well as for loading point gas velocity were proposed by (Kolev and Darakchiev, 1973; 1974; Kolev, 2006). Subsequently, after many years of practical (incl. industrial) experience (Semkov, 2006), three new improved dependences were developed, firstly presented in this work – for dry and irrigated pressure drop and for gas loading point velocity for HOLPACK.

Materials and method

For the new equations the same experimental data are used as for in the old ones (Kolev and Darakchiev, 1974). The principal differences evolve from the more accurate and well-founded structure of the new equations and the better estimation of the geometric dimensions . The main characteristics of the packings used for pressure drop investigation are presented in the Table:

No.	Sym-bol	A mm	B mm	C mm	δ mm	s mm	s_1 mm	h_1 mm	h_2 mm	d_h mm	ε_1 %	a m^2/m^3
						D_c = 190 mm						
1*	◇	22.2	30.7	6.4	1.0	4.8	4.2	3.2	20	6.2	76.6	76.6
2	□	22.2	30.7	6.4	0.8	5.0	4.0	3.0	40	6.5	81.2	37.8
3	⊕	22.2	42.7	7.7	1.0	4.5	6.2	4.6	20	6.4	86.0	63.1
						D_c = 470 mm						
4	■	85.0	114	36.0	4.0	16.0	24.0	17.5	10	20.8	83.0	61.6
5	◔	90.0	121	27.0	1.5	13.0	16.5	13.2	50	17.1	91.6	22.1

* The sheets are covered with polyethylene.

The equations are derived using the dimensional analysis and the least square approach regression. For each equation the main statistic parameters (the mean arithmetic error and the standard deviation) are given. The confidence intervals of the constants based on Student distribution at 95% confidence level are presented as well. The comparison with the experimental data is illustrated in appropriate diagrams. The accuracy of the new equations is substantially improved, offering a stable base for industrial design and applications.

Packing element and arrangement

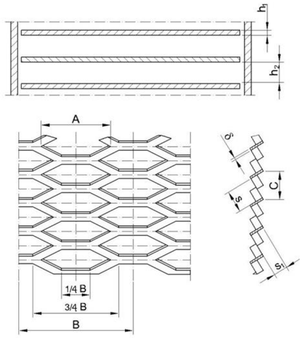

Pressure drop of dry HOLPACK packing (ΔP_0)

$$Eu = \left(0.0343 + \frac{2.16}{\mathrm{Re}_G}\right) N_1 \left(\frac{H}{d_h}\right)\left(\frac{h_1}{d_h}\right)^{2.47} \mathrm{Re}_G^{0.112}$$

The mean relative arithmetic error is 7.88% and the standard deviation 12.6%.

Pressure drop of irrigated packing (ΔP)

$$\frac{\Delta P}{\Delta P_0} = 0.89\,\mathrm{Re}_L^{0.17}\left(\frac{s_1}{d_h}\right)^{-0.25} \mathrm{Re}_G^{-0.054}$$

The mean relative arithmetic error is 5.5% and the standard deviation 8.6%.

Loading point gas velocity (w_{0G})

$$MFr_G = 2.0\left(\frac{s_1}{d_h}\right)^{-0.90} Fr_L^{-0.11}$$

The mean relative arithmetic error is 4.56% and the standard deviation 7.67%.

Results and discussions

Dimensionless numbers and notations used:

$$Eu = \frac{2\Delta P_0 \varepsilon_1^2}{w_0^2 \rho_G};\quad \mathrm{Re}_G = \frac{w_0 d_h}{\nu_G \varepsilon_1};\quad \mathrm{Re}_L = \frac{L_0 d_h}{\varepsilon_1 \nu_L};\quad Fr_L = \frac{L_0^2}{g d_h \varepsilon_1^2};\quad MFr_G = \sqrt{\frac{w_{0G}^2}{\varepsilon_1^2 d_h g}\left(\frac{\rho_G}{\rho_A}\right)}$$

$$d_h = \frac{s(B+4A)}{8X+B};\qquad \varepsilon_1 = 1 - \frac{2\delta(B/4+2X)}{BC};\quad X = \frac{1}{2}\sqrt{s^2 + \left(A - \frac{B}{4}\right)^2}$$

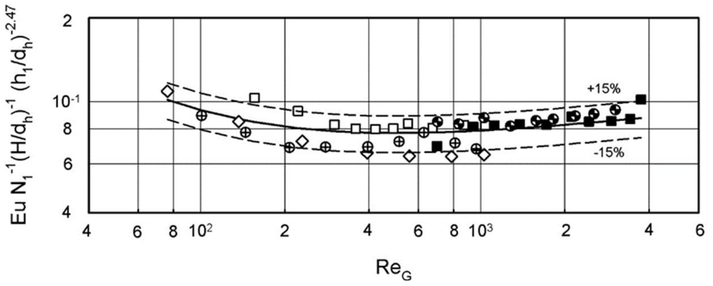

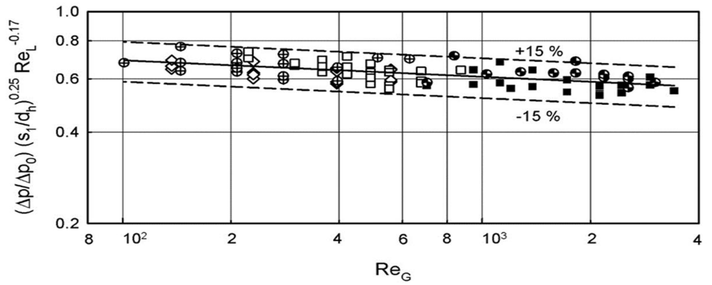

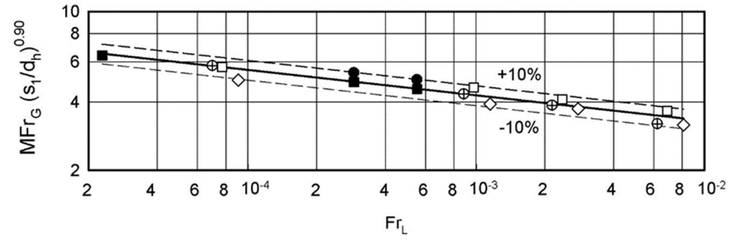

Conclusions

The development of new more accurate equations for determination of the pressure drop and especially the loading point velocity provides further opportunity for process performance improvement in wide area of industrial applications of HOLPACK packing (decarbonizers, absorbers, rectification columns, contact economizers for flue gases waste heat recovery, etc.)

Four column rectification plant for high quality ethanol > 96.3% ; Productivity 20 000 l/day.

Top view of a column section

References

Kolev, N. Packed bed columns: For absorption, desorption, rectification and direct transfer, 1st ed.; Elsevier, Amsterdam, 2006.

Kolev, N., Darakchiev, R. A new packing for mass transfer apparatus. Verfahrenstechnik 1973, 7 (7), 214-218 (in German).

Kolev, N.; Darakchiev, R. Horizontal expanded metal sheet packing. Part II: Pressure drop, *Chem.-Ing.-Tech.* **1974**, *46 (1)*, 33-33 (in German). https://doi.org/10.1002/cite.330460109

Semkov, K. Highly effective rectification plants for ethanol production. News of the Bulgarian Academy of Sciences 2006, 6, 39-42.

Acknowledgment

This study is financially supported by the National Science Fund at the Bulgarian Ministry of Education and Science, Contract No. DN 07/14/15.12.2016.

Contact: semkov@bas.bg; t.petrova@iche.bas.bg

Investigation of the influence of chitosan on the properties of bleached cellulose papers

D. A. Todorova, V. G. Lasheva

Department of Pulp, Paper and Graphic art at University of Chemical Technology and Metallurgy 8 Kl. Ohridski Blvd., 1756 Sofia, Bulgaria; E-mail: todorova.dimitrina@uctm.edu

Introduction

Latest tendencies show that packaging materials, with which producers reduce the environmental pollution, are based on bio polymers and increases its consumption due to its biodegradable, nontoxic and environmentally friendly nature, as well sufficient barrier properties.

Polymers which are produced naturally or genetically from microorganisms have a great potential as fillers, coatings or films used in paper and packaging field. At polysaccharides mostly used are chitosan, starches and alginates. They have great properties such as nontoxicity, can be used in many fields of material science and are available in the market also as waste materials.

Due to the positive charge on the amino group under acidic conditions, chitosan binds negatively charged molecules and therefore represents a greater barrier against grease. Due to its good barrier properties, chitosan coatings can be used also as barriers in packaging (Brodnjak, 2017). In the production of different paper grades either printing or packaging, bleached celluloses of different wood species are used, in different proportions and have to have different hydrophobicity, which is done with the help of various sizing agents such as rosin size and aluminium sulphate and other synthetic sizing agents. These synthetic sizing agents can be replaced by some natural polymers; such natural biopolymer is chitosan.

Materials and methods

The used chitosan was with molecular weight lower than 30 kDa and deacetylation degree higher than 85%, The chitosan solution was prepared by dissolving 4g chitosan in 200ml 2% acetic acid with continuous stirring on a magnetic stirrer for 1 day. The grammage of the obtained samples was 70 g/m^2 .

The obtained paper samples were examined for its:

1) *Tensile strength – Tensile length, m (*ISO 1924-2:1999)
2) *Bending resistance – double endurance, number (*ISO 5626:1993)
3) *Water absorptiveness - Cobb60,* g/m^2 (ISO 535:2014)

Paper samples	Fiber composition	Chitosan consumption, % of o.d.f.			Rosin size consumption, % of o.d.f.	$Al_2(SO_4)_3$ consumption, % of o.d.f.
1.	100% BSWP	-			-	-
2.	80% BSWP:20% BHWP	-			-	-
3.	50% BSWP:50% BHWP	-			-	-
4.	100% BHWP	-			-	-
5.	100% BSWP	0,2	1	2	-	-
6.	80% BSWP:20% BHWP	0,2	1	2	-	-
7.	50% BSWP:50% BHWP	0,2	1	2	-	-
8.	100% BHWP	0,2	1	2	-	-
9.	100% BSWP	0,2	1	2	3	4,5
10.	80% BSWP:20% BHWP	0,2	1	2	3	4,5
11.	50% BSWP:50% BHWP	0,2	1	2	3	4,5
12.	100% BHWP	0,2	1	2	3	4,5

Results and discussions

Tensile strength

Water absorptiveness

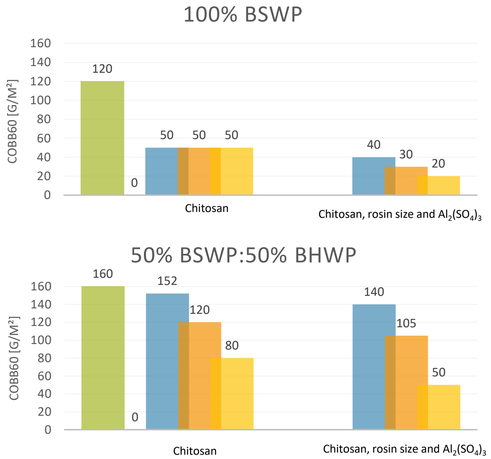

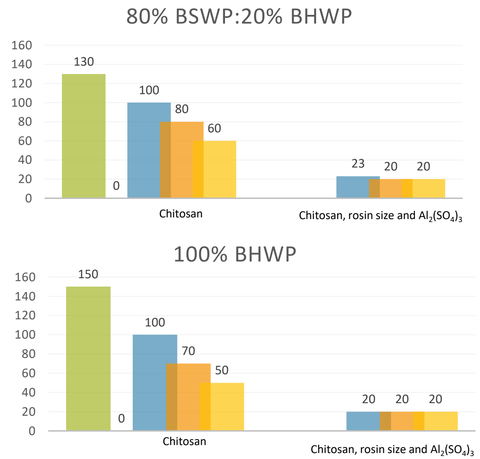

With increasing the chitosan consumption the properties of all examined paper samples are improved. Best strength properties are obtained for the samples with fiber content of 80% BSWP:20% BHWP and maximum consumption of chitosan - 2% and 3% rosin size together with 4,5% Al2(SO4)3. The effect of the chitosan on the water absorptiveness of the paper samples is greater for paper samples with fiber content of 100% BSWP.

Conclusions

- It was found out that the use of chitosan additives in the composition of bleached cellulose paper samples leads to improved strength and hygroscopic properties.
- Cobb$_{60}$, (g/m^2) water absorptiveness studies, shows that the addition of chitosan solution reduces its values. In paper samples from 100% BSWP, the addition of 0.2% chitosan solution is sufficient to impart hydrophobicity.
- The addition of rosin size and Al2(SO4)3 to the paper samples after the addition of chitosan with 2% consumption doubled the reduction of the water absorption capacity of the paper.

References

U. V., Brodnjak, Experimental investigation of novel curdlan/chitosan coatings on packaging paper, Progress in Organic Coatings 112, 86-92 (2017)

Acknowledgment

This research was funded from University of Chemical Technology and Metallurgy, Sofia under “Scientific research sector” Project# 11962/2020 and Project#11968/2020.

Thiourea-chitosan hydrogels: preparation and sorption of heavy metal ions

Claudiu-Augustin Ghiorghiță[1], Konstantin B. L. Borchert[2], Marius Zaharia[1], Ana-Lavinia Vasiliu[1], Dana Schwarz[2], Marcela Mihai[1]

[1]"Petru Poni" Institute of Macromolecular Chemistry, Grigore Ghica Voda Alley 41A, 700487 Iasi, Romania

[2] Leibniz-Institut für Polymerforschung Dresden e.V., Hohe Str. 6, 01069 Dresden, Germany

Introduction

Among the numerous materials designed for water purification purposes, sorbents based on bio-available polymers, such as chitosan (CHI), are widely investigated as environmentally-friendly and renewable solutions. Chemical modification of CHI to either hydroxyl or amino groups is often used to improve its heavy metal ions chelating properties [1].

In this work, thiourea-chitosan (CHITU) was synthesized by N-thiocarbamoylation of CHI using ammonium thiocyanate [2]. Further, porous hydrogels based on CHITU were prepared through the cryogelation technique using glutaric aldehyde (GA) as cross-linker. The obtained hydrogels were evaluated for the sorption of Cu^{2+}, Co^{2+}, Cd^{2+} and Ni^{2+} in batch experiments.

Materials and methods

The synthesis of CHITU. CHITU was obtained by the reaction of CHI with NH_4SCN (**Scheme 1**). Briefly, CHI powder (*Sigma, low molecular weight, deacetylation degree of 83%*) and NH_4SCN (*Sigma-Aldrich*), in a molar ratio of 1:2, were added in a single-neck round bottomed flask, followed by the addition of 15 mL of ethanol (*Chemical Company*). The reaction was conducted under reflux at 95 °C for 12 h. After cooling to room temperature, the precipitate was filtered and thoroughly washed with ethanol.

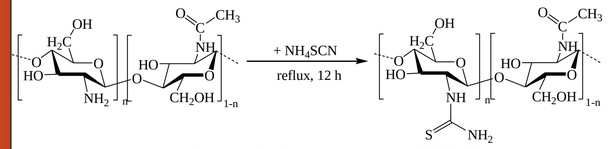

Scheme 1. The synthesis of CHITU

Preparation of the CHITU hydrogel. The CHITU hydrogel was synthesized by means of the cryogelation technique. Prior hydrogel synthesis, a 2% (w/v) CHITU solution in 1% acetic acid was prepared. Then, a certain volume of 2.5% GA (*Sigma-Aldrich*) solution was added dropwise over the CHITU solution, under strong magnetic stirring, so that the final CHITU:GA weight ratio was 10:1. After a supplementary 30 min stirring for homogenization, the solution was transferred in 5 mL syringes and frozen for 24h at -18 °C. Then, the hydrogels were thawed at room temperature for 60 min, cut into 5 mm thick pieces, washed several times with water and dried by lyophilization

Results and discussion

Hydrogel characterization. The morphological features, viscoelastic properties and thermal degradation behavior of the CHITU hydrogel were followed by scanning electron microscopy (SEM), rheology measurements and thermogravimetry (**Figure 1**).

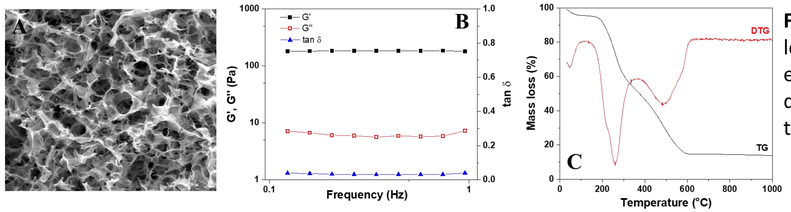

Figure 1. SEM image (A), storage modulus (G`), loss modulus (G``) and tan δ vs frequency evolution (B) and thermogravimetric (TG) and differential thermogravimetric (DTG) curves (C) of the CHITU hydrogel.

- The pores of the CHITU hydrogel were interconnected and had the average diameter between 88 µm and 110 µm (**Figure 1A**).
- G' was higher than G'', while the shear loss tangent (*tan δ*) was between 0.03 and 0.04 in all frequency range (**Figure 1B**), thus indicating the formation of a strong hydrogel network due to the efficient cross-linking with GA.
- The thermal degradation of CHITU hydrogel proceeded by a three-step process (**Figure 1C**): 3% weight loss at temperature below 100 °C due to residual water evaporation, 34.5% weight loss between 235 °C and 375 °C due to the destruction of CHI skeleton and 28.5% weight loss between 375 °C and 540 °C due to the further degradation of organic residues.

Sorption of heavy metal ions. The sorption of Cu^{2+}, Cd^{2+}, Co^{2+} and Ni^{2+} by the CHITU hydrogels were investigated as a function of initial pH, metal ion concentration and contact time using *Inductively Coupled Plasma Optical Emission Spectrometry* (ICP-OES) (**Figure 2**).

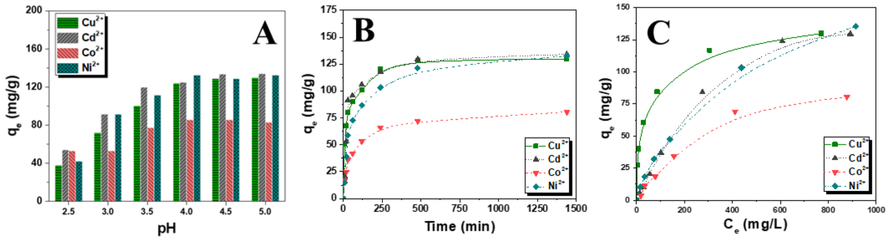

Figure 2. The influence of initial pH (A), contact time (B) and metal ion concentration (C) on the sorption of Cu^{2+}, Cd^{2+}, Co^{2+} and Ni^{2+} by the CHITU hydrogel.

- The uptake of metal ions by the CHITU hydrogel at pH 5 was 129.8 mg/g, 134 mg/g, 83.4 mg/g and 132.5 mg/g for Cu^{2+}, Cd^{2+}, Co^{2+} and Ni^{2+}, respectively (**Figure 2A**).
- The affinity of CHITU hydrogel towards the heavy metal ions increased with the decrease of the ionic radii, first ionization energies and softness indices of the metal ions.
- The amounts of metal ions adsorbed by the CHITU hydrogel increased rapidly for the first approximately four hours due to the availability of binding sites, then flattened towards the equilibrium (**Figure 2B**).
- The sorption capacity (q_e, mg/g) for all metal ions increased progressively towards saturation with the increase of equilibrium concentrations (**Figure 2C**).
- The fitting of equilibrium and kinetics sorption data with various empirical models showed that the sorption process of all metal ions was best described by the ***Sips*** and ***Pseudo-Second Order*** models, respectively.

Reutilization in successive sorption/desorption cycles

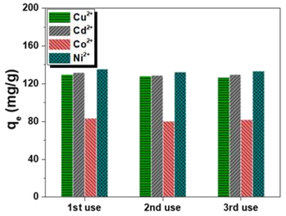

Figure 3. Reuse of the CHITU hydrogel in successive sorption/desorption/regeneration cycles.

- The CHITU hydrogel completely preserved its sorption capacity for all heavy metal ions, indicating that the desorption/regeneration cycles proceeded without alteration of the hydrogel network and its functional groups.

Conclusions

A porous hydrogel based on thiourea-chitosan (CHITU) was prepared through the cryogelation technique and was evaluated for the sorption of Cu^{2+}, Cd^{2+}, Co^{2+} and Ni^{2+}. The hydrogel was characterized by SEM, TGA and rheology measurements, while the heavy metal ions sorption capacity was determined using ICP-OES. The maximum experimental sorption capacities towards Cu^{2+}, Cd^{2+}, Co^{2+} and Ni^{2+} were 129.8 mg/g, 134 mg/g, 83.4 mg/g and 132.5 mg/g, respectively. The fitting of equilibrium and kinetics sorption data with various empirical models evidenced that the sorption process of all metal ions was best described by the Sips and Pseudo-Second Order models, respectively. Reutilization of the CHITU hydrogel in three consecutive sorption/desorption/regeneration cycles showed that it possesses completely renewable sorption properties.

References

1. L. Zhang, Y. Zeng, Z. Chen, *J. Mol. Liq.*, 214, **2016**, 175-191.
2. C.-A. Ghiorghita, K.B.L. Borchert, A.-L. Vasiliu, M.-M. Zaharia, D. Schwarz, M. Mihai, *Colloids Surf. A*, 607, **2020**, 125504

Acknowledgments

This work was supported by a grant of Romanian Ministry of Research and Innovation (CCCDI-UEFISCDI, project no. 26PCCDI/2018), *Integrated and sustainable processes for environmental clean-up, wastewater reuse and waste valorization,* ***SUSTENVPRO***, within PNCDI III, and the project *Lego-style approach for problematic water streams treatment,* ***WATERLEGO***, ERA.Net RUS Plus S&T Project, id 224.

Chitosan copolymers with improved solubility by Ring-Opening Polymerization technique

Bianca-Iustina Andreica[1], Daniela Ailincai[1], Luminita Marin[1]

[1] "Petru Poni" Institute of Macromolecular Chemistry, Grigore Ghica Voda Alley, 41A, Iasi, Romania; E-mail: andreica.bianca@icmpp.ro

Introduction

In this study we present the synthesis and characterization of novel chitosan derivatives obtained by ring-opening polymerization of trimethylene carbonate (TMC). The motivation for the topic of this study was the limited solubility of chitosan (Ch) at physiological pH, thus leading to restricted applicability [1,2].

Materials and methods

Different chitosan derivatives were synthesized by varying the molar ratio between chitosan and trimethylene carbonate and the reaction conditions (melt bulk or heterogeneous system, in toluene).

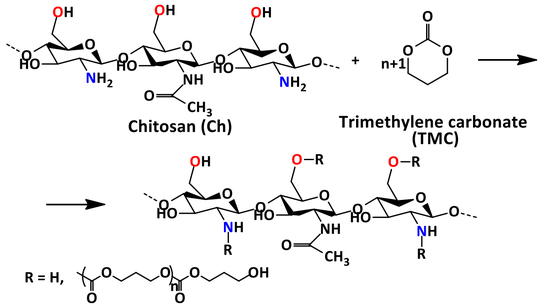

Scheme 1. *Synthetic route of obtaining the chitosan derivatives*

Table 1. *Molar ratio of the components of the chitosan derivatives*

Code	Molar ratio (TMC:Ch)	
Ch-*g*-PTMC1	20:1	Bulk
Ch-*g*-PTMC2	10:10	Bulk
Ch-*g*-PTMC3	10:1	Heterogeneous system
Ch-*g*-PTMC4	5:1	Heterogeneous system
Ch-*g*-PTMC5	1:5	Heterogeneous system
Ch-*g*-PTMC6	1:10	Heterogeneous system

Results and discussions

a) Structural characterization

NMR Spectroscopy

The ^{1}H-NMR spectrum of Ch-*g*-PTMC3 (1a) shows the main proton signals of the chitosan backbone and those corresponding to the methylene protons of the PTMC side chains.

FTIR Spectroscopy

The spectra of the grafted copolymers (1b) present new peaks around 1740 cm^{-1} (C=O) and at 1225 cm^{-1} (C-O), corresponding to the carbonate groups.

b) Morphological characterization

Polarized light microscopy (POM)

All the chitosan-grafted derivatives presented strong birefringence, with a fine texture. Compared to the pristine chitosan, the texture transformed into a clearer one, suggesting that the side PTMC chains favored the depletion of the chitosan backbones, and so the ordering pattern.

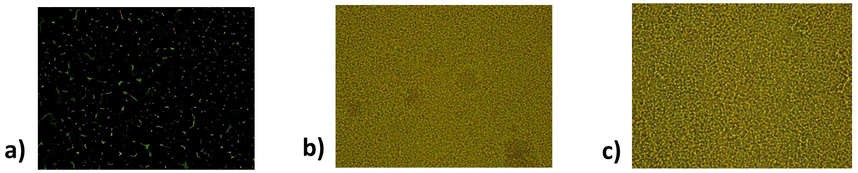

Figure 2. *POM images a) PTMC b) Chitosan c) Ch-g-PTMC6*

Atomic force microscopy (AFM)

The analysis of the surface of the films prepared from the synthetized chitosan derivatives showed more planar surfaces, with lower roughness exponent (R.E.) values compared to chitosan and PTMC references.

c) Solubility test

The solubility of the chitosan derivatives was investigated in different solvents. The results presented (Table 2) were achieved after 48 h swelling time, at 50° C, on lyophilized samples.

d) Biocompatibility

The investigated chitosan derivative (Ch-*g*-PTMC3) was biocompatible with NDFH at concentrations higher than the pristine chitosan.

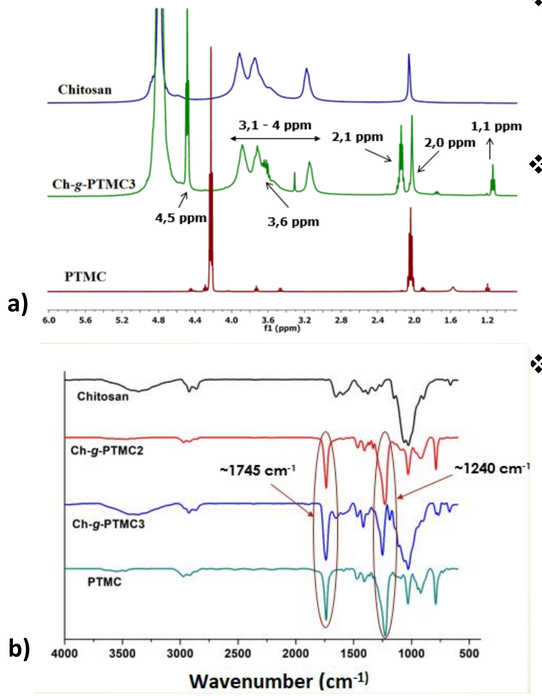

Figure 1. *Representative NMR (a) and FTIR (b) spectra of the copolymers*

Table 2. *Solubility of the copolymers*

Code	H_2O	DMF	DMSO	Methanol
Ch-*g*-PTMC3	+	-	+	-
Ch-*g*-PTMC5	+	s	±	-
Ch-*g*-PTMC6	+	±	±	±

+ Soluble **-** Insoluble **±** Partially soluble **s** Swelling

Conclusions

- A series of chitosan derivatives were prepared by grafting of polycarbonate side chains via the ring-opening polymerization technique, in melt bulk or in heterogeneous system.
- The novel grafted copolymers were structural characterized, confirming that the primary amino or hydroxyl groups of chitosan can act as initiators for the ring opening of trimethylene carbonate.
- Some derivatives presented the property of being soluble in water, in comparison to chitosan that is soluble only in acidic media, providing promising results for further research.

References

1. C. K. S. Pillai, W. Paul, S. P. Sharma, *Prog. Polym. Sci.* **2009**, 34(7), 641–678.

2. V. K. Mourya, N. N. Inamdar, *React. Funct. Polym.* **2008**, 68, 1013–1051.

Acknowledgment

This work was supported by the Romanian National Authority for Scientific Research MEN–UEFISCDI (grant number PN-III-P1-1.2-PCCDI2017-0569, no. 10PCCDI/2018) and by the project H2020-MSCA-RISE-2019: Smart Wound Monitoring Restorative Dressings (SWORD) (no. 873123).

Iminoboronate chitosan hydrogels – a promising tool in the treatment of Candida infections

D. Ailincai, L. Marin

"Petru Poni" Institute of Macromolecular Chemistry, Iasi, Romania

Introduction

This study had as main objective the obtaining of biocompatible hydrogels based on chitosan and **2-formyl phenyl boronic acid (2-FPBA)** - a monoaldehyde with strong antifungal properties. Two series of hydrogels based on imino-boronate motif were prepared and characterized and their antifungal properties were evaluated on Candida albicans and glabrata.

Materials and methods

The hydrogels have been obtained by the acid condensation of **chitosan** amine groups and aldehyde group of **2-formylphenyl boronic acid** (**2-FPBA**). In order to confirm the synthetic pathway, a model compound (M) has been obtained by reacting **2-FPBA** with **D-glucosamine,** the structural unit of chitosan.

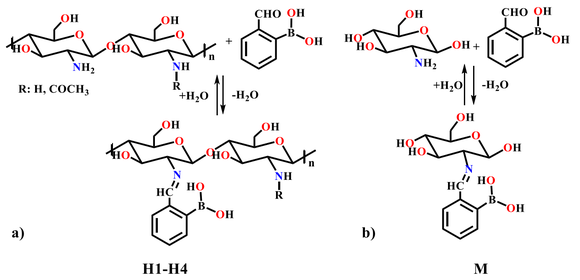

Different hydrogels were obtained by varying the ratio between the amine groups on chitosan backbone and the aldehyde groups of **2-FPBA** .

Code	H1	H2	H2.5	H3	H3.5	H3.75	H4
NH_2:CHO (f. p.)	1:1	2: 1	2.5:1	3:1	3.5:1	3.75:1	4:1
Code	H1*	H2*	H2.5*	H3*	H3.5 *	H3.75*	H4 *
NH_2:CHO (7 days)	1:1	2:1	2.5:1	3:1	3.5:1	3.75:1	4:1

Results and discussions

FTIR spectroscopy & NMR spectroscopy

The IR spectra of the obtained hydrogels showed significant change of their shape compared to chitosan, indicating the formation of the imine bond and also some supramolecular rearrangements.

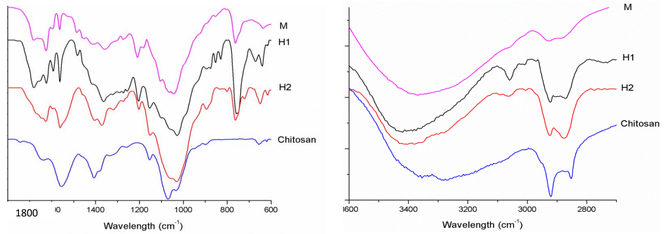

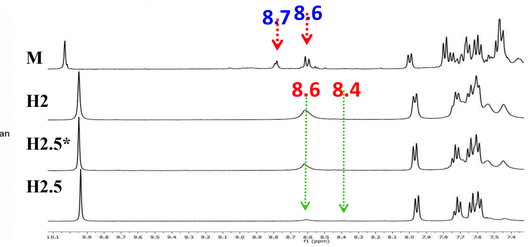

The NMR spectra of the model compound and of the hydrogels exhibited the characteristic chemical shift of the imine proton at 8.7, 8.6 and 8.6, 8.4 ppm respectively

Wide angle X-ray diffraction

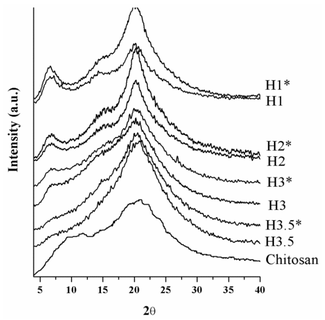

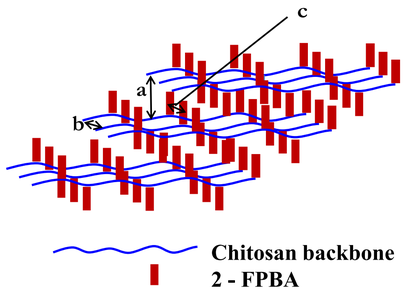

The hydrogels presented three diffraction peaks suggesting a supramolecular layered architecture: a reflection in the region of small angles around 6 degrees characteristic to hydrophilic/hydrophobic segregation, a second one at middle angle around 14.2 degrees which corresponds to the inter-chain distance between the chitosan backbones, and a last one at 20 degrees which corresponds to the intermolecular distances which appeared between two rigid imine units within a layer.

Scanning electron microscopy

As expected, the hydrogels have a highly porous interconnected network due to the large amount of water encapsulated (97 – 98%), forming a sponge-like microstructure. The hydrogels obtained using a higher amount of **2-FPBA** showed a tighter microstructure with smaller pores due to the higher crosslinking degree.

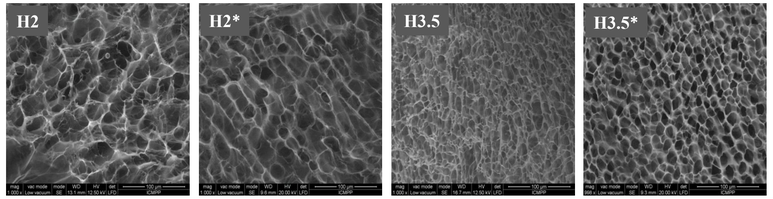

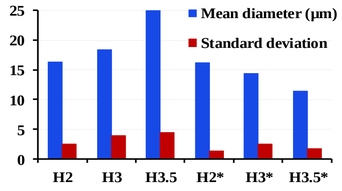

Rheological measurements

The rheological measurements were in agreement with the visual monitoring of the samples, a gel like behaviour being obtained for a NH_2/CHO < 3.75.

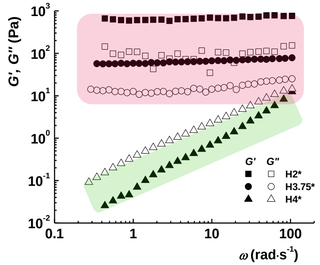

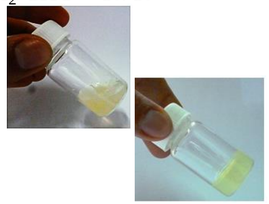

Gel like behavior

Liquid like behavior

Antifungal activity on planktonic yeast & biofilm

The hydrogels presented strong fungicidal effect, against both planktonic yeast and biofilm, the microbial burden reduction on biofilm exceeding 5log (99.999 % killing).

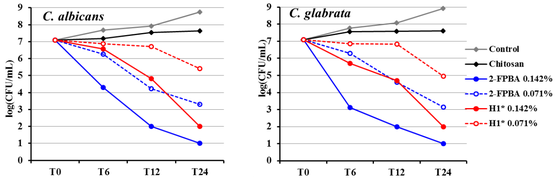

Conclusions

- New imino-boronate hydrogels were obtained using **2-FPBA** and **chitosan**
- The hydrogels presented a porous morphology, a supramolecular layered architecture and strong antifungal activity on planktonic yeast and biofilm

Acknowledgments

This work was supported by MEN – UEFISCDI (grant number PN-III-P1-1.2-PCCDI2017-0569, no. 10PCCDI/2018 and by H2020-MSCA-RISE-2019: Smart Wound Monitoring Restorative Dress-ings (SWORD) (no. 873123).

Ionic composites based on chitosan and poly(amidoxime) grafted on starch as beads for binding metal ions

Diana Felicia Loghin, Marcela Mihai

"Petru Poni" Institute of Macromolecular Chemistry, Aleea Gr. Ghica Voda 41A, 700487 Iasi, Romania

Introduction

Contamination Bv Heavv Metal Ions

Sources of contamination

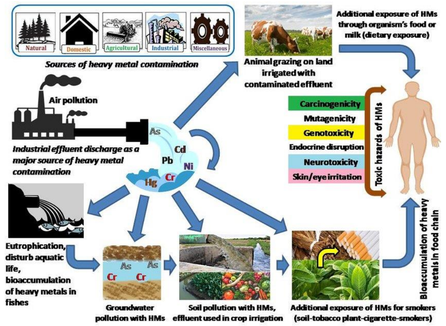

Polyssacharides Used in Removal of Heavy Metal Ions

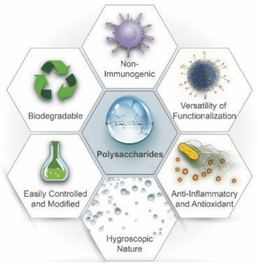

Materials and method

Starch and Chitosan

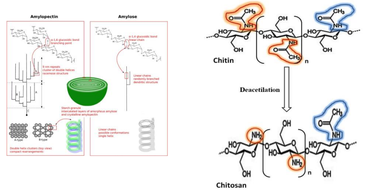

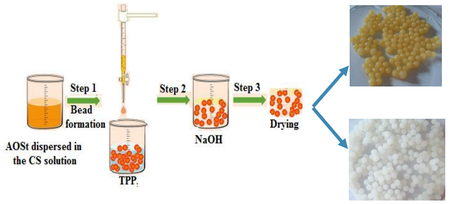

(type A) mixing of the AOSt powder with CS solution, followed by bead formation

(type D) mixing of the grafted starch with polyacrilonitrile (GSt) powder with CS solution, followed by bead formation and the amidoximation of the nitrile groups inside the beads.

Results and discussions

Ionic composites as beads --- Sorption of Cu^{2+}

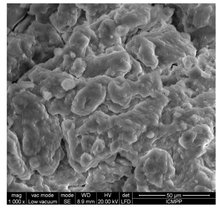

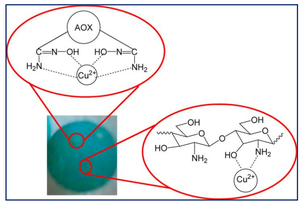

Two possible mechanisms of chelation of Cu^{2+} ions: chelation by the amidoxime groups, which belong to the entrapped component (AOX), and chelation by the functional groups of the CS matrix.

Preparation of $CaCO_3$ based composite beads-----Cu(II) interaction

(1) (beads + 0.2 M $CaCl_2$ aqueous solution) + 0.2 M Na_2CO_3
(2) beads alternately immersed in 0.2M $CaCl_2$ and 0.2 M Na_2CO_3 aqueous solutions, each step repeated for 4 times.
(3) (beads + 0.2M $CaCl_2$) + DEC + NaOH
(4) similar to (3), except that instead of DEC was used DMC.
(5) (beads + 0.2M $CaCl_2$ aqueous solutions) + 25% NH_4OH solution + DEC, under stirring then 24 h under static conditions.
(6) similar to (5), except that instead of DEC was used DMC

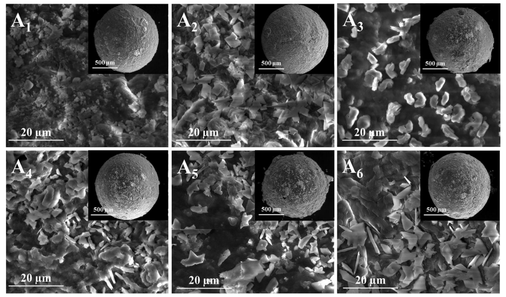

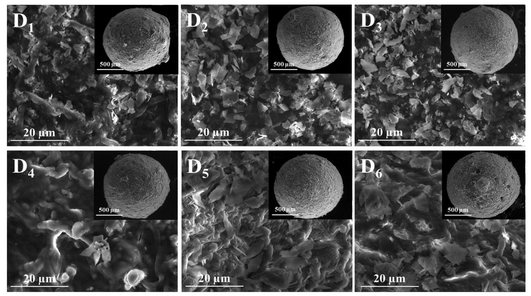

Conclusions

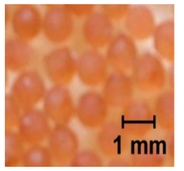

(type A) CS/AOX

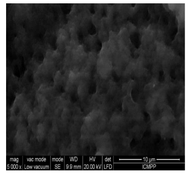

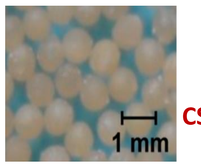

(type D) CS/(PS-g-PAN)

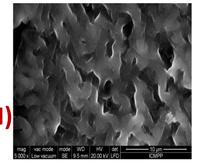

The optical microscope was used to show the size and shape of the wet beads

The SEM images show the difference between the surface morphology of the CS/AOX composite and the pristine CS/(PS-g-PAN) composite beads.

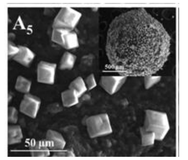

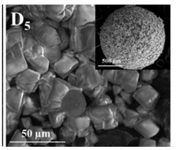

A correlation between the bead synthesis strategy and the formed $CaCO_3$ the beads prepared by in situ amidoximation of PS-g-PAN (type D beads) leading to the formation of larger $CaCO_3$ crystals than the beads obtained by the mixing of amidoximated starch with chitosan (type A beads).

Acknowledgments

This work was supported by a grant of the Ministry of Research and Innovation, CNCS-UEFSCDI, Project number PN-III-P1.1.PD-2016-1313, within PNCDI III.

Microparticulate systems based on polysaccharides and methacrylic monomers for wastewater treatment

S. Racovita, S. Vasiliu, M. Mihai

"Petru Poni" Institute of Macromolecular Chemistry, Grigore Ghica Voda Alley, No. 41A, Iasi, Romania

Objective

The main objective of this study was to investigate the capacity of porous microparticles based on polysaccharides and methacrylic monomers for removal of Cu (II) and Ni (II) from aqueous solution.

Materials and method

Synthesis of porous microparticles

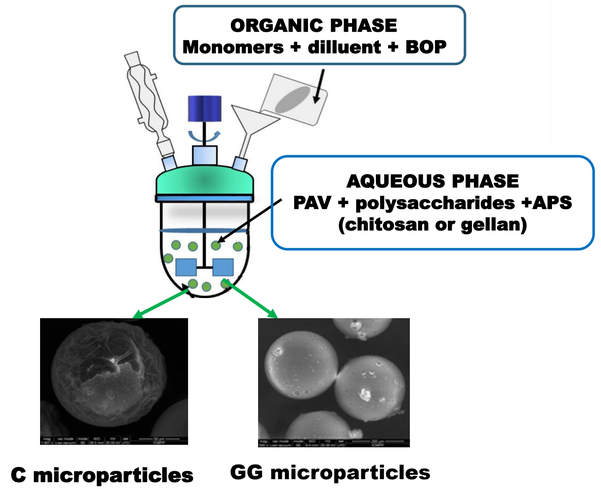

Batch sorption experiments

Results and discussions

Sorption isotherm

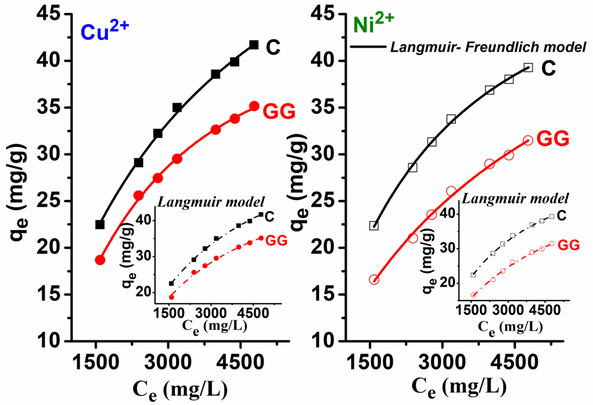

Table 1. Langmuir-Freundlich and Langmuir parameters for the adsorption of Cu^{2+}/Ni^{2+} ions on C and GG microparticles

Sample cod	C		GG	
	Cu^{2+}	Ni^{2+}	Cu^{2+}	Ni^{2+}
Langmuir-Freundlich model $q_e = \frac{q_m (K_a c_e)^{1/n}}{1+(K_a c_e)^{1/n}}$				
q_m (mg/g)	51.32	46,72	45.95	40,13
K_a x10^4 (L/mg)	1.22	0,59	0.25	1,04
n	1.03	1,06	1.08	1,09
R^2	0.998	0,999	0.998	0,996
χ^2	0.085	0,049	0.063	0,159
Langmuir model $q_e = \frac{q_m K_a c_e}{1+K_a c_e}$				
q_m (mg/g)	58.15	50.48	54.83	48.68
K_a x10^4 (L/mg)	3.52	2.67	3.01	1.37
R^2	0.998	0.997	0.997	0.997
χ^2	0.095	0.075	0.994	0.123

q_e is the amount of metal ions adsorbed per mass unit of adsorbent at equilibrium (mg/g); q_m is the maximum adsorption capacity of adsorbents (mg/g), C_e is the equilibrium concentration of remaining metal ions in the solution (mg/L), K_a is a constant related to the affinity between the adsorbent and adsorbate (L/mg) and n is the index of heterogeneity and ranges from 0 to 1.

Sorption kinetics

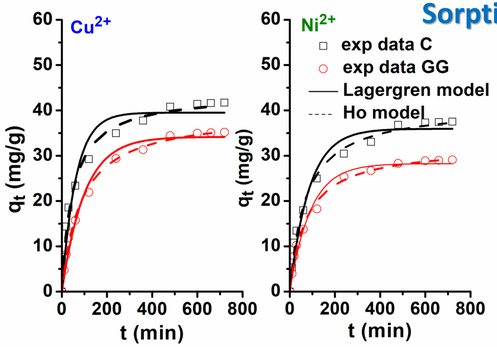

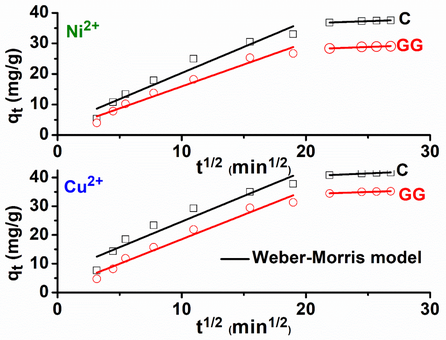

Table 2. The parameters corresponding to the kinetic models used in the case of adsorption of Cu^{2+}/Ni^{2+} ions onto C and GG microparticles

Kinetic models		C		GG	
		Cu^{2+}	Ni^{2+}	Cu^{2+}	Ni^{2+}
	$q_{e,exp}$ (mg/g)	41.70	37.50	35.16	29.07
	$q_{e,calc}$ (mg/g)	32.50	30.94	30.16	21.27
Lagergren	k_1x10^2 (min^{-1})	1.62	1.16	1.01	1.09
$q_t = q_e(1 - e^{-k_1 t})$	R^2	0.962	0.974	0.983	0.982
	χ^2	7.955	4.935	2.86	2.097
	$q_{e,calc}$ (mg/g)	43.83	40.91	38.45	31.27
Ho	k_2x10^2 (g/mg·min)	0.05	0.03	0.03	0.04
$q_t = \frac{k_2 \cdot q_e^2 \cdot t}{1 + k_2 \cdot q_e \cdot t}$	R^2	0.998	0.997	0.997	0.996
	χ^2	1.595	1.076	0.637	0.586
Weber-Morris	k_{i1} (mg/(g·$min^{1/2}$))	1.78	1.71	1.70	1.25
$q_t = k_{id} \cdot t^{0.5} + C_i$	R^2	0.965	0.964	0.964	0.963

q_e and q_t are the amounts of metal ion retained at equilibrium and at time t (mg/g), k_1 is the rate constant of the pseudo-first order model (min^{-1}), k_2 is the rate constant of the pseudo-second order model (g/mg·min), k_{id} is the intraparticle diffusion rate constant (mg/g·$min^{1/2}$) and C_i is the constant that gives information about the thickness of the boundary layer.

Conclusions

- **Sorption studies of copper and nickel showed that the presence of polysaccharides, especially chitosan and gellan in the crosslinked microparticles structure could improve the materials adsorption capacity**
- **The sorption data were found to fit well to the Langmuir-Freundlich and also Langmuir models**
- **Sorption kinetic was found to follow pseudo-second order kinetic model.**

References (if necesarly)

Mittal, H., Ray, S. S., Okamoto, M., *Macromol. Mater. Eng.* **301**, 496 (2016).

Rinaudo, M., *Prog. Polym. Sci.* **31**, 603 (2006).

Siqueria, C., Picone, R., Lopes, C., *Carbohydr. Polym.* **84**, 662 (2011).

Vasiliu, S., Lungan, M. A., Gugoasa, I., Drobota, M., Popa M., Mihai, M., Racovita, S., *ChemistrySelect* **4**, 1 (2019).

Lungan, M. A., Popa M., Desbrieres, J., Racovita S., Vasiliu, S. *Carbohydr. Polym.* **104**, 213 (2014).

Acknowledgment

This work was supported by a grant of the Romanian Ministry of Research and Innovation, CCCDI-UEFISCDI, project number 26PCCDI/01.03.2018, Integrated and sustainable processes for environmental clean-up, wastewater reuse and waste valorisation (SUSTENVPRO) within PNCDI III.

New urea delivery systems based on salicyl-imine-chitosan hydrogels

M.M. Iftime[1], L. Marin[1]

[1] "Petru Poni" Institute of Macromolecular Chemistry of Romanian Academy, Iasi, Romania; E-mail: ciobanum@icmpp.ro, web site: http://www.mail.icmpp.ro

Introduction

The demographic and technological evolution imposes the necessity to improve the agricultural production, especially in the arid areas. A realistic solution to do this is the development of novel multifunctional formulations based on renewable resources, which are capable to release nutrients in a controlled manner and also to control the moisture of the soil (Abobatta, 2018). Chitosan based hydrogels are proper materials for this purpose, as they are able to encapsulate nutrients and to adsorb a large amount of water (Pereira et al., 2017). In line with these premises, we have designed and prepared soil conditioner systems originating from renewable resources by *in situ* hydrogelation of chitosan with salicylaldehyde in the presence of urea, the oldest soil nutrient used in agriculture (Iftime et al., 2017; Iftime et al., 2019).

Materials and method

A series of formulations with different crosslinking degrees (NH_2/CHO ratio of glucosamine units of chitosan and salicylaldehyde from 1/1 to 3/1) and different content of fertilizer (0- 66 %) was prepared by encapsulation of urea into salicyl-imine-chitosan hydrogels by *in situ* hydrogelation.

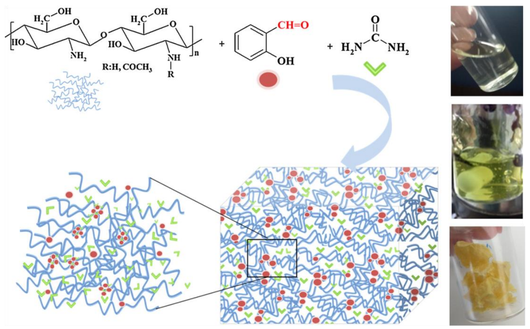

Code	CS1-Ux	CS1.5-Ux	CS2-Ux	CS3-Ux
Molar ratio NH_2:CHO	1:1	1.5:1	2:1	3:1

U_X=0; 33; 50; 66 %

The obtaining of the formulations

The wide angle X-ray diffraction patterns of the formulations confirmed their layered supramolecular architecture by the appearance of the distinct reflection peak at lower angles, characteristic to the inter-layer distance and by the presence of broad reflections at wide angle corresponding to the inter-molecular and inter-chain distances inside them. Also, the X-ray diffractograms of the formulations show the reflection bands characteristic to the urea crystals.

FTIR spectroscopy

The FTIR spectroscopy demonstrated the formation of the imine linkage between chitosan and salicylaldehyde and confirmed the presence of urea in the resulted systems.

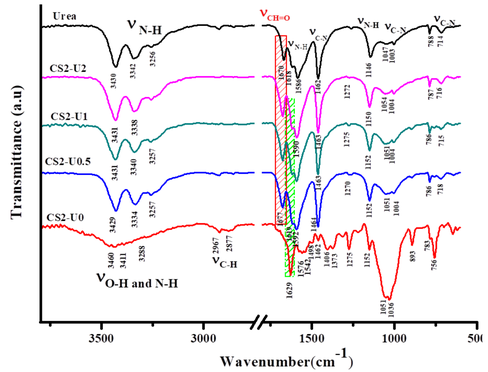

FTIR spectra of the understudy formulations and urea

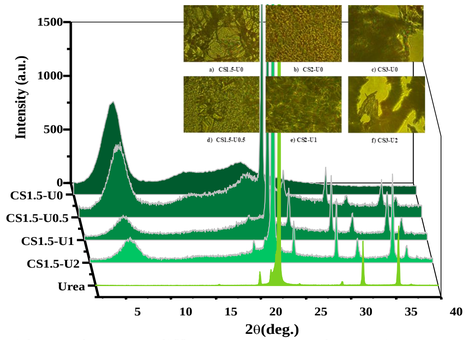

Wide angle X-ray diffractograms and POM images

Results and discussions

Scanning electron microscopy

The morphology of the xerogel formulations is dependent on the crosslinking degree and the content of urea. The increasing of the crosslinking degree resulted in a denser structure, while the increasing of the content of urea led to thicker pore walls.

The **in vitro release kinetics of urea** in distillated water was evaluated by NMR spectroscopy, revealing that the formulations are able to provide a sustained release of the encapsulated urea during 35 days.

Practical application

By measuring the ***water retention capacity, the nitrogen dynamics*** *in soil* and ***the morphological parameters of the tomato seeds***, it was demonstrated excellent water retention, increased nitrogen percent in soil, and higher morphological parameters of the tomato seedlings.

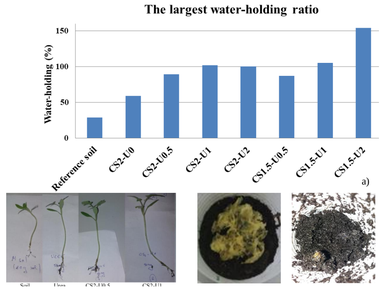

Photographs of the tomato seedlings at the end of the experiment

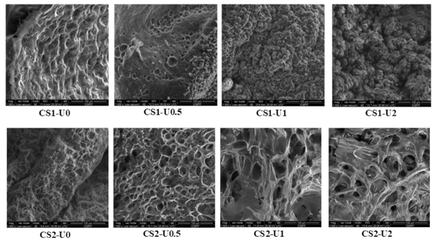

Representative SEM images

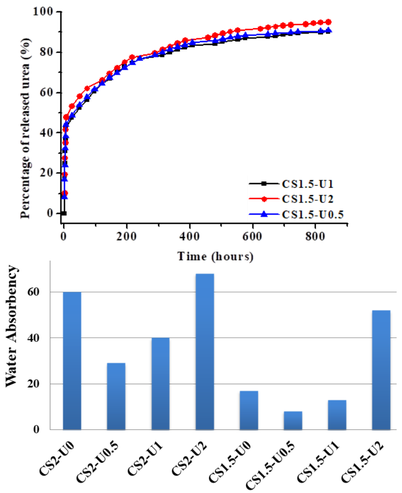

Growth parameters of tomato seeds

Culture medium	FW/mg	DW/mg	PL/cm	GP%	Nt%	No
Soil	250.7	41.5	10.1	100	0.87	3
Urea 50 mg	258.9	47.8	10.2	43.13	1.87	2
Chitosan	290.1	66.7	11.1	58.82	1.09	2
CS2-U0	153.3	28.2	10.1	70.58	1.23	3
CS2-U0.5 (10 mg)	352.8	49.3	10.4	31.37	1.32	1
CS2-U0.5 (50 mg)	421.1	88.3	11.2	100	2.01	3
CS2-U1 (10 mg)	262.0	27.8	10.3	76.47	1.41	3
CS2-U1 (50 mg)	329.9	87.1	12.4	54.90	2.07	2

Water absorbency

The formulations quickly swollen when were immersed in distilled water and their hydrolytic stability and water absorbency was correlated with the crosslinking density and urea content; a higher crosslinking density led to a higher hydrolytic stability but a lower absorption capacity.

Conclusions

The formulations present attractive properties: they are biodegradable, have the capacity to release urea in a controlled manner, which is reflected in the improvement of the morphological parameters of the tomato plants and the nitrogen percentage of the soil.

References

Abobatta, W., Adv. Agr. Environ. Sci 1, 59 (2018).

Iftime, M.M., Ailiesei, G.L., Ungureanu, E., Marin, L., Carbohydr. Polym 223, 115040 (2019).

Iftime, M.M., Morariu, S., Marin, L., Carbohydr. Polym. 165, 39 (2017).

Pereira, A.G.B., Martins, A.F., Paulino, A.T., Fajardo, A.R., Guilherme, M.R., Faria, M.G.I., Linde, G.A., Rubira, A.F., Muniz, E.C., Rev. Virtual Quim 9, 370 (2017).

Acknowledgment

This work was supported by the Romanian National Authority for Scientific Research MEN–UEFISCDI (grant number PN-III-P1-1.2-PCCDI2017-0569, no. 10PCCDI/2018).

Effect of metal doped ZnO ceramic nanostructures on photocatalytic properties

P. Pascariu and N. Olaru

"Petru Poni" Institute of Macromolecular Chemistry, 41A Gr. Ghica Voda Alley, Iaşi-700487, Romania

Introduction

Nowadays, the ceramic nanostructures based on pure ZnO and doped with various metals (La, Er, Sm, Ag, Mo, Sn, and so on) with one dimensional shape are intensively studied due to their remarkable performances in photocatalysis, optics, electronics, semiconductor materials, etc [1-3]. It is known that ZnO is a semiconductor material with a band gap energy of 3–3.37 eV and a large exciton binding energy of 60 meV. Likewise, undoped/doped ZnO materials are often used in waste water treatments by degradation of the organic dyes. Therefore, in this work we proposed to obtain ZnO doped with La, Er, Sm, Ag, Mo in various concentrations (from 0 to 4%) using electrospinning-calcination method. Polyvinylpyrrolidone (PVP) was utilized as a matrix in the electrospinning process. Scanning electron microscopy (SEM) and X-ray diffraction (XRD) were used for morphological and structural characterization of resulting materials. SEM and TEM analysis show the formation of uniform, long and continuous fibers with diameters in the range 0.39 to 1.19 µm and major differences in the size and shape of the crystalline grains. Optical band gaps of these ceramic nanostructures were estimated from reflectance data using Kubelka-Munk theory and were found to vary between 2.5 and 3.5 eV, depending on the type of dopant and doping concentration (0 to 4%). The photocatalytic activity of ZnO:Me products was investigated by using different dyes (Methylene blue, Congo-Red, Rhodamine B, Amaranth) under UV and visible light irradiation. Good performance and significant improvements were observed for all doped materials with maximum efficiency values of up to 98%.

Materials and method

Ceramic nanofiber composites of Sm, La, Er, Ag, Mo doped ZnO

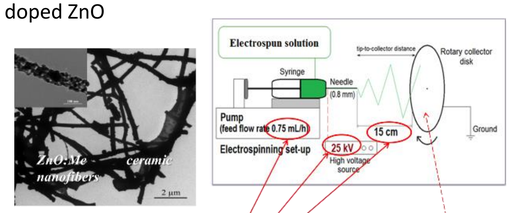

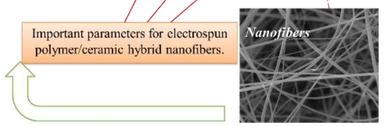

Electrospinning setup

Results and discussions

1. Ceramic nanofiber composites of Sm, La, Er doped ZnO

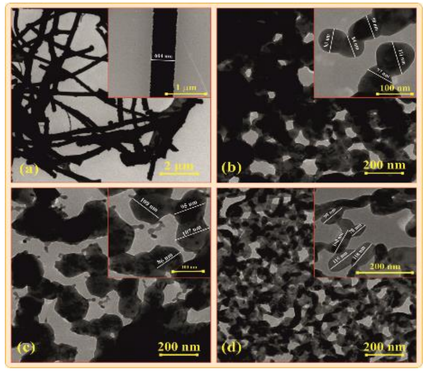

Transmission electron microscope (TEM) images of ceramic samples: (a) ZnO, (b) ZnO:Sm), (c) ZnO:Er and (d) ZnO:La

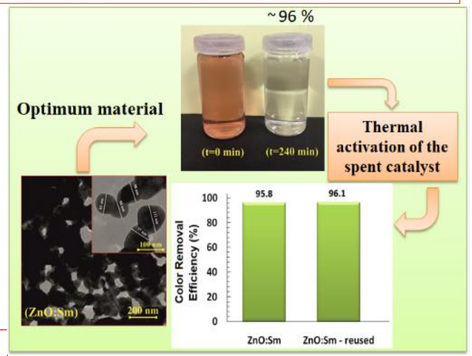

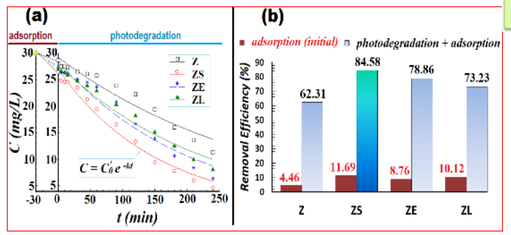

(**a**) concentration decay of CR dye against reaction time (solid and dash lines denote predictions by pseudo-first-order kinetic model); (**b**) color removal efficiency after adsorption-equilibration phase and at the end of the photocatalytic reaction (t=240 min) depending on the type of material; experimental conditions: C_0=30 mg/L; dosage of catalyst DS = 0.167 g/L; T = 20 ± 2 °C; pH 6.8 ± 0.2.

2. Ceramic nanofiber composites of Ag doped ZnO

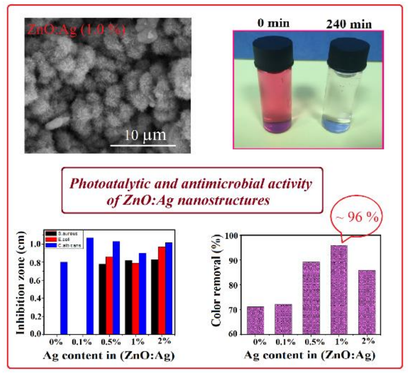

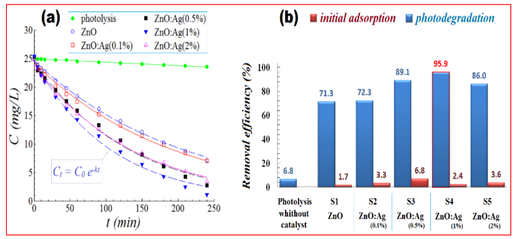

Decreasing of Amaranth dye concentration in aqueous solutions during photodegradation processes in the presence of ZnO and ZnO:Ag catalysts; (**a**) concentration decay of Amaranth dye against reaction time (solid and dash lines denote predictions by pseudo-first-order kinetic model); (**b**) color removal efficiency after adsorption-equilibration phase and at the end of the photocatalytic reaction (t=240 min) depending on the type of material; experimental conditions: C_0=25 mg/L; dosage of catalyst DS = 0.167 g/L; T = 25 °C; pH 7.0 ± 0.2.

3. Ceramic nanofiber composites of MoO_3 doped ZnO

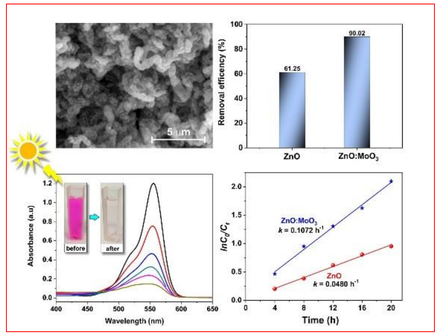

New MoO_3 incorporated ZnO materials were prepared through electrospinning method, followed by calcination at 500 °C. The obtained ZnO:MoO_3 materials were characterized by XRD and SEM. The presence of MoO_3 in ZnO was highlighted by UV-Vis where a blue shift of the absorption band maxima (from 382 to 371 nm), along with a decrease in the optical band gap. The photocatalytic performance of ZnO and ZnO:MoO_3 was assessed in the degradation of Rhodamine B dye (C_0=5 mg/L), under visible light irradiation. The values of the reaction rate constants were 0.0480 h^{-1} for ZnO, and 0.1072 h^{-1} for ZnO:MoO_3, respectively.

Conclusions

- Novel nanostructured materials were produced based on ZnO matrix doped with Sm, Er, La, Ag and Mo by using theelectrospinning technique followed by thermal heating.
- SEM images confirm the obtaining of one-dimensional structures.
- The XRD patterns of the inorganic products confirmed the hexagonal wurtzite structure of ZnO.
- The produced ZnO-based nanostructures were applied for the photodegradation of Congo Red, Rhodamine B, Amaranth dyes from aqueous solutions under UV and visible light irradiation.
- Good performance and significant improvements were observed for all doped materials with maximum efficiency values of up to 98%.

References

[1] P. Pascariu, M. Homocianu, Ceram. Int. 2019, 45, 11158–11173.

[2] P. Pascariu, C. Cojocaru, P. Samoila, A. Airinei, N. Olaru, D. Rusu, I. Rosca, M. Suchea, Journal of Alloys and Compounds 834 (2020) 155144.

[3] P. Pascariu, C. Cojocaru, N. Olaru, P. Samoila, A. Airinei, M. Ignat, L. Sacarescu, D. Timpu, Journal of Environmental Management 239 (2019) 225–234.

Novel chitosan-based nanofibers for wound healing applications

O. M. Ionescu[1], M. Drăgan[1], A. T. Iacob[1], C. Ibănescu[2], M. Dan[2], L. Profire[1]

1 Faculty of Pharmacy, "Grigore T. Popa" University of Medicine and Pharmacy of Iași, 16 University Street, Iași, Romania

2 Faculty of Chemical Engineering and Environmental Protection,"Gh. Asachi" Technical University of Iași, Mangeron Avenue 73, Iași, Romania

Introduction

The classical method of producing nanofibers is via electrospinning technique, which offers the possibility of working at a nano-scale with a high yield (Sarhan, W., 2015, Rieger, K. A., 2016). The aim of this study is to encapsulate and characterise new chitosan-based nanofibers for medical applications.

Materials and method

Electrospinning method:

- **polymeric solution:** Propolis extract (7.5% v/v), L-arginine HCl (7.5% wt/v) and Manuka Honey (7.5% wt/v), propolis-Calendula officinalis extract respectively were dissolved in a mixture (1:1 volume ratio) of polyethylene-oxide (2% wt/v) and chitosan (3% wt/v) acetic acid solution (50% v/v).

- **Viscosity** of the solutions was measured using a parallel-plate measuring system.
- **Fiber morphology** and average diameters were observed by a scanning electron microscope.
- **Four antioxidant tests** (DPPH, ABTS, FRAP, phosphomolybdate assay) were performed in order to assess the best antioxidant matrix.
- **Haemocompatibility** was performed to assess in vitro properties.
- **Cytotoxicity** was assessed on human dermal fibroblasts (MTS assay).

Results and discussions

A good correlation between viscosity, superficial tension and obtaining of proper, smooth nanofibers was established. The chitosan-based nanofibers loaded with propolis-*Calendula officinalis* (Figure 1) extract showed the best antioxidant potential in all four antioxidant tests. *Calendula officinalis* has also been used in dermatological issues traditionally and has proven beneficial in modern applications, too and provided best haemocompatibility score. All samples showed good hemocompatibility scores and no cytotoxic effect up to 100 mg/mL.

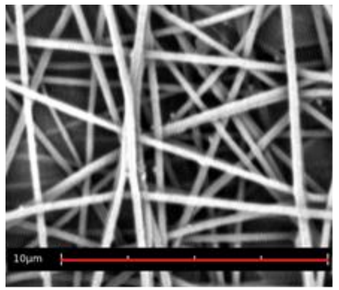

Figure 1. SEM micrograph of propolis/*Calendula officinalis* nanofibers and mean diameter

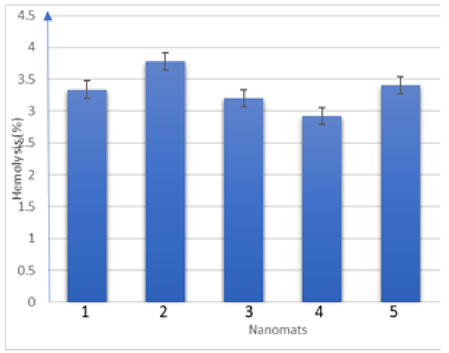

Figure 3. Hemocompatibility assay of samples

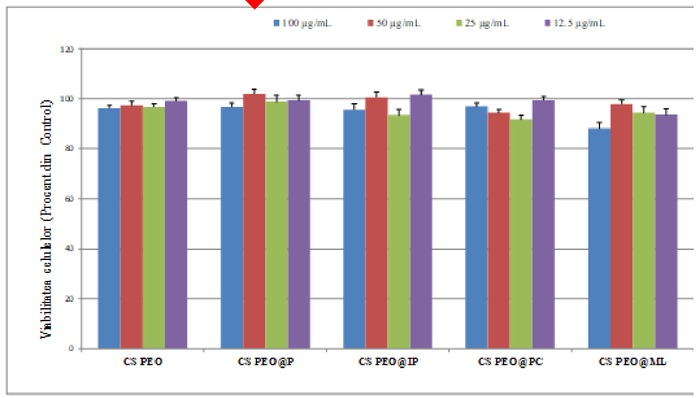

Figure 2. MTS assay of samples

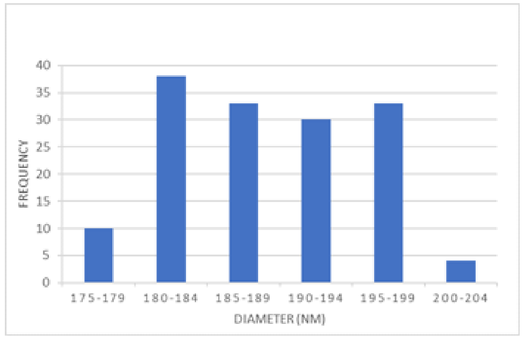

Figure 4. Mean diameter values (mn) of propolis/Calendula sample

Conclusions

In this work, we successfully developed smooth, continuous, randomly oriented L-arginine/Manuka honey/Propolis/Calendula officinalis nanofibers providing a new option for developing wound dressings.

References

Sarhan, W., &Azzazy, H. M. E., Carbohydrate Polymers, 122:135-143. (2015).

Rieger, K. A., Birch, N. P., & Schiffman, J. D., Carbohydrate Polymers. 139:131-138 (2016).

Acknowledgment or Contact

This work was financially supported by UEFISCDI grants PN-III-P1-1.1-MC-2017-2462, PN-III-P1-1.1-MC-2018-2451, ECOST-STSM-Request-CA16122-45799 and by the University of Medicine and Pharmacy "Grigore T Popa Iasi", contract no. 27496/20.12.2018.

A new sponge-type hydrogel as a 3D support for tumoral cell culture

S. Bucătariu[1], M. Constantin[1], G. Fundueanu[1], M. Călin[2]

[1] Department of Natural Polymers, Bioactive and Biocompatible Materials, "Petru Poni" Institute of Macromolecular Chemistry, 700487 Iassy, Romania; E-mail: sanda.bucatariu@icmpp.ro
[2] "Medical and Pharmaceutical Bionanotechnologies" Laboratory, Institute of Cellular Biology and Pathology "Nicolae Simionescu" of the Romanian Academy, 050568 Bucharest, Romania;

Introduction

In the near future, sponge-type HA hydrogels could be used as supports for delivery of drugs [1] or other biomedical engineering applications due to their resemblance to soft tissues in biological systems [2,3]. In fact, these materials are very attractive for drug transport and release as well as cell (fibroblasts, stem cells, etc.) seeding and growth, their properties being influenced by the high porosity of the polymer networks [4]. The development of highly porous HA hydrogels with the pore diameter ranging between 20 and 200 µm is a requirement for scaffolds in tissue engineering, since cells need sufficient space to grow and to stick to the material [2,4].

Materials and method

In the present work, a new sponge-type hydrogel was obtained by cross-linking hyaluronic acid (HA) and poly(methylvinylether-alt-maleic acid) P(MVE-alt-MA) through a solvent-free thermal method and characterized by Environmental Scanning Electron Microscopy (ESEM) and *In vitro* biocompatibility tests.

The 3D cell culture was performed as follows. The hydrogel chosen for biological assessment was HA^{3}P50, where "3" is the concentration of both polymers (%, w/v) in the initial mixture, and "50", the P(MVE-alt-MA) content (%, w/w). Pieces (approx. 2 mm × 2 mm × 1 mm) of lyophilized HA^{3}P50 hydrogels were cut under a stereomicroscope and then weighed and sterilized by exposure to UV radiation for 3 minutes on each side. Without any washing procedure, the hydrogels were populated with HepG2 cells at a cell density of 2.5 × 105 cells/3D support by spotting 10 µL of cell suspension. Cell populated hydrogels were examined after medium replacement by light microscopy (ZEISS Microscope)

Results and discussions

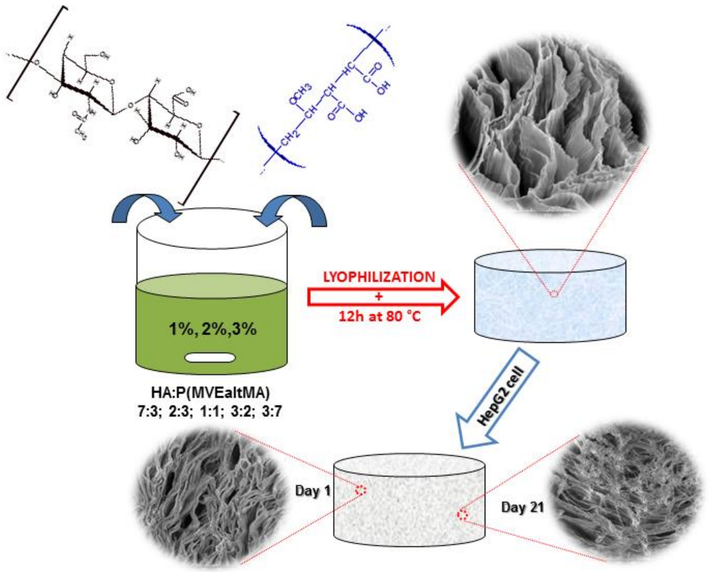

The light microscopy images of cell populated hydrogels taken on day 1 and day 21 (bottom figure C) reveal the individual and small groups of cells that adhered to the HA^{3}P50 fibers observed at D1 (pointed by yellow arrows), while after 21 days of culturing, cells proliferate leading to the formation of cell clusters (depicted by the red square). The adhesion of the HepG2 cells to the hydrogel may occur mainly through HA residues. Accordingly, the adhesion of hepatocytes increases to a chitosan matrix by adding HA [5]. These data indicate that HA^{3}P50 is not a non-cytotoxic 3D support for HepG2 cells, ensuring cell interaction and proliferation.

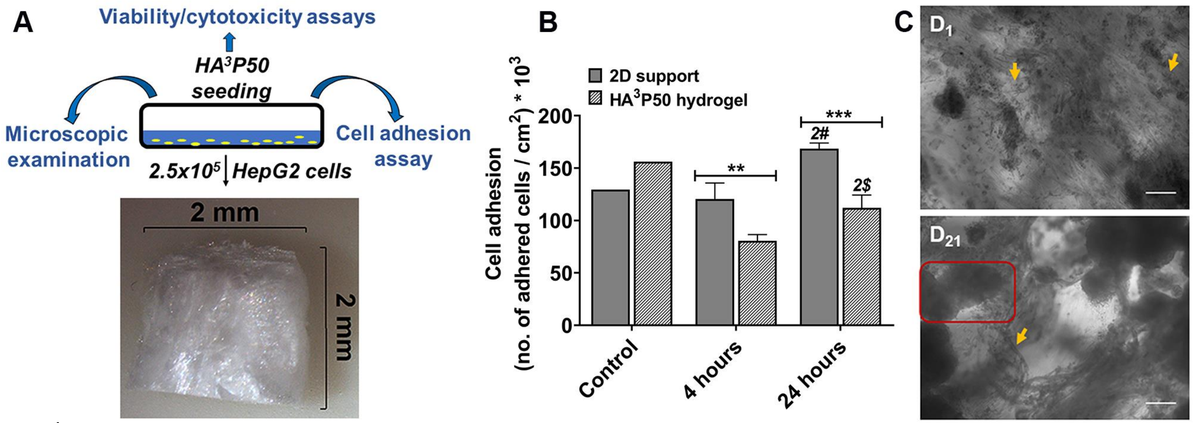

(A) The schematic representation of the experimental procedure used for biological assays; (B) Cell number of HepG2 cells seeded on the 2D support and HA3P50 hydrogel counted at two adhesion times (4 and 24 hours);(C) The light microscopy images of cell populated hydrogels are taken on day 1 and day 21.

Conclusions

The polymer concentration of 3 % (w/w) and the 1:1 P(MVE-alt-MA):HA weight ratio between polymers were found to be the optimal parameters for the synthesis of porous and stable hydrogel that allows cell proliferation.

The biological investigations demonstrate that HA^{3}P50 hydrogel is a biocompatible material supporting tumour cell growth that provides a 3D platform to mimic the tumour functionality suitable for anti-tumor drug screening.

References

1. Y. Matsumoto, Y. Kuroyanagi, Development of a Wound Dressing Composed of Hyaluronic Acid Sponge Containing Arginine and Epidermal Growth Factor, J. Biomater. Sci. Polym. Ed. 21(2010) 715-726.
2. J.L. Baier, K.A. Bivens, C.W. Patrick, C.E. Schmidt, Photocrosslinked hyaluronic acid hydrogels: natural, biodegradable tissue engineering scaffolds, Biotechnol. Bioeng. 82 (2003) 578-589.
3. J. Kim, Y. Park, G.Tae, K.B. Lee, C.M. Hwang, S.J. Hwang, I.S. Kim, I. Noh, K. Sun, Characterization of low-molecular-weight hyaluronic acid-based hydrogel and differential stem cell responses in the hydrogel microenvironments, J. Biomed. Mater. Res. A 88 (2009) 967-975.
4. W. Hassan, Y. Dong, W. Wang, Encapsulation and 3D culture of human adipose-derived stem cells in an in-situ crosslinked hybrid hydrogel composed of PEG-based hyperbranched copolymer and hyaluronic acid, Stem Cell Res. Ther. 4 (2013) 1-11.
5. D. Sgorla, A. Almeida, C. Azevedo, E.J. Bunhak, Development and characterization of crosslinked hyaluronic acid polymeric films for use in coating processes, Int. J. Pharm 511 (2016) 380-390.

Acknowledgment

This work was supported by a grant of Ministry of Research and Innovation, CNCS - UEFISCDI, project number PN-III-P4-ID-PCCF-2016-0050, within PNCDI III.

Effect of metal synergy and loading on binary W-Mo/HZSM-5 catalyst for non-oxidative conversion of methane into carbon and petrochemicals.

R.W.Musamali, Y.M Isa

Chemical Engineering department, Durban University of Technology, P.o box 1334 Durban,4000, South Africa

Introduction

- Primary energy sources; Oil, natural gas, and coal are of fossil origin.
- Processing of energy from fossil fuels is associated with emission of carbonaceous compounds into the atmosphere.
- Non-oxidative conversion of methane into carbon and valuable petrochemicals remediates emission of this greenhouse gas into the atmosphere.

Materials and methods

- Catalyst materials: Ammonium paratungstate, Ammonium heptamolybdate and HZSM-5 (Al/Si =50).
- Synthesis method: Incipient wetness impregnation, drying and calcination.
- Fresh catalyst: characterized by XRD, BET, SEM, and FT-IR.
- Spent catalysts: Characterized by TGA, and TEM for quantity, type, and morphology of deposited carbon nanomaterial.
- Catalytic activity: Evaluated in a stainless-steel reactor under different process conditions.
- Reactor effluent products were analyzed using gas chromatography.

Results and discussions

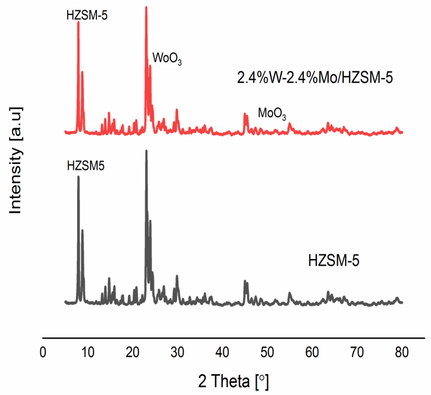

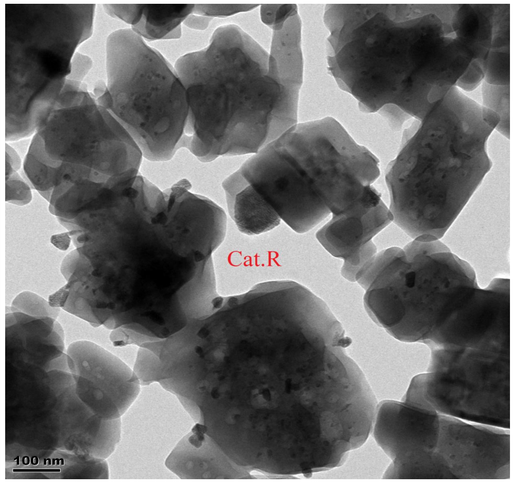

Fig.1. Combined XRD pattern of catalysts Fig.2. TEM image of catalyst 3.

Table 1. Catalyst activity at 4.8%metal loading on HZSM-5 at 750℃ and GHSV of 1200mL$g^{-1}_{cat}h^{-1}$,and 1 atm

Catalyst	Conv. (%)	C2 (%)	C6H6 (%)	C7H8 (%)	C8H10 (%)	Coke (%)
P	3.89	12.31	47.72	11.93	0.00	40.35
Q	15.19	8.48	44.78	9.8	0.00	45.42
R	11.34	6.22	63.14	10.14	0.46	26.42

- Catalyst nomenclature; P (4.8%Mo/HZSM-5), Q (4.8%W/HZSM-5) and R (2.4%W-2.4%Mo/HZSM-5)
- From Table 1 above, catalyst 2.4%W-2.4%Mo/HZSM-5 is more selective to benzene than individual 4.8%W/HZSM-5 and 4.8%Mo/HZSM-5 catalysts.

Conclusions

- From the study, we demonstrate that, competing reactions between different species of W and Mo plays a significant role in determining methane conversion and product distribution
- Combining W and Mo catalysts on HZSM-5 lowers methane conversion but increases selectivity towards aromatics

References

[1] M. Höök, X. Tang, *Energy policy* **2013**, *52*, 797-809.

[2] A. R. Brandt, M. S. Masnadi, J. G. Englander, J. Koomey, D. Gordon, *Environmental Research Letters* **2018**, *13*, 044027.

[3] J. P. Myllykangas, S. Hietanen, T. Jilbert, *Estuaries and Coasts* **2020**, *43*, 189-206.

Acknowledgment

We sincerely thank Durban university of technology for material and financial support towards this research work.

Intelligent Micro-vehicles for Drug Transport and Controlled Release to Cancer Cells

Gheorghe Fundueanu, Marieta Constantin

Department of Natural Polymers, Bioactive and Biocompatible Materials, "Petru Poni" Institute of Macromolecular Chemistry, 700487 Iassy, Romania;

E-mail:ghefun@icmpp.ro

Introduction

The idea that pH decreases significantly in tumours is widespread, however recent progress in the measurement of pH in cancer tissues has revealed that the intracellular pH of cancer cells is neutral or even mildly alkaline compared to normal tissues (Hao et al., 2018). However, in both cancer and normal cells the pH drops from 6.0-5.5 in endosomes to 5.0 in lysosomes after particle internalization by EPR effect.

PURPOSE: Design and development of "intelligent" delivery systems (mini-vehicles) able to exploit these pH variations: safely transport of drug and release it to the tumor site.

Materials and method

Materials

N-isopropylacrylamide (NIPAAm), obtained from Aldrich Chemical Corp. (Milwaukee, WI, USA), was recrystallized with hexane. 4-vinylpyridine (4-VP), potassium persulfate (KPS), *N,N,N',N'*-tetramethylethylenediamine (TEMED), and cyclohexane were supplied from Fluka AG (Buchs, Switzerland). Soybean lecithin and dexamethasone (Dex) was obtained from Iassyfarm S.A. (Iassy, Romania).

Copolymer synthesis

Linear poly(NIPAAm-co-4-VP) was synthesized by free radical co-polymerization of corresponding monomers in aqueous solution. In an illustrative example, 1.13 g of NIPAAm (10 mmol) and 160 µL of 4-VP (1.5 mmol) were dissolved in 10 mL of distilled water. 1 mL 1M HCl solution was added to complete the solubilisation of 4-VP. Dried nitrogen was flushed through the monomer solution for 60 min before polymerization. Subsequently, the initiator (0.020 g of KPS) and the accelerator (50 µL of TEMED) were added to the monomer solution and the copolymerization lasted 24 h at room temperature (20 ± 2 ºC). Afterward, the polymer solution was neutralized with 0.1M NaOH, dialyzed against distilled water for 7 days at 20 °C (molecular weight cut off 10,000-12,000 Da; from Medicell International, London, United Kingdom), and recovered by freeze-drying.

Synthesis of poly(NIPAAm-co-4-VP) microspheres

Copolymer microspheres were synthesized by the o/o solvent evaporation method. Typically, poly(NIPAAm-co-4-VP) (0.2 g) and Dex (0.020 g) were solubilized in methanol (4 mL). Then, the solution was dispersed in cyclohexane (60 mL) containing soybean lecithin (0.25 g) as the dispersing agent. The mixture was stirred at 600 rpm by a three-blade turbine impeller for 5 hours at 25 ° C and then for 1 hour at 45 °C. After each hour, 10 mL of cyclohexane are added dropwise to restore the volume of the evaporated solvent. Finally, the solid microspheres were washed with cyclohexane and dried from diethyl ether.

Results and discussions

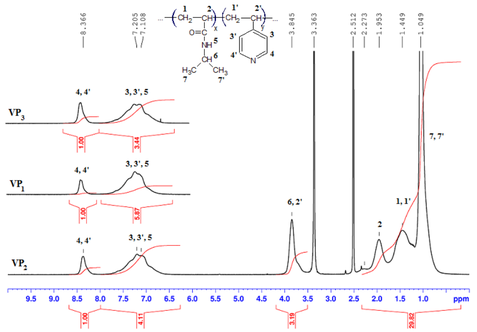

Fig. 1. ^{1}H-NMR spectrum of poly(NIPAAm-co-4-VP)

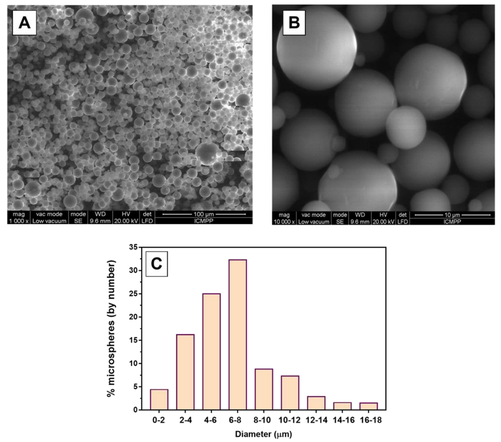

Fig.2. Scanning electron micrographs of poly(NIPAAm-co-4-VP) microspheres loaded with Dex: general view (panel A) and surface detail (panel B). Size distribution of microspheres (panel C).

Table 1. Dependence of LCST on the co-monomer ratio in the initial mixture and in the copolymer

Sample code	Co-monomer composition				LCST (°C)				
	In the feed × 10^{-3} M (% mol ratio)		In copolymer (% mol ratio)		H_2O	pH=7.4	pH=6.0	pH=5.5	pH=5.0
	NIPAAm	4-VP	NIPAAm	4-VP					
VP_0	10 (100)	0 (0)	100	0	32.6±0.2	28.8±0.3	30.2±0.2	29.2±0.2	31.2±0.3
VP_1	10 (90.9)	1 (9.1)	90.69	9.31	30.1±0.3	26.8±0.2	27.9±0.3	28.6±0.3	33.8±0.1
VP_2	10 (86.96)	1.5 (13.04)	86.30	13.70	27.8±0.3	22.1±0.3	23.5±0.4	27.7±0.3	36.8±0.3
VP_3	10 (83.33)	2 (16.67)	83.0	17.0	23.1±0.2	12.4±0.5	21.1±0.3	24.2±0.4	37.3±0.4

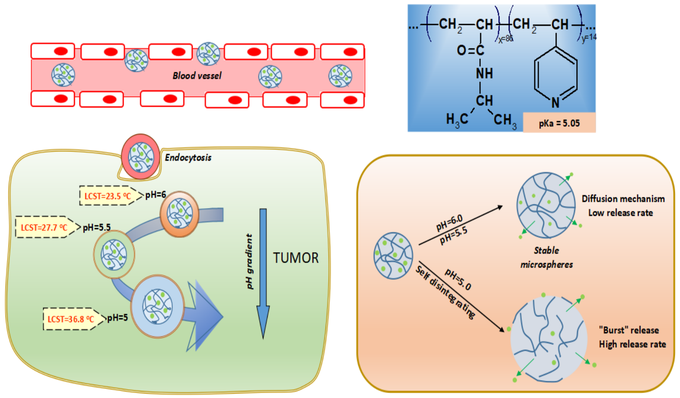

Fig. 4. Schematic representation of intelligent micro-vehicles action

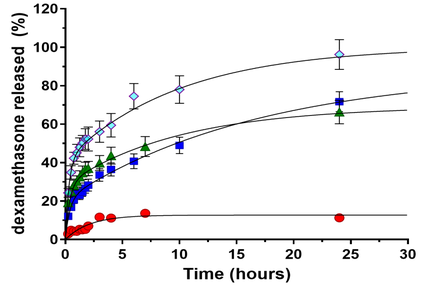

Fig. 3. Release profiles of dexamethasone from pH/thermoresponive poly(NIPAAm-co-4-VP) microspheres under normal physiological conditions (PB) at pH = 7.4 (circles) and under acidic conditions at pH = 6.0 (squares), 5.5 (triangles), and 5.0 (diamonds).

Conclusions

Perfectly spherical drug-loaded microspheres were obtained using this unusual binary system of immiscible organic solvents methanol and cyclohexane. The microspheres were appropriated to support loading and release of Dex. The release rates are pH dependent; however, although at pH = 7.4 the LCST of the copolymer is lower than the body temperature, a very small fraction of the drug is released. Then, although above the LCST, the copolymer is completely insoluble, it still has a certain degree of wettability as proven by contact angle measurements. As a whole, the design of insoluble pH / temperature sensitive copolymers fully hydrophobic under physiological conditions (pH = 7.4) and soluble in slight acidic environments remains a major concern for researchers.

References

G. Hao, Z.P. Xu, L. Li, Manipulating extracellular tumour pH: an effective target for cancer therapy, RSC Adv. 8 (2018) 22182-22192.

Acknowledgment

This work was supported by a grant of the Romanian Ministry of Research and Innovation, CCDI-UEFISCDI, project number PN-III-P1-1.2.-PCCDI-2017-0697/contract nr. 13 PCCDI/2018 within PNCDI III.

Development and characterization of new polymeric systems for sustained release of hypoglycemic sulfonylureas

L. G. Confederat[1,*], C. Tuchiluș[1], I. M. Condurache[1], M. Drăgan[1], F.G. Lupașcu[1], A. Iacob[1], I. Vasincu[1], M. Apotrosoaei[1], A. Focșa[1], A. Sava[1], L. Profire[1]

[1]University of Medicine and Pharmacy "Grigore T. Popa" Iasi, University Street no 16, 700115;

**E-mail: luminita.confederat@yahoo.com*

Introduction

In recent years, the interest in using natural polymers as drug delivery systems significantly increased. Consequently, a wide range of studies are focused on the development of systems type polymeric matrix-drug, in order to improve the pharmacokinetic and pharmacological profile of some drugs. Chitosan is a natural polymer obtained by alkaline deacetylation of chitin, presenting some important properties as biocompatibility, biodegradability, lack of toxicity and low immunogenicity. In addition to this, chitosan presents some pharmacological effects including hypoglycemic, cholesterol-lowering, antihypertensive, antioxidant, antimicrobial and favorable effects in reducing obesity, making it suitable for the development of different multi-target drug-polymer systems. The aim of this study was the development and *in vitro* characterization of new polymeric systems based on chitosan, in whose matrix was included gliclazide, a hypoglycaemic sulfonylurea extensively used in diabetes treatment.

Materials and method

The new polymeric systems were prepared as microparticles, through inotropic gelation method, using pentasodium tripolyphosphate (TPP) as cross-linking agent. Medium molecular weight chitosan in concentration of 1.5% was used, the concentration of cross-linking agent was 2% and the chitosan: gliclazide ratio ranged between 1:0.5, 1:0.75, 1:1. The microparticles obtained were characterized in terms of size, structure and morphology using IR Spectroscopy and Scanning Electronic Microscopy (SEM). The hydration ability was studied in distilled water and simulated gastric fluid. The encapsulation efficiency and the release of the drug from the polymeric matrix in conditions that simulate gastric and intestinal media, were determined using a HPLC method.

Results and discussions

It were obtained stable systems, the most favorable ratio between chitosan and gliclazide being 1:1. The size of the microparticles obtained ranged between 528.8 and 563 µm. The IR analyses proved the drug encapsulation and the SEM analyses showed the surface morphology. The encapsulation efficiency was 62.17%.

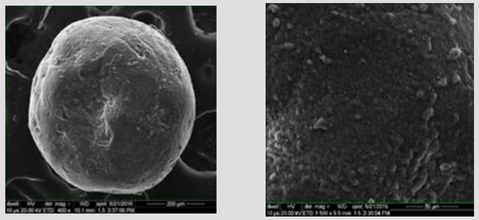

Fig. 1. SEM images of the microparticles type chitosan-gliclazide

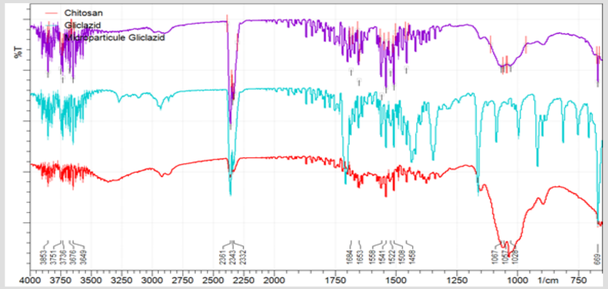

Fig. 2. IR spectrum of the microparticles obtained

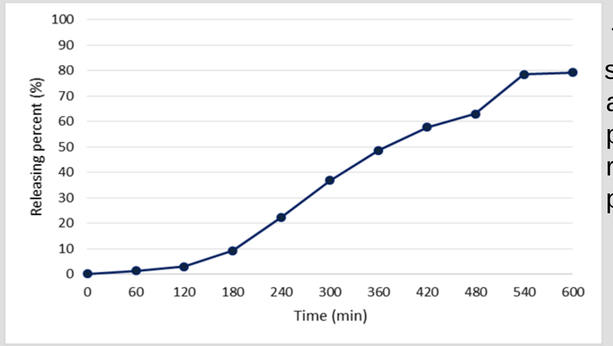

The systems obtained showed good hydration ability and the percentage of drug release from the polymeric matrix was 79.28% (Fig. 3)

Conclusions

The chitosan-gliclazide developed systems represent a step in the attempt to modulate the pharmacokinetic and the pharmaco-toxicological profile of some consecrated antidiabetic drugs.

References

1. Mitra, A., Dey, B, *Indian Journal of Pharmaceutical Sciences* **73,** 355 (2011).

2. Dash, M., Chielini, F., Ottenbrite R.M., Chiellini E, *Progress in Polymer Science* **36,** 981 (2011).

3. Oprea, A.M., Nistor, M.T., Popa, M. et al., *Carbohydrate Polymers* **90,** 127 (2012).

Acknowledgment

The authors acknowledge the financial support from the L'Oréal – UNESCO through the fellowship programme "For women in science".

Dual silicone-based elastomeric networks as electromechanical transducers

A. Bele[1], L. Yu[2], C.D. Varganici[1], D. Ionita[1], C. Racles[1], M. Cazacu[1], A. Skov[2]

1"Petru Poni" Institute of Macromolecular Chemistry, Aleea Grigore Ghica Veda, 41A, 700487, Iasi, Romania, **bele.adrian@iampp.ro**
2Technical University of Denmark, Department of Chemical and Biochemical Engineering, Danish Polymer Centre, 2800 Kgs. Lyngby, Denmark

Abstract

Interpenetrating polymer networks (IPNs) represent an interesting methodology for tuning the properties of silicone elastomers due to the possible synergism that may arise between the two networks. A new approach is presented, which consists of mixing two silicone-based networks with different crosslinking pathways, the first network being cured by condensation route and the second network by UV curing. The networks were mixed in different ratios and the resulted samples yield good mechanical properties (moderate elongations, 100 – 250 %, and reduced Young's modulus, 0.03 MPa), thermal properties (one glass transition temperature, ~-123 ^{o}C), good dielectric strength (40 – 60 MV/m) and actuation properties (estimated from figures of merit).

Crosslinking pathways and sample preparation

The samples were obtained based on two siloxane-based polymer networks combined in different ratios (see table below) and crosslinked by different pathway.

Chosen crosslinking pathways

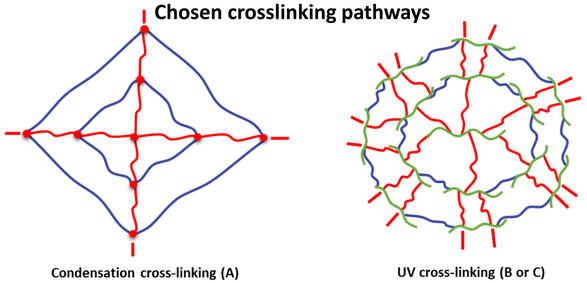

Condensation cross-linking (A) UV cross-linking (B or C)

The wt% rations used to obtain the IPNs; * - condensation crosslinking; ** - UV crosslinking

Network	Sample								
	A1	A0 B1	A0 C1	A1 B1	A2 B1	A1 B2	A1 C1	A2 C1	A1 C2
A* (Mn=70 000 g/mol)	1	0	0	1	2	1	1	2	1
B** (Mn=28 000 g/mol)	0	1	0	1	1	2	0	0	0
C** (Mn=9600 g/mol)	0	0	1	0	0	0	1	1	2

Mechanical Properties

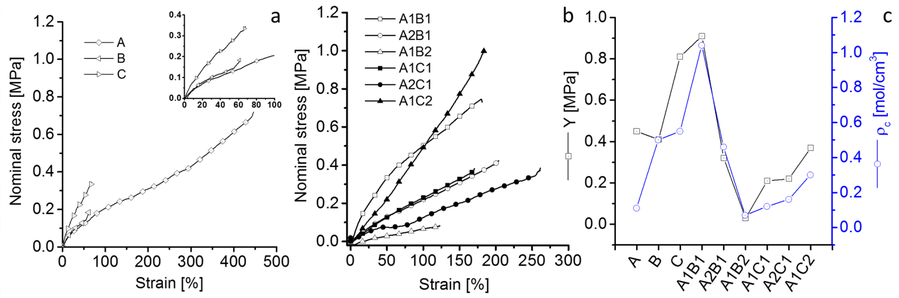

DSC

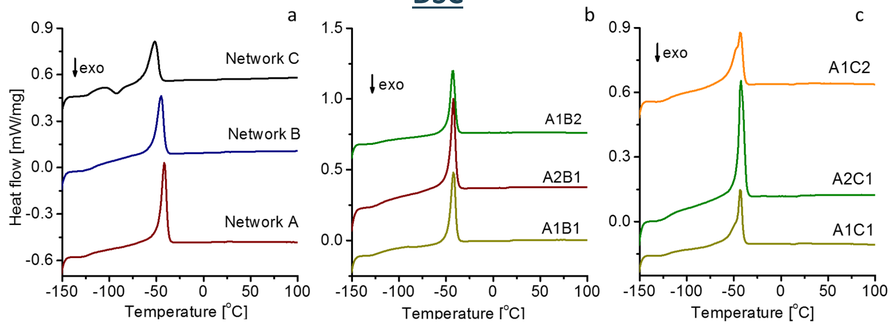

Rheological characterisation

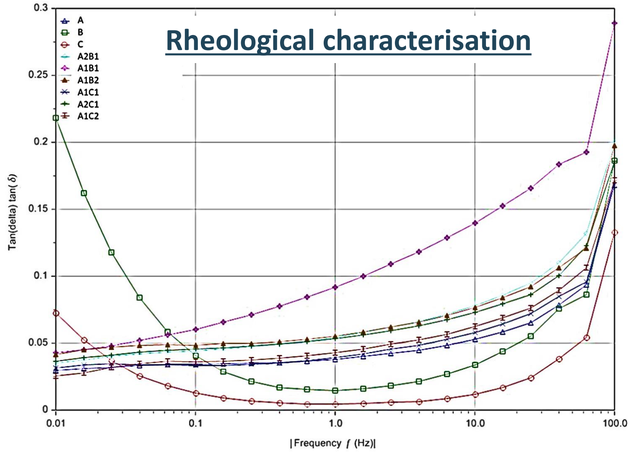

Mechanical and dielectric data

Sample	T_{nm} [MPa]	S_m [%]	Y@10% [MPa]	ε' @1kHz	ε'' @1kHz	Ebd [V/μm]
A	0.71	446	0.45	3.25	0.100	41
B	0.18	61	0.41	3.00	0.002	39
C	0.34	68	0.81	3.17	0.003	39
A1B1	0.73	181	0.91	4.08	0.016	40
A2B1	0.42	203	0.32	3.72	0.006	63
A1B2	0.08	122	0.03	3.71	0.016	25
A1C1	0.38	170	0.21	3.66	0.003	35
A2C1	0.39	261	0.22	3.86	0.036	47
A1C2	1.01	184	0.37	3.97	0.005	46

T_{tm}- Nominal stress at break; S_m-Maximum strain at break; Y-Young's modulus; ε_r- dielectric permittivity; ε''- dielectric loss; E_{bd}- breakdown strength

Conclusions

- The mechanical properties are drastically influenced by the wt% rations between the two networks and by the molecular masses used.
- The rheological studies show that one-step network B present a more pronounced relaxation at low frequencies in tan δ spectrum compared with one-step network C, due to the longer relaxation times exhibited by long dangling chains remained uncross linked [2].
- Both networks, B and C, act as plasticisers when combined with network A, resulting in low values of Young's modulus.
- The dielectric permittivity values remain low, not drastically influenced by the rations used between the networks;
- Young's modulus is the main parameter that influenced the FOM and the electromechanical sensitivity
- The DSC measurements reveal only one Tg at low temperatures, thus no phase separations occurs between the networks.

Acknowledgment

Authors gratefully acknowledge to project: **SilWebWEH**, **PN-III-P1-1.1-PD-2019-0148** and to EuroEAP society through The Scientific Mission Grants.

New Multitarget Polymer Systems For The Treatment Of Diabetes Mellitus

F.G. Lupașcu, I. Vasincu, A.T. Iacob, M. Apotrosoaei, A. Sava, L.G. Confederat, M. Drăgan, G. Taușer, L. Profire

University of Medicine and Pharmacy "Grigore. T. Popa" Iași, Universității Street, no. 16, 700115, Iași, Romania

Introduction

Diabetes mellitus (DM) is a one of the major diseases in the world that affects more than 8% of adults meaning approximately 380 million people

improving the antidiabetic agents bioavailability is a major concern of researchers. Obtaining micro/nanoparticles have attracted a considerable attention as potential carriers for drugs controlled delivery. This research was focused on the development of new polymeric systems, as chitosan microparticles, to improve the pharmacological and pharmacokinetic profile of two oral antidiabetic agents: metformin (M) and glibenclamide (G). Chitosan (CH) is a biocompatible and biodegradable polymer, with many biological action. Therefore we have used chitosan as matrix for different compounds.

Materials and method

Chitosan microparticles, chitosan-drugs were obtained by ionic gelation method using pentasodium tripolyphosphate (TPP) as crosslinking agent.

In order to optimize the method for obtaining chitosan microparticles, the chitosan concentration (1%, 0.75%, 0.5%), TPP (1%, 2%) and the concentration of the active drug (30 mg, 22.5 mg and 15 mg) was varied. The particle size, structure and morphology was studied by scanning electron microscopy; the swelling degree was evaluated in simulated gastric fluid (SGF). The drugs loading efficiency was evaluated using UV spectrophotometric method (Chellappan et al 2019; Raghavendra and Kumar 2017). Type 2 diabetes mellitus was induced by streptozotocin on Wistar rats.

The antidiabetic drugs (M, G) and chitosan-antidiabetic drug microparticles (CS-M, CS-G, CS-MG) were orally administered, once per day, for a period of 45 days. During the experiment it were investigated the biochemical parameters such as glycaemia and glycosylated haemoglobin (Avram et al 2017).

Results and discussions

Following the optimization process, it has been established the optimal formula for loading the two active substances in the polymer matrix. For glibenclamide, the percentage varied depending on the ratio of drug: polymer used, and it has been at the same time proved higher than that registered for metformin. In combination of the two substances, similar levels of individual loaded were obtained. The swelling degree of polymeric systems developed in SGF was higher compared in distilled water. Oral administration of these new polymeric systems significantly reduced the blood glucose levels in reference with the diabetic rats. The best hypoglycaemic effect was recorded for CS-MG formulation.

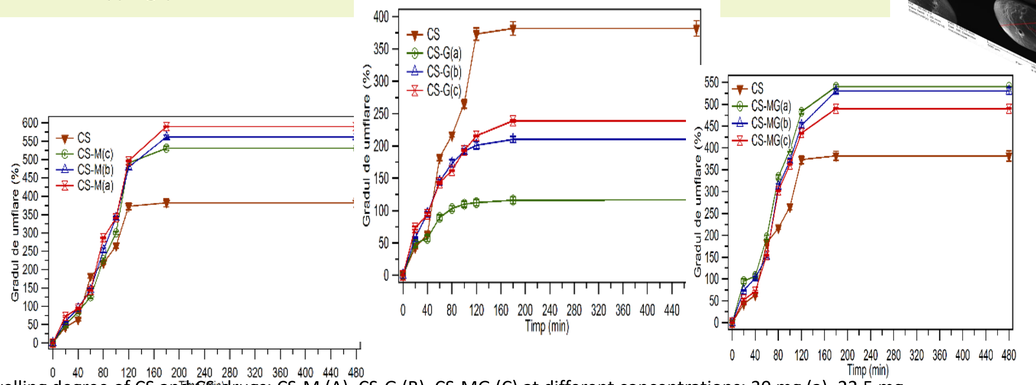

The swelling degree of CS and CS-drugs: CS-M (A), CS-G (B), CS-MG (C) at different concentrations: 30 mg (a), 22.5 mg (b) 15 mg (c) in simulated gastric fluid

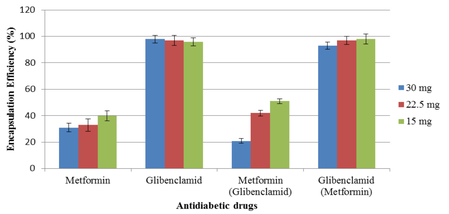

Fig.1. Drugs loading efficiency of Metformin, Glibenclamid, Metformin and Glibenclamid at different concentrations: CS-Metf. (30 mg/22,5 mg/15 mg), CS-Glib. (30 mg/22,5 mg/15 mg), CS-Metf.-Glib. (30 mg/22,5 mg/15 mg)

Glycosylated haemoglobin level

The effect of chitosan formulations (CS-M, CS-G, CS-MG) was improved compared with the standard antidiabetic drugs . The best results were obtained with chitosan-metformin-glibenclamide formulation, for which the values of HbA1c recorded at the 21st day and 45th day of the experiment was 6.32% and 7.78%, respectively. In the similar conditions the values of HbA1c recorded for diabetic rats were 11.50% and 12.07% respectively.

Blood glucose level

At the end of the experiment the chitosan microparticles loaded with drugs significantly reduced the blood glucose levels in reference with the diabetic rats for wich the value of the glucose level was 512 mg/dL. The best hypoglycaemic effect was recorded for chitosan-meformin-glibenclamide formulation. For this polymeric system the value of the glucose level was 167 mg/dL while for CS-M and CS-G the values recorded were 312 mg/dL and 220 mg/dL, respectively.

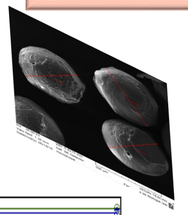

Conclusions

In this study, it was obtained three polymer-drug systems: CS-M, CS-G, CS-MG, which were physico-chemical, morphological and spectral characterized. Also was tested in vivo hypoglycemic activity of these new polymeric systems.

References

I., Avram, F.G., Lupaşcu, L., Confederat, S.M., Constantin, C.I., Stan, L., Profire, *Farmacia* **65(3)**, 443 (2017).

D. K., Chellappan, N. J., Yee, B. J. K. A. J., Singh, J., Panneerselvam T., Madheswaran J., Chellian S., Satija, M., Mehta , M., Gulati, G., Gupta, K., Dua, *Therapeutic Delivery* **10(5)**, 281 (2019).

H.L., Raghavendra, G.P., Kumar, *Journal of Bioequivalence & Bioavailability* **9(1)**, 324 (2017).

Antioxidant and anti-hemolytic evaluation of nanofibrous mats derived from chitosan/PEO blend embedded with active biomolecules for wound healing application

A. T. Iacob[1*], O. M. Ionescu[1], F. G. Lupașcu[1], I. M. Vasincu[1], M. Apotrosoaei[1], L. G. Confederat[1], M. Drăgan[1], A. Sava[1], G. R. Taușer[1], L. Profire[1]

[1]University of Medicine and Pharmacy "Grigore T. Popa"Iasi, University Street no 16, 700115;

*E-mail: andreea.panzariu@umfiasi.ro

Introduction

Nanotechnology offers a superlative approach to hasten the healing of acute and chronic wounds, by stimulating proper movement through the different healing phases. In nanotechnology, the small sized nanomaterials, nanoscaffolds,nanofibes and biomaterials are used for topical drug delivery for wound healing [1, 2].

In recent years, the use of nanomaterials for biomedical and pharmaceutical applications have gained significant attraction [1].

Chitosan (CS) provides a non-protein matrix for 3D tissue growth and activates macrophages for tumoricidal activity. It stimulates cell proliferation and histoarchitectural tissue organization, and also has hemostatic effects, which helps in natural blood clotting and blocks nerve endings reducing pain [2].

Materials and method

The preparation of CS/PEO matrices was performed in two stages: (i) the formation of biopolymeric solutions by dissolving CS and PEO in 50% acetic acid stirring at r.t. The two solutions will be mixed in appropriate ratios, then, over the resulting mixture, the active substances: arginine (Arg) and propolis (Pr) were added and stirred until a homogeneous solution is obtained; an INOVENSO nanospinner was used, a needle syringe of appropriate size filled with the polymer solution and then different values of flow rate, applied voltage and also different distances from the tip of the syringe to the collecting plate were applied, in depending on each sample [3, 4]. The evaluation of the antiradical ability was performed using the free radical DPPH and the cation radical $ABTS^{+\cdot}$. The antiradical capacity was calculated as a percentage of inhibition (I%) using the formula: $I\%=(A_0-A_s/A_0) \times 100$ where, A_0 = the absorbance value of the 0.1 mM DPPH methanolic solution /$ABTS^{+\cdot}$ ethanolic solution and A_s = the absorbance value of the formulation, read at 30 minutes and 60 minutes after the addition of the DPPH methanol solution/read at 6 minutes after the addition of the ABTS solution^{+} (**Fig. 1a, b**) [4]. The evaluation of the anti-hemolytic potential was also performed by a spectrophotometric method, by the ability to stabilize erythrocyte membranes at lysis induced by hypotonicity (**Fig.1c**).

Results and discussions

The preparation of CS/PEO matrices was done in two stages: (i) the formation of 3 biopolymeric solutions starts by dissolving CH and PEO in 50% acetic acid by stirring at room temperature. The two solutions will be mixed in appropriate ratios, then, over the resulting mixture, the active substances (arginine and propolis) were added and stirred until a homogeneous solution is obtained;

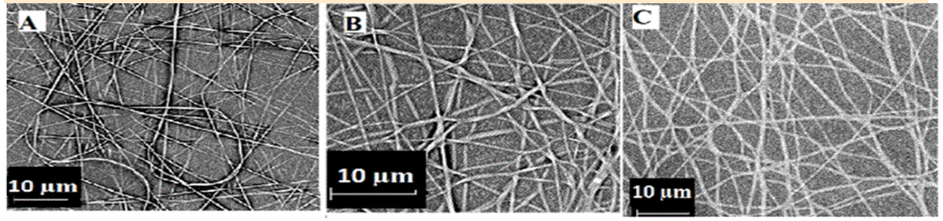

The 3 nanofibrous matrices developed were: PEO/CS/Arg (A); PEO/CS/Arg-dry Propolis (B); PEO/CS-Arg-alcoholic solution Propolis (C) as seen in the SEM micrographs upwards.

The results obtained after performing the in vitro evaluation by spectrophotometric methods.

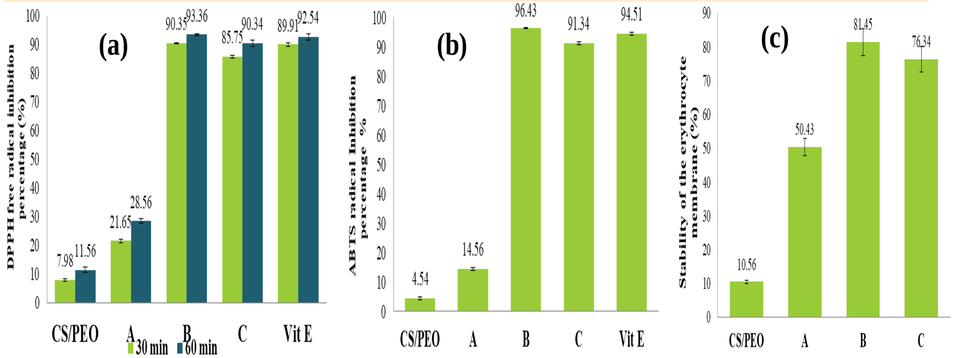

Fig. 1. Determination of **(a)** DPPH antiradical ability **(b)** ABTS antiradical capacity **(c)** anti-hemolytic potential, where PEO/CS/Arg (A); PEO/CS/Arg-dry Pr (B); PEO/CS-Arg-alcoholic solution Pr (C).

Conclusions

After analyzing the data obtained, it was concluded that nanofibers with propolis incorporated in solid state obtained the best results. The studies and results obtained justify the evaluation of the biological, antibacterial and pro-healing potential in the treatment of various wounds, starting from the antibacterial/antioxidant effects of chitosan and the beneficial role of topical propolis applied in the treatment of wounds.

References

1. Li, X. Wu, Y. Wu, Z.Tang, H. Liu. Mater Sci Eng: C 77-1 (2017) 411-419;
2. Nordin, N .A.V. Sainik, M.S. Zulfarina, I. Naina-Mohamed, R.B .H. Idrus. Wound Med. 18 (2017) 8-20;
3. Rajendran , S.S.D. Kumar, H. Abrahams. J Drug Deliv Sci Technol. 44 (2018) 421-430;
4. Thakur, G. Sharma, B. Singh, S. Chhibber, A.B. Patil, O.P. Katare. Int J Biol Macromol. 115 (2018) 1012-1025.
5. Feng, X., Li, J., Zhang, X., Liu, T., Ding, J., Chen, X. J. Control Release (2019).302, 19-41.

Acknowledgment

The work has been funded by the Operational Programme Human Capital of the Ministry of European Funds through the Financial Agreement 51668/09.07.2019, SMIS code 124705 and by the University of Medicine and Pharmacy "Grigore T. Popa Iasi", based on grant number. 27496/20.12.2018.

Treatment of Pesticides in Wastewater by Heterogeneous and Homogeneous Photocatalysis

M. Drăgan*, A. T. Iacob, O. M. Ionescu, F. G. Lupașcu, I. M. Vasincu, M. Apotrosoaei, L. G. Confederat, A. Focșa, O. M. Dragostin, L.Profire, C. D. Stan

University of Medicine and Pharmacy "Grigore T. Popa", Faculty of Pharmacy, Iasi 700115, Romania
University of Medicine and Pharmacy "Dunărea de Jos", Faculty of Pharmacy, Galaţi, 800008, Romania

Introduction

Mepiquat chloride or 1,1 - dimethyl-piperidine chloride, also known as DPC, is a new plant growth regulator that can be used in a variety of crops and play a variety of effects. It works inhibiting gibberellic acid synthesis, reduces internode length, hastens maturity and retards abscission. In addition, DPC is used to prevent the lodging of winter wheat; for apples, it can increase calcium absorption, reduced from depression disease; for citrus it can increase sugar content. In agrochemical products it is formulated as emulsifiable concentrate, water dispersible granulate and as technical product. This pesticide was first registered in the USA in 1980 to be used as a growth regulator of cotton and in 1997 it was reregistered by the Environmental Protection Agency (EPA) for its use in the USA. Now it is formulated as emulsifiable concentrate at concentrations lower than 5% (w/v).
Mepiquat chloride has the molecular formula C7H16ClN and a molecular weight of 149.66 g/mol. Fig. 1 presents the structural formula of 1,1 - dimethyl-piperidine chloride.

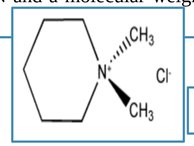

Fig. 1. Structural formula of 1,1 - dimethyl-piperidine chloride

Materials and method

Vessels and reactives:

For the photocatalytic experiments, a sollution of mepiquat chloride pesticide was used. As catalysts, TiO_2 P-25, TiO_2 UV-100, TiO_2-A, TiONa and ZnO were studied.

A 500 mL photoreactor was used to build the experimental plot, presented in Fig. 2. The reactor was covered with a black cloth to avoid interactions with ambiental light.

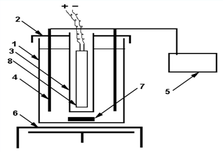

Fig. 2. Photocatalysis experimental plot (1 – photochemical reactor, 2 – pierced cap, 3 – quartz glass tube, 4 – plastic tubes , 5 – compressor, 6 – magnetic range, 7 – magnetic agitator, 8 – UV lamp)

Procedures and analyses:

In the initial 300 mL pesticide aqueous solution (C=10mg/L), different quantities of catalysts were added. The reaction solutions were magnetically stirred in the dark for 30 min until adsorption/ desorption equilibrium was reached. The solutions were then irradiated under UV light with continuous magnetic stirring. A fixed quantity of each mepiquat chloride solution was taken at regular time intervals during the illumination period and filtered through a syringe filter to analyze the amount of pesticide remaining in the solution. DPC concentrations during the experiments were monitored by a Total Organic Carbon Analyzer from Shimadzu.

Conclusions

(i) The present study demonstrated the possibility of oxidative degradation of persistent organic pesticides by heterogeneous photocatalysis.
(ii) Nearly complete degradation of mepiquat chloride was obtained after about 180 minutes in the presence of an acid medium (pH 3) using a UV-A lamp and the TiO_2 P-25 catalyst (0.5 g/L), for an initial pesticide concentration of 10 ppm.
(iii) The remnant pesticide concentrations were higher when homogeneous photocatalytic oxidation was involved, in comparison with levels obtained in a heterogeneous photocatalytic degradation process based on TiO_2.
(iv) Degradation rates corresponding to homogeneous photocatalysis were lower compared to those corresponding to the use of TiO_2 as the photocatalyst. In this way, the remnant concentrations of mepiquat chloride were below the drinking water level of comparison for acute and chronic risk range for infants and children (6 ppm), but as a consequence of the heterogeneous photocatalysis degradation process, this remnant concentration was about 10 times lower than the abovementioned level (0.54 ppm for 0.5 g/L TiO_2 P-25, *Ci* = 10 ppm pesticide).
(v) Moreover, we tested the possibility of reusing TiO_2 P-25 three times and found comparable photocatalytic activity for the solids with each use. The TiO_2 Degussa was recovered by simple washing, providing an economic advantage to this process.
(vi) Our study succeeded in achieving the task of finding a suitable photocatalytic system to provide a mepiquat chloride remnant concentration in accordance with EPA standards.

Results and discussions

Influence of the Type of Catalyst

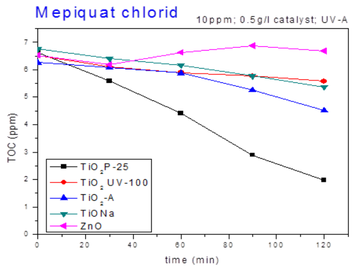

Fig.3. Pesticide degradation by heterogeneous photocatalysisusing different catalysts

Five types of catalysts were analysed during this study: TiO_2 P-25, TiO_2 UV-100, TiO_2-A, TiONa, ZnO, the results being plotted in Figure 3. The corresponding amounts of catalyst were added to 10 ppm solutions of mepiquat chloride in order to obtain a dose of 0.5 g catalyst/L and then irradiated with UV-A light. From Figure 3, it can be seen that the TiO_2 P-25 catalyst exhibited the best behaviour in the degradation of mepiquat chloride and was thus considered the reference catalyst. The increase of the TOC values in the case of the ZnO catalyst might be assigned to the desorption of the pesticide from the ZnO surface, taking into consideration that the adsorption of mepiquat chloride on this material is less intense in comparison with the other photocatalysts.

Influence of Catalyst Concentration

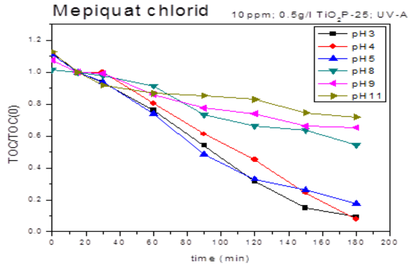

Fig.4. The TiO_2 P-25 concentration influence on the degradation of mepiquat chloride

The influence of catalyst concentration was studied for the TiO_2 P-25 catalyst, which was chosen as the reference.
The degradation experiments were conducted using the same pesticide concentration (10 ppm), the same UV-A lamp, and different concentrations of the same photocatalyst. The results are depicted in Figure 4.
As expected, Figure 4 shows that the most advanced pesticide degradation occurred when heterogeneous photocatalysis was conducted with a higher dose of the catalyst (TiO_2 P-25).

Influence of pH

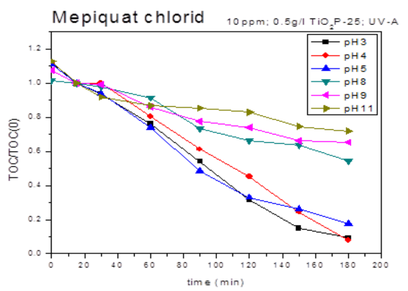

Fig. 5. Pesticide degradation in time at different pH values of the initial solution

Influence of pH. The influence of the pH of the solution was studied by conducting the photocatalyst experiments with 0.5 g/L TiO_2 P-25 catalyst in 10 ppm mepiquat chloride solution, using the UV-A lamp but adjusting the solution pH from acidic values (pH 3, 4, and 5) to basic values (pH 8, 9 and 11).
Figure 5 illustrates the variation in TOC/TOC(0) values over time at different pH values. The positive effect of acidic pH on pesticide degradation noted in the figure can be assigned to the fact that the TiO_2 surface is positively charged when the solution pH is lower than 6.8, thus facilitating the photocatalytic process.

References

1. C. Pastravanu, I. Poulios, E. Popovici, and I. Cretescu, "A case study of textile wastewater treatment by heterogeneous photocatalytic degradation," *The Annals of the "Dunarea de Jos" University of Galati Fascicle II—Mathematics, Physics, Chemistry, Informatics*, vol. 32, pp. 31–38, 2009.
2. I. Poulios, E. Micropoulou, R. Panou, and E. Kostopoulou, "Photooxidation of eosin Y in the presence of semiconducting oxides," *Applied Catalysis B*, vol. 41, no. 4, pp. 345–355, 2003.
3. G. D. Suditu, M. Secula, C. G. Piuleac, S. Curteanu, and I. Poulios, "Genetic algorithms and neural networks based optimization applied to the wastewater decolorization by photocatalytic reaction," *Revista de Chimie*, vol. 59, no. 7, pp. 816–825, 2008.

Quantum efficiency and bandgap assessment of various TiZr oxide nanostrucutres

Andrei Bogdan Stoian[1], Cristian Pirvu[1]

[1]University Politehnica of Bucharest, 1-7 Polizu str., sector 1, 011061, Bucharest, Romania

Introduction

For efficient photoexcitation of Ti and Zr oxides, it is necessary the application of light with energy higher than their band-gap energy, resulting in the formation of electron-hole pairs.

The excited electrons and holes can either recombine in the material and dissipate as heat or combine with suitable electron/hole acceptors in photocatalytic reactions).

Other aspects that influence the efficiency of the reactions are the surface architecture and chemistry of the material.

Nanostructuring provides a high surface to volume ratio for the material, rendering it the possibility to absorb light more efficiently and doping is usually employed to reduce the band-gap.

Materials and methods

Nanochannels (NC)

- Polished and cleaned Ti50Zr pieces were chemically etched in a cold acid mixture ($3HNO_3$:1HF:$2H_2O$).
- The electrolyte (10 wt.% K_2HPO_4/glycerol) was kept at 200°C for 4 h for water removal.
- Etched Ti50Zr was anodized for 2 h at 180°C by applying 50V.

Nanotubes (NT)

- Step 1: polished and cleaned Ti50Zr samples were immersed in the electrolyte (1M $(NH_4)_2SO_4$ + 0.5%wt NH_4F in H_2O), applying 45V for 2 h.
- The oxides produced during Step 1 were removed by ultrasonication.
- Step 2: same Ti50Zr piece was anodized again in the same conditions.

Results and discussions

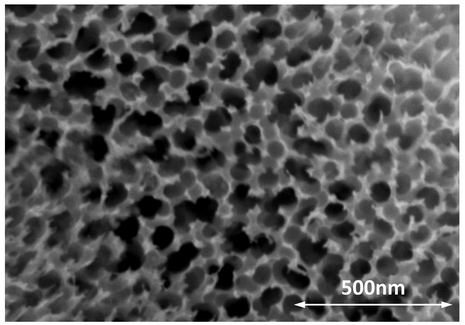

The needle-like microstructure of the etched Ti50Zr alloy is reflected in the structure of the obtained nanochannels layer. The nanochannels have a diameter of ≈50nm and length of ≈3.2µm.

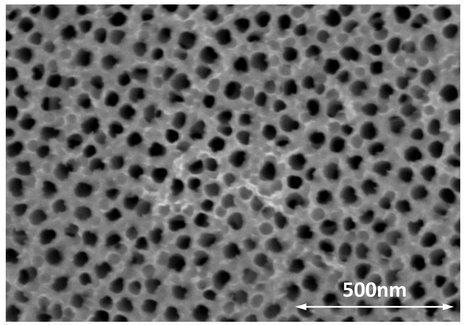

The surface microstructure of the Ti50Zr sample covered with nanotubes was extremly smooth. The obtained nanonanotubes have a diameters between 40-60 nm and lengths of ≈15µm.

Sample	Nitration temperature (˚C)	Band-gap (eV)
Ti50Zr NT	800	2.66
Ti50Zr NC	800	1.92
Ti50Zr NC	900	2.24
Ti50Zr NC	1000	1.78

Band-gap approximation of the samples was calculated with the formula E (eV) = 1240/λ (nm). λ is the highest wavelength at wich photon conversion occurs.

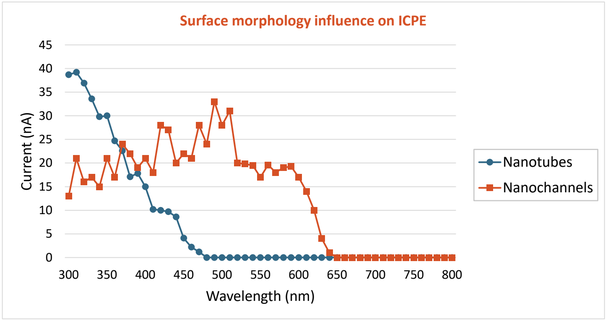

Photochemical experiments were performed in 0.1M Na_2SO_4 solution in the range of 300–800 nm. This graph represents Quantum Efficiency as Incident Photon Conversion Efficiency (ICPE) of NT and NC nitrated at 800°C for 10 min in NH_3. The NT exhibit good conversion in the near UV domain (300-400 nm), rapidly decreasing in the visible domain. After 480 nm, no activity was detected. The NC, although producing a lower and fluctuating current, exhibit a wider range of activity (up to 650 nm).

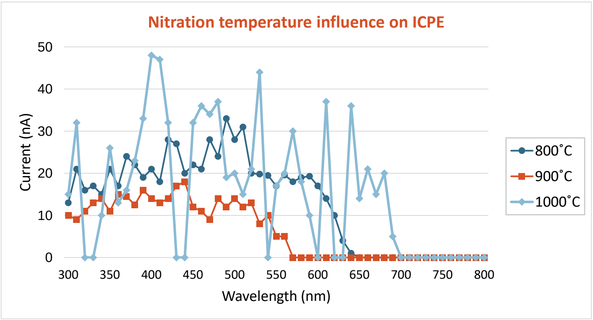

The effect of nitration temperature on ICPE was tested for TiZr samples covered with NC.

The increase of nitration temperature, leading to a higher nitrogen concentration in the samples did not have a beneficial effect on photon conversion. At 900°C there is a overall decrease of current generation as well as a narrowing of the active domain. At 1000°C, although there is an increase of current and active domain, the fluctuation of the current hints to a recombination of electron-hole pairs in the sample.

Conclusions

ICPE can be improved by modifying the surface of a semiconductor with organised nanostructures, thus increasing the active surface. Depending on the type of nanostructures reflection of light from the surface of the sample can be decreased.

The addition of dopants in the oxide crystal lattice is ussualy employed to reduce the band-gap of the samples and increase their active rangerange.

The density of nanocrystals decreases with the increase in dopant concentration, whereas it increases with the annealing temperature. A balance should be achieved for maximum efficiency.

Acknowledgment

The work has been supported by the Operational Programme Human Capital of the Ministry of European Funds through the Financial Agreement 51668/09.07.2019, SMIS code 124705.

The correlation between structural parameters and electromechanical performance of silicone elastomers

Codrin Tugui

Department of Inorganic Polymers, "Petru Poni" Institute of Macromolecular Chemistry, Aleea Grigore Ghica Voda 41A, 700487 Iasi, Romania

tugui.codrin@icmpp.ro

Introduction

Silicone elastomers are one of the most promising materials for dielectric elastomer transducers (DETs). In the simplest form, a DET consists of thin elastomeric membranes coated on both sides with compliant electrodes being able to deform under the action of an electrical stimulus. To enhance the electromechanical performance of silicones, the academic research has primarily been directed on improving the dielectric permittivity, Young's modulus and dielectric strength. Many of these studies include sophisticate approaches such as incorporation of different filler or chemical modifying commercial polysiloxanes by attaching polar groups while, the simple way of optimizing the elastomer have remained less explored. However, the properties of silicone elastomers can be significantly modified within certain appreciable limits by properly designing the elastomeric network. To demonstrate this, multiple series of silicone elastomer films differing by crosslinking pattern and molecular weight were prepared. The obtained results revealed that the mechanical and electromechanical behavior of silicone-based elastomers can be easily optimized by choosing the right molecular mass of the polymer and the cross-linking pattern.

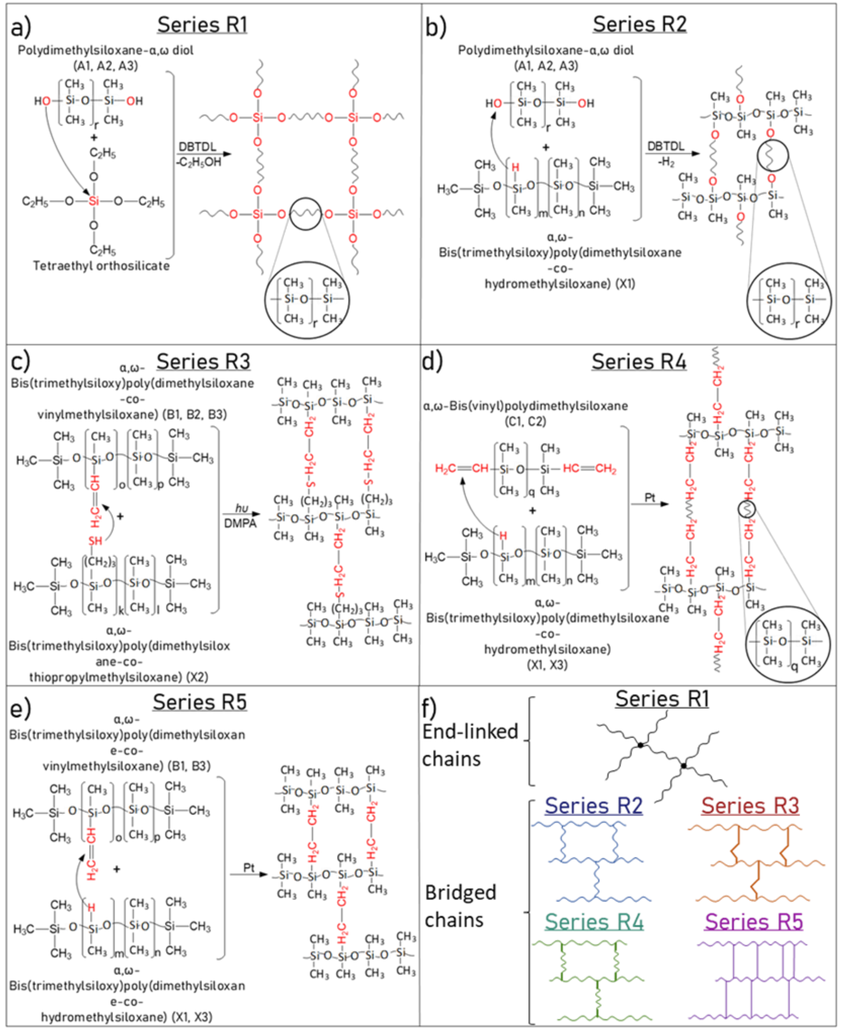

Results and discussions

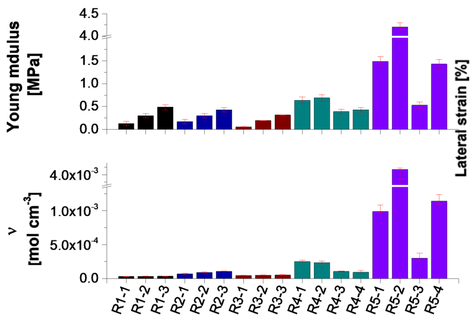

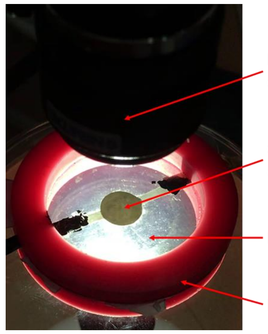

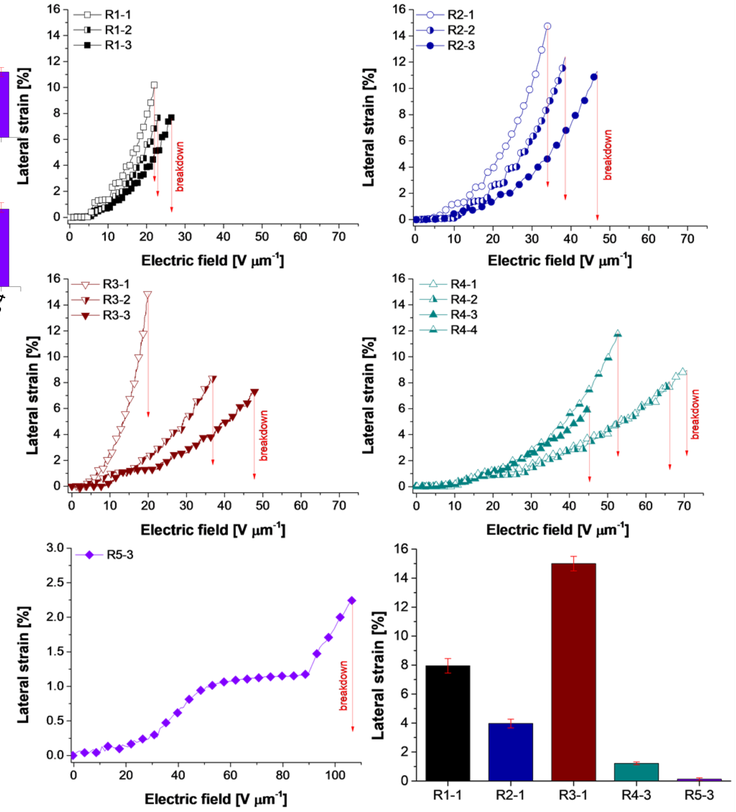

Conclusions

The mechanical behaviour of the elastomers changes substantially depending on the molecular mass and crosslinking pattern. The electromechanical properties were evaluated by actuation measurements and the elastomer R3-1 showed the best actuation strain of 15 % at an electric field of E = 20 V μm^{-1}. The electromechanical performances of silicone dielectric elastomers can be tuned only by the molecular mass and the crosslinking pattern without complicating the system with other additives.

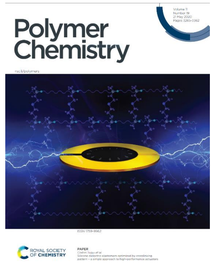

Acknowledgment

This work was supported by a grant of the Romanian National Authority for Scientific Research and Innovation, CNCS/CCCDI -UEFISCDI, project number PN-III-P1-1.1-PD-2019-0649, SwitchACT, within PNCDI III.

Comparative assessment of different dielectric elastomer actuators (DEAs)

Codrin Tugui, Maria Cazacu

Department of Inorganic Polymers, “Petru Poni” Institute of Macromolecular Chemistry, Aleea Grigore Ghica Voda 41A, 700487 Iasi, Romania

tugui.codrin@icmpp.ro

Introduction

Dielectric elastomer actuators (DEAs) are electromechanical transducers that convert electrical energy to mechanical work. Compared with other actuators, DEAs have a series of advantages such as flexibility, large actuation strain, fast response, high energy density and high reliability. Currently, DEAs are being studied extensively due to their ability to be used in a wide range of applications. To obtained the best electromechanical results, was designed an elastomer based on high molecular weight polydimethylsiloxane-α,ω-diol. Furthermore, for comparison, was tested in same conditions two commercial elastomers and the results were compared with those obtained for the in-house prepared elastomer. To better understand the electromechanical behaviour in terms of microstructure of polymer network, it was determined the gel fraction for all elastomers. Further, stack actuators based on the three types of elastomer each of them having 30 active layers, were fabricated and evaluated. All experimental results were deeply analyzed in a correlative manner to identify the best actuator configuration.

Results and discussions

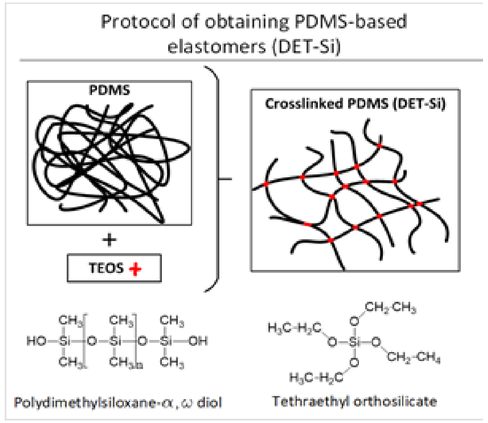

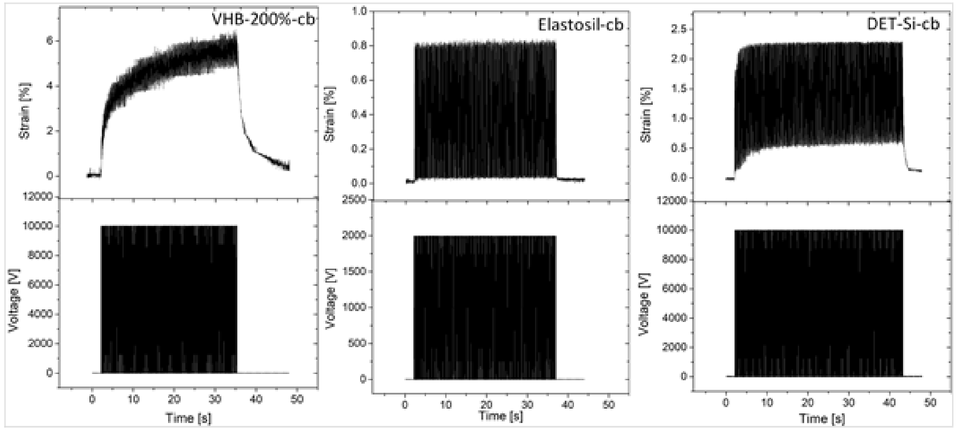

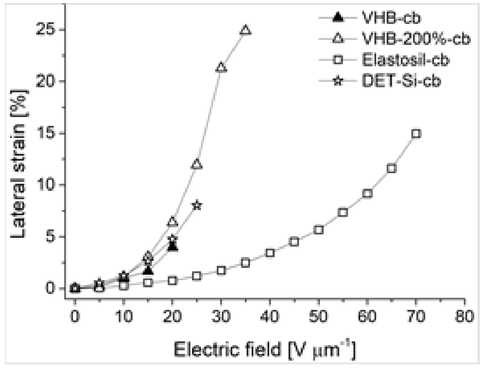

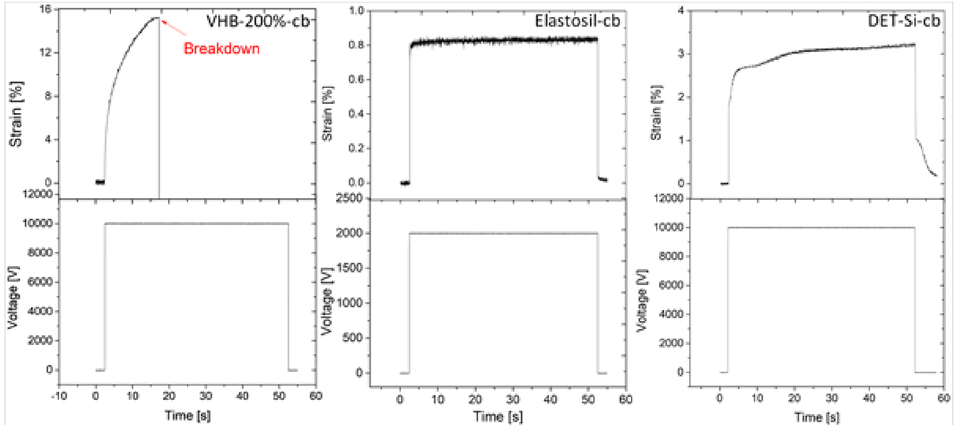

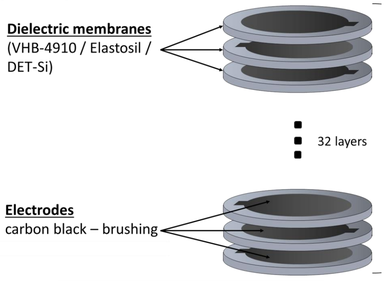

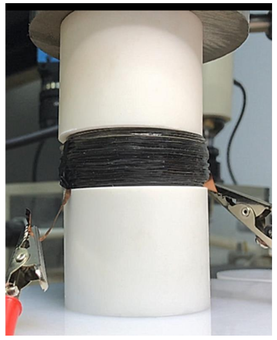

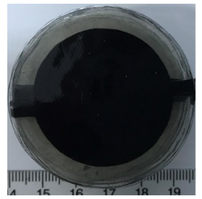

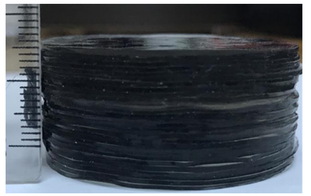

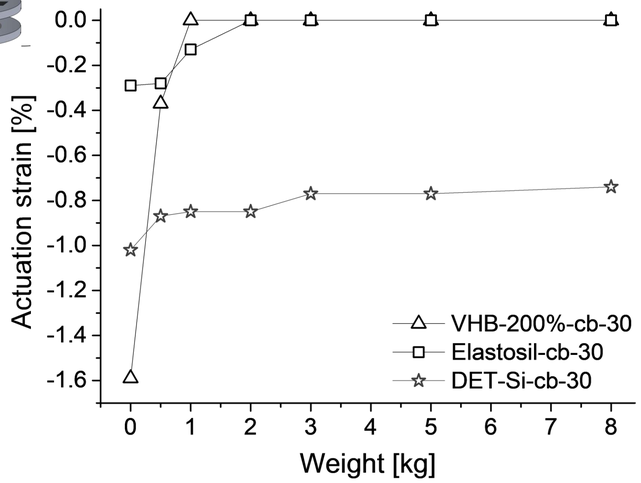

Conclusions

Considering the frequency response and lateral strain values at 20 V μm^{-1}, DET-Si membrane shows a better behaviour having a lateral strain around 2.5% between 10 Hz - 10 mHz.

The actuators contraction decrease as the load increase until the actuators does not respond any more to the applied electric field. However, the DET-Si / carbon black actuator shows a similar behavior regardless of load until 80 N.

Acknowledgment

This work was supported by a grant of the Romanian National Authority for Scientific Research and Innovation, CNCS/CCCDI -UEFISCDI, project number PN-III-P2-2.1-PED-2019-3652, 3DETSi, within PNCDI III.

Considerations on the evaluation of the tribological and mechanical behavior for samples made by additive technology

A. Dinita[1], R. G. Ripeanu[1], A. Neacsa[1], M. G. Petrescu[1]

[1]Petroleum – Gas University of Ploiesti, Blvd. Bucuresti, no. 39, Ploiesti, Romania

Introduction

In the last period of time there has been experimented with a new technique of making parts, known as Additive manufacturing (AM). Instead of taking a block of raw material and applying some milling or/and turning processes, the piece is built from the base, depositing layer by layer in the thinnest slices, whose shape is determined by an IT program.

Materials and method

A. Wear tests on CSM ball -on-disk microtribometer

Disk samples with Ø 30 mm and thickness of 10mm were prepared from 3D printed specimen (filled with PLA material), triangle, 3D infill and lines structure made of polymer. Static partner was Ø 6 ball of 100Cr6. Tests were conducted in dry conditions in air with RH=57%, at temperature of 20^0C, normal load of 2N, sliding speed of 0.2 m/s at a radius of 8 mm, friction length of 100 m, and by immersion in water.

B. Determination of the Wohler curve of the material

The rotating beam fatigue behavior of 3D printed specimen (filled with PLA material) has been determined on eight samples using the conventional constant amplitude fully revised test method and plotting the fatigue data in from of Wöhler / S – N Curve (S – stress vs. N – number of cycles to failure), by using the staircase method.

Results and discussions

Ball-on-disk testing device in dry conditions, [1]

Ball-on- disk testing device in water lubricated, [2]

Figure 1. Ball-on-disk testing device

Table 1. Friction coefficient and linear wear

Disk sample	Normal load [N]	Maximum value of COF [-]	Mean value of COF [-]	COF at 100m [-]	Linear wear [µm]	Lubricant
Hexagonal	2	0.397	0.252	**0.376**	31	dry
Hexagonal		0.262	0.228	**0.254**	45	water
Triangle		0.281	0.180	**0.281**	10	dry
Triangle		0.234	0.202	**0.213**	63	water
3D infill		0.172	0.141	**0.172**	21	dry
3D infill		0.162	0.125	**0.093**	34	water
Lines		0.438	0.299	**0.435**	7	dry
Lines		0.243	0.135	**0.204**	9	water

We could observe from table 1 that lubrication by water conditions reduce COF at all tested samples. 3D infill structure has the smallest COF in dry and wet conditions. Highest COF in dry condition was obtained for Lines structure and in lubricated conditions for Hexagonal structure. Due to the grate hardness difference between ball sample and polymer samples the cumulate linear wear represents in fact the linear wear of the polymer samples.

i	σ_i N/mm²	Number of cycles	No. of samples			$i \cdot n_i$	$i^2 \cdot n_i$
			Failures	Survivors	n_i		
1	4		4	-	4	1	1
0	3		-	5	0	0	0
		Σ	4	5	$F=4$	$A=1$	$B=1$
$\sigma_0 = \sigma + \Delta\sigma \cdot \left(\frac{A}{F} \pm \frac{1}{2}\right)$ $\sigma = 4\ \frac{N}{mm^2}$ – smalest stress value of the less encountered $\Delta\sigma = 1\ \frac{N}{mm^2}$ – stress increment			$S = 1{,}62 \cdot \Delta\sigma \cdot \left(\frac{F \cdot B - A^2}{F^2} + 0{,}029\right)$				
$\sigma_0 = 4 + 1 \cdot \left(\frac{1}{4} - \frac{1}{2}\right)$ $\sigma_0 = 3{,}75\ \frac{N}{mm^2}$			$S = 1{,}26\ \frac{N}{mm^2}$				
● Survivors (4 specimens)			● Failures (4 specimens)				

Figure 2. *Staircase test results*

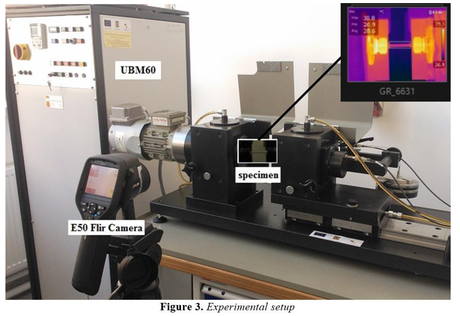

Figure 3. *Experimental setup*

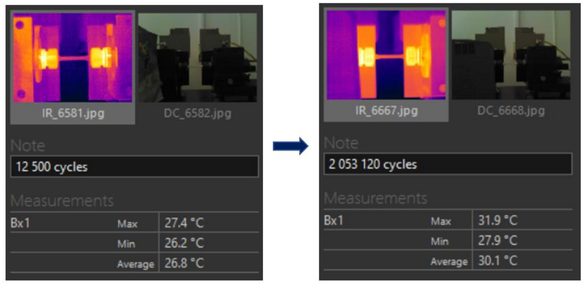

Figure 4. 3D printed specimen temperature evolution

The fatigue limit at 2 x 10^6 cycles was determined by using the staircase method. The data are analyzed as shown in Figure 2. The surface temperature in the mid position of each sample was every 5 seconds acquired during fatigue tests using an infrared camera type E50 FLIR, placed approximately at 1000 mm from the surface of the specimen, as is presented in Figure 3.

Conclusions

The cumulated linear wear measured in real time by the tribometer in lubricated conditions was smaller than in dry conditions because in dry conditions the effect of temperature was much important, and the polymer samples dimensions were modified due to dilatation. The mechanical performance in terms of fatigue it depends of infill %, layer height and infill pattern. The infrared thermographic technique used to assess the fatigue damage by measuring the thermal increment evolution of the specimen during fatigue testing (Figure 4), can provides a valid, nondestructive, tool for rapid estimation of high cycle fatigue properties.

References

1. Tudor, I., Popescu, A., Rîpeanu, R.G., Drumeanu, A.C., Braic, V., Balaceanu, M., Vladescu, A., Braic, M., Tribological behavior of TiSiN/Ti and TiSiN/Cu multilayer coatings, Journal of the Balkan Tribological Association, Ed.SciBulCom.Ltd, Vol.15, No.2, **2009**, pp.156-162, ISSN 1310-4772, http://scibulcom.net/jbtan.php, Sofia, Bulgaria, 2009

2. *Ripeanu R G, Badicioiu M, Caltaru M, Dinita A, Laudacescu E, Tribological characterization of the drill collars and casing friction couples, 9th International Conference on Tribology, BALKANTRIB'17 13-15 September, Cappadocia, TURKEY, 2017, Book Series: IOP Conference Series-Materials Science and Engineering Vol. 295, **2018**, pp.1-10, ISSN 1757-8981, https://doi.org/:10.1088/1757-899X/295/1/012009, Bristol BS1 6BE, England,2018*

3. *O. H. Ezeh and L. Susmel, On the fatigue strength of 3D-printed polylactide (PLA),, Structural Integrity Procedia 9 (2018) 29-36*

4. *Lauren Safai Juan, Sebastian Cuellar, Gerw Smit, Amir A. Zadpoor, A review of the fatigue behavior of 3D printed polymers, Additive Manufacturing, Volume 28, August 2019, Pages 87-97*

5. *M. M. Padzi1, M. M. Bazin, W. M. W. Muhamad, Fatigue Characteristics of 3D Printed Acrylonitrile Butadiene Styrene (ABS), IOP Conf. Series: Materials Science and Engineering 269 (2017) 012060 doi:10.1088/1757-899X/269/1/012060*

Contact

Alin DINITA adinita@upg-ploiesti.ro

A NEW METHOD TO OBTAIN O/W AND W/O EMULSIONS

Eugenia T. Iacob Tudose[1*], Simona Petraru[2]

[1,2] "Gheorghe Asachi" Technical University of Iasi, Faculty of Chemical Engineering and Environmental Protection, 73 Prof. Dr. Docent D.Mangeron Blvd, 700050, Iasi, Romania, e-mail: et_tudose@yahoo.com

Introduction

Emulsions, containing two immiscible liquids, one dispersed in another, with one or two added hydrophilic-lipophilic surfactants, exhibit excellent properties (stability in time, adjustable rheological properties etc.) that make them suitable for new applications, such as thermal energy storage or new cooling systems.

Objectives

The main objective is related to O/W and W/O emulsions preparation using a new method, namely vapor condensation on a liquid layer [1], in order to establish the main parameters influence on the emulsion stability, namely: the system initial temperature, the feeding vapour flow rate, the condensation time period, the emulgators : oil ratio, the water : oil ratio.

Materials and experimental setup

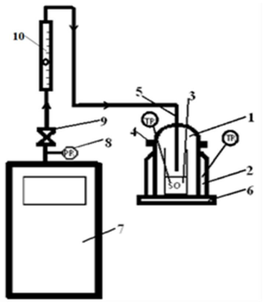

Figure 1 Experimental setup for O/W and W/O emulsions using vapour condensation

Water vapor was condensed onto a sunflower oil layer, containing a mixture of Span 80 and Tween 80 emulgators.

Inside a special chamber 1, with a heating jacket 2 (filled with water), a beaker 3 containing a mixture of sunflower oil (SO) and two emulgators was placed.

In the chamber, sealed with a lid 4, vapour was admitted through an inlet tube 5. The whole system was placed on a heating plate 6. A steam generator 7 with a pressure gauge 8 and an admission valve 9 was used to deliver vapour with an adjustable flow rate, measured with a flowmeter 10. Digital thermometers (TR) were used to verify the temperatures within the system. All the emulsions and their characteristics are presented in Table 1.

Results and discussions

Parameter influence on emulsion stability:

1. ***Bottom temperature*** -for two identically prepared emulsions (10 mL sunflower oil, a mixture of Tween 80 and Span 80 with a HLB_f of 10 or 11.6), two set-ups with different bottom temperatures of 20°C and respectively, 90°C, were tested. Always, the higher temperature bottom condition rendered more stable emulsions.
2. ***Vapour flow rate***: the lowest flowrate produces rather stable emulsions which probably can be explained as follows: a lower vapour flowrate condensing on the liquid layer will induce a more gradual formation and stabilization of the droplets within the liquid layer.
3. As the ***condensation time*** period increases, larger amounts of steam can be incorporated in the liquid substrate. However, for the emulsion stability, the data seem to indicate that the condensation time is a less important factor in comparison to the vapour flowrate.
4. ***Emulgators:oil ratio*** - stable emulsions were obtained at all investigated ratios, however, one can observe that these values correspond to lower vapor flowrates, suggesting that the latter is a key parameter for stability.
5. ***HLBf value*** Stable or unstable emulsions were obtained for both investigate HLB_f values of 10 and 11,6, thus a clear conclusion cannot be drawn for now.

Tabel 1 Emulsion composition

Emulsion sample no.	HLB_f	Oil: Surfactant ratio(w)	Condensation conditions		Emulsion stability/CI
			Water vapour flowrate (m^3/h)	Time (min)	
E1	10	1:1	5	5	Unstable/82.76-27.57
E2					***Stable O/W***
E3	11.6				Unstable/28.57
E4			3		Unstable/50
E5	10	4:5	5	5	Unstable/20
E6			3	5	Unstable/18.60
E7			5	3	Unstable/65.12
E8			7	2.1	(un)stable/90.9
E9	11.6	2:3	5	5	unstable/20
E10			3	5	***Stable O/W***
E11	10		5	3	Unstable/16.22
E12			3	5	Unstable/31.82
E13			7	2.1	Unstable/46.34
E14	11.6	1:2	5	5	Unstable/20
E15	10		7	2.1	***Stable W/O***
E16			5	3	***Stable W/O***
E17			3	5	***Stable W/O***

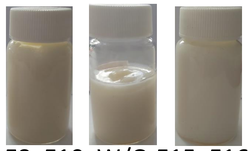

Figure 2 Stabilized emulsions: O/W:E2, E8, E10, W/O:E15, E16, E17 (4 weeks after preparation)

Stability of prepared emulsions

Established visually within 48 h and over several weeks. The emulsion pH was measured over ~60 hours after their preparation and the stable emulsions (E2, E8, E10) were characterized by an almost

By an almost constant pH value, while the unstable ones (E6, E7, E11, E12), by a decreasing pH value, as seen in Figure 3. Also, thermal stability tests performed onto the room temperature-stable emulsions, consisting of several increasing-decreasing temperature ramps (20°C– 50°C -20°C), using an Eccocell 55BMT oven, confirmed their stability.

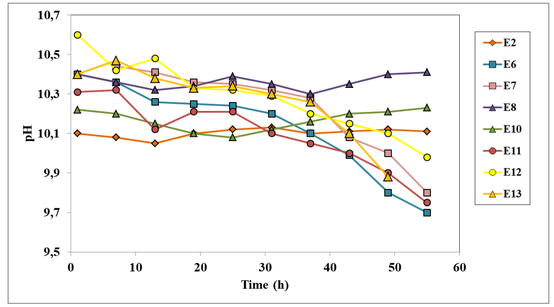

Figure 3. Emulsion pH variation in time, in the first ~50 h after preparation

The unstable emulsions were characterized by a creaming index, CI, defined as the ratio between the cream layer height and the emulsion total height, presented in Table1.

Conclusions

The major parameters influencing the stability of the emulsions obtained using vapour condensation, is the condensing vapour flow rate and the bottom temperature, besides the emulgator:oil/water ratio.

References

1. Guha I F, Anand S, Varanasi KK 2017 *Nat. Commun.*, 8, 1-7

Scheme 1.Chemical structure of tartrazine azo dye

Tartrazine dye decoloration and chromate reduction simultaneously in acid medium

Sibiescu Doina†, Vizitiu Mihaela†

† *Gheorghe Asachi Technical University of Iasi, Faculty of Chemical Engineering and Environmental Protection, 73 D. Mangeron Rd., Iasi - 700050, Romania*

Introduction

Tartrazine dye belongs to the azo-dye class which can be used in many areas: wool, silk, paper, wood stains, tanning and leather processing. Tartrazine dye has also food colouring and histological dye role. It can be used in the form of salt or even with much better results as ligand being complexed with different transitional metal cations.

Due to these multiple uses, we have found it useful to study its behavior in an acidic medium in the presence of an oxidizing agent. Chromate [Cr(VI)] and azo dyes like Tartrazine dye are common pollutants which may co-exist in some industrial effluents.

The degradation kinetics of the oxidation process of Tartrazine dye using inorganic oxidizing agent (K_2CrO_4) have been investigated under various experimental conditions: different concentrations of H_2SO_4 [10^{-2} -5·10^{-1} M] and temperatures [296 and 308 K].

A kinetic model for oxidation of Tartrazine dye by the combination of chromate was developed based on experimental results.

The thermodynamic activation energy parameter was calculated from the rate constants of the oxidation process of the dye, measured at two different temperatures, 296 and 308 K. We concluded that the negative value of entropies of activation indicate that the reaction occurs between ions of similar charge.

Based on our experimental and literature data , we conclude that the destruction of azo-chromophore group by the inorganic oxidizing agent (K_2CrO_4) is explained by the highest oxidation state of this dye.

Materials and method

Spectrophotometry was used as the study method and the reagents used were tartrazine, sulfuric acid and potassium dichromate.Tartrazine dye, with the molecular formula = $C_{16}H_9N_4Na_3O_9S_2$ of molar Weight = 534.36 g·mol^{-1} , present the following structure (figure 1):

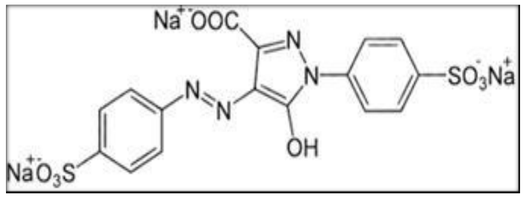

Figure 1.Chemical structure of tartrazine azo dye

Results and discussions

RESULTS AND DISCUSSION

Degradation and reduction reaction

The immediate change of the yellow-coloured (λ_{max}= 430 nm) solution of azo dye (10^{-4} M) to colorless was observed after addition the inorganic oxidizing agent K_2CrO_4 into the protonated form of Tartrazine dye after 24 h.

The highest oxidized form of this dye obtained (the quinoid one), which undergoes a hydrolysis reaction to produce p-hydroquinone (H_2Q) by a mechanism similar to Schiff-base hydrolysis could be attributed to this observation. The cationic form of this matrix is a crucial feature for the hydrolysis process.

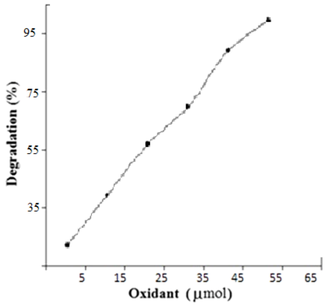

Figure 2.

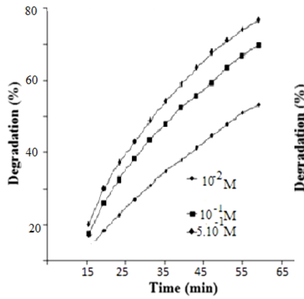

Figure 3.

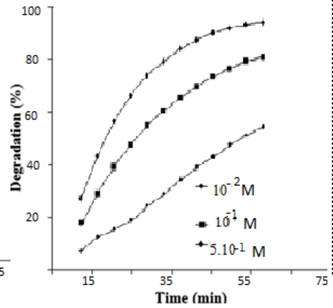

Figure 4

Figure 2. Relation between the degradation efficiency of Tartrazine dye and oxidant (K_2CrO_4) concentration.
Figure 3. Degradation efficiencies of Tartrazine dye with potassium chromate in different concentrations of H_2SO_4 at a temp. 23 ^{0} C
Figure 4. Degradation efficencies of Tartrazine dye with oxidant in different concentrations of H_2SO_4 at 35^{0}C

Kinetics of the degradation reaction

Degradation kinetics is important for physical-chemical studies for the evaluation of the basic traits of good oxidation and reduction rates .

The rate constants were calculated using pseudo-first order and pseudo-second order kinetic models. The first order expression is given as:

A_0 is the initial absorbance of Tartrazine dye before beginning the oxidation process (without oxidant);
At the absorbance of dye after oxidation at any given time t; k_1 is the rate constant.
The values of k_1 were calculated from slope of the linear plot of ln At versus t
The pseudo-second-order kinetic rate equation is given as:

$$\ln A_t = \ln A_o - k_1 t$$

where k_2 is the rate constant of pseudo-second order reaction.

Pseudo-first order model provides better correlation than pseudo-second order model. The low correlation coefficient values obtained for the pseudo-second order model indicates that oxidation of dye did not follow the pseudo-second order reaction.

The correlation coefficients (r^2) for the linear plots of ln At against t for the pseudo-first order equation were larger than pseudo-second order at all concentrations of acid and temperatures.

$$\frac{1}{A_t} = \frac{1}{A_o} + k_2 t$$

Using Arrhenius equation in the logarithmic form:

$$lnk = lnA - \frac{E_a}{RT}$$ and determining two values of the reaction rate constant, k, at two different temperatures (296K and 308K) we can calculate the activation energy, E_a:

$$\ln\frac{k_{308}}{k_{296}} = \frac{E_a}{R}\cdot\left(\frac{1}{296} - \frac{1}{308}\right)$$

k_{296} , k_{308} are the rate constants of the oxidation reaction at two different temperatures 296 K and 308 K, respectively, R = 8.314 J/K mol, and Ea is the activation energy[20-25].

From the activation energy, we can calculate the activation enthalpy, ΔH^* using the equation:

$$\Delta H^* = E_a - RT$$

Temperature, K	Acid conc. (M)	E_a(J/mol)	ΔH^* (J/mol)	- ΔS^* (J/mol·K)	ΔG^* (J/mol)
296	0.01	11400.41	8939.47	253.72	84040.59
	0.10	33250.77	30789.83	176.32	82980.55
	0.50	57092.14	54631.20	94.56	82620.96
308	0.01	11400.41	8839.70	254.05	87087.71
	0.10	33250.77	28129.35	184.96	85097.03
	0.50	57092.14	54531.43	94.89	83757.55

Temperature	Acid conc.	First -order			Second-order		
	(M)	k_1	r^2	$t_{1/2}$(min)	k_2	r^2	$t_{1/2}$(min)
296	0.01	0.0091	0.999	76.15	0.009	0.996	80.24
	0.1	0.0140	0.998	49.50	0.017	0.993	42.50
	0.5	0.0162	0.998	42.77	0.020	0.991	30.15
308	0.01	0.0109	0.992	63.50	0.017	0.972	50.20
	0.1	0.0237	0.994	29.18	0.050	0.988	15.70
	0.5	0.0400	0.986	17.33	0.140	0.976	6.30

Conclusions

The dicoloration and kinetic degradation reaction of Tartrazine dye using potassium chromate have been studied. The immediately change of the yellow-colored (λ_{max}= 430 nm) to colorless was observed after addition of inorganic oxidizing agent (K_2CrO_4) into the protonated form of Tartrazine dye after 24 h.

This observation could be attributed to the highest oxidized form of this dye obtained (the quinoid one), which undergoes a hydrolysis reaction to produce p-hydroquinone (H2Q) by a mechanism similar to Schiff-base hydrolysis .The cationic form of this matrix is a crucial feature for the hydrolysis process.

A kinetic model for oxidation of Tartrazine dye by the combination of chromate was developed based on experimental results.The observed kinetic reaction coefficient was determined and correlated as a function of UV spectral intensity of Tartrazine dye at 430 nm. The degradation rate follows pseudo-first order kinetics with respect to dye concentration.

References

- Aaron D . B., Reha A., Madison, O., Robert J. O., Danica J. W., Thomas B., James N W., Light-based 3D printing of hydrogels with high-resolution channels, Biomedical Physics & Engineering Express, 5 (2), (2019).
- E102 Tartrazine, FD&C yellow No.5". UK Food Guide. Retrieved, 30,11, (2007).
- Fernández-López JA, Angosto JM, Giménez PJ, León G., Thermal stability of selected natural red extracts used as food colorants, Plant Foods Hum Nutr., 68(1), 11-7, (2013).
- Mohammad M., MoridiA., "Efficiency of electro-Fenton process in removing Acid Red 18 dye from aqueous solutions", Process Safety and Environmental Protection, Volume 111, Pages 138-147,(2017).
- Crudu, M., Sibiescu, D., Rosca, I., Sutiman, D., Vizitiu, M., Apostolescu, G.,"New coordination compounds of Cr(III) used in leather tanning", Proc. SPIE 7297, Advanced Topics in Optoelectronics, Microelectronics, and Nanotechnologies IV, 72970S, 7 January (2009).
- Kotas, J., Stasicka, Z.,Chromium occurrence in the environment and methods of its speciation.Environ. Pollut. 107, 263, (2000).

Contact : dsibiesc@ch.tuiasi.ro
mvizitiu@ch.tuiasi.ro

S1-P27

Photocatalytic degradation of organic contaminants using mesoporous ZnS

N. Apostolescu, C. Cernătescu, R. E. Tătaru Fărmuș, C. Cobzaru, M. A. Vizitiu, G. A. Apostolescu

"Gheorghe Asachi" Technical University of Iași, "Cristofor Simionescu" Faculty of Chemical Engineering and Environmental Protection, Iași, Romania

Introduction

Reducing contaminants in water is still a priority on the agenda of many research groups. Among the multitude of semiconductor materials with photocatalytic properties, Zn-based materials (oxides, sulfides, simple or doped mixtures) have the advantages of low cost and low toxicity. This study has as main objective the testing of the photocatalytic properties of some ZnS samples synthesized by the hydrothermal method. ZnS samples were prepared varying the reaction parameters, especially the amount of directing agent of the structure, presenting only the most relevant results. Photocatalytic studies showed that the maximum degree of discoloration obtained was 84% for 90 minutes of irradiation. The influence of parameters such as catalyst dose, dye concentration or pH of the reaction medium was also studied

Materials and method

ZnS nanoparticles synthesis by hydrothermal reaction

$Zn(CH_3COO)_2 \cdot 2H_2O$ as Zn^{2+} source,

$(NH_4)_2CS$ as S^{2-} source

PVA as capping surfactant and dispersing agent.

$$(NH_2)_2CS + Zn(CH_3COO)_2 + H_2O \rightarrow ZnS + 2CH_3COOH + (NH_2)_2CO$$

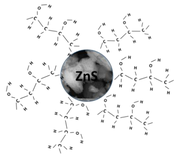

Photocatalytic test

Variable amounts of photocatalytic ZnS (S1 and S2) were introduced into 50 mL aqueous dyes solutions (4 ppm). The reaction systems thus prepared were stirred magnetically for 30 minutes in the dark to establish the adsorption-desorption balance between the pollutant dye and the photocatalyst surface. The best results were obtained by working at the natural pH of MB

Results and discussions

Zinc sulfide (ZnS) is a type II-VI semiconductor with a high bandwidth value (3.68 eV) [1-2]. Being a non-toxic and affordable material, ZnS has been used successfully to remove organic contaminants from wastewater through photodegradation processes [3-4]. As a photocatalyst, it has the ability to quickly produce electron - hollow electron pairs upon UV irradiation, also reporting good results even under visible light irradiation.

Characterization

The presence of PVA in samples were measured using Fourier transform infrared spectra (FTIR)

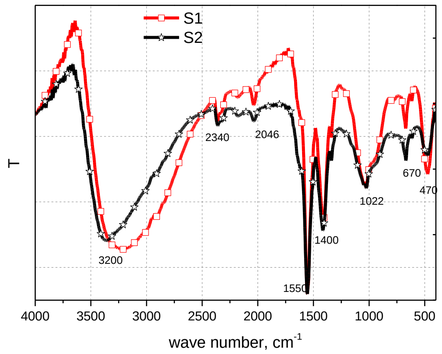

The peaks observed at 470 and 670 cm^{-1} are the characteristic of the ZnS symmetric bending vibration. The organic phase (PVA) is responsible from 1022 cm^{-1} (secondary OH), 1400 cm^{-1} (vinil CH in plane blend, δ_{CH2}), 2855 cm^{-1} ν_{sCH2}, 2920cm^{-1} ν_{aCH3} asimetric /simetric stretch, the band at around 1550 cm^{-1} are due the C-O stretching from PVA molecule [4] and the broad band at 3200 cm^{-1} is attributed to the polymeric OH stretch (ν_{OH}) from the intermolecular and intramolecular hydrogen bonds.

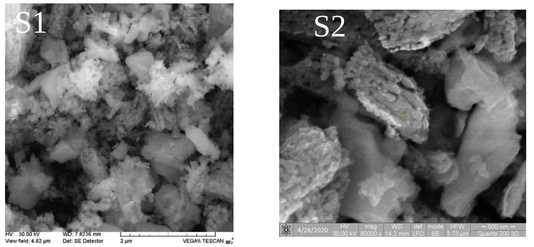

Two samples (S1 and S2) were selected for catalytic tests, varying by the PVA amount (S1-10^{-3}M PVA, S2-10^{-4}M PVA), the SEM images obtained being similar (indicating a porous structure).

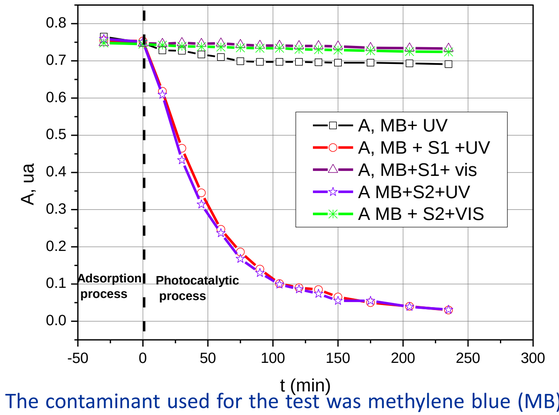

The contaminant used for the test was methylene blue (MB) as it has multiple applications (disinfectant, antimicrobial, dye) found in many drugs that treat respiratory tract problems (and is not always completely metabolized or eliminated properly). We worked with a concentration of 4 ppm.

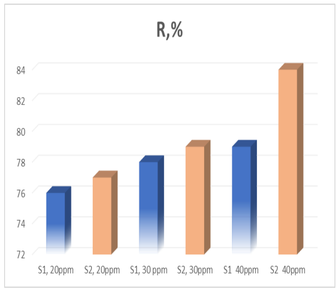

$$R(\%) = \frac{A_0 - A}{A_0} \times 100$$

The experimental results showed that although the initial concentration of the directing agent of the structure was different, the photocatalytic tests were quite similar. The influence of the photocatalyst dose, analyzed in terms of photodegradation yield showed that for the low concentrations used, too high a catalyst dose is not justified, choosing the lowest dose (economic and environmental considerations).

Conclusions

The paper brings to attention the pressing issue of combating water pollution, with a focus on removing contaminants from water through photocatalytic processes. The possibility of using ZnS for the degradation of thiazine dye organic compounds from wastewater was analyzed, experimental data suggesting that ZnS has a good photocatalytic action (R = 84%). The percentage of photodegradation increases with increasing ZnS concentration, the reaction systems being monitored for 230 min, at the natural pH of the solution. Given that the concentration of the photocatalyst (30ppm) and the dose of ultraviolet radiation used (2.1mW / cm^2) were very low, it can be concluded that ZnS can be used successfully to remove dyes from water.

References

1. D. Ayodhya, G. Veerabhadram, A review on recent advances in photodegradation of dyes using doped and heterojunction based semiconductor metal sulfide nanostructures for environmental protection, Mater. Today Energy 9 (2018) 83–113, https://doi.org/10.1016/j.mtener.2018.05.007

2. C. Feng, X. Meng, X. Song, X. Feng, Y. Zhao, G. Liu, Controllable synthesis of hierarchical CuS/ZnS hetero-nanowires as high-performance visible-light photocatalysts, RSC Adv. 6 (2016) 110266–110273, https://doi.org/10.1039/c6ra20306j.

3. G. Mendoza-Damian, A. Hernandez-Gordillo, M.E. Fernandez-García, P. Acevedo-Pena, F.J. Tzompantzi-Morales, R. Perez-Hernandez, Influence of ZnS wurtzite-sphalerite junctions on ZnO_{Core}-ZnS_{Shell}-1D photocatalysts for H_2 production, Int. J. Hydrogen Energy 44 (2019) 10528e10540.

4. H.S. Mansur, C.M. Sadahira, A.N. Souza, A.A.P. Mansur, FTIR spectroscopy characterization of poly (vinyl alcohol) hydrogel with different hydrolysis degree and chemically crosslinked with glutaraldehyde, Mater. Sci. Eng. C 28 (2008) 539–548.

The kinetics of the drying process of spent coffee grounds

V. Bejenari, C. Lisa, I. Mămăligă, G. Lisa

"Gheorghe Asachi" Technical University of Iaşi, "Cristofor Simionescu" Faculty of Chemical Engineering and Environmental Protection, Romania

Introduction

Drying spent coffee grounds (SCG) involves high energy consumption and is an important step in using it as green energy. It is known that in the coffee production process a double amount of wet SCG is obtained in relation to the amount of coffee used. Biodiesel, bioethanol, bio-oil and pellets can be obtained from coffee waste [1]. There are very few studies in the literature that address this topic, but that use pilot-scale dryers [1-3].

Materials and method

The spent coffee grounds represent residues that generally come from coffees containing blends of Arabica and Robusta in different proportions.

For this reason, in this paper we analyzed the kinetics of the drying process of SCG containing equal proportions of Arabica and Robusta coffee, in isothermal conditions at different temperatures: 50, 60, 70 and 80°C and sample layer thicknesses of: 0.6 , 1.2, 1.8 and 2.4 mm.

The coffee grounds analyzed resulted from the use of a commercial type of coffee, which according to the manufacturers' specifications contains 50% Arabica and 50% Robusta. A professional DeLonghi coffee machine was used and the following coffee recipe was followed to obtain comparable results: 12g coffee and 40 ml water.

The drying process, respectively the recording of the thermogravimetric (TG) and derived thermogravimetric (DTG) curves in isothermal conditions was performed using a Mettler Toledo TGA-SDTA851^e equipment.

The processing of the experimental data on the time dependence of the moisture content to obtain kinetic models of the coffee bean drying process was performed with the SigmaPlot 11.2 program.

Results and discussions

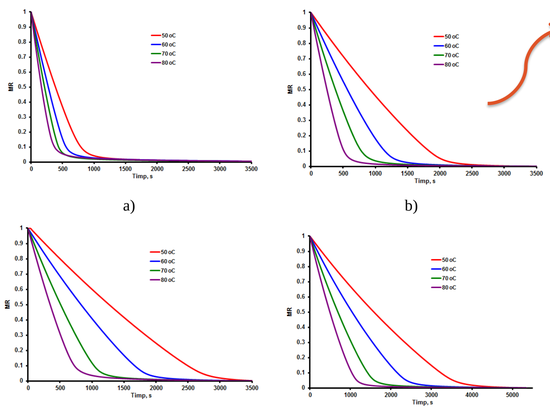

Figure. 1 Drying curve (material moisture – drying time): a) 0.6 mm, b) 1.2 mm, c) 1.8 mm, d) 2.4 mm

Experimental data MR=f(t) were processed to verify existing kinetic drying model in the literature. [4] It has been found for the drying process of spent coffee grounds the best results are obtained with the **modified Henderson and Pabis model**.

Table 1. The values of the parameters in the modified Henderson and Pabis model and its performances

No.	Layer thickness, mm	Temperature, °C	Model	Model parameters	r^2	σ
1.	0.6 mm	50	Modified Henderson and Pabis	a=1.1674 b=1.8260*10^{-6} c=-0.0775 k=0.0016	0.9931	0.0287
		60	Modified Henderson and Pabis	a=1.1099 b=4.8962*10^{-6} c=-0.0161 k=0.0030	0.9917	0.0255
		70	Modified Henderson and Pabis	a=1.0798 b=9.9879*10^{-7} c=-0.0002 k=0.0043	0.9928	0.0208
		80	Modified Henderson and Pabis	a=1.0474 b=-2.0596*10^{-6} c=0.0126 k=0.0053	0.9954	0.0152
2.	1.2 mm	50	Logarithmic	a=1.2073 c=-0.1297 k=0.0008	0.9925	0.0393
		60	Modified Henderson and Pabis	a=1.4671 b=0.0001 c=-0.3951 k=0.0011	0.9948	0.0293
		70	Modified Henderson and Pabis	a=1.2249 b=4.5332*10^{-5} c=-0.1379 k=0.0018	0.9934	0.0300
		80	Modified Henderson and Pabis	a=1.1213 b=1.1873*10^{-5} c=-0.0303 k=0.0035	0.9931	0.0253
3.	1.8 mm	50	Logarithmic	a=1.4724 c=-0.4370 k=0.0004	0.9971	0.0243
		60	Modified Henderson and Pabis	a=12.7591 b=0.0013 c=-11.7242 k=0.0002	0.9975	0.0222
		70	Modified Henderson and Pabis	a=1.3328 b=7.7482*10^{-5} c=-0.2558 k=0.0013	0.9942	0.0301
		80	Modified Henderson and Pabis	a=1.1483 b=2.2764*10^{-6} c=-0.0638 k=0.0024	0.9942	0.0262
4.	2.4 mm	50	Logarithmic	a=1.2662 c=-0.2151 k=0.0004	0.9950	0.0319
		60	Modified Henderson and Pabis	a=2.3774 b=0.0002 c=-1.3318 k=0.0004	0.9968	0.0244
		70	Modified Henderson and Pabis	a=1.2807 b=4.2844*10^{-5} c=-0.2056 k=0.0010	0.9942	0.0290
		80	Modified Henderson and Pabis	a=1.1584 b=1.7511*10^{-5} c=-0.0747 k=0.0017	0.9934	0.0274

Due to the fact that the surface of the crucible (in which spent coffee ground was introduces in layers of different thickness) is known, the drying rate at the four temperatures was calculated and represented graphically in figure 2 depending on the moisture content.

Table 2. Values of the effective diffusion coefficient at different temperatures

No.	Layer thickness δ, mm	Temperature, °C	D_{eff}·10^{10}, m^2/s	r^2
1.	0.6	50	0.37	0.9039
		60	0.42	0.8694
		70	0.45	0.8551
		80	0.48	0.8638
2.	1.2	50	4.12	0.9820
		60	4.48	0.9826
		70	4.78	0.9217
		80	5.49	0.9515
3.	1.8	50	5.57	0.8640
		60	5.80	0.9090
		70	6.38	0.9715
		80	6.64	0.9480
4.	2.4	50	6.99	0.9004
		60	7.84	0.9193
		70	7.98	0.9619
		80	9.99	0.9214

From the graphical representation ln(MR)=f(t) for the calculation D_{eff}, lines with a negative slope and correlation coefficients higher than 0.855 were obtained.

It was found that the values of the effective diffusion coefficient D_{eff} increase with the increase of temperature and thickness of spent coffee ground layer subjected to the drying process.

Table 3. Values of the kinetics parameters of the drying process of spent coffee ground

No.	Layer thickness δ, mm	lnD_0	Ea (J/mol)	r^2
1.	0.6	-20.92	8289.46	0.9805
2.	1.2	-18.36	8741.12	0.9634
3.	1.8	-18.02	9066.81	0.9685
4.	2.4	-17.27	10261.23	0.8753

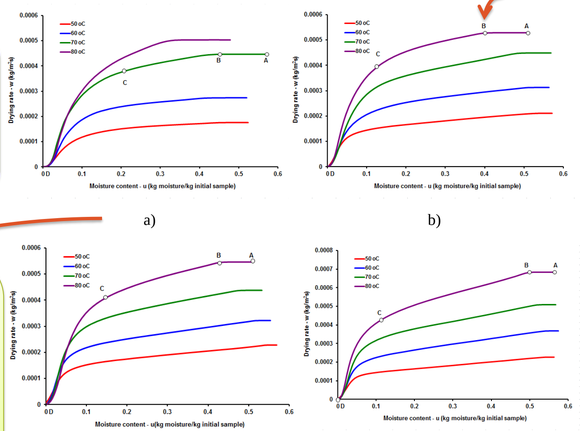

Figure 2. Variation of drying rate depending of moisture content: a) 0.6 mm, b) 1.2 mm, c) 1.8 mm, d) 2.4 mm

During the process several drying stages are observed: drying stage with constant rate (AB) and decreasing rate (BC and CD). At the T= 50 and 60°C the drying period with constant rate is much longer. The drying stages are more obvious at the T= 70 and 80°C.

Conclusions

- The kinetic study of the drying process of SCG in conditions of constant temperature and different thickness layer, performed for the first time in a Mettler Toledo TGA-SDTA851^e equipment, which can be used to simulate conditions of industrial tubular dryers, allowed determination of the time dependence of the moisture content (MR), the effective diffusion coefficients (D_{eff}) and the kinetic parameters (activation energy and preexponential factor).
- It has been observed that among the models in the literature describing the drying process of some foods the best results can be obtained for drying SCG with a modified Henderson and Pabis model.
- The drying rate increases with increasing temperature and thickness of the SCG layer. The constant rate has the values between 0.000176 kg/m²·s (δ=0.6 mm, T=50°C) and 0.000683 kg/m²·s (δ=2.4 mm, T=80°C).
- The activation energy is influenced by the thickness of the SCG layer subjected to the drying process and has values between 8.3 kJ/mol and 10.3 kJ/mol.
- The values obtained are comparable to those reported by other researches in the literature, but for drying SCG in conventional convective dryers.

References

[1] Gómez-De La Cruz, F.J., Cruz-Peragón, F., Casanova-Peláez, P.J., Palomar-Carnicero, J.M., 2015. A vital stage in the large-scale production of biofuels from spent coffee grounds: The drying kinetics. Fuel Process. Technol. 130, 188–196. https://doi.org/10.1016/j.fuproc.2014.10.012

[2] Martinez, E.N., 2019. The Drying of Spent Coffee Grounds in a Tray Drier. Am. J. Biomed. Sci. Res. 6, 416–425. https://doi.org/10.34297/ajbsr.2019.06.001074

[3] Gómez-de la Cruz, F.J., Palomar-Carnicero, J.M., Hernández-Escobedo, Q., Cruz-Peragón, F., 2020. Experimental studies on mass transfer during convective drying of spent coffee grounds generated in the soluble coffee industry. J. Therm. Anal. Calorim. https://doi.org/10.1007/s10973-020-09600-3

[4] Erbay, Z., Icier, F., 2010. A review of thin layer drying of foods: Theory, modeling, and experimental results. Crit. Rev. Food Sci. Nutr. 50, 441–464. https://doi.org/10.1080/10408390802437063

Contact

victoria.bejenari@tuiasi.ro

Thiolated chitosan for biomedical applications

I. Fusteș-Dămoc[1], C. A. Peptu[1], C. Peptu[2], T. Măluțan[1]

[1]Technical University "Gheorghe Asachi" Iași, Faculty of Chemical Engineering and Environmental Protection "Cristofor Simionescu", Department of Natural and Synthetic Polymers, Street Profesor Dimitrie Mangeron 73, Iași 700050, iolanda.fustes-damoc@tuiasi.ro.

[2]"Petru Poni" Institute of Macromolecular Chemistry, Iasi, Grigore Ghica Voda Alley 41A, Iasi 700487.

Introduction

The chitosan is synthesized from chitin. It is cationic polysaccharide obtained from the shells of crustaceans, in particular crabs and shrimps, by the alkaline partially de-acetylation of chitin.

The biodegradability, non-toxicity, bacteriostatic and biocompatibility proprieties represent the reasons why it is promising in different applications. The solubility of the polymer is influenced by the degree of de-acetylation.

The free amino groups are very important in chitosan chemical modifications. Among all chitosan derivatives, thiolated chitosan is a promising candidate for various biomedical applications due to mucoadhesive properties.

In addition thiolated chitosan open the possibility for thiol-ene reaction with other polymers obtaining interesting networks without use supplementary crosslinking agents which are sometime toxic.

Materials and method

Materials

Chitosan with 84% deacetylation (Mw of 100 kDa), homocysteine thiolactone(HT) hydrochloride, imidazole, lactic acid were obtained from Aldrich Co., USA and used without further purification. 5,5-Dithio-bis(2-nitrobenzoic acid), used for quantitatively analyzing the thiol groups, was purchased from Aldrich Co., USA. Dialysis tubing (Mw cut-off 12–14 kDa) was obtained by Membrane Filtration Products, Inc., USA.

Synthesis of HT-chitosan

Synthesis of HT-chitosan

- Chitosan were thiolated using HT by covalent attachment using a modified method reported by K. Juntapram et al., as schematically summarized in Fig. 1.
- Briefly, 100 mL of 1% (w/v) of chitosan in 1% (v/v) lactic acid was added to an aqueous solution of imidazole (0.68 g in 2.5 mL water), followed by the dropwise addition of HT (0.5 g in 100 mL water) and stirred at room temperature in an argon atmosphere for 12 h.
- The reaction mixture was precipitated with excess acetone and harvested by centrifugation (2,000 rpm for 2 min).
- The pellet was re-dissolved in water and dialyzed (MW cut-off 12–14 kDa) against distilled water for 1 day prior to being lyophilized at −30 ◦C and 0.01 mbar.
- The dry product was stored at 4 ◦C and dark before use.

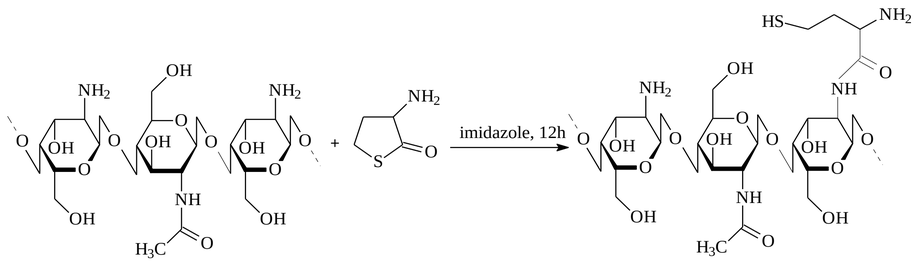

Fig. 1 – The synthesis of thiolated chitosan by reaction with homocysteine thiolactone (Juntapram et al., 2012)

Physical – chemical analysis

- Determination of the contents of thiol and disulfide groups
- Fourier transformed infrared spectroscopy (FT-IR)
- ^{1}H Nuclear Magnetic Resonance spectroscopy (NMR)

Results and discussions

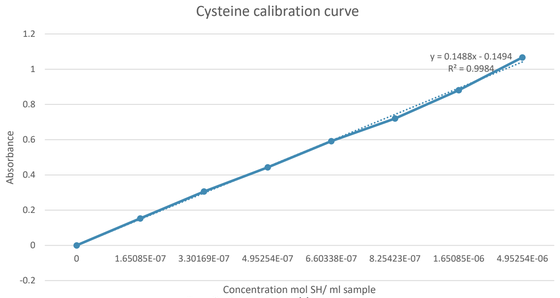

Fig. 2. Cysteine calibration curve

Determination of the contents of thiol and disulfide groups

The degree of modification was determined spectrophotometrically with Ellman's reagent. The amount of thiol moieties on the HT-chitosan samples was calculated by reference to a standard curve, itself obtained from evaluation of a chitosan solution with increasing known amounts of cysteine HCl (0.02–0.6 g/L) standards at a wavelength of 412 nm. The amount of free thiol groups was calculated by subtracting the quantity of free thiol groups, as determined above, from the total number of thiol moieties present on the polymer.

The HT-chitosan derived from a 1:0.5 (w/w) ratio of chitosan:HT exhibited the amount of free thiol groups: 0,02289 mol SH/mol chitosan, which implies that this polymer will be stronger mucoadhesive compared to the simple chitosan.

Fourier transformed infrared spectroscopy (FT-IR)

The FTIR spectra of chitosan and the chitosan derivative (HT-chitosan) are shown in Fig. 3. The FTIR spectrum of chitosan showed the characteristic absorption bands of chitosan at 1639 cm^{-1} (C=O amide) and 1077 cm^{-1} (C–O stretching). After grafting of the HT onto the C2-amine groups of chitosan, the characteristic signal at 1640 cm^{-1}, attributed to the stretching vibration of the C=O acetamide of HT-chitosan (amide I band) appeared. In addition, the absorption peak at 1586 cm^{-1} (amide II band) and 1318 cm^{-1} (amide III band) were stronger than those seen in chitosan, which can be attributed to the additional amide group of HT. The peaks at 1256 cm^{-1} and 2499,65 cm^{-1} correspond to the disulfide and thiol groups, respectively.

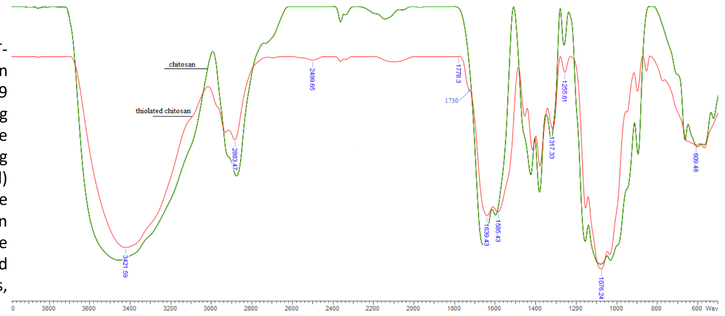

Fig. 3. The FTIR spectra of chitosan and the chitosan derivative (HT-chitosan)

^{1}H Nuclear Magnetic Resonance spectroscopy (NMR)

Chitosan and thiolated chitosan have been analysed also by Nuclear Magnetic Resonance Spectroscopy (NMR), especially using ^{1}H NMR spectroscopy. There was used deuterium water as solvent, thiolated chitosan being soluble in water. The new peak of methylene protons at 2.65-2.92 ppm in the spectrum of modified chitosan and others peaks detected at 2.25-2.43 ppm for thiol groups indicated the successful of functionalization.

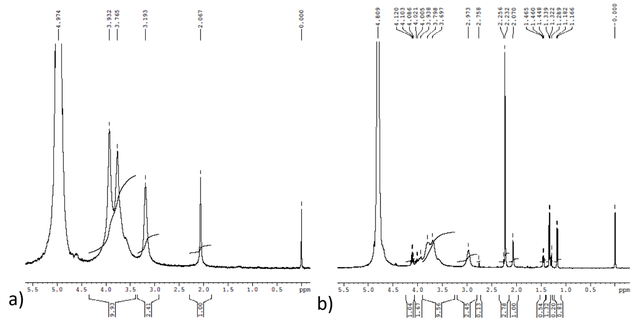

Fig. 4. Representative **^{1}H** NMR spectra of (a) chitosan, (b) thiolated chitosan.

Conclusions

- In this study, thiolated chitosan have been successfully synthesized by covalent attachment of HT onto the amino group of chitosan under mild conditions.
- The characterizations at UV-Vis spectroscopy with Ellman's reagent, Fourier transformed infrared spectroscopy (FT-IR) and ^{1}H Nuclear Magnetic Resonance spectroscopy (NMR) for chitosan and thiolated chitosan were investigated. These analysis proved that the modification was succeeded.
- The chitosan:HT with the mass ratio of 1:0.5 (w/w) resulted in strongly improved solubility properties at neutral pH.

References

Juntapram K., Praphairaksit N., Siraleartmukul K., Muangsin N., *Synthesis and characterization of chitosan-homocysteine thiolactone as a mucoadhesive polymer*, Carbohydr. Polym., 82(4), 2399-2408 (2012).

Acknowledgment

This work was supported by Faculty of Chemical Engineering and Environmental Protection "Cristofor Simionescu" and by a grant of the Romanian National Authority for Scientific Research and Innovation **UEFISCDI**, PN-III-P1-1.2-PCCDI-2017-0083, 37PCCDI/2018.

Chemical and structural characterization of carbon rich material from hydrothermal conversion of spruce bark

I. Bejenari [1], O. Petuhov [2], G. Lisa [1], G. Hristea [3], I. Volf [1]

[1] Gheorghe Asachi Technical University of Iasi, Faculty of Chemical Engineering and Environmental Protection, 73 Prof. dr. doc D. Mangeron Street, Iasi 700050, Romania
[2] Institute of Chemistry of the Academy of Sciences of Moldova", 3 Academiei str., MD 2028, Chisinau, Republic of Moldova
[3] National Research and Development Institute for Electrical Engineering ICPE-CA, Splaiul Unirii no. 313 Bucuresti, Romania

Introduction

The hydrothermal carbonization (HTC) is an efficient technique for biomass conversion into valuable carbon rich materials [1]. The HTC process has the advantages of being non-toxic, environmentally friendly. Noteworthy that drying of feedstocks is not compulsory, thus avoids additional costs [2].

Materials and method

- The biomass used in this work is spruce bark discarded from forestry and wood processing industries;
- The spruce bark hydrothermal carbonization process was conducted in a stainless-steel autoclave, with a 0.1 L glass vessel inside and a distillated water as solvent.
- The optimal process parameters were set using MiniTab software; [Temperature – 280 °, time – 1 h, solid to liquid ratio 1:5 (w/w)]
- In order to determine the physical, chemical, thermal and structural changes what occur after hydrothermal conversion, several characterization method was applied: Fourier Transform Infrared Spectroscopy (FTIR), Thermogravimetric Analysis (TGA), Scanning Electron Microscopy (SEM) and Energy-Dispersive X-Ray (EDX), Brunauer-Emmett-Teller Surface Area Analysis (BET) .

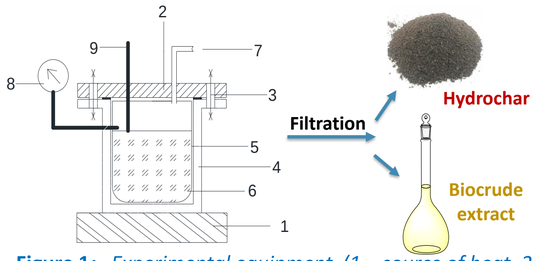

Figure 1: *Experimental equipment (1 – source of heat, 2 – autoclave cover, 3 – screws, 4 – stainless steel autoclave, 5 – glass vessel, 6 – spruce bark and distilled water, 7 - drain valve, 8 – manometer, 9 - temperature sensor)*

Results and discussions

PHYSICAL, CHEMICAL, THERMAL AND MORPHOLOGICAL CHARACTERIATION OF SPRUCE BARK (SB) AND HYDROCHAR (HC)

Table 1: *Characterization of spruce bark and hydrochar*

PROPERTY	UNIT	VALUE SB	VALUE HC
Proximate analysis			
Moisture content	Wt.%	8.35	1.98
Ash content at 600° C	Wt.%	2.17	0.66
Ultimate analysis (macroelements)			
Carbon	Wt. %	58.26	71.32
Hydrogen	Wt. %	5.84	5.20
Oxygen	Wt. %	33.15	20.2
Magnesium	Wt. %	0.05	-
Aluminum	Wt. %	0.01	-
Silicon	Wt. %	0.01	1.0
Phosphorus	Wt. %	0.04	-
Sulfur	Wt. %	0.05	-
Chlorine	Wt. %	0.01	-
Potassium	Wt. %	0.33	-
Calcium	Wt. %	1.59	1.44
Manganese	Wt. %	0.02	-
Copper	Wt. %	0.38	0.38
Zinc	Wt. %	0.27	0.26
Heating value			
Heat release capacity	J/(g*K)	87.75	59.7
Total heat release	kJ/g	8.85	8.44
Physical characterizations			
Specific surface area	m^2/g	7.9	13
Particle size	mm	0.5-1.5	0.3-0.5

The decrease of moisture and ash content of hydrochar is due to the decomposition of lignocellulosic components during hydrothermal conversion of biomass and some part of ash are dissolved in solvent.

Table 2: *Functional groups*

Wavenumber, cm^{-1}	Functional groups
3272	O-H
2927	C-H
1599	C=C
1462	C-H
1032	C-O

The figure 3 shows that the spectra of SB and HC are very similar which leads to the conclusion that samples have a close composition and structure. The identified functional groups could be assigned to typical features of lignocellulosic materials.

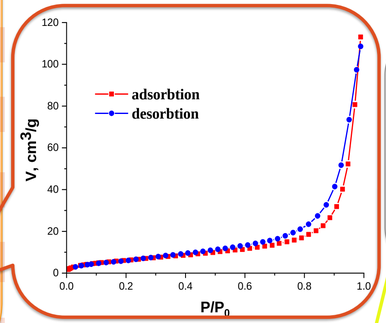

Figure 2: *Adsorption-desorption isotherms of nitrogen for HC*

FT-IR ANALYSIS

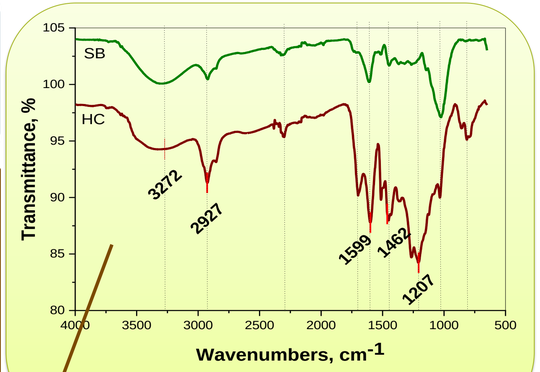

Figure 3: *FT-IR analysis of SB and HC*

Through TGA analysis the combustion behavior of hydrochar was investigated. The combustion process took place in three steps. The first step was characteristic for moisture loss, the second step was attributed to decomposition of hemicellulose and cellulose, while the final one is specific for degradation of lignin.

SEM ANALYSIS

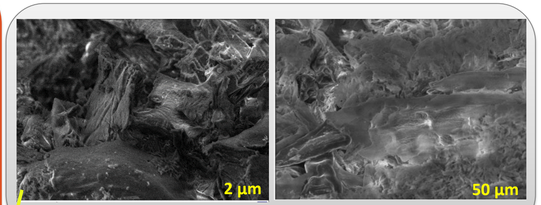

Figure 5: *SEM analysis of HC*

SEM images (fig.5) of hydrochar shows some modification instructure, which probably are attributed to some breakdown of the lignocellulosic material during the hydrothermal conversion.

THERMOGRAVIMETRIC ANALYSIS

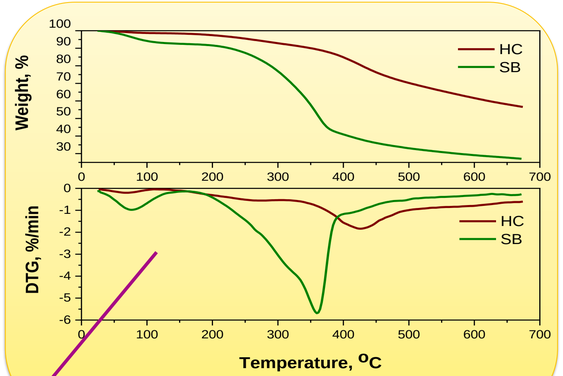

Figure 4: *Thermogravimetric analysis of SB and HC*

Conclusions

The HTC method is suitable for spruce bark waste conversion in order to obtain value added products with improved properties:

- A less moisture presented in HC makes it to present a hydrophobic character.
- HC has an increase in carbon content and a decrease in hydrogen and oxygen content.
- After HTC process an improvement of specific surface area of HC have been observed.
- From thermograms it was been observed that HC is more thermostable comparatively with SB.

References

1. Volf, I., Bejenari, I., Popa, V., Valuable biobased products through hydrothermal decomposition, in Pulp Producing and Processing. High-tech applications, V.I. Popa Ed., De Gruyter, Berlin, Boston, 141-163 (2020).
2. Evcil, T., Simsir, H., Ucar, S., Tekin, K., Karagoz, S., "Hydrothermal carbonization of lignocellulosic biomass and effects of combined Lewis and Brønsted acid catalysts," Fuel, vol. 279, no. May, p. 118458, (2020)

Epoxidized vegetable oil for anti-corrosion coatings

R.S. Komartin[1], B. Balanuca[1,2], M. Necolau[2], R. Stan[1]

[1]"Costin Nenitzescu" Department of Organic Chemistry, University "Politehnica" of Bucharest; 1-7, Gh. Polizu Street, Bucharest, Romania; Email: ralu.komartin@gmail.com

[2]Advanced Polymer Materials Group, University "Politehnica" of Bucharest, 1-7, Gh. Polizu Street, Bucharest, Romania

Introduction

The current research study aims to obtain new composite materials based on ***epoxidized linseed oil (ELO)*** and ***kraft lignin (LnK)*** by crosslinking them in varying proportions, under specific reaction conditions, as potential anticorrosion coatings. Conversion of the unsaturated vegetable oils in more reactive epoxides, represents an important intermediary step to produce ***polymeric and composite materials*** suitable for different applications (J. Chen et al., 2019). Beside this, using ***lignin as filler*** for epoxidized vegetable oils – derived systems could improve general material performances as ***corrosion resistance***, mechanical strength, and ***thermal stability***.

Materials and method

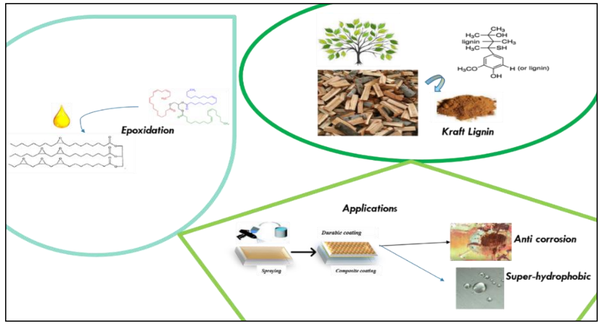

Methods

Anti-corrosion films on metal support:

- The formulations based on ELO (with 5,10,15% / without LnK content) were deposited on cleaned steel plates, in uniform film;
- Dual curing was applied:
  - UV irradiation 15 min (THA photoinitiator – triarylsulfonium hexafluoro–antimonate)
  - Thermal treatment (80 °C) 24 h (Araldite crosslinker).

Results and discussions

Investigation of thermal stability of ELO and LnK based coatings

TGA in air (***Table 1***) was performed in the temperature range 25 – 800 °C, with a heating rate of 10 °C/min, for all the synthesized ELO-LnK composites.

All recorded thermograms showed a similar thermal degradation profile, their degradation being registered in 4 stages, with the first stage after 220°C.

The tests in aerobic atmosphere showed a higher thermal stability for the ELO_5% LnK system (***Figure 1 a,b***) compared to the rest of the synthesized materials. The control system obtained only by heat treatment, records lower values of thermostability over the entire temperature regime studied. This phenomenon was the first indication that the materials derived from ELO through the double crosslinking process reach superior properties.

Table 1. TGA results for ELO_LnK new composite materials (air)

Sample Code	T_d^a 3% (°C)	T_d^a 10% (°C)	T_d^a 30% (°C)	T_d^a 50% (°C)	$T_{max}1^b$ (°C)	$T_{max}2^b$ (°C)	$T_{max}3^b$ (°C)	$T_{max}4^b$ (°C)	Mass loss at 800°C (%)
ELO_double crosslinking	193	242	336	383	230	336	373 + 419s	527	87.93
ELO_thermal crosslinking	195	252	331	368	226	333	371 419	527	99.92
ELO_5%LnK	199	256	346	387	257	341	375 425s 448s	517	85.24
ELO_10%LnK	191	243	332	374	230	338	376 412s	510	98.24
ELO_15%LnK	182	229	325	373	221	335	371 401 436s	504	98.57

[a] – T_d = the temperature at which the mass loss is 3, 10, 30, 50%;
[b] – T_{max} = maximum decomposition temperature;
[s] – shoulder

Figure 1. TGA and DTG curves for ELO-5% LnK sample

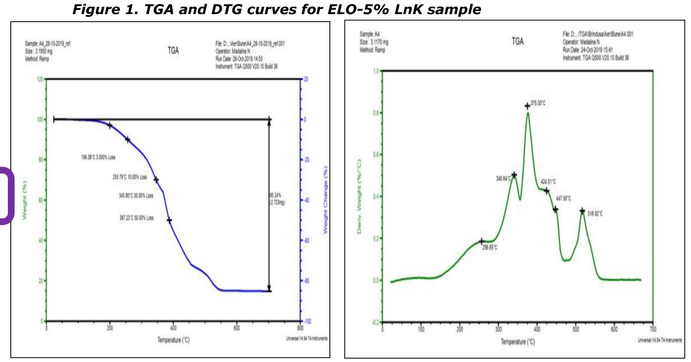

a) TGA

b) DTG

Investigation of corrosion protection capacity of EVO and LnK based coatings

Potentiodynamic polarization curves (Tafel) were recorded, with a speed of 2.5 mV/s on the potential range -0.8 V/Ag, AgCl/KCl and +0.8 V/Ag, AgCl/KCl, respectively. The results obtained are shown in ***Figure 2***. By processing the Tafel curves, the corrosion parameters for the new super-hydrophobic composite systems studied were obtained (S. Pan et al., 2016) . These parameters are presented in ***Table 2***. The Tafel curves show that:

- all the studied coatings have a corrosion inhibiting effect, significantly reducing the density of the corrosion current
- the addition of LnK in the continuous oil phase (ELO) leads to a reduction in the corrosion rate by up to 2 orders of magnitude compared to the sample without LnK.

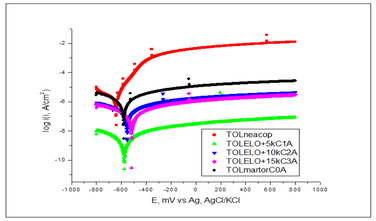

Figure 2. Tafel curves in 3.5% NaCl solution for coated carbon steel samples

***Legend: TOL**-uncovered sample; **C0A**-sample covered with material without LnK (control sample); **C1A**-sample coated with ELO-5% LnK; **C2A**-sample coated with ELO-10% LnK; **C3A**-sample coated with ELO-15% LnK.*

Table 2. Electrochemical parameters calculated according to Tafel curves

Sample Code	E cor (mV)	i corr (μA/cm²)	Rp (kohm.cm²)	βa (mV)	- βc (mV)	Coefficient	IE (%)
OL (Uncovered sample)	-646	1.5531	12.64	75.3	257.3	0.9999	-
C0A (Sample covered with material without LnK)	-584	0.5562	52.71	180.8	185.0	0.9977	64.19
C1A (Sample covered with ELO+5%LnK)	-581	0.0015	199.30	186.1	188.3	0.9974	99.90
C2A (Sample covered with ELO+10%LnK)	-558	0.1036	282.20	185.1	183.3	0.9977	93.33
C3A (Sample covered with ELO+15%LnK)	-523	0.0601	450.26	171.0	170.6	0.9977	96.13

***E cor (i = 0)**-corrosion potential, **i corr**-corrosion current density, **Rp**-polarization resistance, **βa**-anodic slope, **βc**-cathodic slope, **IE**-inhibition efficiency.*

Conclusions

- ✓ A series of composite materials based on ***ELO*** and ***LnK*** were synthesized, with the role of superhydrophobic coatings against metal corrosion.
- ✓ Aerobic studies have shown a higher thermal stability for the ***ELO_5% LnK*** system compared to other ELO-based composites.
- ✓ The inhibition efficiency (IE) values show that the composite coatings have a better corrosion resistance compared to the control sample, the best efficiency being obtained in the case of the sample with 5% LnK (99.90%).
- ✓ As the LnK content increases, the IE value decreases slightly, but the result is clearly superior to the control sample. This validates the corrosion inhibitory effect that LnK exerts in combination with ELO on the studied metal surfaces.
- ✓ Super-hydrophobic composite systems, derived from ***ELO***, containing ***LnK***, have the ability to inhibit corrosion of carbon-steel surfaces exposed to aggressive environments, being potential candidates in such applications.

References

Chen, J., Beaufort, M., Gyurik, J., Dorresteijn, J., Otte, M., Klein Gebbink, R. J. M., Green Chemistry **21**, 2436-2447 (**2019**).

Pan, S., Wang, N., Xiong, D., Deng, Y., Shi, Y., Applied Surface Science **389**, 547-553 (**2016**).

Acknowledgment

R. S. Komartin gratefully acknowledges the financial support of the Operational Programme Human Capital of the Ministry of European Funds through the Financial Agreement 51668/09.07.2019, SMIS code 124705.

Synthesis of chitosan-based nanoparticles

I. M. Vasincu[1], A. Vasincu[1], M. Apotrosoaei[1], S. Constantin[1], F. Lupașcu[1], A. Iacob[1], M. Drăgan[1], L. Confederat[2], A. Sava[1], D. Lupașcu[1], L. Profire[1]

[1]***Grigore T. Popa*** *University of Medicine and Pharmacy Iasi, Faculty of Pharmacy, Iasi, Romania*

[2]***Grigore T. Popa*** *University of Medicine and Pharmacy Iasi, Faculty of Medicine, Iasi, Romania*

Introduction

Nanotechnology

- important applications in different fields - **drug delivery systems**
- improved some drugs properties: solubility, bioavailability, biological effects, toxicity degree

Chitosan Nanoparticles

- important advantages:
  - small particle size (10-1000 nm)
  - biodegradable
  - large ratio active surface area/volume
  - high stability
  - feasibility of different drugs encapsulation
  - high carrier capacity
  - targeted release of loaded drugs

Materials and method

✓ Preparation → *ionic gelation technique*

- *2 types of chitosan (CS): low molecular weight (CSLMW), medium molecular weight (CSMMW)*
- *sodium tripolyphosphate (TPP) as cross-linking agent*

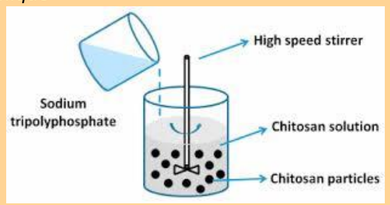

✓ Optimization:

- CS and TPP concentrations
- pH of CS solution
- reticulation time
- stirring speed

✓ Characterization
dynamic light scattering

- hydrodynamic diameter (size)
- polydispersity index (PDI)

Aims

optimize the synthesis of chitosan-based nanoparticles (CSNPs)

study the influence of different parameters on the formulation process

Results and discussions

Influence of pH of CS solution

TPP conc (%)	CSLMW conc (%)	Initial pH (3.6-3.8) PDI value	Initial pH (3.6-3.8) Size (nm)	pH = 4.7-7.8 PDI value	pH = 4.7-7.8 Size (nm)
0.1	0.05	>0.9	x	0.503	MP
	0.1	0.204	290.1	0.291	231.4
	0.133	0.245	403.8	0.271	342.3
	0.167	>0.9	MP	0.195	459.2
	0.2	>0.9	MP	0.303	615.9
0.15	0.05	>0.9	MP	0.73	MP
	0.1	0.277	343.8	0.296	280.7
	0.133	0.303	302.6	0.281	255.7
	0.167	0.313	390.5	0.235	440.7
	0.2	0.293	592.2	0.299	579.8
0.2	0.05	>0.9	MP	>0.9	MP
	0.1	>0.9	MP	>0.9	x
	0.133	0.291	MP	0.583	MP
	0.167	>0.9	MP	>0.9	MP
	0.2	0.287	531.1	0.262	349

TPP conc (%)	CSMMW conc (%)	Initial pH (3.6-3.8) PDI value	Initial pH (3.6-3.8) Size (nm)	pH = 4.7-7.8 PDI value	pH = 4.7-7.8 Size (nm)
0.1	0.05	0.245	NP+MP	0.317	NP+MP
	0.1	0.235	NP+MP	0.278	251.3
	0.133	0.312	NP+MP	0.215	385.6
	0.167	0.367	NP+MP	0.311	MP
	0.2	0.652	NP+MP	0.458	MP
0.15	0.05	>0.9	MP	>0.9	MP
	0.1	0.266	NP+MP	0.26	282
	0.133	0.224	410.9??	0.267	477.2
	0.167	0.258	NP+MP	0.215	524.3
	0.2	0.457	NP+MP	0.37	NP+MP
0.2	0.05	>0.9	MP	>0.9	x
	0.1	>0.9	NP+MP	>0.9	MP
	0.133	0.224	NP+MP	0.232	NP+MP
	0.167	0.205	NP+MP	0.249	NP+MP
	0.2	0.365	NP+MP	0.364	NP+MP

*MPs= microparticles (>1000 nm)

Influence of CS and TPP concentrations

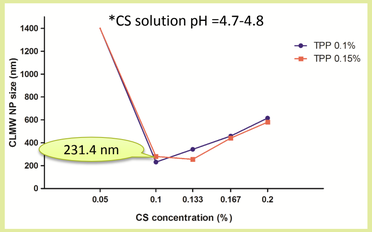

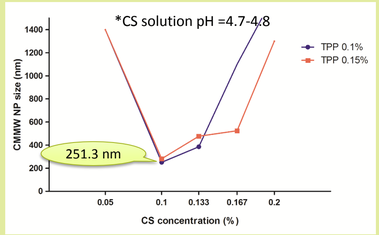

Influence of reticulation time

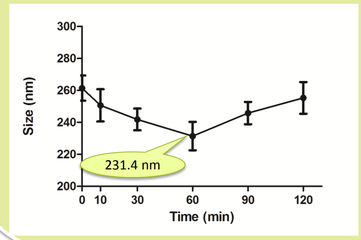

Influence of stirring speed

Stirring speed (rpm)	CSLMW PDI value	CSLMW Size (nm)
700	0.291	231.4
850	0.275	226.9
1000	0.151	208.8
1150	0.138	Bimodal
1300	0.149	NPs+MPs
1400	0.141	NPs+MPs

Conclusions

Optimized CSNPs

size of **208.8 ± 8.5 nm** were obtained using:

- ✓ 0.1% CS low molecular weight solution (pH=4.7-4.8)
- ✓ 0.1% TPP solution
- ✓ stirring for one hour at 1000 rpm

✓ potential drug delivery systems for **antidiabetic** and **anti-inflammatory** drugs

Selected references

- *Al-Nemrawi, N.K. et al. Int J App Pharm. 2018, 10(5), 60-65.*
- *Tao, X. et al. J Nanomat. 2018, 1-12.*
- *Sreekumar, S. et al. Sci Rep.2 2018, 8, 4695.*
- Fan, W. et al. *Colloids Surf B Biointerfaces 2012,* 90, 21-27.

Acknowledgments/Contact

Scientific research was funded by the grant of UEFISCDI, PN III Program, AUF-RO, AUF-IFA 2019-2020, contract no. ***28/2019*** *and by "Grigore T. Popa" University of Medicine and Pharmacy Iasi, based on contract no* ***30341****/28.12.2017.*

e-mail:ioana-mirela.vasincu@umfiasi.ro

S1-P33

Approaches to increase the electromechanical performance of silicone elastomers

Mihaela Dascalu,* Mihail Iacob, Codrin Tugui, Adrian Bele, George-Theodor Stiubianu, Carmen Racles, Maria Cazacu

[1]"Petru Poni" Institute of Macromolecular Chemistry, 41A Grigore Ghica Voda Alley, 700487 Iasi, Romania
amihaela@icmpp.ro

PETRU PONI

Introduction

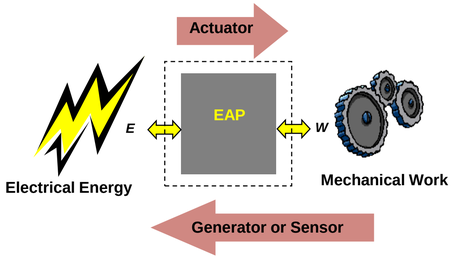

!!! Materials in DET:

- ✓ increased dielectric permittivity,
- ✓ high breakdown field strength,
- ✓ large strains,
- ✓ moderate Young modulus.

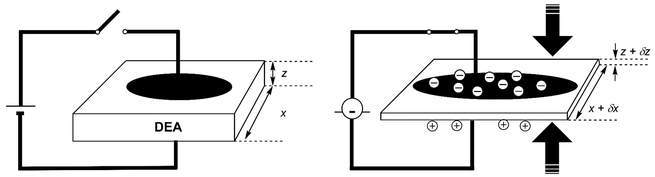

Advantages

- ✓ high flexibility of the Si-O bond→large achievable strains;
- ✓ large strain at break, fast response time, low ε",
- ✓ resistant to weathering, biocompatible, stable properties over a wide range of T(°C) and ν (Hz),
- ✓ good dielectric strength >100 V/μm
- ✓ maintain their specific energy over a wide frequency domain.

Drawbacks:
low mechanical properties and *low e'* (~2.3).

Results and discussions

1. Chemical modification with polar groups

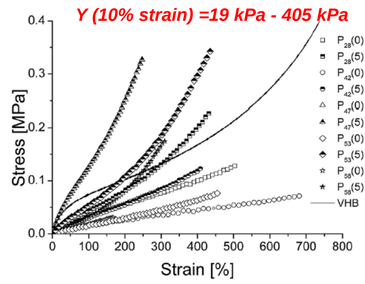

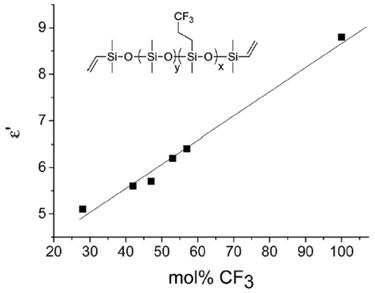

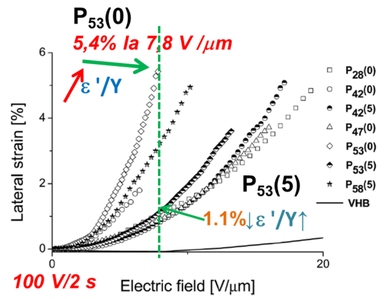

2. Fillers with high permittivity

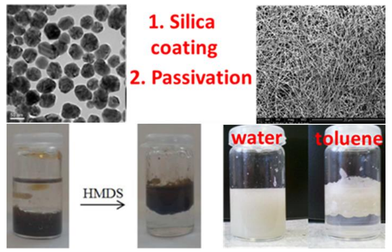

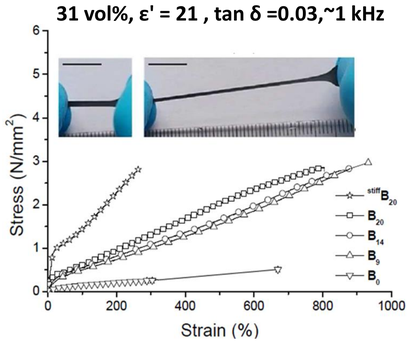

Specific energy density per volume

$$\frac{\Delta W}{Vol} = \frac{1}{2}\varepsilon\varepsilon_0 E_B^2\left(1-\frac{1}{(s_{max}+1)^2}\right)$$

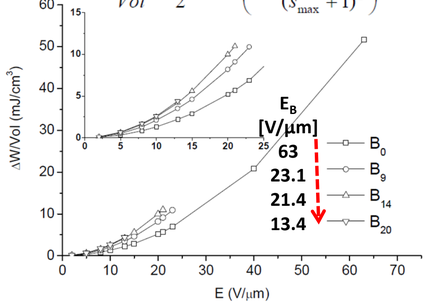

3. Octakis(phenyl)-T8-silsesquioxane-filled silicone elastomers

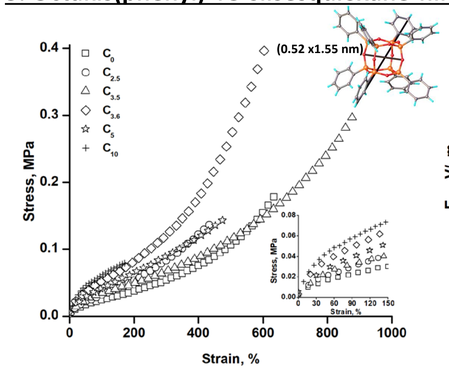

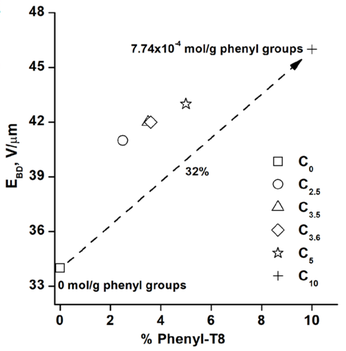

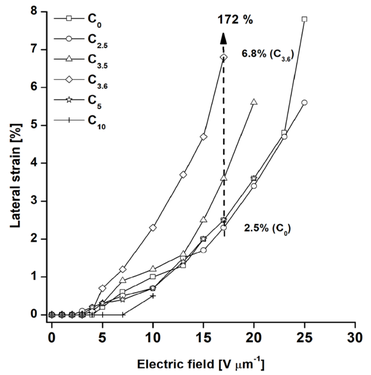

Conclusions

- ❑ the increased permittivity and the low actuation voltage recommend CF_3 based materials as dielectrics in sensors and actuators;
- ❑ *AgNPs@SiO$_2$@SiMe$_3$* (ε' = 90 and very low ε") – fillers for PDMS → composites with different vol%Ag: increased ε', low ε" and high values for the dielectric breakdown strength → these materials might find application as dielectric in energy harvesting devices operated at low electric fields.
- ❑ the use of *phenyl-T8* in a silicone matrix led to increased electric breakdown strengths, resulting in electroactive films with fast response specific to dielectric elastomers.

References

[1] M. Dascalu, S.J. Dünki, J.-E.Q. Quinsaat, Y.S. Ko, D.M. Opris, *RSC Adv.* **5**, 104516 (2015).

[2] J.E.Q. Quinsaat, M. Alexandru, F.A. Nuesch, H. Hofmann, A. Borgschulte, D.M. Opris, *J. Mater. Chem. A* **3**, 14675 (2015).

[3] M. Dascalu, M. Iacob, C. Tugui, A. Bele, G.-T. Stiubianu, C. Racles, M. Cazacu, *J. Appl. Polym. Sci., (2020).*

Acknowledgment

This work was supported by a grant of the Romanian National Authority for Scientific Research and Innovation, CNCS/CCCDI-UEFISCDI, project number PN-III-P2-2.1-PED2019-3652, 3DETSi, within PNCDI III.

Advances in Polysaccharide-Based Composite Cryogels: From Synthesis To Applications

Maria Valentina Dinu, Maria Marinela Lazar, Irina Elena Raschip, Ionel Adrian Dinu, Nicusor Fifere

"Petru Poni" Institute of Macromolecular Chemistry, Aleea Grigore Ghica Voda 41A, 700487, Iasi, Romania; E-mail address vdinu@icmpp.ro

Introduction

Cryogels are porous materials endowed with superfast responsiveness for water absorption and improved mechanical properties. They are very tough and can withstand high levels of deformation such as elongation and torsion. Polysaccharides are ideal candidates to obtain films, membranes, hydrogels, particles or capsules as carriers of biologically active compounds due to their outstanding properties, such as biodegradability, biocompatibility and antibacterial activity. In this context, novel polysaccharide-based cryogels were designed using cryogelation [1-3]. Effect of several synthesis parameters including (i) freezing and thawing conditions, (ii) cross-linking degree, and (iii) ratio between the cryogel components onto the morphological and swelling properties of cryogels has been systematically investigated. Furthermore, the sorption performance on the removal of Fe^{3+} ions removal from multicomponent mixtures (Cu^{2+}, Zn^{2+}, Ni^{2+}, and Cr^{3+}) of chitosan-based cryogels was systematically studied. The antioxidant and antimicrobial properties of xanthan-based composites were also demonstrated .

Materials and method

Chitosan or xanthan have been used as biopolymer matrix for the fabrication of novel macroporous composite hydrogels. The biopolymer matrices were physically or chemically cross-linked in the presence of a wide variety of synthetic polymers or embedded with natural zeolites.

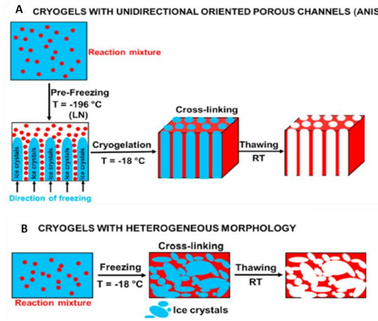

Figure 1. Preparation steps of polysaccharide-based composite cryogels with tailored porous morphologies.

Results and discussions

Chitosan-based cryogel composites for removal of heavy metal ions

A

Sample code	Feed composition			P_t[a]	V_p[b]	S_{BET}[c]	Pore	WU_t[d]
	CS, wt.%	GA, v/v%	CPLH⁺, g	%	$cm^3 \cdot g^{-1}$	$m^2 \cdot g^{-1}$	sizes, μm	$g \cdot g^{-1}$
CPLH⁺	-	-	-	-	0.042 ± 0.003	22.87 ± 0.02	-	0.74 ± 0.11
CGCS	2	2.5	-	93.74 ± 1.25	0.941 ± 0.05	-	26.81 ± 8	31.21 ± 1.08
CGCS_CPLH⁺	2	2.5	0.075	92.73 ± 2.05	0.916 ± 0.02	-	18.11 ± 4	26.42 ± 0.67

[a]Porosity; [b]Pore total volume; [c]BET surface area; [d]Water uptake.

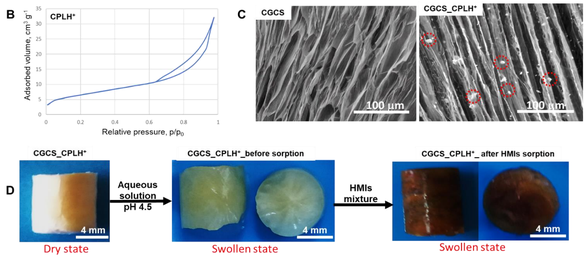

Figure 2. (A) Some characteristics of the sorbents; (B) N_2 adsorption–desorption isotherm on $CPLH^+$ sorbent; (C) SEM micrographs of CS–based sorbents; the red circles on the SEM micrograph of $CGCS\_CPLH^+$ composite cryogel represent $CPLH^+$ particles; (D) Optical pictures of $CGCS\_CPLH^+$ composite cryogels before and after HMIs loading.

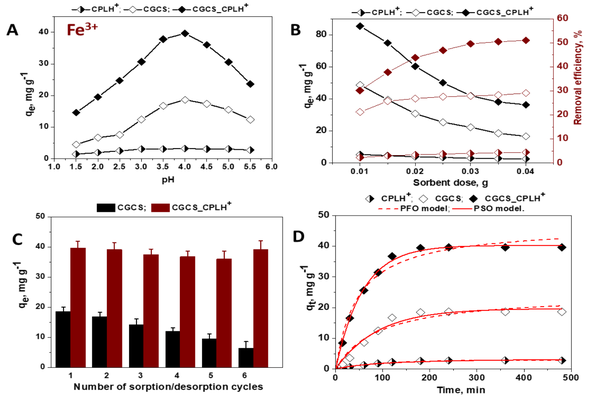

Figure 3. Influence of pH values (A), sorbent dose (B), successive sorption/desorption cycles (C), and contact time (D) onto Fe^{3+} ions removal from multicomponent mixtures by $CPLH^+$, CGCS, and $CGCS\_CPLH^+$ sorbents.

Xanthan-based cryogel composite films with antioxidant and antimicrobial activity

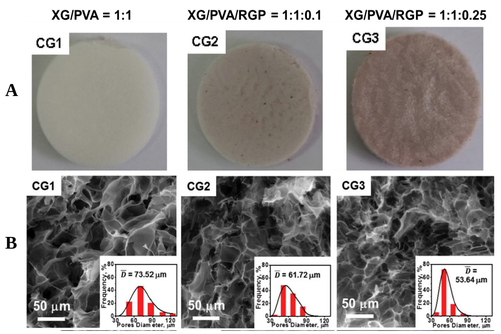

Figure 4. (A) Optical images of the XG/PVA cryogels prepared without red grape pomace (RGP) (**CG1**) and with a RGP content of 0.2 w/w% (**CG2**), and respectively of 0.5 w/w% (**CG3**). (B) SEM micrographs and the corresponding pore distribution diagrams for XG/PVA cryogels differ by RGP content.

Figure 5. Optical images of **CG1**, **CG2**, and **CG3** samples after performing the DPPH test.

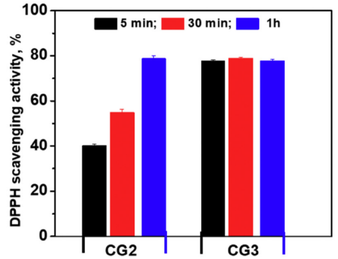

Figure 6. DPPH scavenging activity of **CG2** and **CG3** samples evaluated after 5 min, 30 min, or 1h of incubation in dark.

The growth rate inhibition of bacteria by XG/PVA cryogels without (**CG1**) and with RGP (**CG3**).

Sample	Growth rate inhibition of *Salmonella Typhymurium*, %	Growth rate inhibition of *Escherichia coli*, %	Growth rate inhibition of *Listeria monocytogenes*, %
Control	0	0	0
CG1	30 ± 5	38 ± 4	82 ± 5
CG3	58 ± 7	86 ± 6	90 ± 7

Conclusions

- **Porous polysaccharide-based cryogel composites with tuned pore sizes and morphology by the freeze/thawing conditions were successfully designed.**
- **The CS-based composite cryogel exhibited the highest sorption capacity, the maximum theoretical sorption capacity of this composite sorbent according to Sips model toward Fe^{3+} ions was 53.46 mg · g^{-1}.**
- **The modeling of kinetics, isotherm, and thermodynamic experimental data indicated a spontaneous chemisorption process for the sorption of Fe^{3+} ions onto CS–based sorbents.**
- **The excellent DPPH scavenging activity was assigned to the presence of trans-resveratrol which is the natural compound identified by HPLC in our RGP sample.**
- **By embedding the RGP within the XG/PVA cryogel matrix (CG3) a significant increase in the inhibition percentages for all tested bacteria was observed, with a more pronounced inhibition for the bacterium *Listeria monocytogenes*.**

References

1. Humelnicu, D., Lazar, M. M., Ignat, M., Dinu, I. A., Dragan, E. S., Dinu, M. V. *J. Hazard. Mater*. **381**, 120980 (2020).
2. Humelnicu, D., Ignat, M., Dragan, E. S., Dinu, M. V. *Molecules* **25**, 2664 (2020).
3. Raschip, I. E., Fifere, N., Varganici, C. -D., Dinu, M. V. *Int. J. Biol. Macromol.* **156**, 608 (2020).

Acknowledgment

The financial support from the Executive Unit for Financing Higher Education, Research, Development and Innovation (UEFISCDI) by PNIII-P1-1.1-TE-2016-1697 [TE117/2018] project is gratefully acknowledged for providing the chemicals and lab consumables.

Novel carbon/ZnO hybrid materials with high efficient removal of azo dyes

D.L. V. Bejenari, C. Lisa, I. Mămăligă, G. Lisa
, N. Olaru, A. Airinei and P. Pascariu

"Petru Poni" Institute of Macromolecular Chemistry, Aleea Grigore Ghica Voda, 41A, Iaşi 700487, Romania

Introduction

Recently, the composites materials based on the combination of metal oxide semiconductor nanomaterials and different types of carbon species have been intensively used as photocatalysts due to the interesting physico-chemical properties and potential applications in water purification and environmental protection [1].

Materials and method

A new type of materials based on carbon/ZnO nanostructures that possess both adsorption and photocatalytic properties was obtained in three stages: cellulose acetate butyrate (CAB) microfiber mats prepared by electrospinning method, ZnO nanostructures growth by dipping and hydrothermal methods, and finally thermal calcination at 600 ºC in N2 for 30 min. X-ray diffraction (XRD) confirms the structural characteristics. It was found that ZnO possesses a hexagonal wurtzite crystalline structure. The ZnO nanocrystals with a star-like and nanorod shapes were evidenced by SEM measurements. A significant decrease in Eg value was found for carbon/ZnO hybrid materials (2.51 eV) as compared to ZnO nanostructures (3.21 eV) [2]. The photocatalytic activity was evaluated by studying the degradation of three dyes Methylene Blue, Rhodamine B and Congo Red under visible-light irradiation. Therefore, the maximum color removal efficiency (both adsorption and photocatalytic processes) was: 97.97 % of MB (C0=10 mg/L), 98.34 % of RhB (C0=5 mg/L), and 91.93 % of CR (C0=10 mg/L). Besides, the value of the rate constant (k) was found to be 0.29×10-2 min-1. The novelty of this study relies on obtaining new photocatalysts based on carbon/ZnO using cheap and accessible raw materials, and low-cost preparation techniques.

Carbon/ZnO hybrid nanostructures preparation

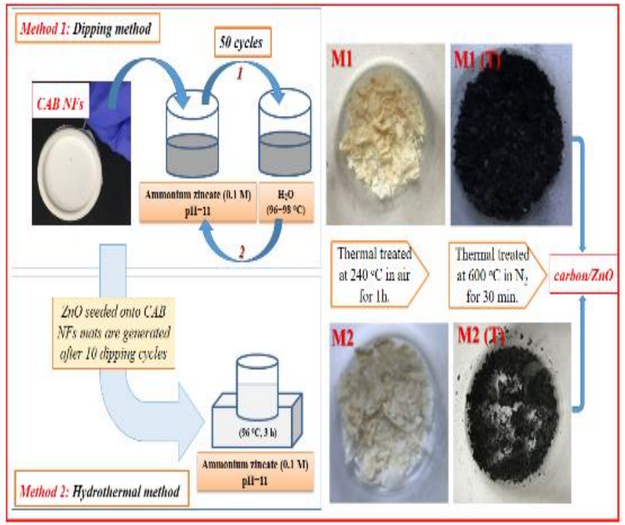

1. Structural characterization

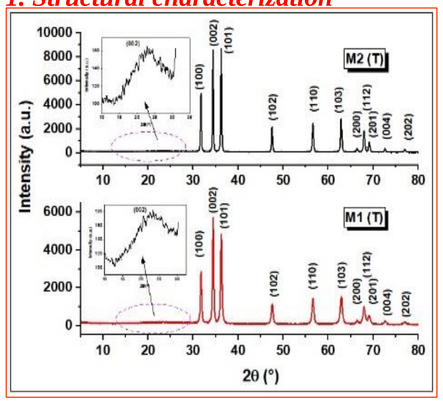

Fig. 1. XRD patterns of M1 (T) and M2 (T) samples.

2. Surface morphology

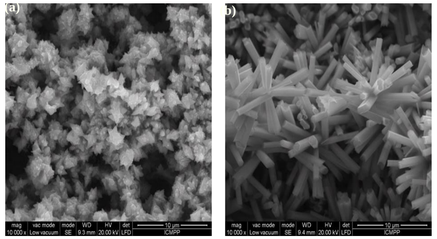

Fig. 2. SEM images of carbon/ZnO hybrid nanostructures obtained by dipping method (a) and hydrothermal method (b), respectively.

3. UV–visible spectra – optical properties

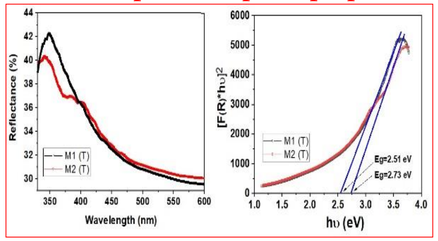

Fig. 3. Optical properties of carbon/ZnO nanostructures (a) diffuse reflectance UV-Vis spectra and (b) plot of [F(R)·hv]2 versus hv and band gap determination.

Results and discussions

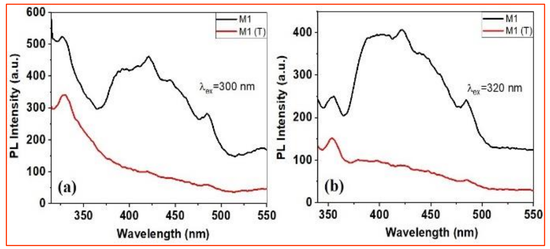

Fig. 4. Photoluminescence spectra of CAB/ZnO and Carbon/ZnO nanostructures as a function of excitation wavelength 300 (a), and 320 nm (b).

4. Adsorption/photocatalytic properties

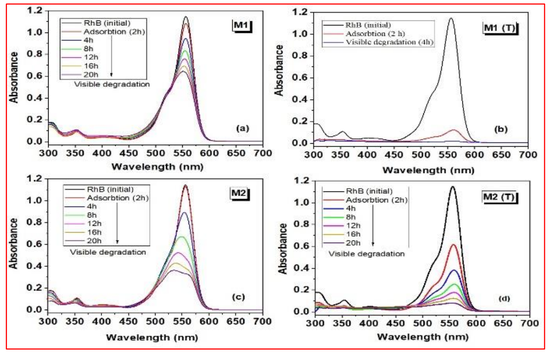

Fig. 5. UV-Vis absorption spectra of RhB recorded after adsorption (2h) (in dark) and photodegradation process under visible light irradiation (up to 20 hours).

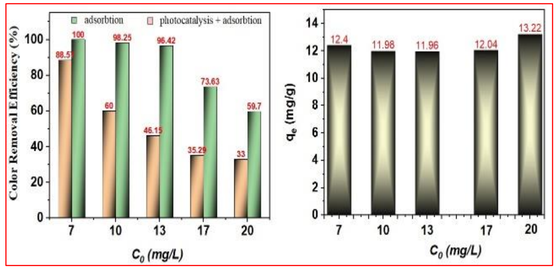

Fig. 6. Color removal efficiency after adsorption and photodegradation (a), and the maximum adsorption capacity of M1 (T) catalyst (b) for MB dye.

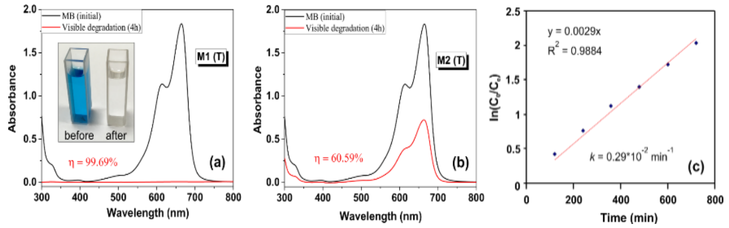

Fig. 7. UV-Vis absorption spectra after visible light irradiation for 4 hours in the presence of sample **M1 (T)** (a) and **M2 (T)** (b), and the degradation kinetics for **M1 (T)** sample (c).

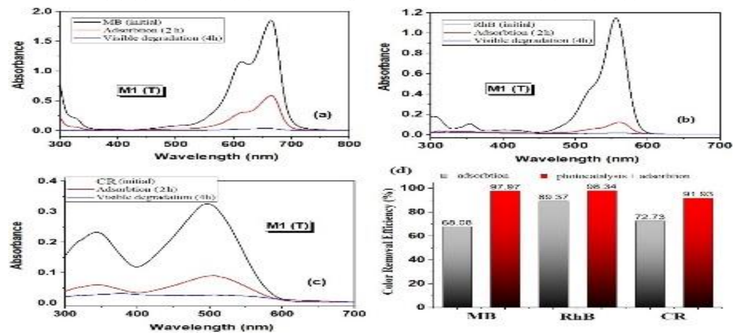

Fig. 8. UV-Vis absorption spectra after adsorption (2h) and visible light irradiation (4h) in the presence of sample **M1 (T)** for degradation of MB (C_0=10 mg/L) (a); RhB (C_0=5 mg/L) (b); CR (C_0=10 mg/L) (c), and color removal efficiency of all dyes degradation for sample **M1 (T)** (d).

Conclusions

Carbon/ZnO nanostructures were obtained in three stages: CAB microfiber mats were prepared by the electrospinning method, ZnO nanostructures were growth by dipping and hydrothermal methods, followed by thermal calcination at 600 ºC in N2 atmosphere for 30 min.. These new materials showed an improvement of the photocatalytic degradation efficiency for the RhB dye with approximately 80% as compared to the ZnO (control samples). The carbon/ZnO hybrid materials recorded a color removal efficiency (adsorption/photocatalytic process) between 91% and 98%, depending on the type of dye. All the experiments were performed under friendly environmental conditions: visible light irradiation at low power and a moderate amount of catalyst (0.5 g/L). Besides, the value of the rate constant was found for this material being 0.29×10-2 min-1. Therefore, the prepared carbon/ZnO materials from easily accessible and low cost materials together with their impressive performance place them among photocatalyst for practical applications in wastewater purification.

Selected references:

[1] P., Pascariu, M., Homocianu, Ceram. Int. 45, 11158–11173 (2019).

[2] P., Pascariu, L., Olaru, A.L., Matricala, N., Olaru, Appl. Surf. Sci. 455 61–69 (2018).

Acknowledgments

This work was supported by a grant of the Romanian Ministry of Research and Innovation, CCCDI-UEFISCDI, project number PN-III-P1-1.2- PCCDI-2017- 0428/40PCCDI/2018 , within PNCDI III.

Interplay of electronic structure in ground and excited states of new di-iminopyrene-di-benzo-18-crown-6-ether derivative by TD-DFT studies

Dragos Lucian Isac*, Adina Coroabă, Tudor Vasiliu, Radu Zonda, Sorin-Alexandru Ibănescu, Cristina Al Matarneh, Anton Airinei, Mariana Pinteală

"Petru Poni" Institute of Macromolecular Chemistry, Centre of Advanced Research in Bionanoconjugates and Biopolymers, 41A Grigore Ghica Voda Alley, Iași 700487, Romania

Introduction

The pyrene and its derivatives have interesting photophysical properties depicted by a strong absorption in UV-Vis range as well as specific emission spectra [1, 2]. The absorption and the fluorescence spectra are sensitive to solvent polarity, this fact suggests the use of this class of compounds as a test to determine environment behavior. Survey of literature indicates that the pyrene moiety presented a strong electron donor effect which can be combined in several materials in order to design the electron donor-acceptor systems which can be used in energy conversion and light harvesting applications.

The presence of a double bond (-HC=N-) in the structure of the pyrene derivatives determines the formation both their trans and cis conformations. In this context, the main goal of the present study was to investigate, by DFT and TD-DFT methods, the conformational effect in the ground and excited states to predict the theoretical electronic absorption spectra and π → π*, n → π* transitions of di-iminopyrene-di-benzo-18-crown-6-ether compound. Also, these studies help us in the identification of the intramolecular interactions, such as charge transfer, π- extended conjugation effect. Our results obtained by theoretical simulations are in line with the experimental data.

Materials and method

In this work, the calculations were performed with Gaussian (G16) package using density functional theory (DFT) and time-dependent density functional theory (TD-DFT) in order to investigate both the ground and the excited states. The ground state level was investigated with PBE0/6-311+G(d,p) method while the excited states and theoretical absorption spectra were computed with TD-CAM-B3LYP functional and 6-311+G(d,p) basis sets.

All calculations were carried on the Tetralith supercomputer from the KTH Royal Institute of Technology, PDC Center for High Performance Computing.

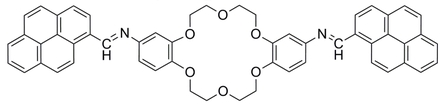

Fig1. Structural formula of di-iminopyrene-di-benzo-18-crown-6-ether

Results and discussions

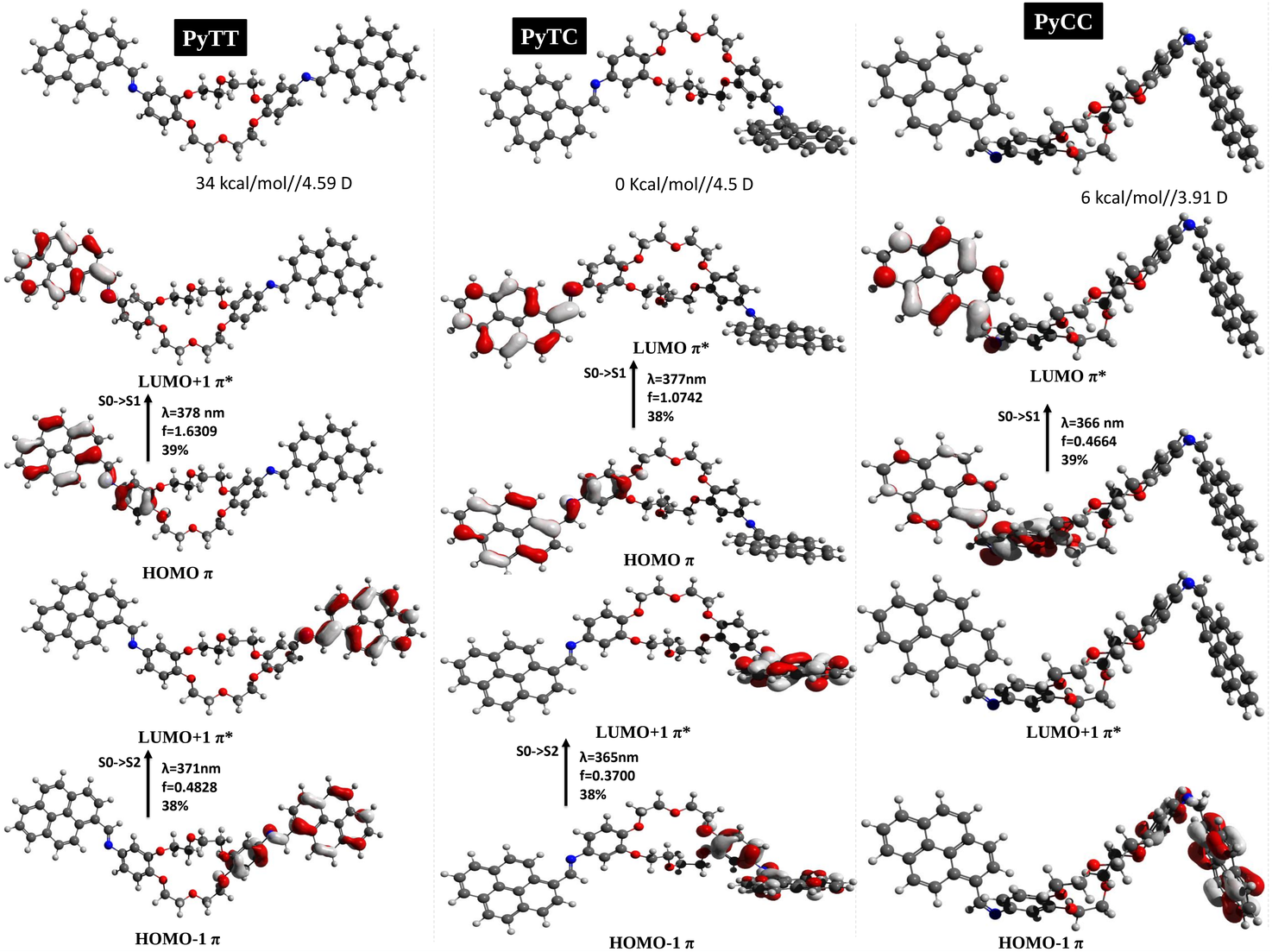

Table 1. Theoretical values of the the oscillator strength (f), calculated at the TD-DFT/6-311++G(d,p) level of theory and experimental absorption wavelengths (λ_{abs}, nm) for the target compounds (trans isomers).

Solvents	TD-CAMB3LYP		TD-PBE0		Exp.
	λ_{abs}	f	λ_{abs}	f	λ_{abs}
toluene	388	1.6324	437	1.7386	396
	382	0.8391	433	0.2384	377
	330	0.0601	389	0.0001	345
ethanol	385	1.7130	433	1.7582	390
	380	0.6972	429	0.2082	380
	316	0.1111	367	0.0284	289

Conclusions

Theoretical results indicated the presence of π→π* transitions, due to π-extended conjugation. All theoretical results are agreement with the experimental determinations.

Acknowledgments

This work was supported by PN-III-P4-ID-PCCF-2016-0050 (acronim 5DNANOP).

References

[1] Shirai, S., Inagaki, S RSC Adv. 10, 12988 (2020).

[2] Baba, M., Saitoh, M., Kowaka, Y., Taguma, K., Yoshida, K., Semba, Y., Kasahara, S., Yamanaka, T.; Ohshima, Y.; Hsu, Y.-C.; et al., J. Chem. Phys. 131, 224318 (2009).

Contact:

* isac.dragos@icmpp.ro

Metallized polyimide films as blood-contacting devices

S. -L. Nica1, D. Popovici1, M. Dobromir2

1 "Petru Poni" Institute of Macromolecular Chemistry, Aleea Grigore Ghica Voda, 41A, 700487, Iasi, Romania; nica.simona@icmpp.ro
2" Alexandru Ioan Cuza" University of Iasi, Interdisciplinary Research Institute, Sciences Department, 11 Carol I Blvd., 700506, Iasi, Romania

Introduction

In this work, a fully aromatic polyimide and a semialiphatic one, were studied. Prior metallization, the polymer surfaces was exposed to plasma. As showed by XPS, the occurrence of polar groups at polyimides surfaces affects polar component of surface free energy. Molecular mechanics simulations were employed to investigate the structure-properties relationship of the polyimide films. Blood-polyimide interactions were assessed.

Materials

Studied polyimides were:

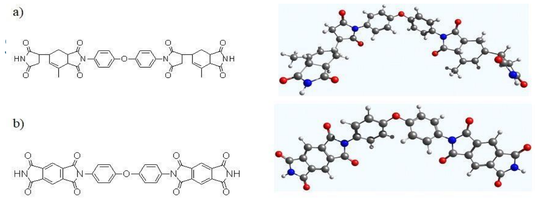

Model structural unit spatial conformation of: a)poly(DOCDA-ODA); b) poly(PMDA-ODA)

Methods

XPS data were recorded with ULVAC-PHI, 5000 Versa Probe spectrometer with monochromated AlKα radiation (1486.7 eV).

The sessile-drop method was used to obtain the static contact angle values.

Nitrogen plasma characteristics: high-frequency system of 1.3 MHz, pressure = 0.56 mbar, power = 100 W . Gold deposition:Sputter Coater system which employs a Magnetron Target Assembly

Molecular simulation

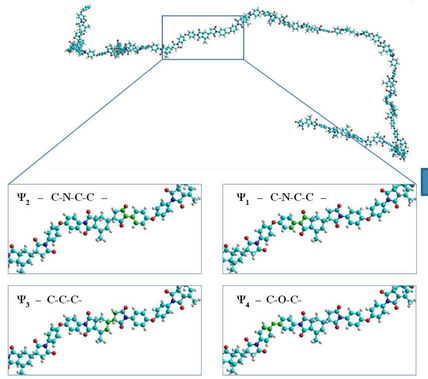

XPS analysis

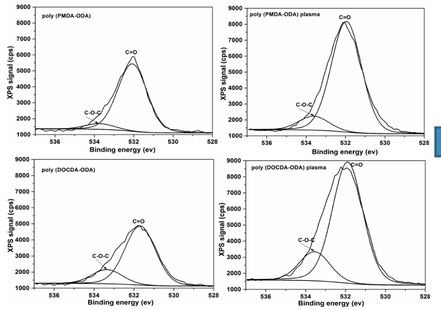

O 1s spectra of untreated and nitrogen plasma treated poly(PMDA-ODA)and poly(DOCDA-ODA).

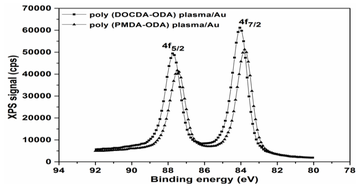

Au 4f5/2, 7/2 photoelectron spectrum of both investigated polyimides.

Results and discussions

- chain conformation of poly(DOCDA-ODA) material is twisted, without a specific orientation
- structural unit of semi-aromatic poly(DOCDA-ODA) has four flexible bonds → flexibility of partially cycloaliphatic polyimide chain is limited to vibrations around equilibrium positions

- two oxygen containing species were detected for untreated poly(DOCDA-ODA): the aliphatic carbonyl species (C=O) at 531.76eV and aromatic ether group (C-O-C) at 533.36 eV while O1s XPS spectra for untreated poly(PMDA-ODA) reveal the presence of two oxygen components: the aromatic carbonyl species (C=O) at532.06 eV and aromatic ether group (C-O-C) at 533.76 eV.
- the peak area corresponding to C=O bonds increases for poly(DOCDA-ODA) while the peak area corresponding to 533.3 eV (C-O-C) decreases
- presence of compact surface metal layer
- poly(DOCDA-ODA) have a higher amount of gold deposition on its surface

Contact angle and bio-interactions

$$W_a = (1+\cos\theta)\cdot\gamma_{lv} = 2\cdot\sqrt{\gamma_{sv}^{LW}\cdot\gamma_{lv}^{LW}} + \sqrt{\gamma_{sv}^{+}\cdot\gamma_{lv}^{-}} + \sqrt{\gamma_{sv}^{-}\cdot\gamma_{lv}^{+}}$$ → van Oss-Chaudry-Good equation

$$W_a = W_{sl}^{d} + W_{sl}^{ab} = P_s^d\cdot P_l^d - (P_s^a\cdot P_l^b - P_s^b\cdot P_l^a) = \gamma_{lv}(\cos\theta+1) + \pi_e \quad (7)$$ → Chang-Qing-Chen (CQC) model

Sample	Model	γ_s^{LW}	γ_s^{ab}	γ_s^{+}	γ_s^{-}	γ_s	P_s^a	P_s^b	nature
poly(DOCDA-ODA)									
Untreated	vOCG	42.74	36.73	6.02	2.88	3.15	-	-	bipolar
	CQC	42.29	36.73	5.56			3.03	-1.83	amphoteric
plasma	vOCG	56.17	44.16	12.01	0.74	48.67	-	-	monopolar
treated	CQC	14.52	44.16	29.69			6.80	4.36	acidic
metallized	vOCG	45.75	43.44	2.32	0.65	2.06			monopolar
	CQC	43.40	43.44	0.04			2.95	-0.11	amphoteric
poly(PMDA-ODA)									
untreated	vOCG	46.77	39	7.76	2.08	7.25	-	-	bipolar
	CQC	41.68	39	2.67			5.16	-0.52	amphoteric
plasma	vOCG	56.76	44.34	12.42	0.75	51.56	-	-	monopolar
treated	CQC	26.38	44.34	17.95			8.76	2.05	acidic
metallized	vOCG	47.26	43.73	3.53	1.16	2.69	-	-	bipolar
	CQC	45.36	43.73	1.64			3.24	-0.51	amphoteric

- bipolarity of untreated polyimides was due to different dianhydride monomers: DOCDA and PMDA , respectively
- bipolarity changed after nitrogen plasma while adhesion to gold metal have a little influence on polyimide surfaces regarding the nature of polyimides
- surfaces of both treated polyimides have a dispersive character
- strong increase of surface polar components for both poly(DOCDA-ODA) and poly(PMDA-ODA) films after plasma treatment, determines an increase of polyimide/gold adhesion.

$$W_s = W_a - W_c = 2\cdot\left[\sqrt{\gamma_{sv}^{LW}\cdot\gamma_{lv}^{d}} + \sqrt{\gamma_{sv}^{+}\cdot\gamma_{lv}^{-}} + \sqrt{\gamma_{sv}^{-}\cdot\gamma_{lv}^{+}}\right] - 2\cdot\gamma_{lv}$$

	poly(DOCDA-ODA)	poly(DOCDA-ODA) plasma	poly(DOCDA-ODA) plasma/Au
W_{blood}	-54.44	-50.52	-50.89
W_{fg-D}	-3.67	4.10	-10.87
$W_{albu\ min}$	-29.20	-8.94	-38.15
$W_{r.b.c.}$	40.52	18.82	16.34
$W_{platelate}$	-94.34	-50.60	-90.78
	poly(PMDA-ODA)	poly(PMDA-ODA) plasma	poly(PMDA-ODA) plasma/Au
W_{blood}	-53.2	-50.43	-50.73
W_{fg-D}	-2.86	4.84	-6.29
$W_{albu\ min}$	-26.31	-7.69	-32.98
$W_{r.b.c.}$	21.13	19.10	20.32
$W_{platelate}$	-85.40	-48.87	-87.43

- the work of spreading of blood and its components on samples takes both negative and positive values
- work of spreading of proteins (Albumin and IgG) is negative suggesting that the cohesive forces prevail
- a slight adhesion of rbc to the polyimide surface concomitantly with a high cohesion of platelets at the bio-interface due to positive values of Ws

Conclusions

- plasma treatment increase s the surface hydrophilicity
- plasma treatment significantly influenced the gold metallization of these polymers leading to a continous gold layer formation
- surface composition reveal the presence of new O-containing functionalities reaching a higher amounts for poly(DOCDA-ODA)
- poly(DOCDA-ODA) polyimide have a good blood compatibility

Testing of sorption capacity of quaternized polysulfones-based membranes: Perspectives for environmental applications

Anca Filimon[1], Alexandra Bargan[1], Cristian Logigan[2]

1 "Petru Poni" Institute of Macromolecular Chemistry, 41A Grigore Ghica Voda Alley, 700487 Iasi, Romania
2 Chemical Company SA, 14 Chimiei Bvd., 707252 Iasi, Romania

Introduction

- Development of new quaternized polysulfones-based systems, which possess multifunctionality, sustainability and antibacterial characteristics, was performed as a result of membrane technology requirements.
- Solutions of quaternized polysulfones (PSFQ) with tunable contents of cellulose acetate phthalate (CAP) and polyvinyl alcohol (PVA) have been processed to obtain new membrane materials explored for wastewater treatment.
- Cumulative effects generated by the molecular functionalization of polysulfone along with CAP and PVA versatile nature were responsible for improving the workability, surface properties, and membranes performance.
- The practical applicability of membranes was tested by evaluation of bacterial adhesion to surface, in order to clarify their suitability for life quality and environmental applications.

Materials and method

Materials: Functionalized polysulfones containing quaternary ammonium groups (PSFQs, Mn=28000g/mol), cellulose acetate phthalate (CAP, Mn=2534 g/mol), polyvinyl alcohol (PVA, Mw=23000g/mol).

Methods: Membranes surface characterization: Fourier transform infrared spectroscopy, Atomic force microscopy

Evaluation of membranes performance: Dynamic vapors sorption measurements, Antimicrobial activity tests

Results and discussions

Tailored polysulfone membranes microstructure by CAP or PVA embedding

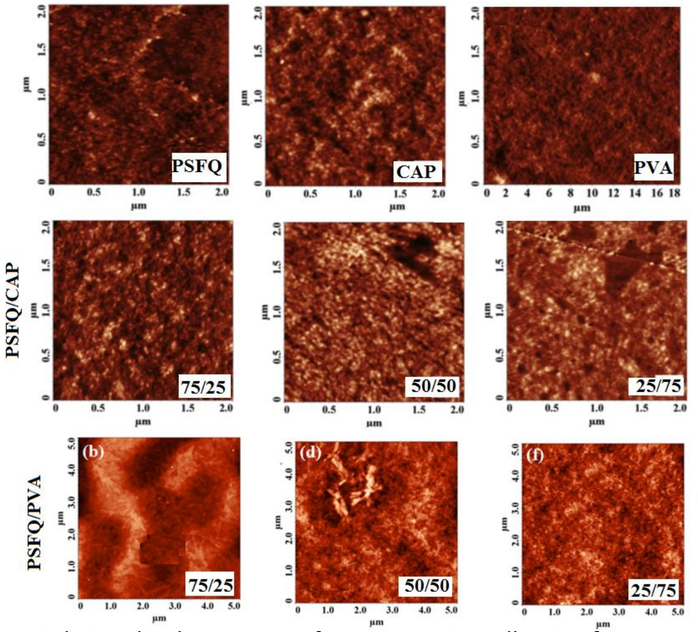

exist nano-sized pores whose number varies from sample to sample, depending on the structural peculiarity and composition of polymers in the blend

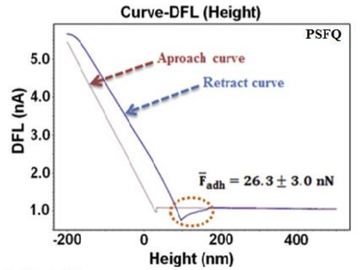

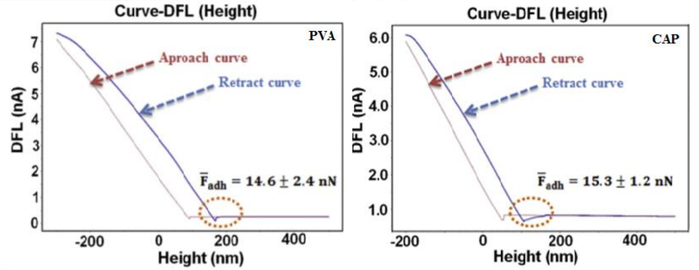

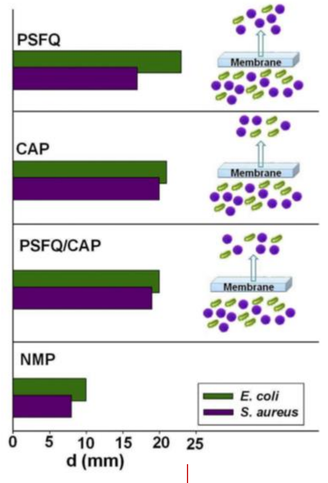

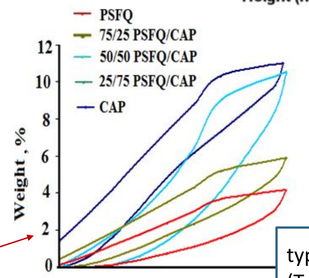

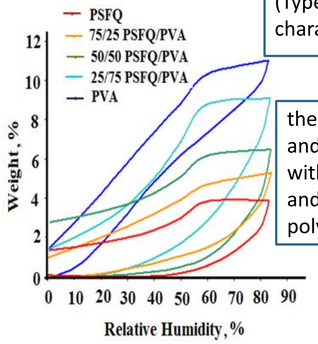

The bactericidal performance in environmental applications of new blends with specific microarchitecture, controlled porosity, and higher hydrophilicity, is measured by its ability to maintain the balance between the biological selectivity and membranes functionalization as disinfection materials.

types of isotherms with hysteresis (Type IV) can be interpreted as being characteristic to the porous surfaces

Relationship between surface properties-adhesion forces-wetting characteristics

Polymer/ Systems	F_{adh} (nN)	γ_{sv}^{AB} (mN/m)	γ_{sv}^{+} (mN/m)	γ_{sv}^{-} (mN/m)	Sorption capacity (%)
PSFQ	26.35±3.01	3.91	10.45	0.37	3.69
PVA	14.6 ±0.80	7.75	38.58	0.39	4.86
CAP	15.30±1.20	6.42	23.59	0.44	11.01
PSFQ/PVA					
75/25	17.85±2.06	3.57	14.45	0.22	5.29
50/50	20.71±1.59	6.74	3.99	2.85	6.47
25/75	29.75±0.97	9.43	13.44	1.65	9.12
PSFQ/CAP					
75/25	14.59±2.44	0.13	24.13	0.002	4.18
50/50	12.92±0.79	2.73	18.60	0.100	5.93
25/75	7.47±3.15	4.47	20.17	0.250	10.52

sorption capacity increase in the order: PSFQ < PSFQ/CAP or PSFQ/PVA < CAP or PVA

the porogen effect of the CAP and PVA generates structures with a high specific surface area and small pore size into the polysulfone matrix

Acknowledgment

The financial support of European Social Fund for Regional Development, Competitiveness Operational Programme Axis 1—Project "Petru Poni Institute of Macromolecular Chemistry—Interdisciplinary Pol for Smart Specialization through Research and Innovation and Technology Transfer in Bio(nano)polymeric Materials and (Eco)Technology", InoMatPol (ID P_36_570, Contract 142/10.10.2016, cod MySMIS: 107464) is gratefully acknowledged.

Bioinspired Elastomer Nanocomposites for Dynamic Harvesting and Control of Infrared Energy Flow

G. T. Stiubianu[1]

[1]Petru Poni Institute of Macromolecular Chemistry, Aleea Grigore Ghica Voda 41A, Iasi, Romania, E-mail: george.stiubianu@icmpp.ro

Introduction

Aim: Use a cost-affordable approach to develop and test a laboratory-scale method for preparation of dual-mode (heating and cooling) nanocomposite material with tunable thermal infrared properties, inspired from rapid mechanical actuation and color changing ability of squid skin.

We prepared nanocomposite materials which possess the ability to regulate a heat flow as large as 40 W/m^2 with a one-time mechanical input of 2-3 W/m^2 and we used as reference material the static infrared-reflecting space blanket developed by NASA in 1960.

Materials and method

To prepare the nanosized metal layer, a ~ 20 nm planar copper film was electron beam evaporated onto a 6-inch diameter silicon wafer (University Wafer) by using an Angstrom Engineering EvoVac system.

Next, to embed the nanosized layer within an infrared-transparent elastomer, a ~ 30 µm thick film from a commercially-available styrene-ethylene-butylene-styrene block copolymer (G1645 SEBS, Kraton Polymers LLC) was spincast directly onto the nanostructure-modified substrate.

Last, the composite was heat-treated on a hot plate at 60 C for 10 minutes and then delaminated from the substrate with a Mylar frame and pressure-sensitive tape. The resulting materials were used for physical, mechanical (Instron 3365 Universal Testing System), morphological (SEM), and infrared (Perkin Elmer (FTIR) Spectrometer outfitted with a Pike Technologies Integrating Sphere) characterization experiments as needed.

Results and discussions

Bioinspired Design for Nanocomposite Materials

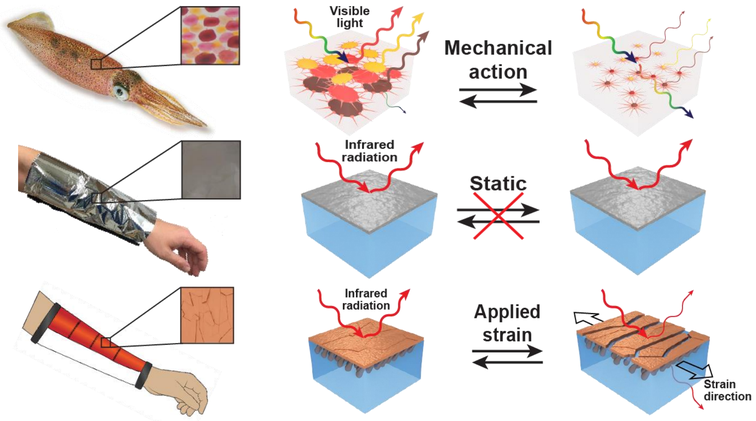

Steps for Preparation and Testing of Nanocomposite Material

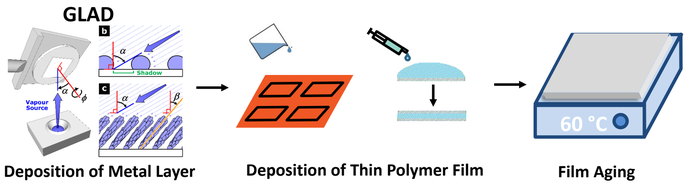

Heat Flow Regulation Using Mechanical Actuation of Nanocomposites

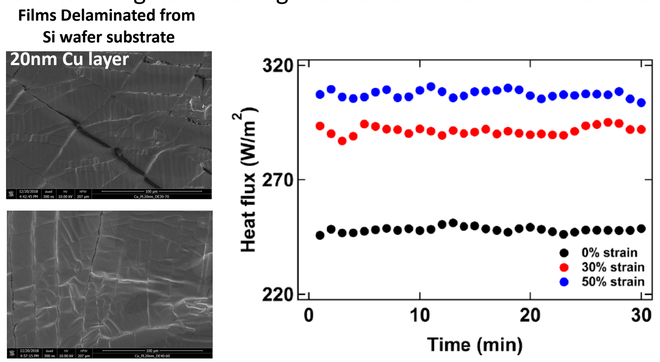

Thermoregulating Mechanism for Mechanically Actuated Nanocomposites

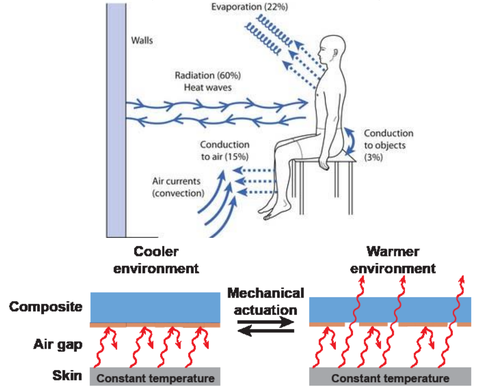

Dynamic Control of Human Skin Thermal Flux

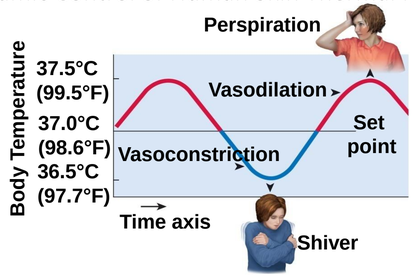

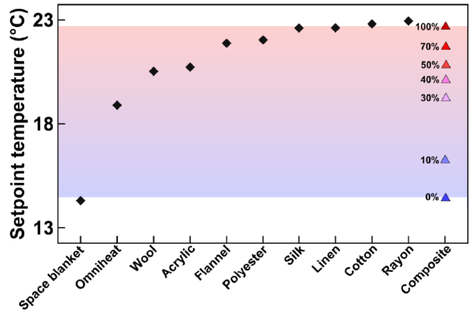

Conclusions

1. We have developed an artificial thermo-regulatory platform.
2. The nanocomposites function via a unique mechanism that relies on reversible, mechanically-actuated changes in surface microstructure.
3. Such materials adaptively alter their reflectance and transmittance within the thermal infrared region of the electromagnetic spectrum and, thus, can adjust their thermoregulatory properties to resemble those of various common wearable materials, such as the space blanket, an Omniheat fleece lining, wool, and cotton.
4. Such nanocomposites behave like radiative thermal switches with straightforward actuation method, reversibility and tunability without hysteresis, dynamic environmental setpoint temperature ranges and can precisely regulate local body temperature changes for wearers in real time.
5. Such materials can be manufactured from low-cost commercial building blocks via scalable and facile processes.

References

1. Ürge-Vorsatz, D., Cabeza, L. F., Serrano, S., Barreneche, C. & Petrichenko, K. *Renew. Sustain. Energy Rev.* **41**, 85-98 (2015).
2. Leung, E. M., Escobar, M. C., Stiubianu, G. T., et al., *Nat. Commun.*, 10, 1947, 10 pp. (2019).

Acknowledgment or Contact

This work was supported by a grant of the Romanian National Authority for Scientific Research and Innovation, CNCS/CCCDI -UEFISCDI, project number PN-III-P2-2.1-PED-2019-3652, 3DETSi, within PNCDI III.

Characterization of silicon quantum dots' properties and hepatic toxicity in mice

Roxana- Elena Cristian[1], Miruna-Silvia Stan[1,2], Anca Dinischiotu[1]

[1] University of Bucharest, Faculty of Biology, Department of Biochemistry and Molecular Biology, 91-95 Splaiul Independentei, 050095 Bucharest, Romania
[2] Department of Science and Engineering of Oxide Materials and Nanomaterials, Faculty of Applied Chemistry and Materials Science, University Politehnica of Bucharest, 1–7 Polizu Street, 011061 Bucharest, Romania

INTRODUCTION

The use of quantum dots (QDs) represents a promising tool for *in vivo* imaging, tumor biology investigation and cancer treatment due to their multiple optical and electronic properties that offer advantages for medical purposes compared to conventional nanoparticles. However, QDs can also trigger toxicity effects in healthy cells as it was previously reviewed by Zhu et al. [1].In this context, the present study aimed to characterize the silicon-based QDs obtained by laser ablation and to evaluate the *in vivo* hepatic toxicity induced by these semiconductor nanocrystals.

Si/SiO_2 QDs

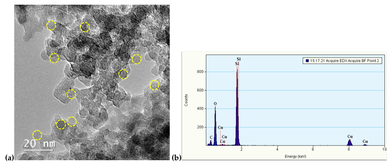

Characterization of Si/SiO_2 QDs by TEM (**a**) and EDXS (**b**) investigations. Note the spherical shape of QDs marked by yellow dot circles (**a**).

RESULTS

- The administration of the highest dose of QDs induced a significant reduction in the activity of catalase, the level being half of the control after all periods of exposure
- After 24 and 72 h, the activities of glutathione peroxidase and glutathione S-transferase diminished in the hepatocytes of mice that received 10 and 100 mg/kg b.w. compared to control.
- No significant changes were observed regarding the activity of superoxide dismutase in the liver of treated mice in comparison with control, suggesting that the QDs administration would not generate superoxide anions inside hepatocytes.

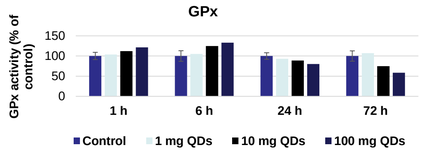

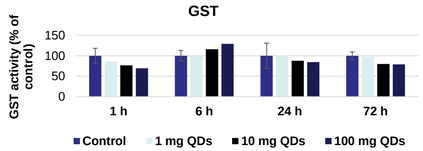

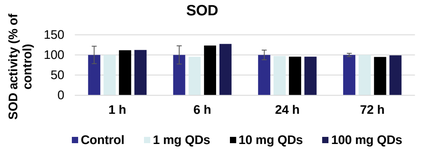

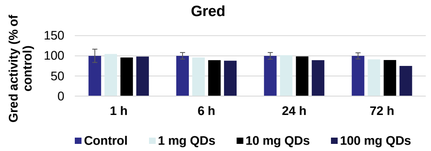

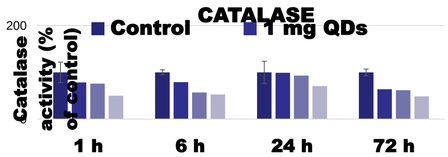

EXPERIMENTAL PROCEDURE

• In order to test their *in vivo* toxicity, different doses of QDs (0, 1 10 and 100 mg QDs/ kg body weight) prepared in 0.9% saline were injected in the codal vein of the Swiss mice. After 1, 6, 24 and 72 hours, the animals were sacrificed and the hepatic tissue was harvested.

• The effects of silicon QDs on antioxidant defense of hepatocytes were investigated throughout the measurement of antioxidant enzymes' activities (catalase, superoxide dismutase, glutathione peroxidase, glutathione reductase and glutathione S-transferase).

CONCLUSION

In conclusion, this study revealed the possible damaging effects on hepatocytes of high doses of silicon-based QDs (>10 mg QDs/kg b.w.) providing useful information for further clinical studies on humans.

Acknowledgments M.S. Stan acknowledges the support of the Operational Programme Human Capital of the Ministry of European Funds through the Financial Agreement 51668/09.07.2019, SMIS code 124705.

Preparation of polybenzoxazine-based graphene oxide nanocomposites

E. I. BÎRU[1], S. A. GÂREA[1], H. IOVU[1,2]

[1]Advanced Polymer Materials Group, University Politehnica of Bucharest, Gheorghe Polizu 1-7, Romania, luliana.biru@upb.ro

[2]Correspondent Member, Academy of Romanian Scientists, Calea Victoriei 125, Bucharest, Romania

Introduction

The benzoxazines are a unique non-halogen thermoset resins. As a novel type of phenolic resins, polybenzoxazines have many unique characteristics: high glass transition temperature, near-zero volumetric shrinkage upon polymerization, better flammability resistance than epoxy resins. However, pure benzoxazine-based polymers exhibit some drawbacks such as: high curing temperature and poor mechanical properties like brittleness and difficulty in processing especially into thin films and coatings.

Graphene oxide exhibit many important properties such as: high flexibility, is high hydrophilic and relatively easy to disperse in aqueous media or other polar solvents and also it can reduce the polymerization temperature. That`s the reason why GO may be the ideal candidate for making new polybenzoxazine – graphene oxide nanocomposites with enhanced properties.

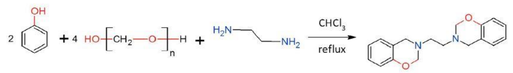

Materials and methods

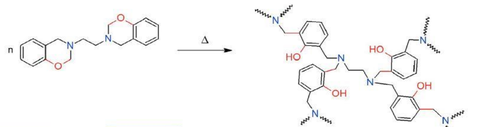

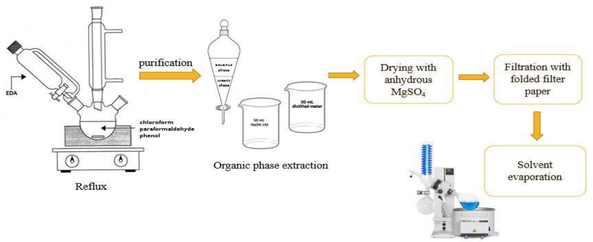

Fig. 1 Synthesis of the benzoxazine monomer and curing reaction

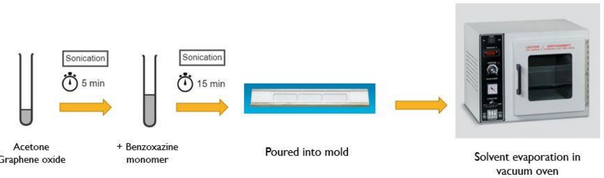

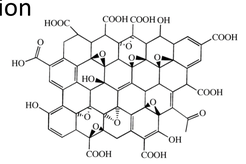

Graphene oxide structure

Fig. 2 Polybenozxazine – graphene oxide composites preparation scheme

Results and discussions

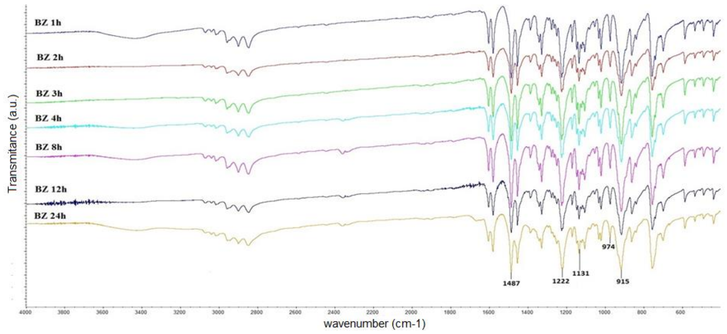

Fig 3. FT-IR spectra for monomers synthesized at different reaction times

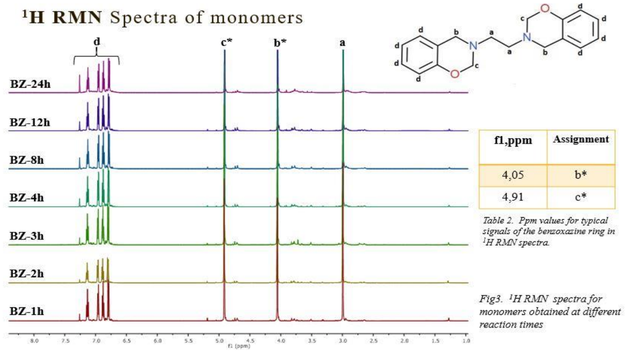

Fig. 4 ^{1}H-NMR spectrum of benzoxazine monomer

Sample	Integrated value (Ar-CH_2-N) I	Integrated value (N-$(CH_2)_2$-N) I'	Benzoxazine ring content (%)
BZ-1 h	4.16	4	48
BZ-2 h	4.16	4	48
BZ-3 h	4.17	4	48
BZ-4 h	3.90	4	51
BZ-8 h	4.18	4	48
BZ-12 h	3.87	4	52
BZ-24 h	4.02	4	50

$$c\ (\%) = \frac{I}{2 * I'} * 100$$

I= integrated area of methylene protons of Ar –CH_2-N

I'= integrated area of methylene protons of N-$(CH_2)_2$-N

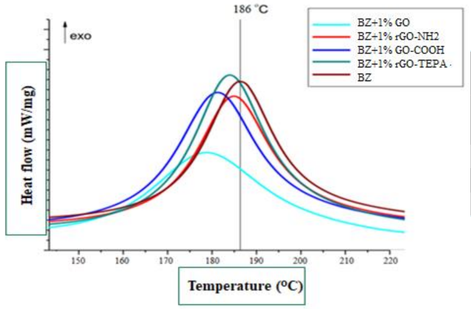

Sample	Polymerization temperature (°C)	Polymerization enthalpy (J/g)
BZ +1% GO	178.9	279.6
BZ +1% rGO NH_2	185.2	279.7
BZ + 1%GO-COOH	181.2	295.4
BZ+1% rGO-TEPA	184.6	314.6
BZ	186	306

Fig 5. DSC curves of EDA-BZ resin and different functionalized GO/EDA-BZ compounds

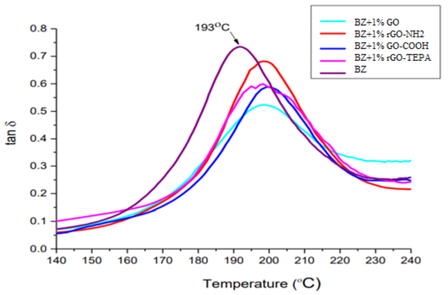

Sample	Tg (°C)	E″ (°C)
PBZ +1% GO	198.7	174.9
PBZ +1% rGO NH_2	198.5	169.1
PBZ + 1%GO-COOH	199.3	172.6
PBZ+1% Rgo-TEPA	198.4	149.5
PBZ	193	168

Fig 6. DMA curves comparing tan δ for EDA based polymer (PBZ) and different functionalized GO/PBZ compounds

Conclusions

The influence of the synthesis duration for EDA-based benzoxazine monomer was determined.

All the synthetized BZ/GO nanocomposites revealed a superior thermal stability with increasing of glass transition Tg compared with simple resin.

Acknowledgment

The work has been funded by the Operational Programme Human Capital of the Ministry of European Funds through the Financial Agreement 51668/09.07.2019, SMIS code 124705.

Development of novel multitarget NSAID, indomethacin associated with 1,3,4-oxadiazole moiety and a nitric oxide releasing group

Alexandru Sava[1,2], Frederic Buron[2], Sylvain Routier[2], Florentina Geanina Lupascu[1]

Ioana Vasincu[1], Maria Apotrosoaei[1], Andreea Iacob[1], Luminita Confederat[1], Oana Maria Dragan[1], Lenuța Profire[1]

[1] „Grigore T. Popa" Universiy of Medicine and Pharmacy Iași, Faculty of Pharmacy, Pharmaceutical Chemistry Department, 16 University Street Iași, 700115, Romania. E-mail: alexandru.i.sava@umfiasi.ro

[2] Institut de Chimie Organique et Analytique, University of Orleans, CNRS, UMR 7311, Rue de Chartres BP 6759, F-45067 Orléans, France

Introduction

NO-image depicts a ***vagabond molecule*** that can freely cross cell borders and cause cell death, transmit messages between cells and can protect the body from pathogens as a weapon of cellular immunity. Artwork by Péter Dráviczky

➢Inflammation is a ***defense reaction*** and crucial ***physiological response*** for the human body to any kind of aggression.[a, b]

➢NSAID inhibits *arachidonic acid cascade* via *prostaglandin H synthase (COX)*[c] *pathway.*

➢ Long term use increase the incidence of ***side effects***[d] : gastrointestinal, renal, allergic skin reactions, increased risk of acute coronary syndromes, bleeding.

➢The release of NO and inhibition of dual COX/LOX → ***a new therapeutic approach*** in the case of inflammatory diseases[c].

➢Coupling a NO-releasing moiety to a NSAID might deliver NO to the site of NSAID-induced damage and thus decrease gastric toxicity

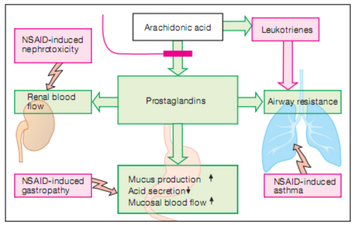

Materials and method

➢Novel heterocyclic compounds that combine two different structural entities (indomethacin and 1,3,4-oxadiazole heterocycle) and that include a NO donor group.

➢The synthesis was preceded by ***molecular docking study*** [(e)]

➢***Preparation of SPACER which contain a nitrate ester group***

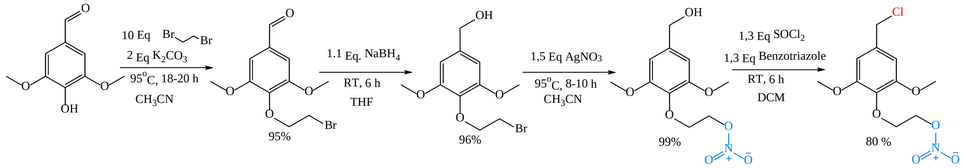

➢ ***Condensation reaction between derivatives with oxadiazole and nitrate ester moiety***

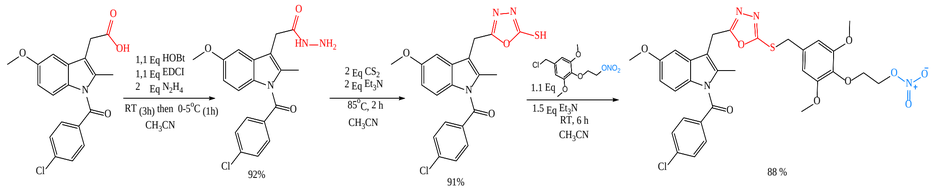

Results and discussions

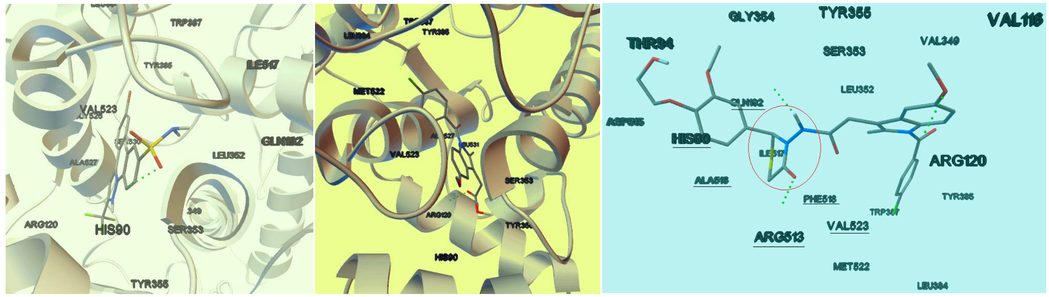

Docking of ***SC-558*** (COX2 selective inhibitor) and ***Indomethacin*** (non selective inhibitor)

Table. **Optimization of cyclisation reaction parameters (6h)**

Entry	Carbon disulfide	Catalyst	Temperature	Conditions	Solvent	Yield
1	1,3 Eq	2,5 Eq KOH	90 °C	18 h	Ethanol	Degradation
2	1,3 Eq	1,3 Eq KOH	100 °C	15 h (Ar atmosphere)	Dioxane	Degradation
3	1,5 Eq	2 Eq Et_3N	120 °C	1 h	DMF	ND
4	1,5 Eq	2 Eq Et_3N	100 °C	2.5 h	Dioxane	ND
5	2 Eq	2 Eq Et_3N	85 °C	2 h	Acetonitrile	91%

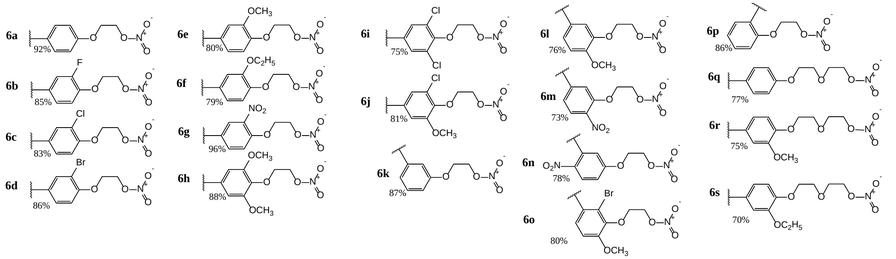

Docking of ***new hybrid molecules***

✓The 1,3,4-oxadiazole moiety interacts with polar side-pocket of COX2 through *hydrogen bonding* with **Arg513** and **Gly354**.

✓The radicals on phenyl moiety can increase the COX selectivity through interaction of ligands with *specific COX2 aminoacids*: **Val523**, **Ala516**, **Phe518**, **Gin192**, **His90.**

Conclusions

➢We described herein the **synthesis** and **molecular docking study** of a **novel indomethacin drug with 1,3,4-oxadiazole moiety.**

➢The most efficient method for synthesis of final products is through use of aldehydes containing NO donor and using 2 Eq of Et_3N for cyclization.

➢The molecular docking studies further help in understanding the various interactions between the ligands and enzyme active site and thereby help to design the novel potent inhibitors.

References

(a) Richard Korbut, Tomasz J. Guzik. Inflammatory mediators and intracellular signalling, Michael J. Parnham Frans P. Nijkamp. [ed.] M.J. Parnham F.P. Nijkamp. *Principles of Immunopharmacology: 3rd revised and extended edition.* III. Switzerland : Springer Basel AG, 2011, A7, pg. 101-126.

(b) Elgazzar, AH. Inflammation. [ed.] Elgazzar Abdelhamid H. *Synopsis of Pathophysiology in Nuclear Medicine.* Switzerland : Springer, 2014, 4, pg. 491-57.

(c) Singh P, Prasher P, Dhillon P, Bhatti R. Indole based peptidomimetics as anti-inflammatory and antihyperalgesic agents: Dual inhibition of 5-LOX and COX-2 enzymes. *European Journal of Medicinal Chemistry.* 2015, Vol. 97, pg. 104-123.

(d) Knights KM, Mangoni AA, Miners JO, Defining the Cox inhibitor selectivity of NSAIDs: implications for understanding toxicity. *Expert Rev Clin Pharmacol.* 2010, Vol 3(6), pg. 769-776.

(e) Forli S, Huey R, Pique ME, Sanner MF, Goodsell DS, Olson AJ. Computational protein-ligand docking and virtual drug screening with AutoDock suite.*Nature Protocols. Vol11(5), 2016.*

Acknowledgment

The scientific research was funded by a grant of the Romanian Ministry of Research and Innovation, UEFISCDI, project number PN-III-3-3.1-AUF-RO-2018-028

The issue of single-value glass transition temperature of polymers as it is determined from DMA

Mariana Cristea[1], Daniela Ionita[1], Doina Dimonie[2]

[1]"Petru Poni" Institute of Macromolecular Chemistry, Iasi, Romania

[2]National Institute of Research & Development in Chemistry and Petrochemistry-ICECHIM, Bucharest, Romania

Introduction

Dynamic mechanical analysis (DMA) determines the relaxations in polymers. Usually, α-relaxation is associated with the glass transition.

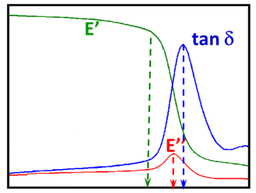

The difference in the glass transition temperature (T_g) that in noticed when using the same/different technique is brought about by the difference in the definition of the T_g (for example the comparison DSC/DMA or the figure above).

Then, in the case of polymers, the glass transition is not a single temperature, but an interval. Given the fact that for the determination of T_g is used a scanning-temperature experiment, glass transition overlapping phenomena are possible that influence the value of T_g.

The paper will exemplify three situation of comple glass transition region for polyimide, poly(lactic acic based copolymers and polyurethane.

Materials and method

Perkin Elmer DMA

Heating rate: 2 °C/min

Frequency: 1 Hz

Deformation mode: tension, bending

Figure 6

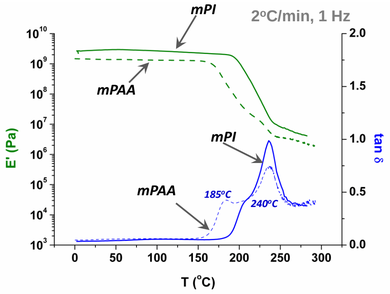

Figure 1

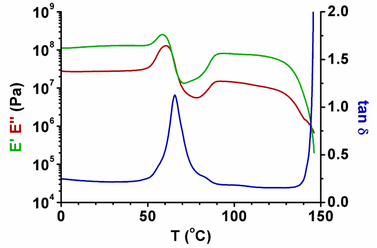

Figure 3

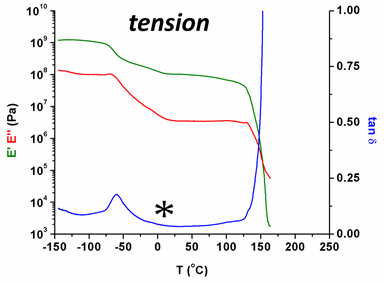

Results and discussions

Poly(amic acid) - Polyimide

When measuring the glass transition temperature of a poly(amic acid), its thermal history is changed during the DMA experiment.

T_g (starting material - mPAA) = 185 °C

T_g (polyimide formed during the experiment) = 240 °C

Rather than determining a precise glass transition temperature, DMA makes visible ***the imidization reaction*** (Figure 1).

When the heating rate is too high, there is no time for reaction and the chains starts to slip past each other due to intense coordinated movements of chains (Figure 2).

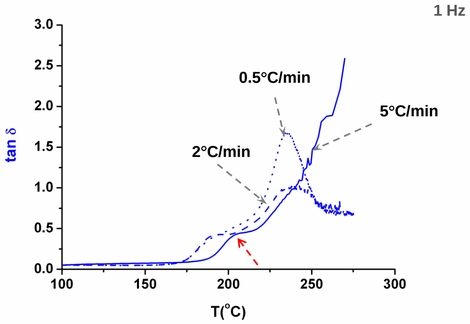

Figure 2

PLGA copolymers

An obvious ***increase of storage modulus (E')*** at the beginning of the glass transition is associated with the enthapic relaxation(Figure 3) – mostly known from DSC (Figure 4), that originates in the tension in the fibers during the melt-electro-spinning process. This relaxation determines a considerable ***shrinking*** of the sample (Figure 5).

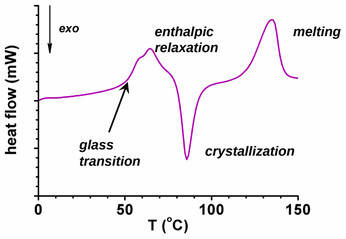

Figure 4

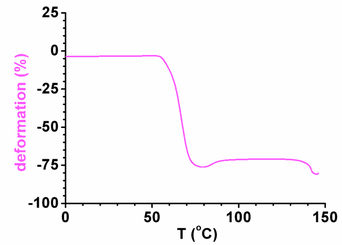

Figure 5

Polyurethane

A frequency independent shoulder (* in Figure 6) is associated with melting (confirmed by DSC). This melting confers some mobility to chains and promotes **stress-induced orientation** which is possible during the experiment performed in *tension* (Figure 6). This orientation confers stability to the sample. In *bending* the same melting makes the sample to lose its load-bearing properties (Figure 7).

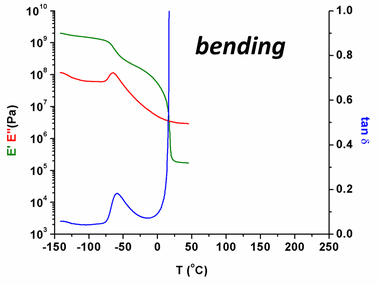

Figure 7

Conclusions

Often a simple temperature value reported as the glass transition temperature does not reflect the array of phenomena that occur in the region of the glass transition: curing, enthalpic relaxation, shrinking, orientation. Any of these phenomena modifies the value of the glass transition temperature.

Contact

mcristea@icmpp.ro

Acknowledgment

This work was supported by a grant of the Romanian Ministry of Research and Innovation, PCCDI-UEFISCDI, project number PN-III-P1.2-PCCDI-2017-0428/PCCDI/2018, contract no. 40PCCDI, within PNCDI III.

Design of functionalized hybrid PLGA-vegetable oils nanoparticles for targeted delivery of lipophilic drugs

Ghitman, Jana[1], Stan, Raluca [2], Iovu, Horia [1,3]

[1] University Politehnica of Bucharest, Advanced Polymer Materials Group, Romania
[2] University Politehnica of Bucharest, Faculty of Applied Chemistry and Material Science, Romania
[3] Academy of Romanian Scientists, Bucharest, Romania
*jana.ghitman@upb.ro

Introduction

The aim of the current research study is to *design hybrid nanoparticles based on PLGA - vegetable oils with functionalized surface,* as nanocarriers for targeted high lipophilic drug delivery and controlled release.

Poly (D,L-lactide-co-glycolide) and Nigella sativa vegetable oil (NSO) were used to engineer hybrid polymeric-vegetable oils formulations (HPON) by emulsion solvent evaporation method. Indomethacin (IMC) COX-1, COX-2 AINS therapeutic agent was used as lipophilic drugs references. Polyethylene glycol (PEG) and mannose (Mn) were selected as targeted agents and were used for the surface functionalization of hybrid formulations.

Materials and method

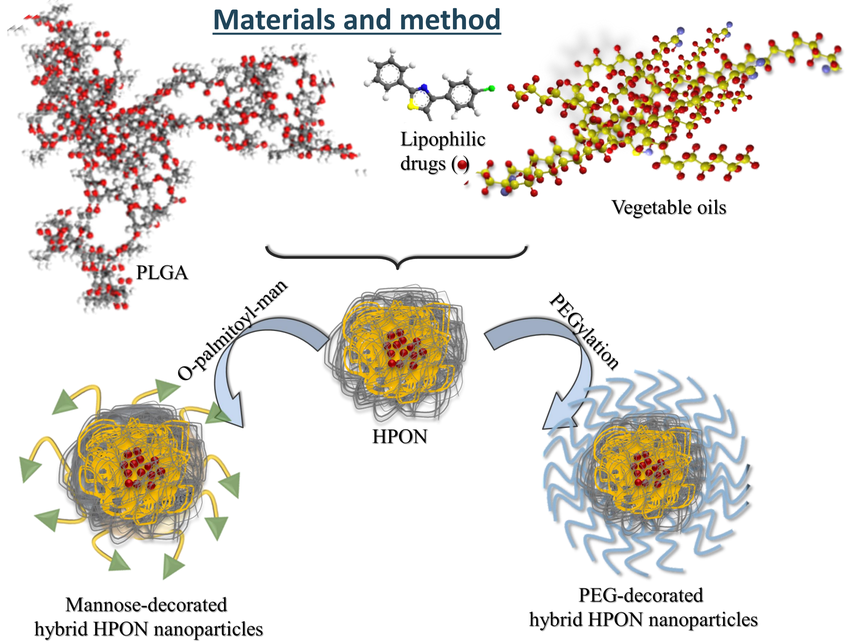

Scheme 1. Hybridization concept of PLGA nanoparticles with vegetable oils in designing the optimal hybrid nanocarriers for lipophilic drugs; surface functionalization of HPON with PEG (in the post-production step) and Mn (during the formulation) for targeted drug delivery

Results and discussions

Table 1. Hydrodynamic characteristics of engineered formulations

No.	System	Particle size (nm)	PdI	ζ (mV)
1	PLGA-IMC	145.8 ± 0.7	0.21 ± 0.02	-12.8 ± 1.9
2	HPON-IMC	147.8 ± 1.3	0.09 ± 0.01	-15.0 ± 2.7
3	PLGA-IMC-Peg	275.8 ± 2.7	0.23 ± 0.03	-10.1 ± 0.2
4	PLGA-IMC-Mn	175.6 ±3.9	0.15 ±0.04	-10.3 ± 1.3
5	HPON-IMC-Peg	179.0 ± 2.5	0.18 ± 0.04	-14.0 ± 0.8
6	HPON-IMC-Mn	221.9 ± 0.2	0.27 ± 0.01	-13.4 ± 0.4

Morphological characteristics

The core-shell structure of hybrid formulations are depicted in TEM images as two different compartments: the oil core (dark color) surrounded by the uniform polymeric shell (bright color).

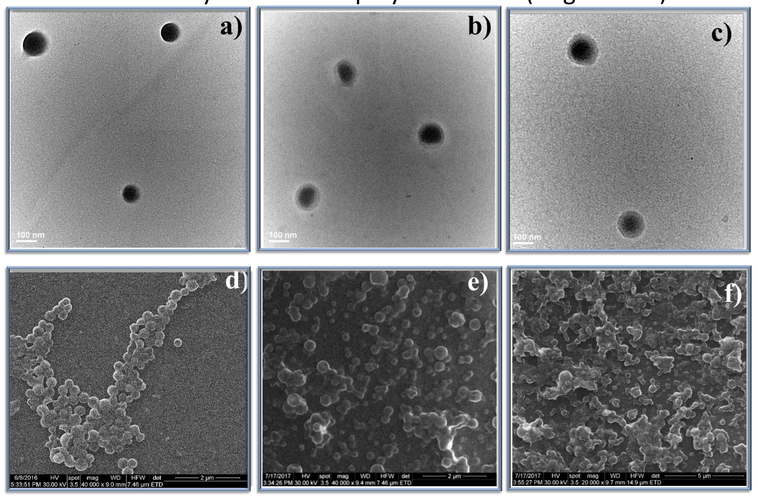

Fig. 2. TEM micrographs of a) – PLGA-NP; b) - HPON and c) – NPON-IMC, respectively SEM images of d) - PLGA-NP; e) – NPON-PEG and f) – NPON-IMC-PEG

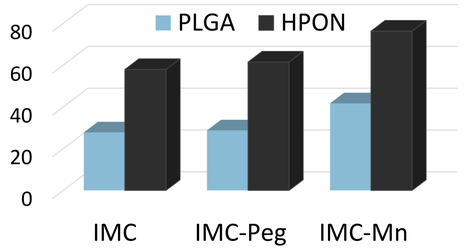

Fig. 1. Encapsulation efficiency of IMC into simple or surface modified standard/hybrid PLGA- vegetable oil nanoparticles

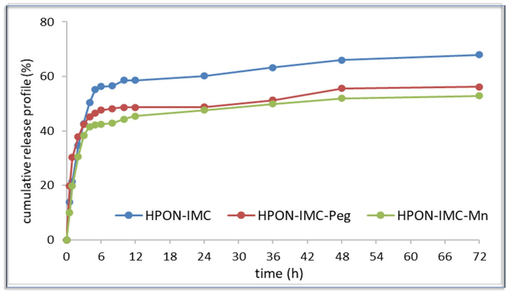

Fig. 3. The in vitro release profile of IMC from PLGA-Np with standard or modified surface with PEG or MN

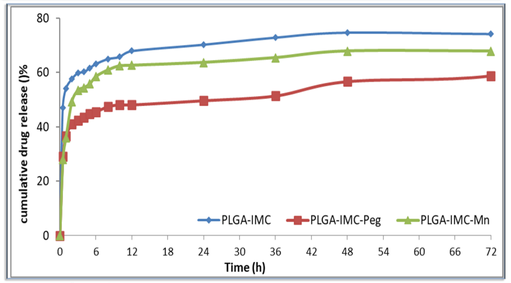

Fig. 4. The in vitro release profile of IMC from hybrid HPON formulation with standard or modified surface with PEG or MN

Conclusions

- New polymer-vegetable oils hybrid nanoparticles as drug delivery devices for high lipophilic drugs were engineered .
- The oil incorporation within the polymeric matrix led to a more amorphous nanostructure which enhanced the drugs loading capacity.

Acknowledgment

The work has been funded by the Operational Programme Human Capital of the Ministry of European Funds through the Financial Agreement 51668/09.07.2019, SMIS code 124705.

Green synthesis of metallic nanoparticles from *Helichrysum arenarium*: kinetics, antioxidant activity and catalytic degradation of azoic dyes

A. A. Sorescu[1,2], A. Nuta[1,3], I. R. Suica – Bunghez[1], V. Raditoiu[1], R. M. Ion[1,2]

[1]The National Research&Development Institute for Chemistry and Petrochemistry ; [2]Valahia University of Targoviste; [3]The Romanian Academy "Stefan S. Nicolau" Institute of Virology

Introduction

Metallic nanoparticles, because of their high surface area, are versatile and can be tailored with a multitude of different molecules that give them good antibacterial, magnetic or catalytic properties. Metallic nanoparticles can be synthesized by applying conventional methods, using two approaches: "top down" or "bottom up" processes. Viable and feasible alternatives are environmentally – friendly methods that use microorganisms, fungi, enzymes or plants and, among them, aqueous plant extract mediated biosynthesis of silver (AgNPs) and gold (AuNPs) nanoparticles are intensively studied since silver and gold are two noble metals widely known for their strong antibacterial properties.

This paper presents the green synthesis of silver (AgNPs), gold (AuNPs) and iron oxide (FeONPs) nanoparticles from Dwarf everlast (*Helichrysum arenarium*), a plant packed with vitamins and nutrients that, among other pharmacological benefits, regenerates the lives, helps in lowering the cholesterol levels, etc. The green synthesis of the three metallic nanoparticles was carried out using two different temperature conditions: room temperature, no stirring, no heating and at 50^{0}C under a constant stirring of 600 rpm for 30 minutes. Also, the potential capacity of AgNPs and FeONPs to catalytic degrade azoic dyes (e.g.: Direct Orange 26, Direct Brown 2, Direct Black 38) was spectroscopically investigated.

Materials and methods

The green synthesis of the three metallic nanoparticles was carried out using two different temperature conditions: room temperature, no stirring, no heating and at 50^{0}C under a constant stirring of 600 rpm for 30 minutes. The as-prepared green metallic nanoparticles were characterized using UV-Vis and FTIR recordings and dynamic light scattering determinations were used to determine the size of the metallic nanoparticles. The UV – Vis spectra were recorded at different time intervals (0 s, 30 min, 60 min, 90 min and 24 h) in order to evaluate the time-dependent evolution and stability of the green synthesized metallic nanoparticles. The antioxidant activity of AgNPs and AuNPs was recorded using DPPH (2,2 – diphenyl – 1 – picryl – hydrazyl – hydrate) assay.

Results and discussions

- *Quantitative determination of phytochemicals*

Quantitative analyses	Aqueous extract of Dwarf everlast (*Helichrysum arenarium*)
Total content of tannins (TCT)	150,86 mg/L
Total content of flavonoids (TCF)	510,23 mg/L
Total content of polyphenols (TCP)	98,55 mg/L
Total content of terpenoids (TCTp)	102,69 mg/L

- *Kinetics of the green synthesized AgNPs* (Figure 1)

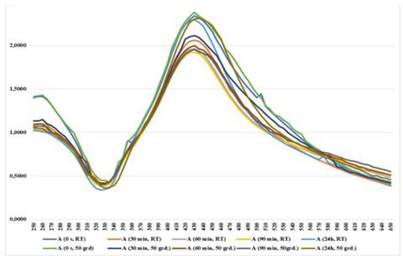

Due to the polydispersity of the Dwarf everlast (*Helichrysum arenarium*) – AgNPs, Figure 1 describes the broad range of the absorption peaks, showing a maximum at 435 nm for room temperature (RT) Dwarf everlast (*Helichrysum arenarium*) – based AgNPs and at 437 for 50^0 C Dwarf everlast (*Helichrysum arenarium*) – based AgNPs respectively.

Aqueous extract	Absorption (nm) AuNPs - RT	Absorption (nm) AuNPs 50^0 C	Absorption (nm) FeONPs
Dwarf everlast (*Helichrysum arenarium*)	540	535	330

- *Antioxidant activity of AgNPs and AuNPs*

$$AA\ \% = [(A_{Control} - A_{sample}) / A_{Control}] \times 100,$$

where: $A_{Control}$ is the absorbance of the blank DPPH solution and A_{Sample} is the absorbance of the aqueous extracts mixed with 0,02 mg/mL DPPH solution.

Aqueous extract	AA of aq. extr.	AA AgNPs - RT	AA AgNPs – 50^0 C	AA AuNPs - RT	AA AuNPs – 50^0 C
Dwarf everlast (*Helichrysum arenarium*)	78,690	86,522	85,956	80,670	81,555

- *DLS and zeta potential*: DLS recordings were used to determine the size distribution profile of the green synthesized AgNPs and AuNPs and the Zeta potential was also measured to analyze the stability of the colloidal suspensions

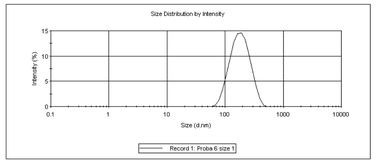

DLS spectrum for the green synthesized AgNPs

Sample	Dm (d.nm)	P_1...i (d.nm)	PdI	PZ (mV)
Dwarf everlast (Helichrysum arenarium) – AgNPs RT	135	P_1 = 178	0.170	-19
Dwarf everlast (Helichrysum arenarium) – AgNPs 50^{0}C	128	P_1 = 175	0.168	-20

- *Catalytic degradation of azoic dyes*

Dye	UV – Vis absorption (nm)
Direct Orange 26 (DO 26)	495
Direct Brown 2 (DBr 2)	470
Direct Black 38 (DBk 38)	520

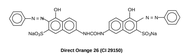
Direct Orange 26 (CI 29150)

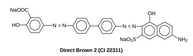
Direct Brown 2 (CI 22311)

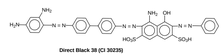
Direct Black 38 (CI 30235)

Sample	Reaction time					
	0 min	15 min	30 min	1 h	24 h	Δ A (%)
DO 26 (sol 50 mg/L)	1.786	-	-	-	-	-
DO26 + AgNPs-S (RT)	1.500	1.458	1.392	1.347	1.280	28.33
DO26 + AgNPs-S (50^0 C)	1.498	1.450	1.390	1.339	1.269	28.95
DO26 + AgNPs-S + RA (RT)	1.187	1.188	1.124	1.072	0.964	46.02
DO26 + AgNPs-S + RA (50^0 C)	1.177	1.159	1.119	1.002	0.988	44.68

Conclusions

- This paper presents the green synthesis of silver (AgNPs), gold (AuNPs) and iron oxide (FeONPs) nanoparticles from Dwarf everlast (*Helichrysum arenarium*).
- The green synthesis of the three metallic nanoparticles was carried out using two different temperature conditions: room temperature, no stirring, no heating and at 50^{0}C under a constant stirring of 600 rpm for 30 minutes.
- The phytosynthesized AgNPs were further used to study the catalytic degradation of three azoic dyes: **Direct Orange 26 (DO 26)**, **Direct Brown 2 (DBr 2)** and **Direct Black 38 (DBk 38)** using the following protocol: 3 mL aqueous solution (50 mg/L) of azo – dye were mixed with 0.2 mL solution reductive agent (RA) and 0.2 mL of green - synthesized AgNPs.

Acknowledgment

This research paper was prepared with the financial support of the Project PN 19.23.03.01.07.

Development of textile materials with antimicrobial activity using Ag/chitosan and ZnO/polyvinyl alcohol nanoparticles and gamma irradiation

O. Căpraru[1], M. Constantin[1], L. Chirilă[2], O. Cinteză[3], I. Stănculescu[1,3]

[1]*Horia Hulubei National Institute for Physics and Nuclear Engineering, IRASM Dept., 30 Reactorului Str, 077125 Magurele, Ilfov Romania*
[2]*National Research & Development Institute for Textile and Leather, 16 Lucretiu Patrascanu Str., 030508, Bucharest, Romania*
[3]*University of Bucharest Dept. of Physical Chemistry, Regina Elisabeta Bld 4-12, 030018 Bucharest Romania, istanculescu@nipne.ro*

Introduction

Advancements in the production and development of new textile technologies are continuous because of their varied uses from clothing to medical, to industrial applications.
By combining different methods and nanoparticles it's hoped to achieve advanced properties materials and with this scope gamma irradiation has been employed being previously used as a green textile functionalization technology. Several studies demonstrated positive result of using gamma irradiation on textile dyeing and antimicrobial functionalization.
Cotton is a natural fiber which has the highest concentration of cellulose. The chemical structure of the cellulose polymer can be observed in Fig 1. In Fig 2 is shown the chemical structure for Chitosan.

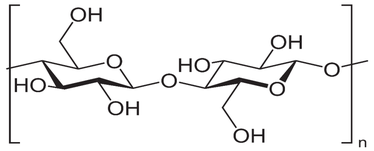

Fig 1: Chemical structure for cellulose

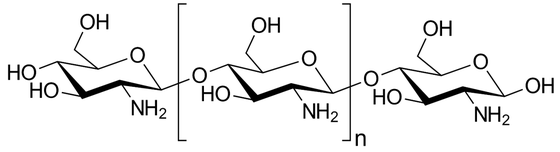

Fig 2: Chemical Structure for Chitosan

Materials and method

In this work cotton textiles were impregnated with Ag/chitosan and ZnO nanoparticles (NP) applied with three different processes. Acrylic acid (AA) was used as binder The processes are separated in padding (**N**), padding-gamma irradiation (**5 kGy**) and padding-drying for 2 min at 100 C-condensation for 3 min at 150 C (**C**). The irradiation was done with a ^{60}Co source at a dose of 1 kGy/hour. The methods used for characterization: FT-IR analysis with a Bruker Vertex 70 spectrometer with 256 scans, resolution 4 cm^{-1} ATR technique with diamond crystal and TG/DSC in the 25-600 C range using Netzsch STA 409 PC Luxx Simultaneous thermal analyzer revealed the modification of the textile materials. Microbiological test have been done by disc diffusion test against Staphylococcus aureus and Pseudomonas aeruginosa.

Results and discussion

The main changes in the ZnO NP treated textiles spectra presented in Fig 3 are the decrease in intensity of the 1545 cm^{-1} peak found in the control sample and a small peak shift in position and intensity at 1004 cm^{-1}. More changes are observed in the Ag/chitosan treated textiles Fig. 4, the chitosan presence is observed at 1577 cm^{-1} only for the C and N samples along with an different band for the N sample at 839 cm^{-1}.

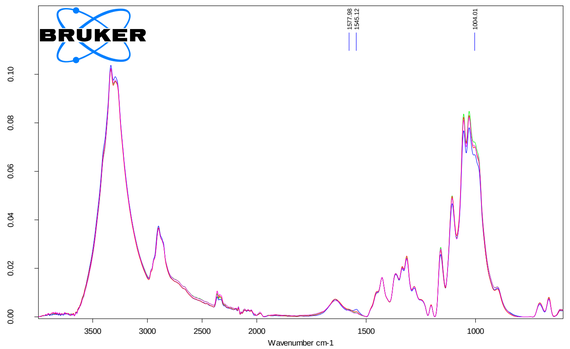

Fig. 3: FTIR-ATR for cotton with ZnO/AA control (blue), padded (red), padded-condensed (pink), padded-irradiated (green)

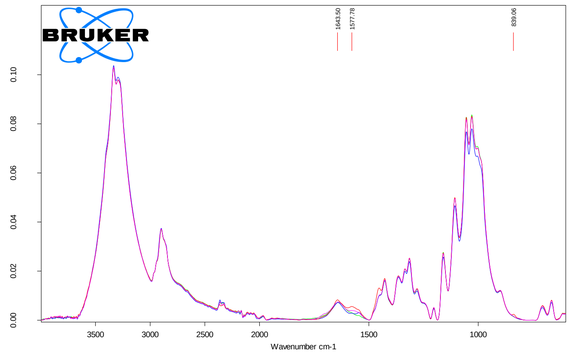

Fig. 4: FTIR-ATR for cotton with Ag/Chitosan control(blue), padded (red), padded-condensed (pink), padded-irradiated (green)

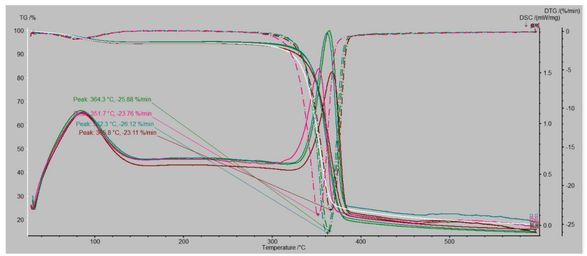

Fig 5: TG/DSC for cotton with ZnO/AA control (green), padded (pink), padded-condensed (red), padded-irradiated (blue)

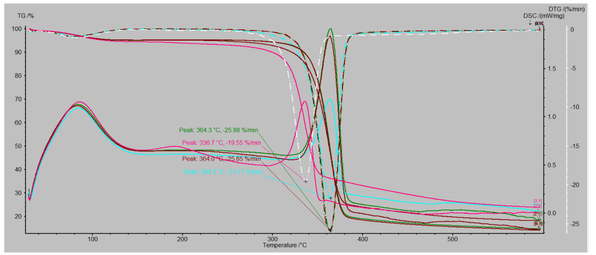

Fig. 6: TG/DSC for cotton with Ag/Chitosan control (green), padded (pink), padded-condensed (blue), padded-irradiated (red)

In Fig 5 and 6 are the TG/DSC for ZnO and Ag/chitosan np textile samples. The curves for both samples are similar with the control and C curves being almost identical, DSC peaks coincide with the DTG peaks, the N sample has the lowest thermal stability.
Two samples produces inhibition zones only against Staphylococcus aureus the N and C samples with the Ag/chitosan nanoparticle. In Fig 8. the N sample has a quite large area while the C sample barely has an inhibition zone.

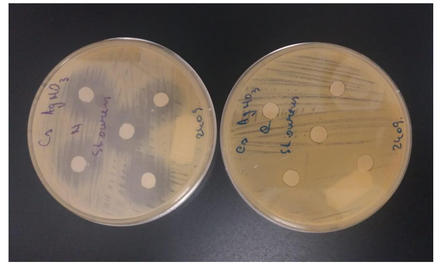

Fig .7 Antimicrobial tests result for the N and C Ag/chitosan NP treated samples

Conclusions

Antimicrobial activity has been obtained only for some samples probably due to the fact that in the irradiated specimens a polymer film has been formed blocking the NP activity. Differences in the TG/DSC curves are produced by the treatments. The FTIR spectra of Ag/chitosan textile samples show the presence of chitosan.

References

1] Chirila L., Popescu A., Cutrubinis M., Stanculescu I. and Moise V. (2018). The influence of gamma irradiation on natural dyeing properties of cotton and flax fabrics. Radiation Physics and Chemistry, 145, 97-103.

[2] Chirila L., Popescu A., Stanculescu I., Cutrubinis M., Cerempei A. and Sandu I. (2016). Gamma Irradiation Effects on natural dyeing performances of wool fabrics. Revista de Chimie. 67, 2628-2633

[3] El-Naggar, A. M., Zohdy, M. H., Hassan, M. S. and Khalil, E. M. (2003). Antimicrobial protection of cotton and cotton/polyester fabrics by radiation and thermal treatments. I. Effect of ZnO formulation on the mechanical and dyeing properties. J. Appl. Polym. Sci., 88: 1129-1137. doi:10.1002/app.11722

[4] Minglei Wang, Maojiang Zhang, Lijuan Pang, Chenguang Yang, Yumei Zhang, Jiangtao Hu, Guozhong Wu, Fabrication of highly durable polysiloxane-zinc oxide (ZnO) coated polyethylene terephthalate (PET) fabric with improved ultraviolet resistance, hydrophobicity, and thermal resistance, Journal of Colloid and Interface Science, Volume 537, 2019, Pages 91-100, ISSN 0021-9797, https://doi.org/10.1016/j.jcis.2018.10.105.

[5] Haytham M.M. Ibrahim, Mahmoud S. Hassan, Characterization and antimicrobial properties of cotton fabric loaded with green synthesized silver nanoparticles, Carbohydrate Polymers, Volume 151, 2016, Pages 841-850, ISSN 0144-8617, https://doi.org/10.1016/j.carbpol.2016.05.041

[6] Tan, Ann & Khoo, Li & Alias, Siti & Mohamad, Ahmad Azmin. (2012). ZnO nanoparticles and poly (acrylic) acid-based polymer gel electrolyte for photo electrochemical cell. Journal of Sol-Gel Science and Technology. 64. 184-192. 10.1007/s10971-012-2846-z.

Acknowledgment

Acknowledgement: Funding through UEFISCDI project PHYSforTeL contr. 44 PCCDI/2018 is gratefully recognized.

Host guest complexes of polychlorinated dibenzo-p-dioxins with cyclodextrins

M. Ghețu[1] , O. Căpraru[2] , I. Stșnculescu[1,2]

1-University of Bucharest, Dept. of Physical Chemistry, Bucharest Romania

2 "Horia Hulubei" National Institute for Physics and Nuclear Engineering, IRASM, Măgurele, Romania

Introduction

Polychlorinated dibenzo-p-dioxins (PCDD) are persistent organic pollutants that induce toxicity in both wildlife and humans (White, SS, 2009). The cyclodextrins (CD) are complexing agents. Inclusion complexes are formed based on the "guest – host" interaction, where the CD's cavity acts as host for a molecule. The outer sphere of CD is hydrophilic, while its cavity is hydrophobic. This means that the cavity can act as a host for compounds with poor solubility in polar solvents (Saokham P, 2018).

Materials and method

In this study we analyzed the molecular interactions between tetrachlorinated dibenzo-p-dioxin (TCDD), pentachlorinated dibenzo-p-dioxin (PCDD), hexachlorinated dibenzo-p-dioxin (H_6CDD), heptachlorinated dibenzo-p-dioxin (H_7CDD), and octachlorinated dibenzo-p-dioxin (OCDD) and β-cyclodextrin and γ-cyclodextrin (Fig. 1), taking into account the different starting geometries with the aim to estimate their adsorbent potential in environmental remediation. The simulation of interaction between the seven PCDD compounds and the two CDs was conducted using the molecular mechanics (MM+), and optimized potential for liquid simulations (OPLS) force fields, both included in the Hyperchem program (Mindrila G, et al 2012). The starting geometry of CDs was obtained from the Protein Data Bank using the X-ray structures 1VFO (β-CD) and 1D3C (γ-CD) (http://www.rcsb.org/pdb/home/home.do).

Results and discussions

The complexation and the binding (see Table 1-4) energy, and their components were calculated for all of the 40 inclusion complexes. Both MM+ and OPLS calculus resulted in close values for the complexation and binding energies. It was observed an interaction difference between the inclusion complexes formed with β-CD, and those formed with γ-CD that may be attributed to the higher flexibility of the γ-CD, which may provide a better inclusion of the PCDDs molecules.

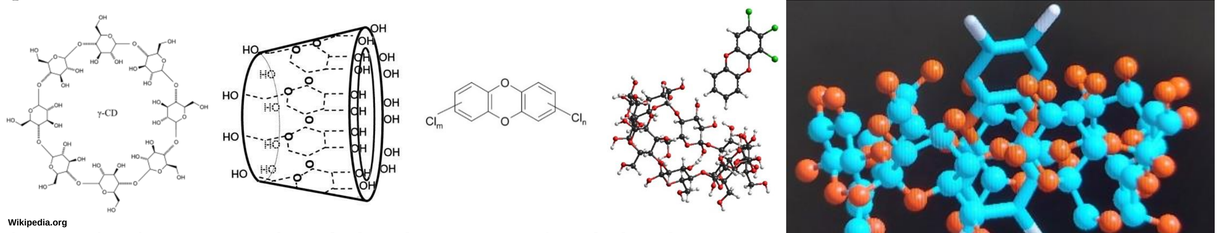

Fig. 1. Molecular structure of: **cyclodextrin**, **PCDD** and **cyclodextrin:PCDD**

Tables 1-4. Binding energy of: **cyclodextrin-PCDD** complexes

BETA	2378TCDD-bCD	PCDD12378-b-CD (TriS)	PCDD12378-b-CD (DiS)	H6CDD123478-b-CD (TetraS)	H6CDD123478 b-CD (DiS)
Et	-24,70747	-21,535577	-21,535577	-18,365538	-23,494935
Eb	-0,076118	-0,073449	-0,044139	0,259934	-0,00239
Ea	-1,19494	-1,11182	0,33638	3,50227	-1,70348
Ed	0,01349	1,2106	1,04532	-3,3685	2,6776
EvdW	-24,26356	-25,89399	-24,0827	-19,8796	-24,3668
Esb	-0,1889731	-0,1114439	-0,0026839	0,1220971	-0,0930476
Eelec	1,00273	0,15433	1,21223	0,9982	-0,0068

GAMA	2378TCDD-bCD	PCDD12378-b-CD (TriS)	PCDD12378-b-CD (DiS)	H6CDD123478-b-CD (TetraS)	H6CDD123478 b-CD (DiS)
Et	-21,434105	-22,05601	-22,05601	-23,559093	-25,729916
Eb	-0,201888	-0,216509	-0,256259	-0,20961	-0,18498
Ea	0,66856	1,33298	1,08998	1,10692	0,08792
Ed	1,79494	2,17195	3,37284	1,91178	0,78837
EvdW	-23,82364	-23,2835	-25,7501	-23,8861	-25,0035
Esb	-0,0584531	-0,0427839	-0,0566239	-0,0181876	-0,0382376
Eelec	0,18633	-0,37357	-0,45577	-2,4639	-1,37944

BETA	H6CDD123678-b-CD (TriS)	H6CDD123789-b-CD (TriS)	H7CDD1234678-b-CD (TetraS)	H7CDD1234678-b-CD(TriS)	OCDD12346789-b-CD (TetraS)
Et	-20,951737	-18,379581	-19,561074	-23,637642	-20,173512
Eb	-0,121056	-0,107993	-0,15266	-0,06695	-2,23809
Ea	0,03187	0,85634	0,84471	0,15441	-57,21272
Ed	1,52473	-0,10767	0,16488	1,48862	-17,0492
EvdW	-23,1004	-19,5987	-20,3784	-26,1297	-23,6294
Esb	-0,1110129	-0,0408652	0,0042636	0,0182536	-1,75068538
Eelec	0,8241	0,6193	-0,04394	0,89765	27,0449

GAMA	H6CDD123678-b-CD (TriS)	H6CDD123789-b-CD (TriS)	H7CDD1234678-b-CD (TetraS)	H7CDD1234678-b-CD(TriS)	OCDD12346789-b-CD (TetraS)
Et	-22,913793	-20,514265	-25,240648	-20,472318	-25,674462
Eb	-0,060136	-0,106733	-0,23258	-0,19976	-0,0643
Ea	3,28267	2,76404	1,59541	-0,69249	1,62261
Ed	-2,5329	-1,86	2,1	1,192	-0,3217
EvdW	-23,4249	-21,3249	-24,5376	-19,4461	-24,0208
Esb	-0,0148429	-0,0185052	-0,0524664	-0,0678064	0,1057936
Eelec	-0,16362	0,03181	-4,11339	-1,2582	0,51844

It was observed an interaction difference between the inclusion complexes formed with β-CD, and those formed with γ-CD that may be attributed to the higher flexibility of the γ-CD, which may provide a better inclusion of the PCDDs molecules.

Conclusions

Taking into account the interaction energy results that γ-CD is more efficient in the interaction with dioxins. γ-CD has a larger cavity and is more flexible, being a better complexant.

The term VdW has the greatest contribution to the realization of the inclusion complex. The number of Cl atoms and the substitution pattern directly influence the interaction CD:PCDD.

This study showed from molecular modelling calculations that PCDD pollutants interact with CDs forming inclusion complexes PCDD:CD and thus cyclodextrins may be used in environmental applications.

References

White SS, Birnbaum LS. J Environ Sci Health C Environ Carcinog Ecotoxicol Rev. 27, 197 (2009).

Saokham P, Muankaew C, Jansook P, Loftsson T. Molecules. 23, 1161. (2018)

Mindrila, G., Mandravel, C., Dobrica, I., Bugheanu, P., Stanculescu. I., R., J Incl Phenom Macrocycl Chem 74, 137 (2012)

Acknowledgment

Funding through UEFISCDI project PHYSforTeL contr. 44 PCCDI /2018 is gratefully recognized.

Aspects encountered in TGA analysis of polymers performed under different heating schedules

Daniela Ionita, Mariana Cristea, Vlad Hurduc

"Petru Poni" Institute of Macromolecular Chemistry, Grigore Ghica Voda Alley 700487, Iasi, Romania

01

PLA/PBAT – STANDARD EXPERIMENT

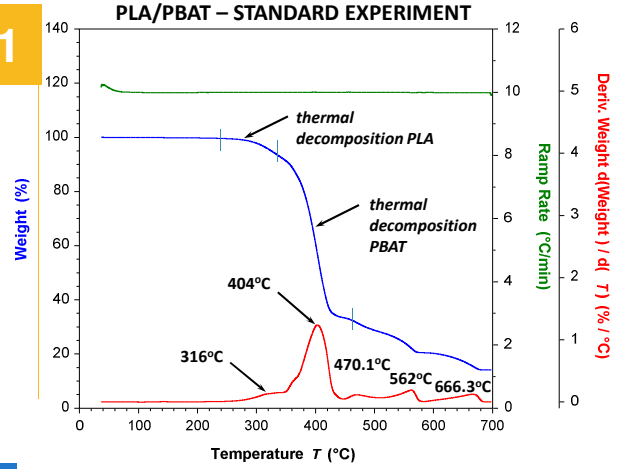

02

Results and discussions

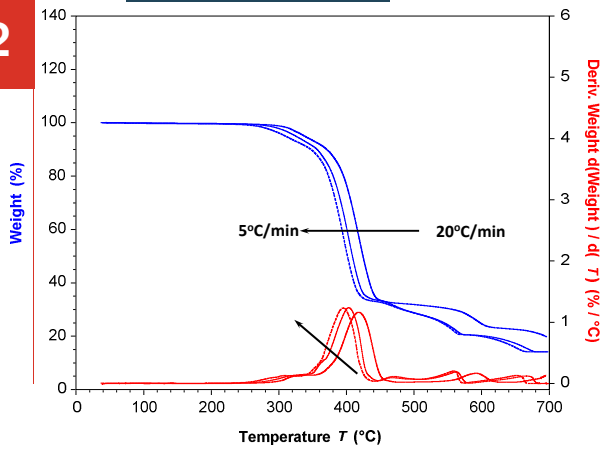

03

PLA/PBAT – Hi–RES EXPERIMENT

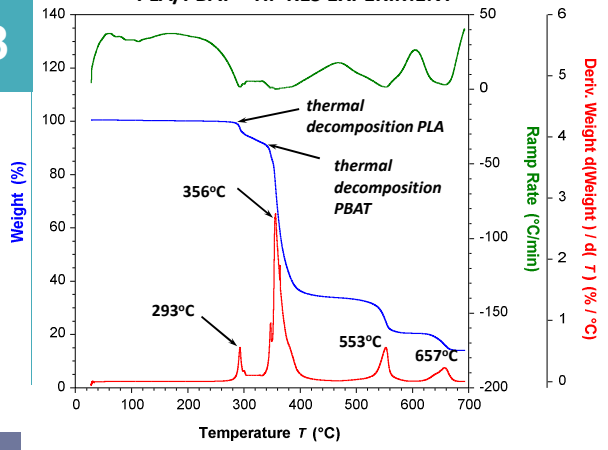

04

PLA/PBAT BioC– STANDARD EXPERIMENT

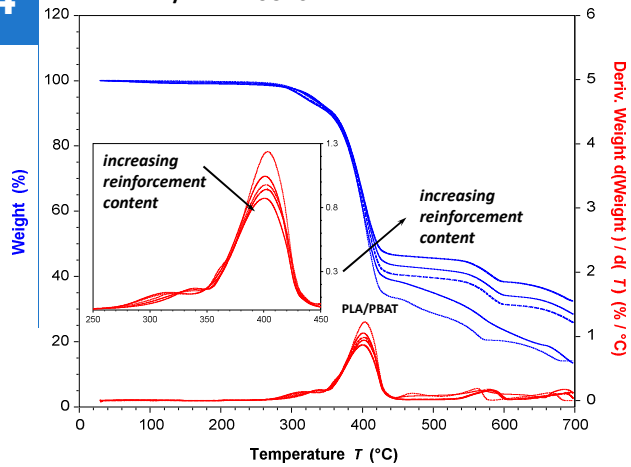

Materials and method

Toughened blend for 3D printing applications reinforced PLA/PBAT (from 10% to 30%)

PLA - poly(lactic acid)

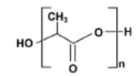

PBAT - poly(butylene adipate-*co*-terephthalate)

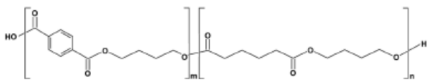

Standard *vs.* Hi Res TGA

05

PLA/PBAT BioC – Hi–RES EXPERIMENT

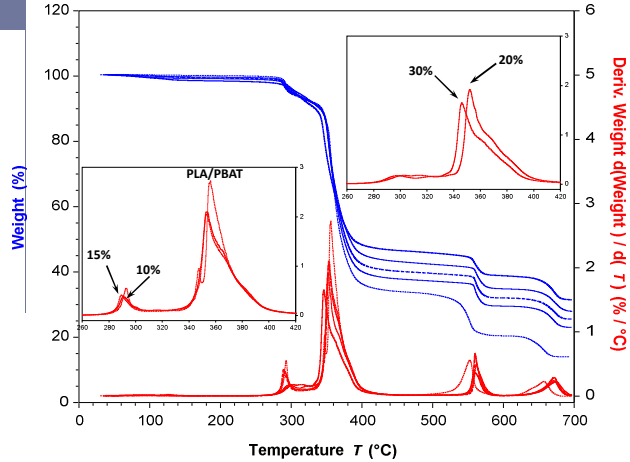

UV protective abilities of cotton fabrics pre-treated with plasma at atmospheric pressure and coated with TiO_2-SiO_2 and TiO_2-SiO_2/reduced graphene oxide composites

M. C. Rosu[1], C. Tudoran[1], M. Coros[1], C. Socaci[1], D. V. Cosma[1], A. Urda[1], L. Chirila[2]

[1]National Institute for Research and Development of Isotopic and Molecular Technologies, 67-103 Donat Street, 400293, Cluj-Napoca, Romania; E-mail: marcela.rosu@itim-cj.ro

[2] National Research & Development Institute for Textiles and Leather, 16 Lucretiu Patrascanu Street, 030508, sector 3, Bucharest, Romania

INCDTIM

Introduction

Textile materials with UV protection are attractive for manufacturing by high value-added products. The aim of this study was to evaluate the UV protection properties of cotton fabrics pre-treated with plasma at atmospheric pressure and coated with TiO_2-SiO_2 and TiO_2-SiO_2/reduced graphene oxide (GR) composites. The UV protection properties of obtained cotton fabrics were investigated by measuring UV transmission in the UVA region (315-400 nm) and the UVB region (280-315 nm). Based on the recorded data, Ultraviolet Protection Factor (UPF) was calculated using the equation that is listed below.

$$UPF = \frac{\sum_{\lambda=280}^{400} E\lambda \times S\lambda \times \Delta\lambda}{\sum_{\lambda=280}^{400} E\lambda \times S\lambda \times T\lambda \times \Delta\lambda}$$

Eλ is the relative erythemal spectral effectiveness
Sλ is the solar spectral irradiance
Tλ is the average spectral transmission of the sample
Δλ is the measured wavelength interval (nm)

Materials and method

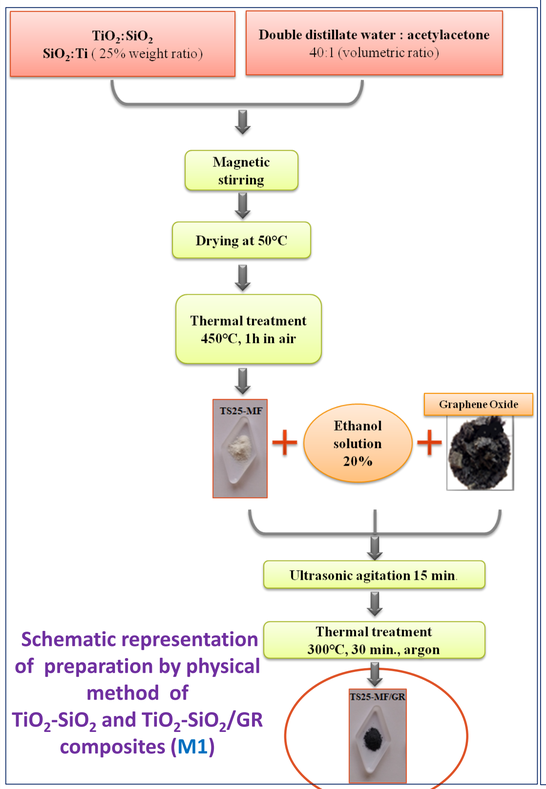

Schematic representation of preparation by physical method of TiO_2-SiO_2 and TiO_2-SiO_2/GR composites (M1)

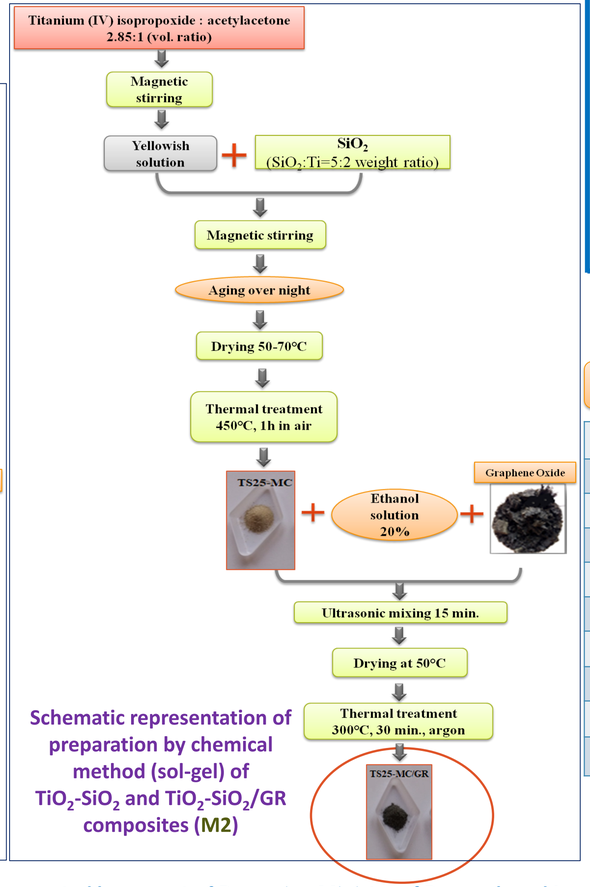

Schematic representation of preparation by chemical method (sol-gel) of TiO_2-SiO_2 and TiO_2-SiO_2/GR composites (M2)

Schematic representation of laboratory procedure to obtain cotton fabrics pre-treated with cold plasma and coated with photocatalytic nanopowders

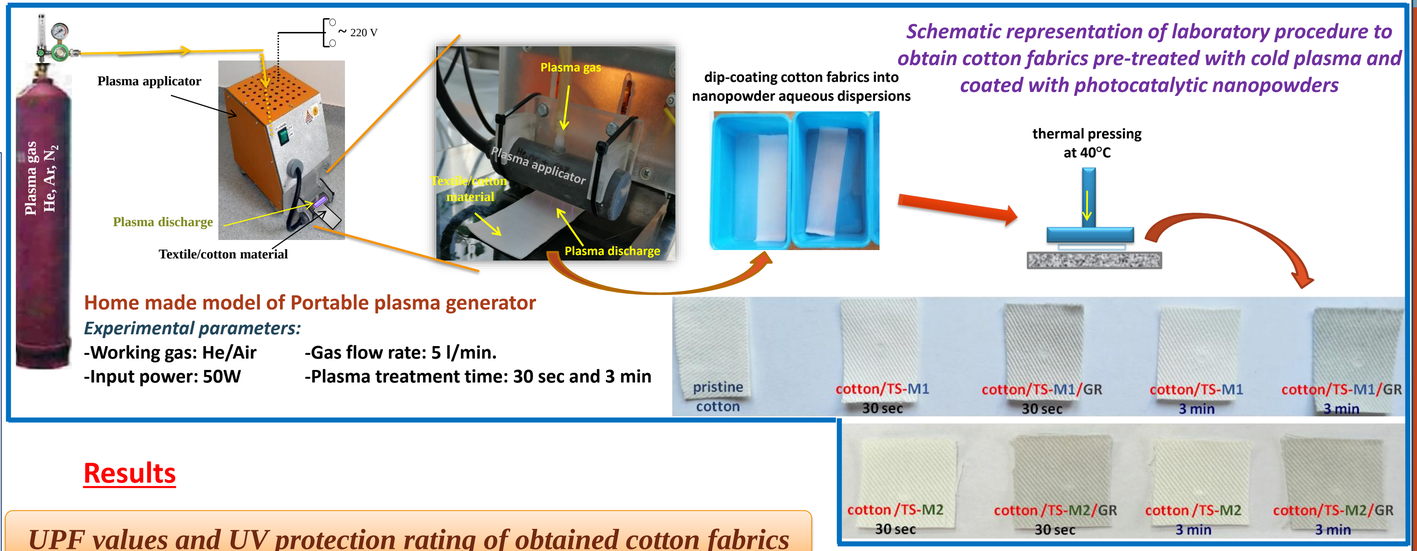

Home made model of Portable plasma generator

Experimental parameters:

-Working gas: He/Air -Gas flow rate: 5 l/min.
-Input power: 50W -Plasma treatment time: 30 sec and 3 min

Results

UPF values and UV protection rating of obtained cotton fabrics

Sample	UVA	UVB	UPF value	UPF range	UPF protection rating
pristine cotton	17.23	7.59	9.4	< 10	non-ratable
cotton/TS-M1 30 sec	5.88	0.92	64.75	50+	excellent
cotton /TS-M1 3 min	6.34	1,08	56.82	50+	excellent
cotton /TS-M1/GR 30 sec	3.29	0.37	134.00	50+	excellent
cotton /TS-M1GR 3 min	4.70	0.82	76.07	50+	excellent
cotton /TS-M2 30 sec	9.34	3.70	20.05	20	good
cotton /TS-M2 3 min	8.67	3.16	22.56	20	good
cotton /TS-M2/GR 30 sec	8.50	3.59	21.61	20	good
cotton/TS-M2/GR 3 min	7.87	3.36	23.03	20	good

Conclusions

The cotton fabrics pre-treated with cold plasma and coated with TiO_2-SiO_2 and TiO_2-SiO_2/reduced graphene oxide composites obtained by the physical method (M1) showed better UV protection than the ones coated by the similar nanopowders obtained through chemical method (M2). A short-time plasma pre-treatment (30 seconds) using He/air caused an increased in UPF values of the cotton fabrics coated with nanopowders obtained by physical method. The plasma treatment allows achieving surface modification of fabrics adding value to end-textile products.

Acknowledgment

This work was supported by a grant of Romanian Ministry of Research and Innovation, CCCDI – UEFISCDI, Project number PN-III-P1-1.2-PCCDI-2017 0743/44PCCDI/2018, within PNCD III.

Analysis of nano-composites with TiO_2 Ag for applications in cotton textile industry

I. D. Timpu[1], M. C. Rosu[2], C. Socaci[2]

[1]"Petru Poni" Institute of Macromolecular Chemistry,41A Grigore Ghica Voda Alley, 700487, Iasi, Romania; E-mail: dtimpu@icmpp.ro

[2]National Institute for Research and Development of Isotopic and Molecular Technologies, 67-103 Donat Street, 400293, Cluj-Napoca, Romania

Interest:

- Silver (Ag) and TiO2 nanoparticles show enhanced antimicrobial and photocatalytic activities and they are used in UV protection, self-cleaning, textile or water treatment applications
- The improvement of the properties for leather and other textile material by using nano-composites has large applications and possibilities

The purpose of this study was to investigate by WAXD - Wide Angle X-Ray Diffraction, TEM, SEM, the thin changes in crystalline structure of precursors after chemical and / or thermal treatment, step-by-step

Precursors: TiO2, SiO2, GO- graphene oxide, GR- reduced graphene oxide, Ag

Precursor: GO

Grafit ==> Hummer's modified method (zero graphite):

SEM / 20um

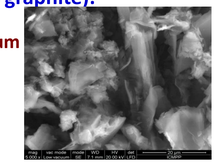

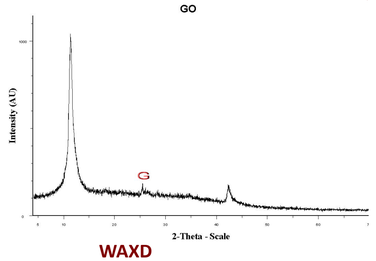

WAXD

TEM / 500 nm

Precursor: Titanium Dioxide TiO2

Synthesis ==> monoclinic / tetragonal / orthorhombic

P25 Degussa, Germany, 99.9% ;

Rutile : Anatase : Brookite / 85 : 15 : 0

standard material in the field of photocatalytic reactions

TEM ==> anatase and rutile particles separately form their agglomerates.

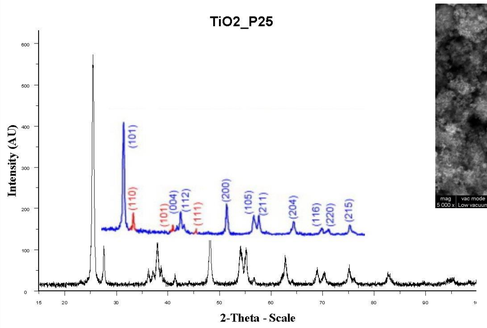

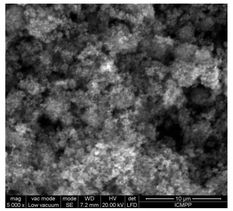

SEM / 10um

Precursor: Titanium Dioxide TiO2 / Rutile

ICDD: nr. 88-1175

2 theta = 27.4158°, 36.0592°, 54.3002°

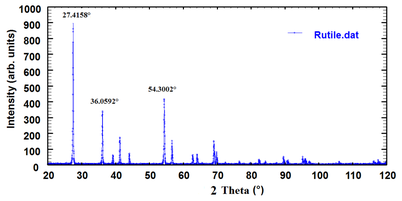

Precursor: Titanium Dioxide TiO2 / Anatase

ICDD: nr. 84-1286

2 theta = 25.2591°, 37.7633°, 48.0060° ,

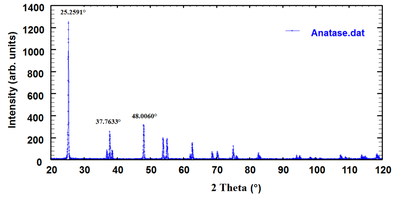

TiO2 Ag 2% chemical reduced

- TiO2 pudra + H2O + Triton X-100 + acetylacetone (vol. 5:1:1:1,5)
+ AgNO3 + ascorbic acid (reducer Ag) (weight 1:2)
+ magnetical stirring 80°C
- White powdwer => grey powder <=> $Ag^+ \rightarrow Ag^0$ ==> drying 50°C

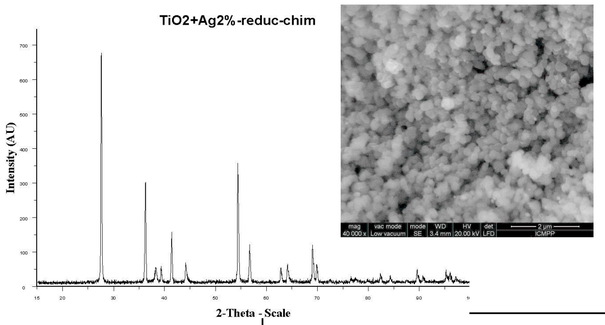

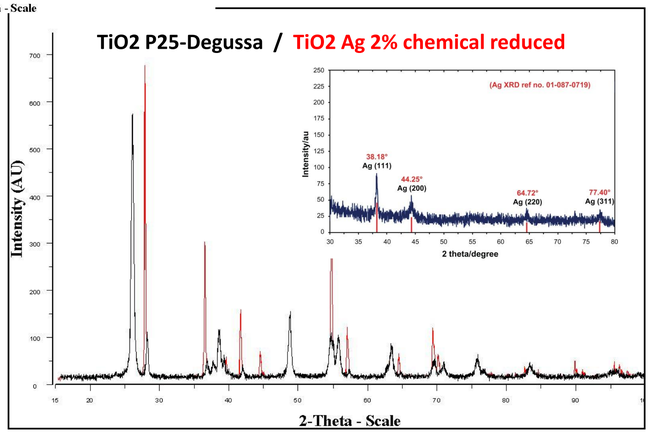

TiO2+Ag2%_GO = TiO2 Ag 2% chemical reduced + GO, 10:1, ultrasound 30 min in ethanol, dry 50°C

TiO2+Ag2%_GR = TiO2+Ag2%_GO + 15min / 300 °C

TiO2+Ag2%_tt = TiO2 Ag 2% chemical reduced + 450 °C / 2h / air

TiO2+Ag2%_TT-GO = TiO2+Ag2%_tt + GO 10:1, ultrasound 30min in ethanol, dry 50°C

SEM / TEM / WAXD / TOPAZ BrukerAXS soft

X-ray diffraction patterns

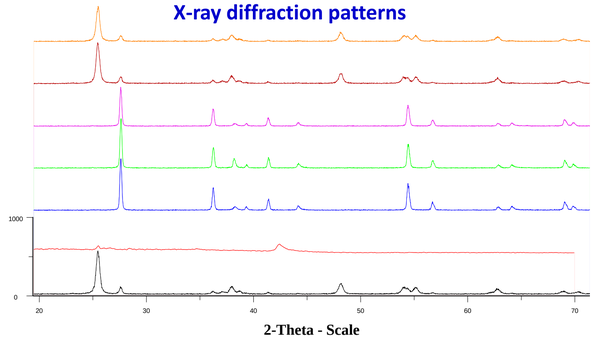

WAXD: D8 Advanced BrukerAXS diffractometer
room temperature, reflection mode, 2θ = 4°–90°, scanning step of 0.02°; Cu*K*α radiation, Goebel Mirror, 36 kV, 35 mA)

Observations:

- we have obtained nano-modified composites material for textile materials impregnation
- composites were investigated by WAXD, TEM, SEM
- WAXD:
  - thin changes in crystalline structure (thin shift of peaks position) of precursors after chemical and / or thermal treatment ➔ deformation / internal stress
  - TiO2 samples: a question to be solver: rutile phase disappearance
- SEM & TEM: changes in surface / volume morphology obtained

Acknowledgements:

This work was supported by a grant of Romanian Ministry of Research and Innovation, CCCDI – UEFISCDI, Project number PN-III-P1-1.2-PCCDI-2017-0743 / 44 PCCDI/2018, within PNCD III.

Thermal process for obtaining titanium nitride nano-powder via vinyl polymer composites

I. D. Timpu[1], A. Sarbu[2], A. L. Radu[2], A. Miron[2]

o[1]"Petru Poni" Institute of Macromolecular Chemistry,41A Grigore Ghica Voda Alley, 700487, Iasi, Romania; E-mail: dtimpu@icmpp.ro
[2]The National Institute for Research & Development in Chemistry and Petrochemistry, Spl. Independentei 202, sector 6, Bucuresti, Romania

Why TiN?

- titanium nitride is a ceramic of considerable interest for both, materials science and industrial applications;
- it shows a high intrinsic hardness of about 18–21 GPa, a high wear and corrosion resistance, high melting point (2950˚C), high chemical and thermal stability, high-temperature strength, high electrical and thermal conductivity;
- is a useful material for a wide range of industrial applications: hard protective coatings on tools for metal cutting and milling, for optical coating, as diffusion barriers in microelectronics, etc.

Conventionally, TiN has been synthesized in different ways, but, these methods can synthesis only small amounts of carbonitrides, rendering them inadequate for industrial needs ➔ we intend to develope a new route to synthesize nanocrystalline ceramic powder, with an economically attractive production method.

The proposal is absolutely new and innovative in our country and at worldwide level by the supramolecular chemical technologies, for TiN manufacturing, starting from a porous TiO_2 inorganic structure, via host guest polymerization.

National project: BIOTIN 6 Universities / Research Institutes

The proposal: to obtain titanium nitride ceramic by a new economically method.

Biomedical aplications

ICMPP work:

- Study of polymer pyrolysis inside of porous inorganic structure, in nitrogen atmosphere, to obtain carbon nanocomposites
- Complex characterization of raw materials, polymer nanocomposites and other intermediate materials
- Establisment of an experimental model / laboratory technology for production of TiN ceramic powder

Precursori: TiO2 comercial

- 30% TiO2 comercial + 70% acrilonitril
- --50% TiO2 comercial + 50% acrilonitril

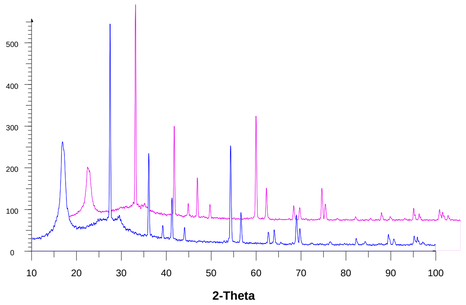

Precursor: Titanium Dioxide TiO2 / Rutile
ICDD: nr. 88-1175
2 theta = 27.4158°, 36.0592°, 54.3002°

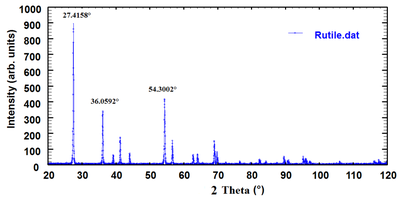

Precursors: set I

TiO2 + monomer solution + 1% AIBN ➔ ampoule ➔ N2 purging 5 minute ➔ closing + ultrasounds, 24 hours at room temperature ➔ polymerization: t=70 ºC / 24 h / ultrasounds.

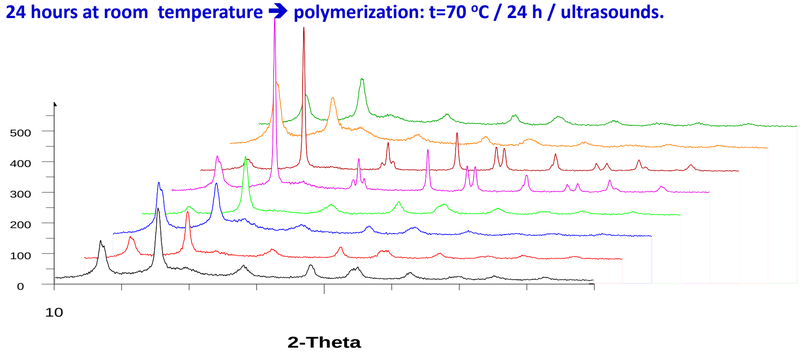

Precursors: MZ2

TiO2 synthesis: sol-gel method

- 30% TiO2 MZ2 + 70% acrylonitril
- --50% TiO2 MZ2 + 50% acrylonitril

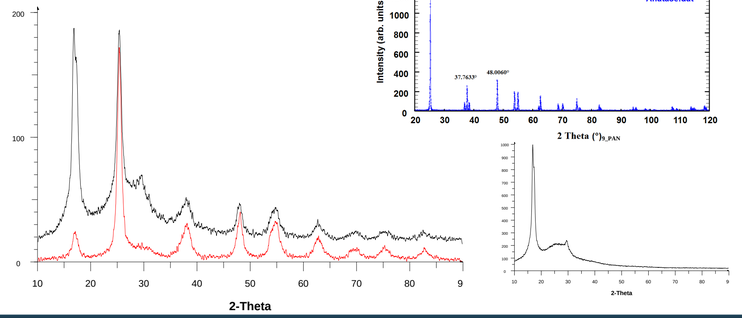

Precursor: Titanium Dioxide TiO2 / Anatase
ICDD: nr. 84-1286
2 theta = 25.2591°, 37.7633°, 48.0060° ,

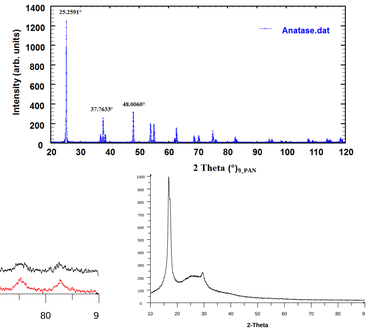

Construction of a high-performance laboratory installation:

Ovens:

A. Main ceramic tubular oven with the following characteristics:

- length 35 cm, inner diameter 35 mm; can work in any position (horizontal, vertical, inclined);
- quartz fiber felt insulation
- inside: quartz or metal tube (with cooling of the terminals) in which the samples will be introduced, the given acquisition thermocouple and where the necessary atmosphere is created
- temperature range: -100 ˚ C ÷ + 1000 ˚ C; the area with an accuracy <= 1% is 10 cm;
- two thermocouples type K (Ni-NiCr), for separating the programming + adjustment paths from the measurement / data acquisition paths;
- controlled atmosphere: vacuum, air, oxygen, inert gases
- controlled pressure, stationary or purge with laminar flow at an imposed flow

B. Different ceramic ovens, for larger samples (diameters of 5 cm and 8 cm, respectively).

Process computer for thermal treatments:

- Traductors: thermocouple K (miniature), manufactured in institute;
- Static relay On/Off: input = 4...32 VCCout= 480 VAC, 40 A;
- Temperature Controller NITTM J4 – Japonia;
- Converter RS 485 – USB ModBus for PC conection;
- SoftWare PC– Controllers comunication. Can perform controller programming recording functions; controller programming; displaying parameters and setting alarms

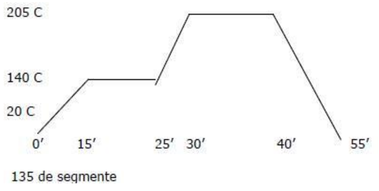

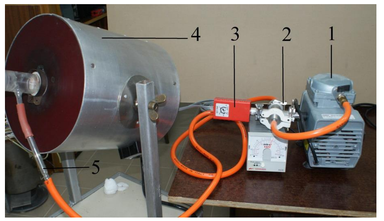

Controller ETS_Brain & Child P91:

FUZZZY & PID; ASIC tehnology; input: 0..10V, 4..20 mA, Pt100, Tc (K, J, L, M); 1 digital imput; 2 outputs : 0..10, 4..20 mA, SSR, relay, alarm; comunication ModBus RS 485; 135 de segments (ramp, landing, slope).

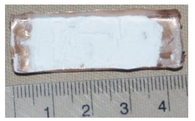

Metallic nacelle with initial PAN

Threated PAN

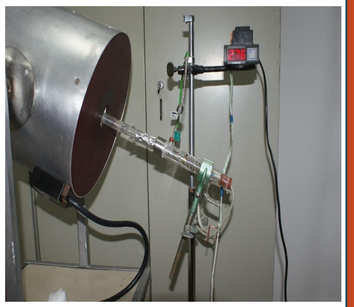

Observations:

- we have obtained nano-modified carbon composites via polymer pyrolysis inside of porous inorganic structure
- composites were investigated by WAXD, TEM, SEM
- WAXD:

- thin changes in crystalline structure (thin shift of peaks position) of precursors after chemical and / or thermal treatment ➔ deformation / internal stress
- SEM & TEM: changes in surface / volume morphology obtained
- Installation for thermal treatment is very performance and versatileness ➔ can be used in an industrial system (ex: 60 kw/oven)

Acknowledgements:

This work was supported by a grant of Romanian Ministry of Research and Innovation, CCCDI – UEFISCDI, Project number PN-III-P1-1.2-PCCDI-2017-0428 / 40 PCCDI/2018, within PNCD III.

Graft Conjugated Polymers: Toward Smarter and Versatile Materials for Biomedical Applications

Anca-Dana Bendrea[1], Luminita Cianga[1], Ioan Cianga[1]

[1]Petru Poni Institute of Macromolecular Chemistry, 41A Grigore Ghica Voda Alley, 700487, Iasi , ROMANIA

Motivation & Introduction

- ✓ Bioinspiration involves the study, understanding and the attempt to apply what the Nature is revealing us after its billions of years of refinement during the process of evolution of life on Earth.
- ✓ Graft conjugated polymers (g- CPs) are versatile and interesting construction of rod-coil type, with capability for various biomedical applications (bioimaging, drug delivery, imaging-guided therapy, tissue engineering or biosensors).
- ✓ The present communication will show how a particular polymers' architecture and appropriate building blocks combination based on CPs and biocompatible/biodegradable polymers counterparts can results in alternative biomaterials with tunable properties for specific envisioned bioapplications.

Materials and method

By usefully combining the electroactivity and photophysical properties of oligo/polythiophene main chains with biocompatibility and / or biodegradability of the side chains, using **thiophene**-containing macromonomers as versatile **building "bricks",** various macromolecular structures were designed and synthesized.

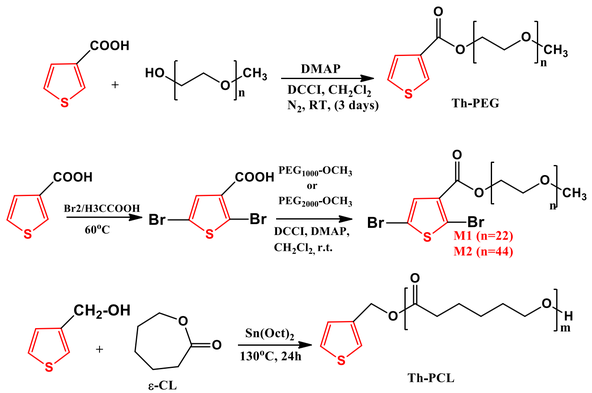

The Building of the " **Basic Bricks** " designed through the biomimetic approach

Results and discussions

- ✓ Carefully selecting the synthesis method and synergistic combining **biocompatible and/ or biodegradable polymers (PEG, PCL**) and **polythiophene (PTh)** units, modulating their properties through structure manipulation we succeeded to produce various multifunctional and versatile polymeric materials.
- ✓ Some of them were used for **biosensors,** or **implantable electrodes construction**, while inherent fluorescence of the PTh in conjunction with biocompatible and functional side chains was exploited for **non-targeted cell imaging.**
- ✓ On the other hand, such materials were found to work as excellent **biocompatible and electroactive cellular matrix**, as well as active surfaces for **selective adsorption of proteins .**

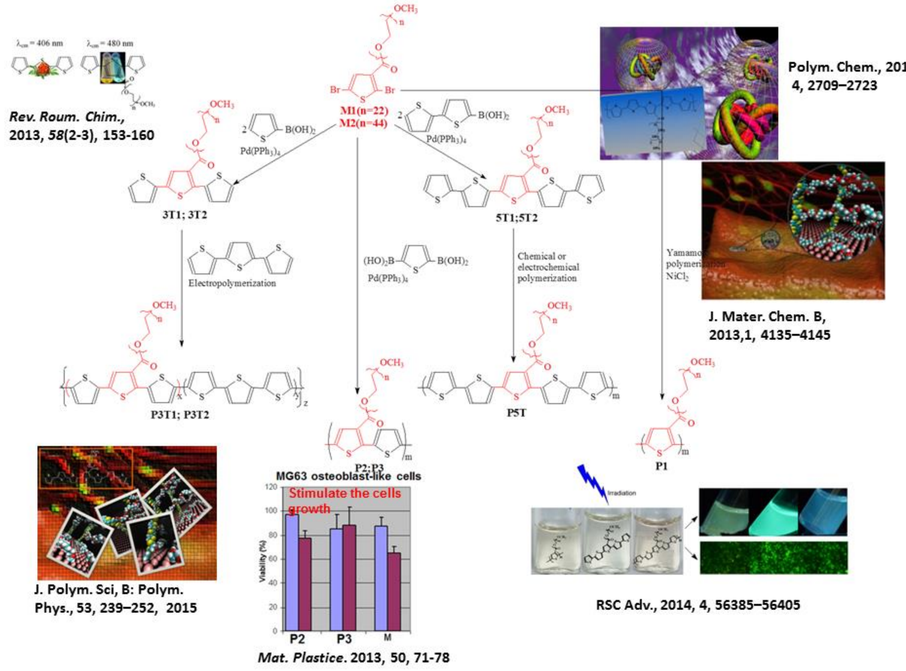

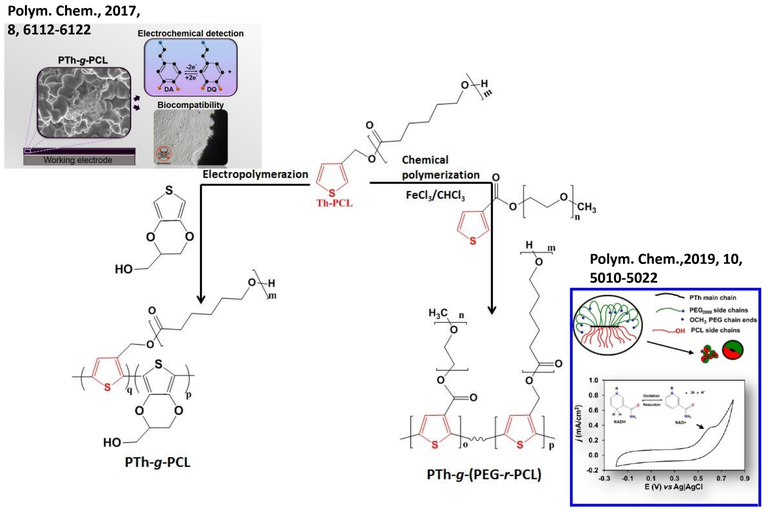

Conclusions

- ✓ **Simple in appearance, working on the composition, on the structural details and on the architecture we were able to produce sophisticated materials endowed with multifunctionality and which could be used in various type of applications , from biosensors to cell imaging or tissue engineering.**

Acknowledgment

The authors acknowledges the financial support of a grant of Ministry of Research and Innovation, CNCS-UEFISCDI, Project number PN-III-P4-ID-PCCF-2016-0050, Acronym 5D-nanoP.

Chitosan/poly(2,2-dimethyl trimethylene carbonate) composites

B. Kost[1], M. Socka[1], M. Basko[1], T. Biela[1], F. Tanasa[2], I. A. Duceac[3,4]

[1]Centre of Molecular and Macromolecular Studies, Polish Academy of Sciences, 112 Sienkiewicza St., 90-363 Lodz, Poland
[2]Department of Photochemistry and Polyaddition, "Petru Poni" Institute of Macromolecular Chemistry, 41A Grigore Ghica Voda Alley, Iasi 700487, Romania
[3]Department of Natural, Bioactive and Biocompatible Polymers, "Petru Poni" Institute of Macromolecular Chemistry, 41A Grigore Ghica Voda Alley, Iasi 700487, Romania
[4] Department of Biomedical Sciences, Faculty of Medical Bioengineering, "Grigore T. Popa" University of Medicine and Pharmacy, 9-13 M. Kogalniceanu St., Iasi 700454, Romania

Introduction

Chitosan is a naturally occurring biodegradable polymer with sought after functionalities and properties.[1] To extend the range of applications of chitosan, various derivatives, including different polymer conjugates and composites were investigated. The purpose of the present work is the preparation of new composites made of biocompatible poly(2,2-dimethyl trimethylene carbonate) (PDTC)[2] and chitosan) by grafting through the ring opening polymerization of monomeric DTC

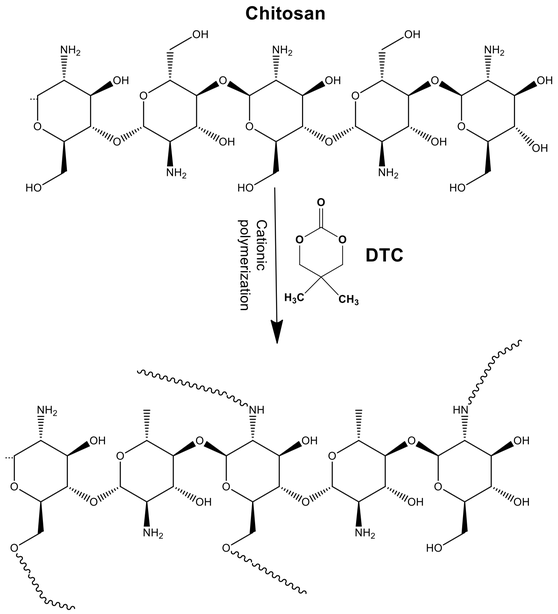

poly(2,2-dimethyl trimethylene carbonate)-chitosan conjugate

CS-g-PDTC

Results and discussions

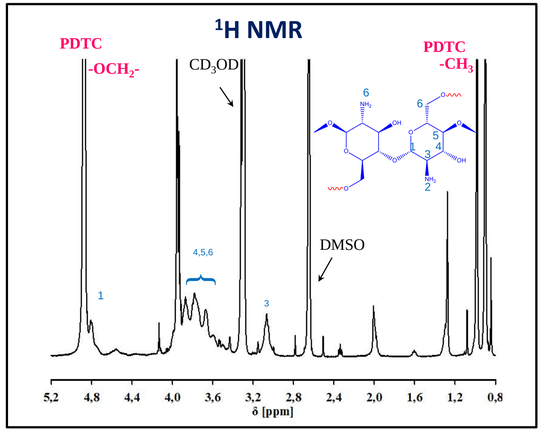

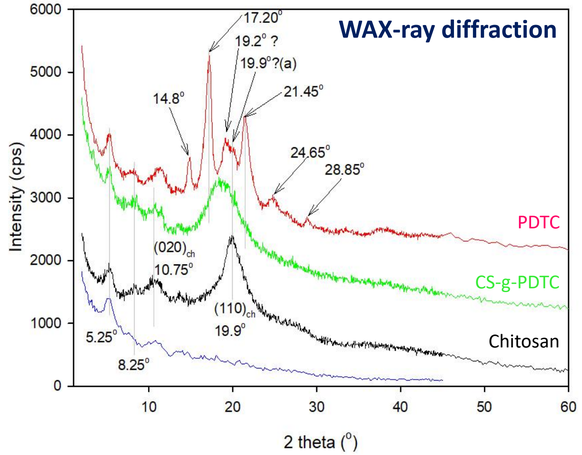

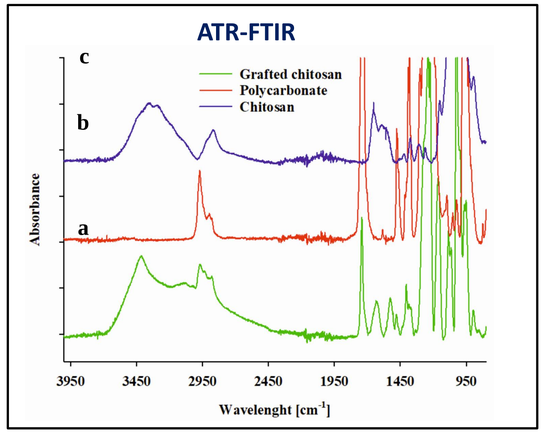

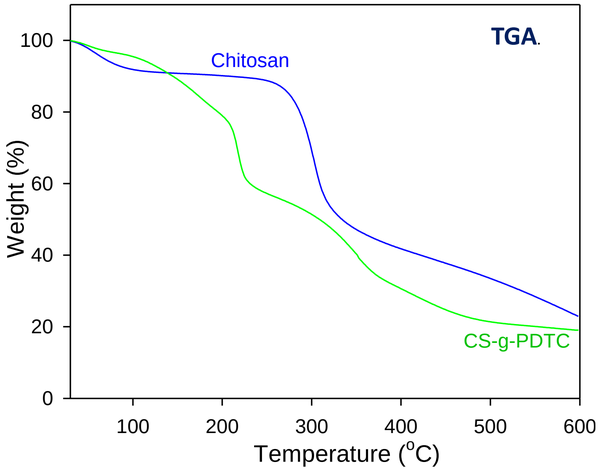

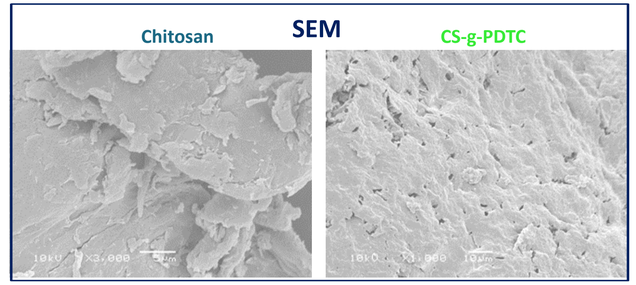

Conclusions

Preliminary results showed that chitosan grafted poly(2,2-dimethyl trimethylene carbonate) copolymer was successfully synthesized by the ring-opening polymerization of DTC

Materials and method

Cationic polymerization was carried out under stirring in DMSO at 80 °C, using triflic acid as the catalyst. After the required time the reactive mixture was cooled down and DMSO was removed on the evaporator. The solid product was washed with cold and warm CH_2Cl_2 then dried under vacuum until a constant weight was reached.

References

1. L. Racine, I. Texiera, R. Auzély-Velty, Polym.Int.; 66: 981, (2017)
2. M. Socka, A. Michalski, I.M. Pelin, A. Pawlak, F. Tanasa, T. Biela, M. Basko, Polymer, 186, 122078, (2020)

Acknowledgment and Contact

The studies are conducted within the joint Polish-Romanian interacademic exchange project developed under the Agreement on scientific cooperation between the Polish Academy of Sciences and the Romanian Academy.
Contact: baskomeg@cbmm.lodz.pl, ftanasa@icmpp.ro

Detection of the biological constituents in solution using metamaterial slabs with special properties

Daniela IONESCU [1,$] and Gabriela APREOTESEI [2]

[1]"Gh. Asachi" Technical University of Iasi, Department of Telecommunications and Informational Technologies, [2] Department of Physics

Introduction

Particular configurations of metamaterials used for different substances **detection in biomedicine** have been analyzed. The 3D structure has periodic geometrical constituents with dimensions of tens of micrometers, consisting of **nested ring resonators** with different configurations, on a RT/Duroid substrate. The exposure **microwave field** propagates distinctly through the structure impregnated with a solution containing biological samples. By estimating the modification of the metamaterial parameters, like refractive index *n* and effective permittivity ε_r, the detection of the concentration level of biomolecules (components of the blood, protein, lipid and carbohydrate) in the biological liquid was performed. A model of the metamaterial structures has been conceived and analyzed by **simulation** methods. Concentration levels up to 20 % have been detected, determining Δn up to 4 % and $\Delta\varepsilon_r$ up to 6 % for the metamaterial. By using this method, the optimal design for the detection structure can be set.

Materials and method

• **3D metamaterial** with periodic geometrical (superlattices dimensions ~ tens of μm), on a RT/Duroid 5880 substrate, exposed to a 7 … 28 GHz field

Superlattices of the detecting metamaterials

Metamaterial configuration / slab thickness	Model for the unit cell (600 x 400 x 80 nm)*
I. first variant	(60 x 40 x 16 μm)**
II. second variant	(42 x 52 x 12 μm)
III. third variant	(74 x 42 x 10 μm)

*l x w x t

** L x W x h

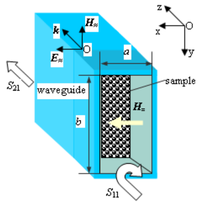

Analysis by simulation
HFSS: $S \cdot x + k_0^2 T \cdot x = b$

• correlation between dimension of the constituents, the wavelength and dimension of the analyte molecules ; each of the geometrical resonances was tunable to a resonant frequency of a particular analyte

Simulation ⇔ *S*-parameters ⇔ resonances ω_0

$$n = -\sqrt{\varepsilon\mu} \qquad \varepsilon(\omega) = 1 - \frac{\omega_p^2}{\omega(\omega + i\gamma)} \qquad \mu(\omega) = 1 - \frac{F\omega^2}{\omega^2 - \omega_0^2 + i\gamma\omega}$$

• detected **analytes in blood**: *a* – protein (*albumin*[#]: 7 nm, *globulin*[#]: 11 – 15 nm, indicating hyperproteinemia), *b* – lipid (triglycerides, fatty acids and *cholesterol*[#]: up to 22-27 nm, indicating hyperlipidemia), *c* – carbohydrate (sugar, *glucose*[#]: 0.9 nm, starches, indicating diabetes)

Results and discussions

• A theoretical **model** for the samples of metamaterial structures + analyte in aqueous solution (diluted blood sample) has been conceived
• Analysis by microwave methods for the domain of 7 – 28 GHz

Determinations:
• **Concentration level** ⇔ modifying the refracted wave intensity
• **Refractive index variation** ⇔ modifying plasmons propagation
• **Effective permittivity variation** ⇔ modifying the electric induction of the sample

E.g.: Analyte: globulin (14 nm) in blood
Detector: metamaterial – 1st variant
MAXIM RESPONSE AT RESONANCE

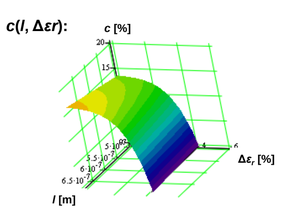

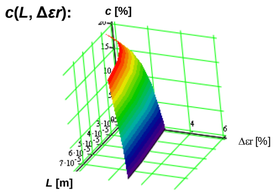

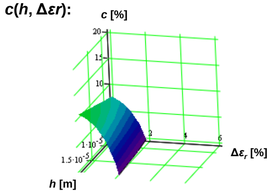

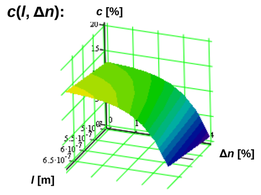

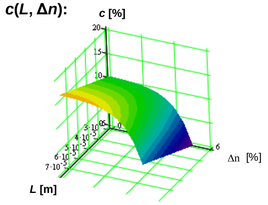

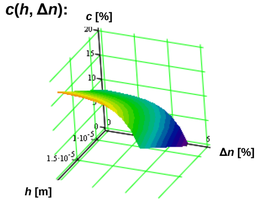

• Concentration level variation: 2-3 …20% demonstrated
• Refractive index variation: up to 4% demonstrated
• Effective permittivity variation: up to 6% demonstrated

• Linear dependence of analyte concentration on metamaterial constituents dimensions

• Higher modification of physical parameters generated by a detection process occurring near the dimensional resonances detector - analyte

Conclusions

• Shift in resonant frequency occurring, depending on analyte molecular dimensions and structure of the metamaterial unit cell; detection process can be controlled by dimensional tuning of the metamaterial constituents

• Strong correlation between physical and chemical parameters (electrical permittivity, refraction index of detector / spatial structure, molecular size of analyte) in the detection process

The analyzing method is solving the task of choosing the optimal design for the detection structure and synthesis of the unit cell in function of the parameter which has to be detected in our nondestructive control. Results: 1st, 2nd and 3rd variant of detectors in the material table for the marked *analytes*[#].

References

• Chen T., Li S., Sun H., *Metamaterials Application in Sensing*, Sensors **12**, 2742-2765 (2012)
• Memoli G., Caleap M., Asakawa M., Sahoo1 D. R., Drinkwater B. W., Subramanian S., *Metamaterial bricks and quantization of meta-surfaces*, Nat. Commun. **8,** 14608 (2017)
• Salim, A., Lim S., Review *of Recent Metamaterial Microfluidic Sensors*, Sensors **18**, 232 (2018)

Contact

$ danaity@yahoo.com

OBSERVATIONS ON THE SPINNING DISC MICROMIXING CHARACTERISTICS

Eugenia T. Iacob Tudose

"Gheorghe Asachi" Technical University of Iasi, „Cristofor Simionescu" Faculty of Chemical Engineering and Environmental Protection, Department of Chemical Engineering, 73 Prof.Dr.Docent D.Mangeron Blvd, 700050, Iasi, Romania, e-mail: et_tudose@yahoo.com

Introduction

The spinning disc technology is one of the most versatile process intensification techniques used in different application fields, from food industry to environmental technologies.

Previous experimental results [1] performed to obtain the residence time distribution, at different liquid flow rates and disc rotational speeds, using the pulse response technique, endorsed the calculation of some characteristic spinning disc parameters such as the dispersion coefficient, the residence and the micro-mixing times, important to emphasize some of its enhanced convective features and also, point out some limitations.

Materials and method

Tap water and a salt (NaCl) solution have been used within the pulse response technique, applied in the experimental setup presented in Fig.1, in order to obtain residence time distributions [1].

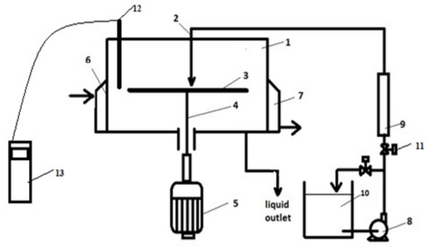

Fig. 1 Spinning disc experimental setup

1-plexi case ; 2- rod; 3- spinning disc; 4 – interlock; 5- electric motor; 6,7- cooling chamber; 8- pump; 9- rotameter; 10- liquid store tank; 11- exit tap; 12- flow control valve; 13- conductometer probe; 14- WTW 315i conductometer

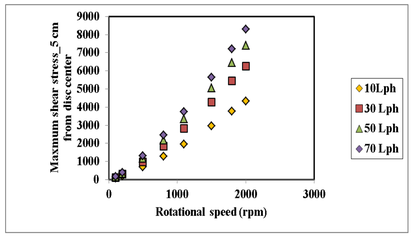

Fig.2 Maximum shear stress at different liquid flow rates and disc rotational speeds, at 5 cm from the disc center

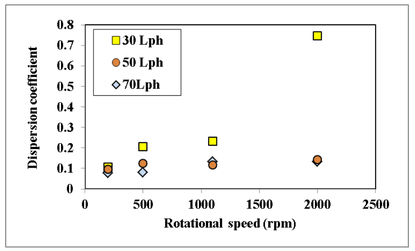

Fig.3 Dispersion coefficient at different liquid flow rates and disc rotational speeds

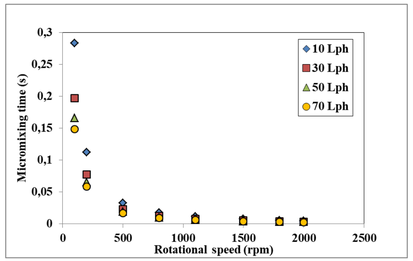

Fig.4 Micro-mixing times at different liquid flow rates and disc rotational speeds

Results and discussions

The maximum shear stress at different locations on the disc can be estimated using eq. (1):

$$\gamma_{max} = \left(\frac{1.5Q\omega^4 r}{\pi\vartheta^2}\right)^{1/3} \qquad (1)$$

For r=5 cm, the maximum shear stress is plotted in Fig.2, where one can observe a more significant increase in the shear stress, especially at the largest liquid flow rates, *Q*, of 70 L/h and at rotational speeds, ω, larger than 800 rpm up to 2000 rpm. Note that the 5 cm location from the disc center provides a more enhanced shear stress in comparison to the 15 cm location from the disc center, according to eq. (1).

Based on the obtained residence time distributions, the dispersion coefficient was calculated and was found to increase significantly with the disc rotational speed, mainly at lower liquid flow rates, of 30 L/h, as presented in Fig.3 .

For Schmidt numbers Sc<4000, Baldyga et al. developed an expression to calculate the micro-mixing time for molecular diffusion accelerated by deformation, approximated by [2]:

$$\tau_m \cong 17.3\left(\frac{\vartheta}{\varepsilon}\right) \qquad (2)$$

with ϑ – the kinematic viscosity, ε – dissipation power calculated based on experimental diffusion coefficients:

$$\varepsilon = 0.5t_{res}\{(r^2\omega^2 + U_m^2)_o - (r^2\omega^2 + U_m^2)_i\} \qquad (3)$$

t_{res} – the residence time, τ_D –time for turbulent dispersion, τ_m - micr-omixing time, *Um*- the average velocity. Based on eqs. (2) and (3), using the calculated dispersion coefficients, the micro-mixing times were calculated and plotted in Fig.4, which clearly indicates decreasing trends with the disc rotational speed increase.

The liquid residence time on the spinning disc can be determined using eq.(4):

$$t_{res} = \frac{3}{4}\left(\frac{12\pi^2\vartheta}{\omega^2 Q^2}\right)^{1/3}\left(r_o^{4/3} - r_i^{4/3}\right) \qquad (4)$$

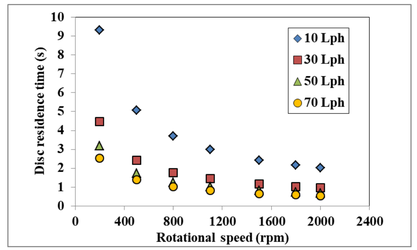

Fig.5 Micro-mixing times at different liquid flow rates and disc rotational speeds

The obtained residence time values, are represented in Fig.5 and indicate, as expected decreasing variations with both increasing liquid flow rates and disc rotational speeds. It is clear that the micro-mixing times decrease faster than the residence times, meaning that the micro-mixing becomes more intense with the increase in the liquid flow rate, but mostly with the increase in disc rotational speed, as long as the liquid does not exit the spinning surface. That is why the optimum separation rates are not attained at the largest flow rates and rotational speeds, but rather at intermediate values.

Conclusions

The presented data demonstrate that a high degree of micro-mixing can be achieved at high disc speeds and/or high liquid feeding flow rates, provided the liquid resides enough time on the disc. The high shear forces act within the liquid film rather at shorter distances from the disc center. These combined effects contribute to the enhancement of the micro-mixing process. Despite the intense turbulence within the liquid film, its benefit can be useless if the residence times are short. One can conclude, that the optimum in a process taking place on a spinning disc, may not be attained at the largest values of the operating parameters.

References

1. E.T. Iacob Tudose - An experimental study on spinning disc key parameters influencing its performance, Rev. Chim. accepted to be published.
2. J.Baldyga, W.Podgorska, R.Pohorecki – Mixing-presipitation model with application to double feed semibatch precipitation, Chem.Eng.Sc., 1995,50.

NON-INTRUSIVE VISUALIZATION TECHNIQUES FOR FLOW, TEMPERATURE AND CONCENTRATION FIELDS

Eugenia T. Iacob Tudose

"Gheorghe Asachi" Technical University of Iasi, Faculty of Chemical Engineering and Environmental Protection, 73 Prof. Dr. Docent D.Mangeron Blvd, 700050, Iasi, Romania, e-mail:et_tudose@yahoo.com

Introduction

The study focuses on convection fields characterization in vertical two-phase (slug) flow occurring in equipment such as chemical/nuclear reactors,oil and gas wells and also, in unstable thermocapillary flow, i.e. temperature induced Marangoni convection, relevant to crystal growth from melts, in both normal and micro-gravity. Both cases were previously investigated [1, 2].

Methods

The ***Photochromic Dye Activation*** *(PDA)* technique utilizes the photochromic properties of a colorless indicator dissolved in a fluid, activated by a laser beam pulse, with a change in color, resulting in traces following the flow. The method was employed to highlight the liquid film penetration along a Taylor bubble, in slug flow and to visualize the instanteneous velocity profiles in the bubble wake.

The ***Particle Image Velocimetry*** *(PIV)*, another non-intrusive optical laser technique, provides instantaneous velocity vectors in a cross-section of a flow. In case of the above-mentioned two-phase flow, the velocity fields around the bubble and in its wake were mapped.

The ***Mach-Zehnder interferometry*** consists of splitting a laser beam into two: one of reference and the other passed through the investigated system. Recombining them, one can obtain a fringe pattern characterizing changes in the system temperature or concentration field. This technique was used to depict the integrated vertical temperature field occurring in the thermocapillary flow, both in steady and non-steady state regimes.

The ***infrared thermal scanning*** of a liquid surface allows temperature scanning and also, instabilities detection.

Examples and discussions

Slug flow (gas-liquid flow)

The PDA technique was applied in order to visualize the flow in the wake of a gas Taylor bubble moving upwards through a liquid, as seen in Fig.1, and afterwards digitized to obtain the velocity vectors in the liquid film around (Fig.2(a)) and in the wake of the bubble (Fig.2(b))

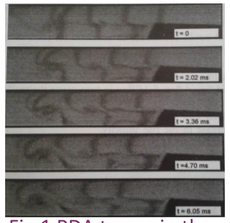

Fig.1 PDA traces in the wake of a Taylor bubble

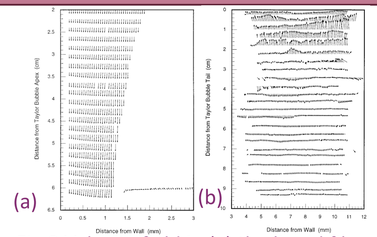

Fig.2 Velocity field in (a) the liquid film near the bubble, (b) in the wake region

Thermocapillary (TC) instabilities

Thermal-induced convection in thin liquid films, of thickness δ<4-5mm is characterized by instabilities developing once the temperature is increased over a critical value. The PIV technique allowed for convective field characterization, highlighting the characteristic oscillating convective cells, i.e. oscillating multicellular convection (OMC), depicted in Fig.3 and the Mach-Zehnder interferometry, oscillating thermal structures depicted in Fig.4. From the analyzed data, the two fields proved to oscillate with the same frequency, indicating a strong interdependence between them.

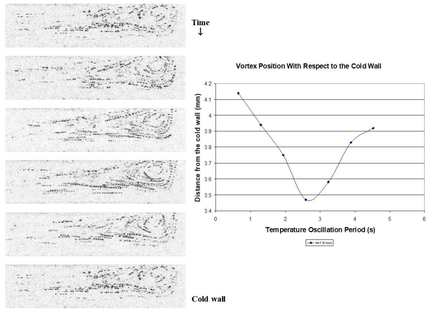

Fig.3 Non-steady convective structures in TC flows (OMC)-*side view*, using PIV

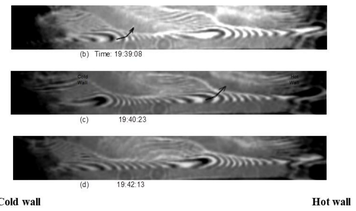

Fig.4 Unstable thermal structures in TC flows – *side view*, using Mach-Zehnder interferometry

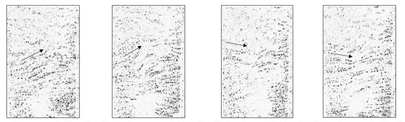

Fig.5 Non-steady convective structures in TC flows-*top view*, using PIV

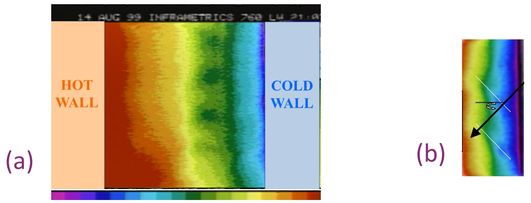

Fig.6 (a) Cold spots, (b) Hydrothermal waves, both travelling on liquid surface in unstable TC flows-*top view*, using IR camera

The convective-thermal field interdependency was confirmed also using PIV depicted in Fig.5 and IR camera scanning, seen in Fig.6 (a), both applied to the top view of the thermocapillary field .

Another type of instability was highlighted for very thin liquid layers, δ<1.5 mm, in thermocapillary flow, namely hydrothermal wave, HW, shown in Fig.6(b), that did not exhibit any particular oscillatory features in the convective field, investigated using PIV. Thus, it was concluded that HW instability was rather different than the oscillatory multicellular flow.

Basically, identical frequency spectra measured from PIV, Interferometry and IR images were obtained, as shown in Figs. 7 (a) and (b) [1].

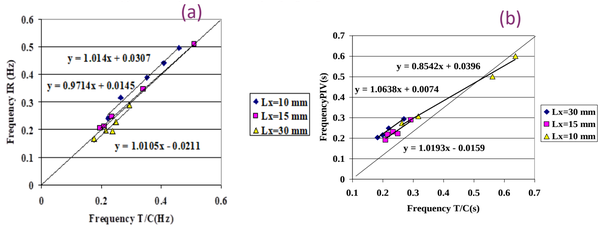

Fig.7 (a) Surface temperature frequency and (b) PIV structure movement frequency vs. liquid bulk frequency

Conclusions

The PDA technique is a valuable tool to characterize thoroughly the convective flow around gas bubbles in slug flow, revealing detailed aspects, useful for two-phase flow modeling. Also, the other presented non-intrusive techniques, PIV, interferometry, IR imaging give information related to the interconnection between the convection and thermal fields in thermocapillary unstable flow, characterized by identical velocity and temperature oscillation frequencies.

References

1.E.T.Tudose - An experimental study of buoyant-thermocapillary convection in a rectangular cavity, Ph.D. thesis, University of Toronto, 2002.

2..M.Kawaji, J.DeLorencez, E.T. Tudose – Investigation of flow structures in vertical slug flow, Nuclear Engineering and Design, 175, 37-48, 1997.

Acknowledgment

The author would like to acknowledge the use of equipment in Thermo-Hidraulics Lab, conducted by Prof. Ph.D. M.Kawaji in University of Toronto.

Iron oxide nanoparticles conjugated with cerium oxide nanoparticles as free radical scavengers with magnetic properties

Adrian Fifere[1], Ana-Lăcrămioara Lungoci[1], Ioana Andreea Turin Moleavin[1], Narcisa Laura Marangoci[1], Anca Roxana Petrovici[1], Mariana Pinteală[1]

[1]Centre of Advanced Research in Bionanoconjugates and Biopolymers Department, "Petru Poni" Institute of Macromolecular Chemistry, 41A Grigore Ghica-Voda Alley, 700487 Iasi, Romania

Introduction

Core-shell magnetic nanoparticles (MNPs) can be successfully used as agents for transport and delivery (at the desired site) of an antioxidant drug capable of inactivating reactive oxygen species (ROS) and/or reactive nitrogen species (RNS), hindering the side effects that may occur, such as DNA mutations and lipid peroxidation [1-4].

Multifunctional magnetic nanoparticles can provide new insights into the development of theranostic medicine. Among inorganic antioxidants, nowadays, cerium oxide nanoparticles (CeNP) are starting to exert a high interest due to their free radical scavenging properties, playing the role of radical scavenger with neuroprotective, radioprotective and anti-inflammatory properties [5].

The purpose of this study is to prepare and to characterise, for the first time, a nanosize cargo-complex, having a magnetic core and a polyethyleneimine (PEI)-based shell, able to load and to deliver precise amounts of the radical scavengers of CeNP type, being spatially guided in the human body (by means of a magnetic field) and supplying species capable of the annihilation of ROS.

Materials and method

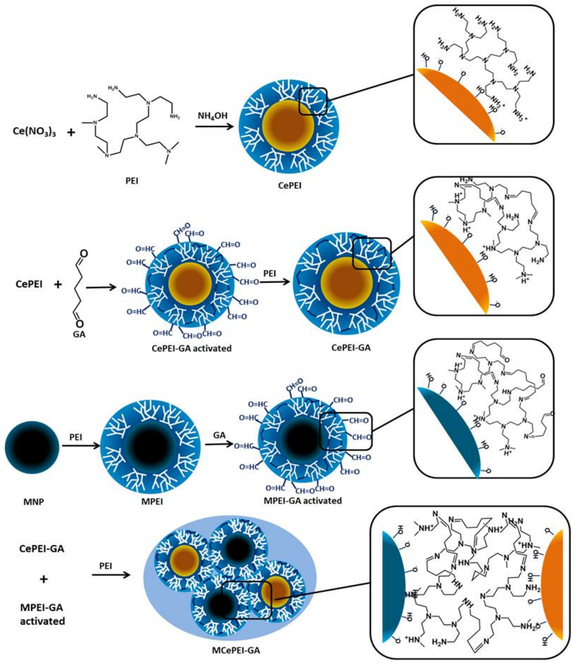

Results and discussions

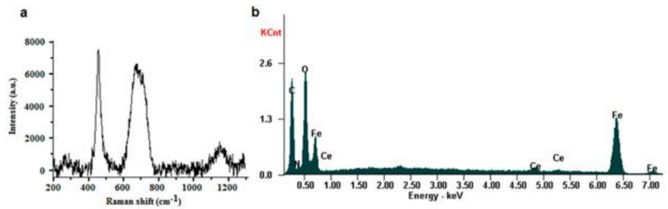

Raman spectra (a) and EDX analysis (b) for the MNP conjugated with CeNP MCePEI-GA.

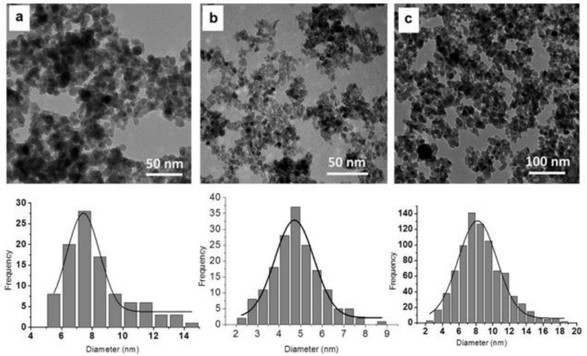

TEM micrographs of MPEI (a) CePEI (b) and MCePEI-GA (c) nanoparticles.

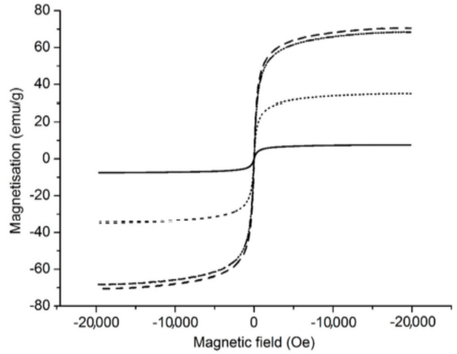

Magnetisation loops for MNPs (dash); MPEI (dash dot); physical mixture of MPEI and CePEI (dot); and MCePEI-GA (solid).

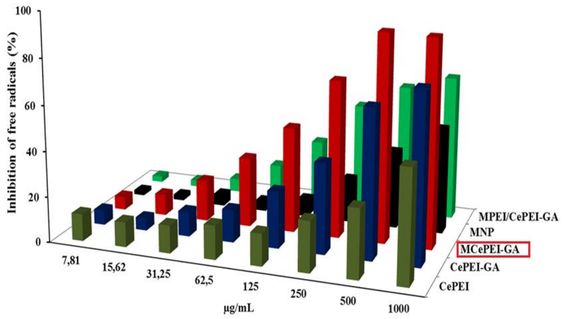

Antioxidant activity against 1,1-diphenyl-2-picryhydrazyl (DPPH) of: (a) CePEI, CePEI-GA, MCePEI-GA, MNP and MPEI/CePEI-GA.

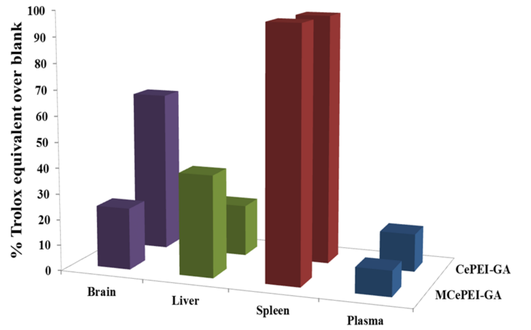

The added antioxidant percentages to the blank samples (in Trolox equivalents) for treated samples with CePEI-GA and MCePEI-GA conjugates.

Conclusions

- The MCePEI-GA magnetic conjugate with spherical shape and mean diameter of 8 nm presents superparamagnetic properties, allowing them to be guided under an external magnetic field to certain targets. Their structure was demonstrated using FT-IR, Raman and EDX methods.
- In vitro, MCePEI-GA demonstrates good biocompatibility on the NHDF cell line and a promising antioxidant activity against DPPH (around 50% for a sample concentration of 125 g/mL), being much higher than those of CePEI and CePEI-GA nanoparticles.
- The added antioxidant percentages to the blank samples are given in the following series: Spleen (97%) > liver (39%) > brain (20%) > plasma (9%).

References

1.Lungoci, A.L.; Turin-Moleavin, I.-A.; Corciova, A.; Mircea, C.; Arvinte, A.; Fifere, A.; Marangoci, N.L.;Pinteala, M. Multifunctional magnetic cargo-complexes with radical scavenging properties. Mater. Sci.Eng. C 2019, 94, 608–618.

2. Kim, K.S.; Lee, D.; Song, C.G.; Kang, P.M. Reactive oxygen species-activated nanomaterials as theranostic agents. Nanomedicine 2015, 10, 2709–2723.

3. Krumova, K.; Cosa, G. Overview of reactive oxygen species. In Singlet Oxygen: Applications in Biosciences and Nanosciences; Nonell, S., Flors, C., Eds.; Royal Society of Chemistry: Cambridge, UK, 2016; pp. 1–21.

4. Fu, S.; Wang, S.; Zhang, X.; Qi, A.; Liu, Z.; Yu, X.; Chen, C.; Li, L. Structural e ect of Fe3O4 nanoparticles on peroxidase-like activity for cancer therapy. Colloids Surf. B Biointerfaces 2017, 154, 239–245.

5. Perez, J.M.; Asati, A.; Nath, S.; Kaittanis, C. Synthesis of Biocompatible Dextran-Coated Nanoceria with pH-Dependent Antioxidant Properties. Small 2008, 4, 552–556.

Acknowledgment

This work was supported by a grant from the Romanian Ministry of Research and Innovation, CCCDI–UEFISCDI, project number PN-III-P1-1.2-PCCDI-2017-0697/13PCCDI/2018, within PNCDI III . Also the authors are grateful for the financial support from a grant of Ministery of Research and Innovation, CNCS - UEFISCDI, project number PN-III-P4-ID-PCCF-2016-0050, within PNCDI III.

Natural compounds architecture for drug delivery system

Iuliana-Marilena Andrei, Maria Valentina Dinu, Narcis Anghel, Iuliana Spiridon

"Petru Poni" Institute of Macromolecular Chemistry, Aleea Grigore Ghica–Vodă 41A, 700487 Iași, Romania; E-mail: anghel.narcis@icmpp.ro

Introduction

Biomacromolecules such as cellulose, collagen and lignin attracted a lot of attention due to their antioxidant and antimicrobial properties while polyurethane is a biocompatible synthetic polymer often used for its elasticity and has a great potential to be utilised for biomedical applications (Spiridon et al., 2020; Tran et al., 2013; Larrañeta et al., 2018).

This work presents the synthesis and characterization of new materials obtained by dissolution of cellulose, collagen and polyurethane in 1-ethyl-3-methyl-imidazolium chloride [EMIm+Cl-] for potential drug delivery. Lignin (L), lignin-metal complex (LMC) and ketoconazole (K) as fillers were added into above mentioned polymeric matrix and ketoconazole (K) as bioactive principle. The new architectures based on natural polymers have been tested in terms of mechanical properties, as well as their ability to function as drug delivery systems.

Materials and method

- Cellulose, collagen, polyurethane were dissolved in [EMIm+Cl-] under magnetic stirring at 50 °C. Lignin, lignin-metal complex and ketoconazole were added as fillers.
- Bruker FTIR Spectrophotometer, Vertex 70 (Billerica, MA, USA) equipped with an attenuated total reflection (ATR) device was used to evidence the interactions between composites' components. The recorded FTIR spectra were used to calculate Total Crystalline Index (TCI), Lateral Order Index (LOI) and Hydrogen Bound Intensity (HBI) for the studied materials.
- The new composites were characterized by mechanical testing. The compressive properties of the materials were determined using a Shimadzu Testing Machine EZTest (EZ-LX/EZ-SX Series, Kyoto, Japan) at a compression rate of 1 mm × min^{-1}. This test was performed at 22 °C and was applied on samples, as plates, with 10 mm thickness, 12 mm width and 4 mm height.
- *In-vitro* release studies were performed at 37 ± 0.5 °C in Phosphate Buffered Saline (PBS) solution (pH 7.2). The concentration of the drug released was analyzed spectrophotometrically at 240 nm using a Jenway 6405 UV/Vis Spectrophotometer.

Results and discussions

The introduction of fillers into the base polymer matrix causes an increase in the strength of hydrogen bonds (HBI) while the degree of structural ordering remains approximately the same (Table 1).

On the other hand, the presence of ketoconazole leads to a substantial increase in the intensity of hydrogen bonds and the degree of ordering, which is reflected in the ability of these biomaterials to function as retard systems for the slow release of bioactive principles.

Table 1. Total Crystalline Index (TCI), Lateral Order Index (LOI) and Hydrogen Bound Intensity (HBI) values obtained from the FTIR spectra analysis of the biomaterials

Sample	TCI (A_{1376}/A_{2902})	HBI (A_{3336}/A_{1336})	LOI (A_{1437}/A_{899})
Cellulose	1.844	5.140	2.174
CCP-K	1.625	4.114	2.849
CCPOL-K	1.143	6.148	4.557
CCPLMC-K	1.855	4.637	3.333
CCP	1.901	3.620	1.842
CCPOL	1.870	3.969	1.979
CCPLMC	1.436	3.985	1.836

The compression stress-strain measurements were performed on swollen samples. The elastic modulus values (Figure 1) were calculated as the slope of the initial linear region in the obtained stress-strain curves. The incorporation of ketoconazole within CCP and CCPOL matrices induces a decrease of the elastic modulus, i.e. the materials become more rigid. However, the formulations containing lignin hybrid have different behavior because of higher degree of structural ordering which reflects the ability of the components to slide side by side.

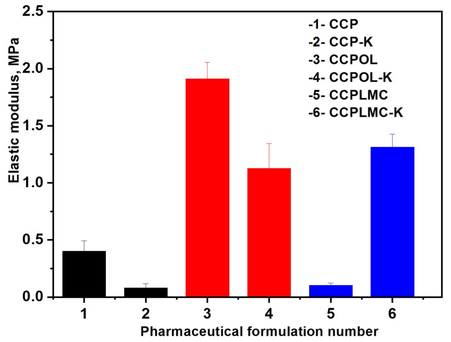

Figure 1. Elastic modulus for each pharmaceutical formulation.

The drug release profile shows that lignin addition into the polymeric matrix induces retard properties and influences the amount of ketoconazole released into medium (Figure 2).

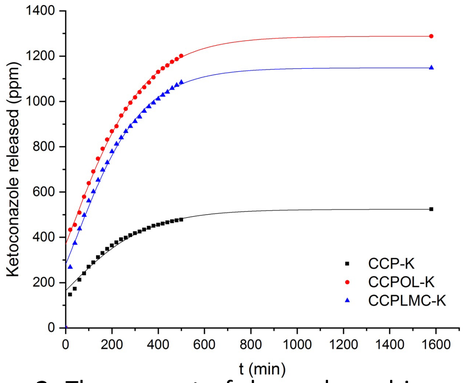

Figure 2. The amount of drug released in medium over time at pH=7.2 for 30h.

Conclusions

The mechanical properties, the release kinetics of the active principles as well as the biocompatibility recommend these polymeric architectures for the manufacture of patches to be used as drug delivery systems.

References

Spiridon I., Anghel N., Dinu M. V., Vlad S., Bele A., Ciubotaru B. I., Verestiuc L., Pamfil D., *Polymers*, **12**, 5, 1191 (2020).

Tran C. D., Duri S., Delneri A., Franko M., *J Hazard Mat*, **252-253**, 355-366 (2013).

Larrañeta E., Imizcoz M., Toh J. X., Irwin N. J., Ripolin A., Perminova A., Domínguez-Robles J., Rodríguez A., Donelly R. F., *ACS Sustainable Chem Eng.*, **6-7**, 9037-9046 (2018).

Acknowledgment

The PN-III-P1-1.1-TE-2016-1697 project [TE117/10.10.2018] is gratefully acknowledged.

THE PROPERTIES OF POTASSIUM CARBONATE/BICARBONATE CONCENTRATED SOLUTIONS PROMOTED WITH ETHYLENEDIAMINE FOR CO_2 CAPTURE

Ramona Elena Tataru – Farmuș, Gabriela Antoaneta Apostolescu, Nicolae Apostolescu, Maria Harja

"Gheorghe Asachi" Technical University of Iași, România,
"Cristofor Simionescu" Faculty of Chemical Engineering and Environmental Protection

Introduction

Potassium carbonate solution (PC) is a widely used solvent for CO_2 removal by absorption (Fig. 1) due to the low toxicity, low tendency of degradation, less energy requirement, high solubility in carbonate/bicarbonate system and other concerns like corrosion problem. The method, widely used in the ammonia industry, has also been extended to retain CO_2 from other gas streams.

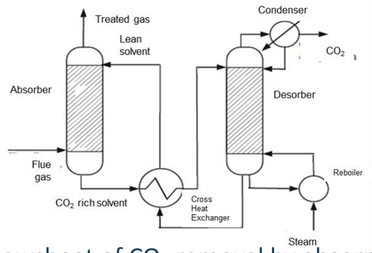

Fig.1. Flowsheet of CO_2 removal by absorption

The transport properties of aqueous blend solution of potassium carbonate (PC)/ potassium bicarbonate (PBC) activated with ethylenediamine (EDA) are studied, in order to find the optimum amine's concentration for absorption process.

Materials

Property	Ethylenediamine	Potassium carbonate	Potassium bicarbonate
Chemical formuala	$C_2H_8N_2$	K_2CO_3	$KHCO_3$
CAS	107-15-3	584-08-7	298-14-6
Molecular weight, kg/ kmol	60.10	138.205	100.115

Each of the solutions contains 25 wt % of potassium carbonate, 4 % wt potassium bicarbonate and amine between 0 and 7 % wt.

Method, results and discussions

The densities for each solution have been measured with an Anton Paar digital vibrating glass tube densimeter, DMA 4500 model. The experimental data have been correlated with temperature through a semi- empirical equation, which depend on the temperature and concentration of EDA.

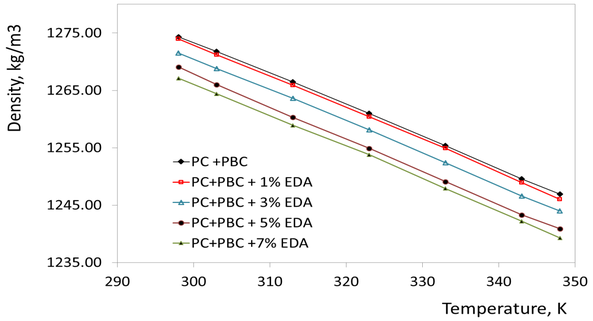

Fig.2. Plot of density of PC+PBC+EDA solution vs temperature

Table 1. Correlation parameters and SD for the density of aqueous blends of PC– PBC – EDA

$w_{PC}+ w_{PBC} +w_{EDA}$	ρ = a T+ b			
	a	*b*	R^2	*SD*
0.25 + 0.04 + 0	-0.5511	1438.8	0.9997	0.1876
0.25 + 0.04 + 0.01	-0.5582	1440.5	0.9996	0.2094
0.25 + 0.04 + 0.03	-0.5527	1436.4	0.9997	0.1821
0.25 + 0.04 + 0.05	-0.5649	1437.3	0.9998	0.1712
0.25 + 0.04 + 0.07	-0.5551	1432.7	0.9996	0.2111

The viscosity was determined with a Ostwald type viscometer. Calibration of the viscometer was based on water values and standard methods accepted by ASTM. The accuracy of the determinations is estimated to be ±1%. The experimental data of viscosity were correlated as a function of temperature.

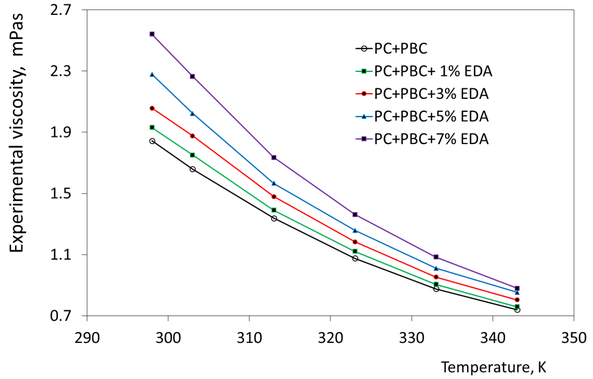

Fig.3. Plot of viscosity of PC+PBC+EDA function of temperature

Table 2. Fitting Parameters and SD for viscosity of aqueous blends of PC– PBC – EDA

T, K	$\eta = a + b\,w + c\,w^2 + d\,w^3$					
	a	*b*	*c*	*d*	R^2	*SD*
298	504.92	13.39	6.47	1.85	0.9985	9.83E-03
303	1848.10	-151.05	10.17	1.66	0.9999	1.79E-03
313	1352.40	-108.98	6.70	1.34	0.9997	2.36E-03
323	624.14	-51.05	4.60	1.08	0.9998	1.34E-03
333	298.48	-20.31	2.93	0.88	0.9998	9.65E-04
343	-441.53	40.99	1.28	0.74	0.9999	6.35E-04

A SP-870 plus METERTECH UV–Vis spectrophotometer was used to monitor the PC-PBC-EDA systems, and to plot the diagram of absorbance, optical path =1 cm.

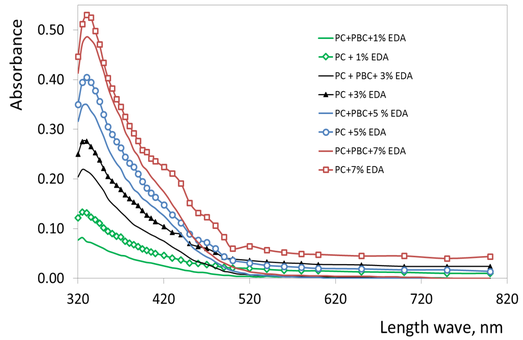

Fig.3. The UV-Vis spectra for PC+PBC+EDA systems

Conclusions

For all the studied solutions it is observed that the density decreases with increasing temperature. The maximum relative error is 0.018 %.

The viscosity continuously increases with concentration and decreases with temperature, for each system, as expected. The experimental viscosities for the PC-PBC-EDA solutions are compared with calculated results, and the identified values of the coefficients a, b, c d verify the experimental points with a relative error of 0.710 %.

Acknowledgment or Contact

This work was supported by a research grant of the TUIASI, project number GnaC2018_10/2019.

ramona-elena.tataru-farmus@academic.tuiasi.ro